Fracture, friction and fragmentation —

brittle processes at lava dome volcanoes

Thesis submitted in accordance with the requirements of the University of Liverpool for the degree of Doctor in Philosophy by

Adrian Hornby

November 2016

Abstract

The extent to which transitions from dominantly viscous to dominantly brittle magma deformation regulate eruptive activity has not been widely explored in volcanology. Within this thesis, investigations combining experiments, petrology and geophysical signals are presented to help decipher and understand the role of brittle deformation during lava dome eruptions.

Lava domes are commonly associated with explosions and dome collapse events, both of which generate volcanic ash. In order to recognise and discriminate fragmentation mechanisms from ash samples, the physical properties and mineralogy of natural ash produced during a typical Vulcanian explosion and a dome collapse event were compared. Measurements of the componentry of several thousand ash particles were conducted using QEMSCAN® Particle Mineralogical Analysis, a rapid automated SEM-EDS mapping technique. Analysis of images obtained by QEMSCAN® reveals that the relative distribution of plagioclase and glass present along the ash particle boundaries varied for both generation mechanisms. Deconvolution of particle size distributions and particle shape analyses shows that ash ejected in Vulcanian explosions has a more complex fragmentation and transport history, while ash produced in pyroclastic flows shows the dominance of a single process. These results suggest mechanism-dependent controls on the surface composition and componentry of volcanic ash – future work is required to discriminate fragmentation mechanisms from ash characteristics through the use of QEMSCAN® data.

Explosive fragmentation at lava dome volcanoes is likely to be triggered by tensile failure of magma following stress accumulation. In order to investigate pressure-driven fracturing of conduit magma, Brazilian tensile tests were conducted on lava samples from Santiaguito volcano at ambient and magmatic temperatures. These tests reveal that deformation style becomes sensitive to small changes in temperature and strain rate at temperatures of 750-800 °C. Higher temperatures generated increasingly viscous deformation, while faster strain rates promoted more brittle behaviour. Experimental constraints on the strain rate and strain leading to failure can be compared to natural deformation timescales recorded in cycles of inflation preceding explosions at Santiaguito, which shows that a viscous component accompanies deformation and suggests that fractures propagate away from a pressure source prior to explosive eruption. Following fracture propagation, any remaining energy is likely to be accommodated by fault slip along the fracture plane. These faulting events are investigated using a high-velocity rotary shear apparatus, showing that the response to faulting generates temperatures sufficient to produce frictional melt within ~10 cm of slip under the slip rates and normal stresses constrained through monitoring of the volcanic behaviour at Santiaguito. The range of mechanical response to slip events in the volcanic conduit and their relation to

concurrent seismic signals are investigated in greater detail during the extrusion of a lava spine at Mt Unzen (Japan). Examination of textures at the spine margins and similarity of the seismic signals that accompanied its extrusion has determined that spine emplacement proceeds by incremental fault slip events in the shallow edifice. Waveform analysis together with spine growth observations allow calculation of the average slip distance (8.9 cm) and slip velocity (0.75 $m.s^{-1}$). These calculations are combined with results from laboratory measurements in a high-velocity rotary shear apparatus to define the range of depths where average faulting events would induce viscous remobilisation (at >275m) and frictional melting along the fault plane (at >500 m). The frictional properties of the dome rocks and the viscosity of the frictional melt in the fault zone suggest that at shallow depths frictional melts act as a viscous brake to fault slip, potentially augmenting stick-slip spine growth.

Taken together, the failure, faulting and fragmentation of dome-forming magma demonstrates that our interpretation of eruptive activity at lava dome volcanoes requires a fundamental understanding of brittle processes.

Acknowledgements

Studying for my PhD has ignited a love for experiments and research, and stoked my passion for exploring and overcoming; every good story has a spark and this one is called Yan. From Mexico to Munich, Japan, Liverpool and Guatemala, Yan has fuelled me with his enthusiasm, and intelligence, diligence and humour. You have continually pushed me to better myself as a researcher, and your sensitivity and tact have often found me smiling in recognition long after the fact. Your energy, excitement and determination for great science are matched by a lucid and creative vision and reams of hard work – I am incredibly lucky to have studied under you.

Throughout my PhD Jackie has guided me, prompted me and prodded me when I needed it. You have always led by example and you taught me how to be an experimentalist. You work harder than anyone else to get the Liverpool groups papers out and you have always kept the show (occasionally the circus) on the road… I couldn't have come close to where I am now without your help.

A number of funding bodies and organisation assisted with me during the PhD and enabled conference attendance, fieldwork and my studies. First and foremost, the department at Liverpool has helped me from start to finish and provided my scholarship. Funding from the European Research Council grant SLiM (Strain localisation in magma) and the Liverpool Earth Observatory (LEO) has allowed me the privilege to work on state-of-the-art laboratory equipment, conduct international fieldwork and attend conferences. I am grateful to have received travel and registration support from IAVCEI, the European Geosciences Union (EGU) and the Euroconference of Rock Physics that enabled conference attendance.

Liverpool was subdued when I started, but there are a few people who helped me integrate – Helen Kinvig in particular mended me, befriended me and gave me a house and home. James showed me the rope(walk)s and generally livened things up, while John and Richard introduced me to a good pint in the Georgian quarter. There were travails of course: Helen, Janine and Sarah are all heartily thanked for an engaging, yet ultimately fruitless, search for a missing American passport in Tenerife.

My enjoyment spiked several notches the moment Felix entered the fray. Felix's sense for a visual innuendo is only matched by his unfettered comradeship. I owe my eyesight to this singular Bavarian, and much more besides. I'll miss Liverpool, but I'll miss you more – until we find post docs somewhere together…

In the spring of 2013 I made the second best decision of my late twenties, and pushed through the lease on a five-bed home in Tochy. The family that lived there filled my heart to the brim

and fired my conviction in a communal way of living. I'm delighted to have lived and shared, broke bread and drank wine (not forgetting the delicious single malts) with all of you. Where is Puzzle anyway?

I've spent many good hours with Steve, but I wish I'd spent many more. I'd love to be out with you on a primeval Scottish scarp, and having a chilly evening beer outside a whitewash seaside pub.

Oliver has been my closest collaborator, and I've learnt vast amounts from our work together. You have most of the qualities I lack and aspire towards – I'm writing this at zero dark thirty – and you keep me keen (whether you're aware or not!).

Fabian pierced my cosy shell with arrows from his creative mind and I'll never be the same again. I miss your curiosity and wit, and your intuitive connection to the good in folk and the enduring in our lives. You are a vital inspiration and your generosity has been magnificent!

I have to thank Takahiro Hirose for memorable times in Kochi (nibbling fillets of still-wriggling fish) and Sarah for spicing the second visit with Pocky, freewheeling, Monet and spidergeddon.

Silvio has been a solid companion and mentor, never far from a big grin and a decent coffee. To Silvio, anything to do with data or instruments is a walk in the park, and that confidence spreads down a treat. I just wish I'd managed to go biking with you!

I've spent happy hours with Anthony on volcanoes in Guatemala and pounding the pavements in Liverpool. Good luck with the PhD and have fun with the new breed! Speaking of which, it's been great to see ViL growing and evolving with brilliant new members – Paul, James, Becky and Guðjón, I hope to get to know you all better in the future.

I've had the some incredible experiences in Guatemala, and one person has made that possible – the man who cannot be fazed, mountaineer and host of infinite resources, Armando Pineda. You have enabled and conducted enough science on Santiaguito to fill a book and none of it would've been half as much fun without you. I can't wait to see you again and return to beautiful Xela.

The scientists at INSIVUMEH have been doing an incredible and vital job despite many obstacles, and their help and hospitality been priceless –particular thanks Gustavo and Julio for going far beyond their duties to help out.

We've been lucky enough to share our house with extraordinary humans. Joe, you have a heart the size of Manchester and it's been a privilege to hear your stories and share our notions of a good life. Keep on writing, I'll go there too. Anna, you were the kindest guest, a curious and gentle kindred spirit, I'm sure we'll see more of you; and Charlie, I hope you're having a brilliant time sailing from one blue to another.

I need to thank a few people who inspired my devotion to rocks and volcanoes before I started in Liverpool. At Royal Holloway Martin Menzies pumped the clutch and jammed my vocation into gear, while Euan Nisbet showed me that human values always have a place in academia. Fieldwork around Monte San Vicino convinced me that I was taking the right course and mapping with the right people - Jake demonstrated that nothing beats hard work and a sound noodle, Niels reminded me how much I love the fringes (and a perle der natur), and Olzhas that growing up is overrated. Let's meet in Apiro for gnoccheti al funghi!

Jamie and Irving, it was incredible to experience Mexico with you guys and it's awesome that we're still in touch. Jamie – congratulations on your marriage, I hope to meet Hannah one day soon! Irving – we have to serialise our Socorro story somewhere (over micheladas and a huge bowl of guacamole).

I am blessed with my upbringing and the sustenance drawn from childhood experiences. I have a reservoir of gratitude for my parents and siblings, who have helped me in any number of situations in my 'adult' life.

During my PhD I've had the mortifying experience of falling properly in love; to Gloria, now my wife and mother of our identical twin boys Maximilian and Ignatius, are due the greatest and deepest thanks. I've shared everything with you and you still love me, which makes you the most incredible woman alive. To say that I couldn't have done it without you is to miss the point entirely – you have opened worlds I hadn't hoped to receive!

Through marriage I've been welcomed into a new family, who have embraced me with love and generosity and kinship – the best qualities of Texas! I am forever grateful and full of admiration.

Apologies are due to the (no doubt) many people I am indebted to for their time, effort and company during my PhD – I can only say that I have limited time my dubious memory forever haunts me. The academic and student communities, especially the volcanologists, have been some of the warmest, funniest and most generous people I've been lucky enough to spend time with, and I look forward to seeing many familiar faces in the future.

After nearly four years I am happy to bring this stage of my life to a close– with twins in hand it certainly feels like a change that's real..!

My grandfather, G.D. Robinson, with Lt. Ray Wilcox and Sgt. C.D. Clawson trekking from Fort Glenn toward Okmok volcano on Umnak Island in the Aleutians in June 1945 as part of the USGS Volcano Investigations unit in Alaska and the Aleutians (1945 -1954).

Table of contents

List of figures

Chapter Five

List of Tables

Glossary of terms and abbreviations

Arc volcano – a chain of volcanoes that erupt above a subducting plate, typically forming a broad arc. The chain of arc volcanoes often reflects the shape of the plate boundary, volcanoes forming at a fixed distance from the trench. Arc volcanism is fed by fluids and volatiles released into the overlying lithosphere by the subducting slab, causing partial melting of the mantle wedge and the generation of magmas.

Ash cloud – the total airborne ash produced by a volcanic eruption. Ash clouds that reach the upper troposphere and lower stratosphere can circumnavigate the globe and ash may remain resident in the atmosphere for many months, posing a serious hazard to aviation.

Ash plume – the buoyant ash column produced following a volcanic explosion. Ash plumes may collapse and generate pyroclastic flows for high ash burdens. Plume rise is dependent upon eruptive factors (rate, mass fraction, duration, grain size distribution) and meteorological conditions (wind speed, atmospheric pressure, humidity, weather conditions).

Brittle deformation – elastic deformation, where stress is stored in the material and increases (directly) proportional to the amount of deformation until catastrophic failure via fracturing.

Brazil (or Brazilian Disc) Test – unconfined radial compression of a sample core until failure via tensile fracturing

Co-pyroclastic ash cloud – an ash cloud produced during transport of a pyroclastic flow. These typically contain smaller and less dense particle than the flow deposits.

Coulee – a highly viscous lava flow that is sustained by efficient insulation. Coulees often form substantial levees and thick carapaces and may form flow kms long and several hundred metres high.

CSD – **Crystal size distribution** - the fractions of crystals in a sample (or a measured zone) of a given size

Compressive strength – the compressive strength required to cause failure by shear fracture or compaction.

CWI – **Coda wave interferometry** – an analysis of seismic coda (or tail) similarity over time to deduce change in source location of clustered waveforms, under the assumptions that clustered waveforms have the same source mechanism, but seismic source locations can change and that seismic scatterers are stable throughout the monitored period.

Deconvolution – breaking down a more complex distribution curve into subcomponents with simpler distributions (e.g. lognormal or gamma distributions), that can be interpreted in terms of processes.

Dome - a spatially restricted mound of lava formed during the extrusion of highly viscous lava around a vent. Domes are often unstable and surrounded by steep-sided talus and scree slopes.

Dilatometer – microanalytical apparatus that uses a pushrod to measure the change in length of a sample with increasing temperature.

Degassing – exsolution of volatiles from a silicate melt to form a gaseous phase (most often as bubbles) during magma ascent and eruption.

Differential Scanning Calorimetry (DSC) – a microanalytical technique that measures the difference in the amount of heat required to increase the temperature of a sample and a reference material with increasing temperature. This is highly sensitive to the internal structure and chemical composition of a sample, and is particularly powerful when paired with a TGA as in the STA

Ductile deformation – plastic deformation whereby stress is dissipated throughout a sample via bulk deformation

EPMA – **Electron Probe Microanalysis** – an analysis tool that fires a focused electron beam onto a sample, causing the elements in the sample to emit x-rays at a given frequency. This provides rapid and accurate spot analyses, however care must be taken when analysing glass to account for high mobility of some elements.

Friction coefficient – the ratio between shear stress and normal stress during prior to or during faulting

Fractal dimension – a measure of the degree to which variations in properties are scale- independent. This is calculated from the slope of a logarithmic frequency-size plot for the characteristic being measured. Classic applications include the outlines of islands (or ash particles!) and GSDs or CSDs.

Frictional melt zone – the molten material is incorporated into the fault and may either lubricate (especially during tectonic faulting) or apply a viscous brake to slip depending on the frictional melt composition and fault depth.

Glass transition – the structural change in a silicate melt from a dominantly viscous material to a rigid structure. Silicate melt may cross the glass transition and rigidify via changes in chemistry, temperature or strain rate, and may cause rapid transitions from ductile to elastic behaviour. The glass transition is a kinetic phenomenon that can be described as a measure of the ability of the melt to structurally reorganise sufficiently quickly to relax, or dissipate an applied stress. If not, the stress is stored within a rigid silicate framework and responds elastically.

GRD viscosity calculator – Giordano, Russell and Dingwell volcanic melt viscosity calculator (Giordano et al. 2008), using melt (or glass) chemical composition to calculate temperature dependence of viscosity

Groundmass – the portion of a rock that is relatively fine-grained or vitreous – hence, typically only used where phenocrysts are also present.

GSD or PSD – **Grain size (or Particle Size) Distribution** – the fractions of particles in a granular sample within given size brackets

HVR friction apparatus – High-Velocity Rotary friction apparatus – designed to simulate natural faulting in the laboratory

Infrasound microphone – an instrument with a microphone that measures variations in atmospheric pressure, typically produced by atmospheric disturbances caused by explosions and ash plumes.

Juvenile – a blanket term for erupted material derived from (newly) ascending magma, rather than existing volcanic or lithic material.

Lahar – a mudflow formed primarily from loose volcanic material – volcanoes with frequent ash plumes are highly susceptible to lahars.

Magma – molten and partially-molten material below the earth's surface. Where magma reservoirs form (i.e. magma chambers) evolution and differentiation often occur prior to further ascent. Magmas are typically less dense and more buoyant than surrounding lithosphere. Dramatic changes in magma rheology can occur at shallow depths if magmas ascend to the surface to feed volcanoes.

Accretionary Lapilli – hydrometeors formed by ash particles adhering in layers due to moisture and electrostatic forces, forming a coarse part of fallout deposits from ash plumes.

Lava flow –a long gravity-driven flow transporting erupted lava away from an elevated vent.

Lobe – a highly viscous lava body that flows over short distances, often showing crease and petal structures as parts of the lobe rigidify. Lobes can overlap, bulldoze and pile up around a vent to form a composite lava dome.

Lava – all erupted magma is generally termed lava, unless it is fragmented into pyroclastic deposits.

Microlite – small crystals in magma or lava formed rapidly during shallow magma ascent and storage. Crystallisation of microlites is usually triggered by decompression and cooling of magma during ascent. The composition and size of microlites can be used to detect shallow magma storage and estimate magma ascent rates and temperatures.

Normal stress – the compressive stress perpendicular to a fault or fracture or elongate feature

Outgassing – loss of gas from a volcanic system to the atmosphere, often via fractures in the shallow magma and edifice.

PDC – Pyroclastic Density Current – an umbrella term covering pyroclastic flows produced by dome collapse, column (plume) collapse and lava flow front collapse.

Permeability – a measurement of the pressure-driven flow of a fluid through a (rock) sample

Phase – a fluid, solid or gas; a number of species of any of these phases.

Phenocryst – large crystals hosted in magma or lava formed over long time periods, usually in a magma chamber. Phenocrysts may fragment or remain intact during ascent if magma is erupted, and play an important role in stress partitioning, fragmentation and rheology.

Phreatomagmatic – explosive eruptions triggered by the sudden transformation of liquid to steam, most often at the beginning of an eruptive episode as ascending magma interacts with water in a hydrothermal system.

Porosity – the volume fraction of a sample (or material) that is void space - e.g. the volume fraction of fractures and vesicles (bubbles). Voids that connect to each other and to the sample surface are referred to as 'open porosity', whereas unconnected voids (e.g. isolated bubbles) are 'closed porosity'.

Pseudotachylyte (or frictional melt) – molten material produced during faulting by bulk or phase-selective melting of adjacent material due to very high slip zone temperatures. Pseudotachylytes often contain crystal fragments and bubbles, and evolve physically and chemically with continuing slip.

Pycnometer – an apparatus used to measure the porosity of a material. A gas-pycnometer measures the change in gas volume accommodated in a sample chamber to calculate the connected porosity of a sample of known surface dimensions.

QEMSCAN® - a system for compositional mapping of geological material, using scanning electron microscope (SEM) electron and x-ray signals to rapidly assign minerals, ores and phases using an optimised reference database. QEMSCAN® is an example of an automated mineralogy method.

Rheology – the behaviour of viscous fluids during flow, in particular the transport mechanisms and organisation of fluids in response to stress and strain. In volcanology, the study of three-phase magma rheology is important in understanding volcanic systems.

Seismometer – an instrument that detects ground motion in order to measure seismic signals produced by earthquakes

Shape factor – a measurement that describes an aspect (or several aspects) of an objects shape. Due to the wide number of measurements possible to describe shapes, a large number of shape factors can be used, and in many disciplines a set of standard shape measurements, or shape factors, are used.

Shear stress – the differential stress parallel to a fault or fracture or in the direction of flow.

Sintering (or welding) – adhering of granular media via viscous or diffusion-driven flow at particle boundaries under elevated temperatures, without bulk melting. Sintering progressively reduces porosity and increase contact area between grains. In volcanic ash, this readily occurs above the glass transition temperature through viscous relaxation of volcanic glass, and is classified as viscous sintering.

Softening point – the temperature at which a material appears to shorten in a dilatometer due to viscous relaxation or the onset of melting.

SP, LP ULP/VLP signals – Short Period, Long Period and Ultra/Very Long Period seismic signals, a nomenclature based on the dominant frequency of the seismic signal.

Spine – lava erupted as a coherent body along bounding faults. Spines may show varying degrees of ductility, from whaleback spines to towering monoliths.

STA – **Simultaneous thermal analysis** – a combination of Thermogravimetric Analysis (TGA) and Differential Scanning Calorimetry

Strain (and strain rate) – a measure of the change in length of media from an initial state, stated at the change in length/initial length. Strain rate is the measure of strain per unit time, defining a universal rate of deformation.

Strain localisation – silicate magmas ascending in confined conduits experience the highest strain at conduit margins, leading to heterogeneous structures and flow rates from the conduit wall to the centre of the conduit that concentrates brittle deformation at the conduit margins.

SVD – Singular value decomposition – factorisation of a matrix of vectors from a set of clustered waveforms that relies on the waveform similarity in all but the first principal component to track temporal changes in magnitude and moment.

Tensile strength – the dilatational stress required to cause failure via a tensile fracture

TGA – Thermogravimetric Analaysis – a microanalysis technique that measures the weight of a sample as temperature is increased

Time-differential stereoscopy – comparison of image sequences recorded from the same vantage point to measure temporal changes. This is a method of photogrammetry, which typically compares photos taken from different vantage points to calculate 3D structure and deformation vectors. This is used to great effect in structure from motion (SfM) calculations to create digital elevation models (DEMs).

UCS test – Uniaxial compressive strength test – unconfined axial compression of a sample core until failure via shear fracturing

Viscoelastic deformation – deformation where stress is accommodated both elastically and viscously (for example simultaneous flow and fracture growth).

Viscosity – the 'thickness' of a fluid – a measure of the resistance of a fluid to flow. In silicate melts, this is analogous to the degree of internal structure in a melt.

Viscous deformation – behaving as a fluid, for example responding to stress by structural rearrangement and flow.

Viscous brake – resistance to movement on a fault by the presence of a highly viscous fluid – i.e. a pseudotachylyte.

Viscous heating (or viscous dissipation) – the thermal energy produced during shearing of a (highly) viscous fluid is called viscous heating, or viscous dissipation. Viscous heating increases with higher viscosity fluids, as the degree of heating depends on the work done to shear the fluid per unit volume.

Volcanic ash – fragmented material <2 mm diameter produced and ejected during a volcanic eruption

Volcanic conduit – the pathway for magma to rise up the vent at the earth's surface, often modelled either as a dyke or a cylinder.

Volcanic glass – quenched and rigidified silicate melt in shallow magmas and lava, preserved as silicate glass.

Volcanic melt – the 'stable' molten silicate phase of a magma, often hosting solid crystals and gas bubbles to collectively comprise a three-phase fluid. Silicate melts usually undergo crystallisation and vesiculation prior to eruption, however most silica-rich eruptions contain quenched melt as volcanic glass

Volcanic plug – a relatively rigid cap of dense magma blocking, or inhibiting, stable magma and gas flow in some volcanoes. Plugs induce episodic pressurisation and cyclic eruptive activity, and push deformation into the brittle field.

Vulcanian activity – repeated, low-to-moderate intensity explosive activity typical at andesitic to dacitic stratovolcanoes and sometime concomitant with lava flow and dome growth.

Chapter One

Introduction

1.1. Motivation

Volcanic deformation spans a huge variety of scales and styles, with outcomes ranging from the benign to catastrophic. Lava dome volcanoes in particular exhibit a broad spectrum of deformation behaviour, with rapid transitions from steady to unsteady behaviour driven by a system pushed far from equilibrium, where volcanic materials are perched at the boundaries between ductile and brittle deformation modes. Transitions from dominantly ductile to brittle behaviour pose substantial hazards to local communities through sudden explosive eruptions and dome collapse events, while the propensity to produce fine, glass-rich ash particles presents severe hazards to aviation, livestock, infrastructure and respiratory health. Better understanding of such transitions in mechanical behaviour under natural disequilibrium conditions, together with the deformation textures produced and the mechanical feedbacks are essential to interpret monitoring data, understand field observations forecast and mitigate hazards.

Due to the substantial scientific challenges presented by unstable, disequilibrium volcanic systems, strong numerical and experimental fields have become established in recent decades to complement more traditional monitoring and forensic disciplines. As the fundamental science governing the physical mechanics during eruptions is far from complete, experimental investigations can offer unique insights into natural processes. Here, I present novel experiment-based and multidisciplinary investigations into the triggers, feedbacks and processes governing brittle deformation processes at lava dome volcanoes.

1.2. Project background

My current research effort began in Mexico, at Volcán De Colima, where I met Yan Lavallée, Jackie Kendrick and others on a research visit. Yan's group were looking for evidence of strain localisation, frictional melting, tuffisites and other deformation textures. The diversity and expression of magmatic activity at lava dome volcanoes has fascinated me, and the approach of Yan's research group in seeking physical mechanics and process-driven insights was highly attractive.

The working title of my PhD was "The mechanics of lava dome eruptions at Santiaguito volcano, Guatemala", offering a broad foundation for investigation. During the first term, I spent five weeks conducting fieldwork at Santiaguito volcano. Anyone who has spent time on a dome volcano can attest to the importance of brittle deformation – textures produced via

friction, fracture and fragmentation litter the volcanic landscape. The deposits from one particular event, the dome collapse on 28 November 2012, spurred the investigation presented in **Chapter 5**, whilst rock samples collected during this (and subsequent) field campaigns provided the basis for the investigations into fracture and friction detailed in **Chapter 4** and the appendices. The direction of my PhD research was therefore somewhat informed by field studies – however the importance of the European research legacy (especially from LMU Munich) which Yan brought to Liverpool cannot be ignored. Through this open-minded and multidisciplinary approach, I have been able to integrate rock mechanics, rheology, earthquake mechanics, geophysical monitoring data and image analysis within my doctoratal research.

During my PhD at the University of Liverpool, the laboratory facilities and research group have expanded dramatically, and the direction of my research has evolved with changes in the research environment. Early work, conducted with Yan and Jackie and later assisted by Felix von Aulock, continued existing research efforts focused on Mt. Unzen (Japan) and the production of pseudotachylyte during volcanic faulting. Although we took significant efforts to describe the viscous rheology and effect of the frictional melt on fault dynamics faulting is an inherently brittle process (see **Chapter 3 and Appendix B**) responsible for a range of deformation signals at dome volcanoes. The synchronisation of geophysical monitoring data with experimental efforts occurred through collaboration with Oliver Lamb and Silvio De Angelis, and during multidisciplinary field expeditions to Santiaguito from 2014-2016. Later work within the laboratory was aided by group work and discussions, especially with Anthony Lamur and Rick Wall.

Throughout my PhD, I have sought to inform a mechanistic understanding of shallow eruptive processes at dome volcanoes. Over time, it became clear that my investigations focussed on evaluating the effects of brittle processes on the eruptive behaviour of lava dome volcanoes. The initial aims, and those developed during the course of my PhD are discussed below.

1.3. Agenda and structure

The work presented in this thesis stemmed from a broad investigation into the mechanics of lava dome volcanoes instigated by my primary supervisor, Yan Lavallée. The approach followed research methods conducted by Yan Lavallée (e.g. Lavallée et al. 2011; Lavallée et al. 2012b; Lavallée et al. 2012a) and Jackie Kendrick (Kendrick et al. 2013a; Kendrick et al. 2013b); that is,

predominantly experimental laboratory investigations of physical processes during dome eruptions, complemented by integrated analytical, rheological and geophysical data. Their network of collaborations with rock deformation departments in the UK and Europe also provided a significant source of inspiration.

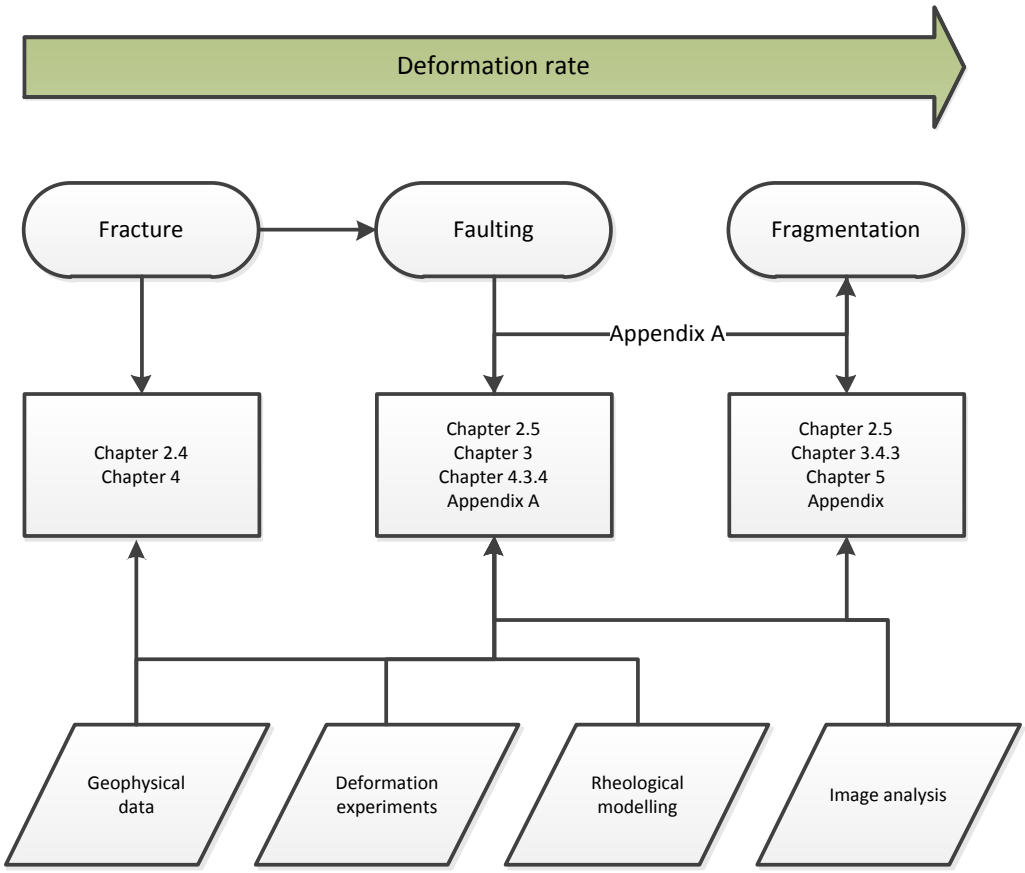

Figure 1. Overview of the thesis, showing how the three main deformation 'themes' are linked within the thesis by disciplines (bottom row) and deformation rate (top arrow). The rectangles indicate where in the thesis the themes and disciplines are explored.

My initial research study was inspired by novel work extending the study of pseudotachylytes to silicic magma ascent (Kendrick et al. 2012; Lavallée et al. 2012b), comprising an experimental study into the frictional properties of Mt. Unzen dome rock during spine growth (**Chapter 3**). This study was conducted using a high-velocity rotary shear apparatus at the Kochi Core Centre, Japan, under additional supervision from Takeshi Hirose. During the initial months of my PhD, I assisted with the planning, installation and testing of apparatus for the experimental volcanology laboratory at the University of Liverpool. In spring 2014, a state-of-the-art high-to-

low velocity friction apparatus was installed, and a study of friction at low velocities using this new apparatus formed part of my study into the frictional properties of faulting during spine growth at Mt. Unzen. Initial experimental research at Santiaguito continued the frictional studies using apparatus in Japan and Liverpool; however, the results were more diverse than for Mt. Unzen, and a strong link to eruption dynamics was elusive. However, mechanical and textural data from this study, together with research into volcanic ash textures provided significant contributions to a paper published in Nature (Lavallée et al. 2015a, **Appendix B**). Following numerous discussions on eruption dynamics, in particular the work of Jeff Johnson and colleagues at Santiaguito, accompanied by development of the experimental volcanology laboratory, I began an investigation into the tensile strength of Santiaguito dome rock at high temperatures (**Chapter 4**). The final research focus came about through the collection and analysis of volcanic ash samples collected at Santiaguito. This study represents a novel research direction within the Volcanology in Liverpool group, and incorporates detailed investigation of particle size distribution and image analysis (**Chapter 5**). Nevertheless, the study is guided by the objective to gain insights into the dynamics of dome eruptions at Santiaguito. A unifying factor within all three studies has been the integration of geophysical data with experimental and analytical datasets. This approach has introduced a range of quantitative constraints and allowed considerably greater application of experimental and analytical data. During the final 15 months of my PhD I have been involved in the deployment and maintenance of a network of geophysical instruments around the Santiaguito dome complex. This has produced the longest continuous geophysical record at Santiaguito and initial results from this deployment have been incorporated into **Chapter 4 and Chapter 5**.

This thesis is compiled from the research efforts described above, together with the relevant scientific background. These investigations have been continually informed and guided by the aims of understanding the physical mechanisms governing eruptive activity at lava dome volcanoes. Each of the three principal investigations (**Chapters 3-5**) were conducted with the objective of eventual dissemination in peer-reviewed journals. Bearing this in mind, and the diverse range of research fields involved within the studies, the logical arrangement is to separate the studies into self-contained chapters that represent the format of a final, published paper.

This thesis is organised into six chapters. **Chapter 1** introduces the subject, structure and motivation of my doctoral studies. **Chapter 2** presents a background and context to deformation at lava dome volcanoes. This chapter also introduces the themes that I focus on in greater depth in **Chapters 3-5**: fracture, friction and fragmentation. I hope that detailed descriptions of the

specific themes are clearer in a research framework within the relevant chapters. The research presented in **Chapters 3-5** was prepared for publication in academic journals (see **Section 1.4**.) and the overall structure of the chapters reflects this. In **Chapter 6**, I summarise and conclude the research conducted during my doctoral studies, before describing ongoing efforts and future research directions. Finally, within **Appendix A**, I present the QEMSCAN phase maps used in **Chapter 5** and in **Appendix B**, a paper published in Nature to which I have significantly contributed as a co-author and which has a direct bearing on the research presented here. For each paper, I explicitly state my contribution and summarise the theme and the research conclusions.

1.4. Declaration

I hereby declare that the work contained within this doctorate thesis is my own, except for the contribution of other authors towards work prepared for publication, as indicated below, and the inclusion of co-authored studies within the appendices, where my contribution has been explicitly stated at the start of the appendix. I conducted the research, experimental work, data analysis, figures and text forming the studies detailed below, with feedback, manuscript corrections, advice, experimental assistance and training provided by co-authors. I have provided a full and detailed account of co-author contributions within the preface for **Chapters 3, 4 and 5** in accordance with the University of Liverpool's code of practise.

1.5. Publications

The majority of the work presented in this thesis was prepared for publication. In particular, **Chapters 3-5** represent studies that have been published or are in preparation for publication in peer-reviewed journals. Previously published content from these chapters is detailed below.

Chapter 3

This chapter has been published in full in the Journal of Geophysical Research. The version presented here has been formatted for this thesis.

Hornby, A. J., Lamb, O. D., Kendrick, J. E., Hirose, T., Henton De Angelis, S., De Angelis, S., Umakoshi, K., Wadsworth, F. B., von Aulock, F. W., Miwa, T., Dingwell, D. B.,

Lavallée, Y. 2015. Spine growth and seismogenic faulting at Mt. Unzen, Japan. Journal of Geophysical Research, doi: 10.1002/2014JB011660

Chapter 4

This is a work in progress and represents a significantly expanded and formatted version of a manuscript currently in preparation for submission to Geology. Parts of the work have been published in conference abstracts:

Hornby, A. J., Lavallée, Y., Collinson, A. S. D., Neuberg, J., De Angelis, S., Kendrick, J. E., Lamur, A. N. Mechanical constraints on the triggering of vulcanian explosions at Santiaguito volcano, Guatemala. Geophysical Research Abstracts Vol. 18, 842, 2016

Hornby, A. J., Lamb, O. D., Lamur, A. N., Lavallée, Y. Tensile strength of dome rocks and lavas at Santiaguito dome complex, Guatemala. Geophysical Research Abstracts Vol. 17, 152, 2015

Hornby, A. J., Rhodes, E., Kennedy B., Hirose T., Kendrick J.E., Clesham S., Lavallée Y. Mechanical properties of lava dome products: from endogenous dome building to effusion at Santiaguito volcano, Guatemala. 10th Euroconference on Rock Physics, Aussois, 2014

Chapter 5

The work presented in this chapter is currently in review at Geochemistry, Geophysics, Geosystems (G^3), first submission March 2016. The version presented here is the same as the submitted manuscript, although it has been formatted for this thesis.

Hornby, A. J., Lavallée, Y., Clesham, S., De Angelis, S., Kendrick, J. E., Rollinson, G., Rietbrock, A., Butcher, A., Cimarelli, C. Characterization of volcanic ash particles produced at Santiaguito volcano, Guatemala: QEMSCAN® insights into fragmentation mechanisms.

Chapter Two

Background

2.1. Introduction

Within this chapter I aim to introduce relevant topics in the fields of physical volcanology, rock deformation, magma rheology and image analysis. Each of the topics has featured within the three mains studies in this thesis, however I have omitted to some passages and descriptions of literature review, some minor methods and critical analysis that are more relevant and useful self-contained within the appropriate study in Chapters 3-5. The introduction is intended to give the necessary background for the non-expert reader to understand the rationale, methods and conclusions presented in the following chapters. The chapter is divided in subsections, covering geophysical monitoring and magma rheology, before homing in on brittle processes: rock fracture, friction, faulting and fragmentation. First, I introduce the grounding for all these studies: dome volcanoes.

2.2. Dome volcanoes

Lava dome volcanoes are defined by the accumulation of mounds of viscous lava around a volcanic vent (Calder et al. 2015). This type of volcanism is most common in subduction-related arc settings, and dome-forming episodes occur at many arc volcanoes. Dome volcanoes often undergo long eruptive episodes characterised by rapid transitions between effusive and eruptive activity. Lava domes often exhibit moderate (VEI 2-4) explosive activity, but can also produce major explosions (e.g. Mt St Helens, 1980; Pinatubo, 1991) with disastrous consequences. Viscous lavas typically form steep-side edifices (Fink and Griffiths 1998; Husain et al. 2014) ringed by talus from near-continuous rockfall. During dome eruptions the emplacement of viscous lava near elevated vents presents a chronic hazard for collapse of unstable portions of the lava dome (Sato et al. 1992; Carn et al. 2004). Dome collapse events trigger pyroclastic density currents (PDCs) that can travel up to 10s of km from the vent and pose an acute risk to mortality and infrastructure in local communities (Auker et al. 2013). Lava domes typically grow by both endogenous and effusive emplacement of viscous magma, forming a heterogeneous dome structure with a cooler and more brittle outer carapace (see Section 2.1).

The chemical composition of dome-forming magma can vary widely although they are usually dacitic to rhyolitic. However, a submarine basaltic lava dome volcano has been described on King George Island, Antarctica, which has a columnar core mantled in a thick carapace breccia.

The dome was extruded under unusual conditions as it was highly crystalline and erupted at low temperature, while the thick carapace maintained the condition necessary for flow (Smellie et al. 1998). Dome magmas tend to have high viscosities upon eruption due to progressive degassing, crystallisation and cooling (Sparks et al. 2000). Dome magma may undergo dramatic changes in viscosity within the final kilometres of magma ascent, manifesting a broad range of processes at shallow depth. The very high viscosities of dome magmas often makes their rheological behaviour akin to those of solid rocks, exhibiting appreciable yield strengths and deforming through brittle processes, including fracture, faulting and fragmentation.

2.2.1. Lava dome structures

Lava domes may form a range of morphologies, depending on the extrusion rate, lava rheology, existing structures and edifice morphology (Anderson et al. 1995; Fink and Griffiths 1998; Husain et al. 2014; Calder et al. 2015). The diversity of deformation modes undergone by magma during ascent result in equally variable lava dome structures. Domes may either form as a single structure or a composite mass of temporally and spatially variable extrusive deposits. At Santiaguito (Guatemala) and Volcán de Colima (Mexico), for instance, mature domes form a shallow, truncated cone morphology (with trapezoid x-section) within the summit crater (Harris et al. 2003; James and Varley 2012). These domes have a highly fractured, blocky outer shell (carapace), and often arcuate and concentric ridges or fractures dome surface (Bluth and Rose 2004; Johnson et al. 2008; James and Varley 2012). This type of dome formation may be associated with steady effusion rates and concurrent lava flow emplacement. In contrast, dome building activity at Soufriere Hills volcano (Montserrat) (Watts et al. 2002), Mt. Unzen (Japan) (Nakada et al. 1999) and Mt. St. Helens (USA) (Vallance et al. 2008) was characterised by effusions of multiple overlapping lobes and spines, forming an irregular dome structure composed of extrusive units with highly variable shape and surface texture. Highly viscous lobate structures, often containing flow textures that are emplaced near to a vent are classed as lava lobes. A number of different types of lava lobes occur at lava domes, from shear lobes, bounded by fault or shear zones in existing material, whaleback lobes, extruded along faults as coherent massive units with arcuate backs, to pancake lobes, which form limited concentric deposits around a vent (Wadge et al. 2014; Calder et al. 2015). Extrusion of highly viscous lavas forms a range of brittle-ductile deformation textures, including compressional ridges, where lobes shear and fold due to rigidification of distal lava within the lobe, tensile crease structures

formed during spreading and cooling joints (Smith et al. 2001; Calder et al. 2015). The most viscous magma is extruded as a solid body, forming massive columnar structures, known as spines, piercing the surface and extruding along faults (Pallister et al. 2013; Hornby et al. 2015a). Spines are emplaced as coherent, self-supporting structures, however they are highly prone to fracture, spalling and collapse due to continued deformation and cooling. Spines and whaleback structures can exhume fault gouge and pseudotachylyte, indicating of the importance of faulting (Cashman et al. 2008; Kendrick et al. 2012). Gouge-hosting faults may provide permeable pathways for gas escape in a lava dome, while pseudotachylyte may act as an impervious barrier (Kendrick et al. 2014a) and alter the frictional properties of faults that regulate spine extrusion (Lavallée et al. 2012b; Kendrick et al. 2014b; Hornby et al. 2015a). Dome formation may also take place through shallow subsurface magma emplacement, causing bulging and doming at the surface (Nakada et al. 1995; Hale and Wadge 2008). Both endogeneous and composite dome growth create structures highly prone to collapse. Tuffisite veins are a common occurrence at some dome volcanoes, especially those with concurrent explosive activity or at rhyolitic lava domes (Tuffen et al. 2003; Lavallée et al. 2012a; Cabrera et al. 2015). Tuffisites veins represent the accommodation of clastic material during fragmentation in fractures within the edifice. These may be variably welded, and can enhance permeability within the lava dome (Kolzenburg et al. 2012; Wadsworth et al. 2014; Kendrick et al. 2016). A characteristic of lava domes is a tendency for dome material failure and generation of rockfalls that may locally accumulate to form talus around the base of the dome structure (Sato et al. 1992; Loughlin et al. 2010). These may extend to the flanks of an edifice where domes are not confined within a summit crater.

Figure 1. A range of structures observed on the peak of El Brujo lava dome, Santiaguito dome complex, Guatemala, during fieldwork in November 2012

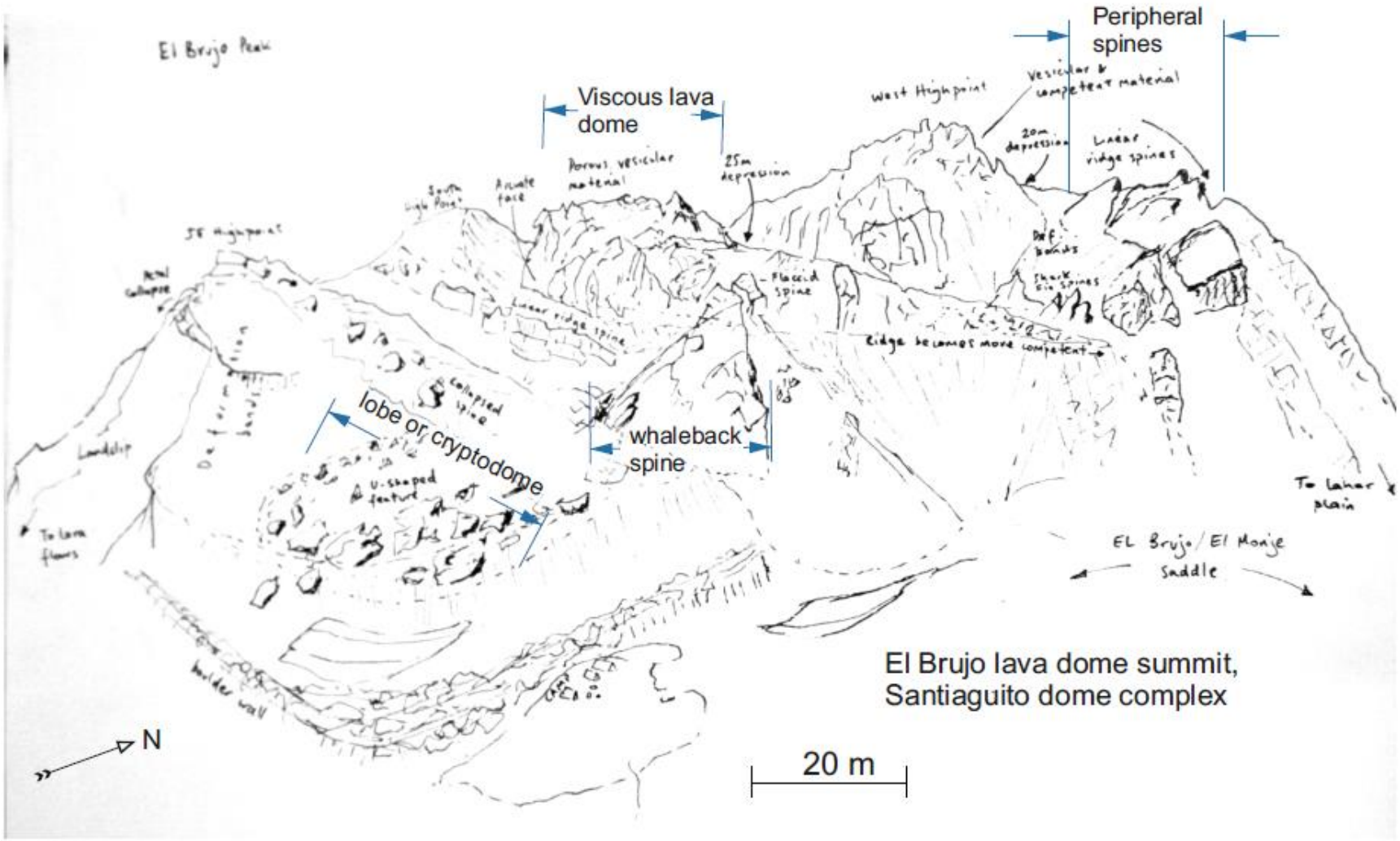

2.2.2. Recent lava dome eruptions

In order to demonstrate the variations and similarities between lava dome eruptions, several recent eruptive episodes at dome volcanoes are summarised below.

Figure 2.2. *The locations of the lava dome volcanoes below are shown on the world map. Major volcanic arcs are indicated on the map as darker grey shading.*

2.2.2.1 Santiaguito dome complex, Guatemala 1922 - present Andesite-dacite

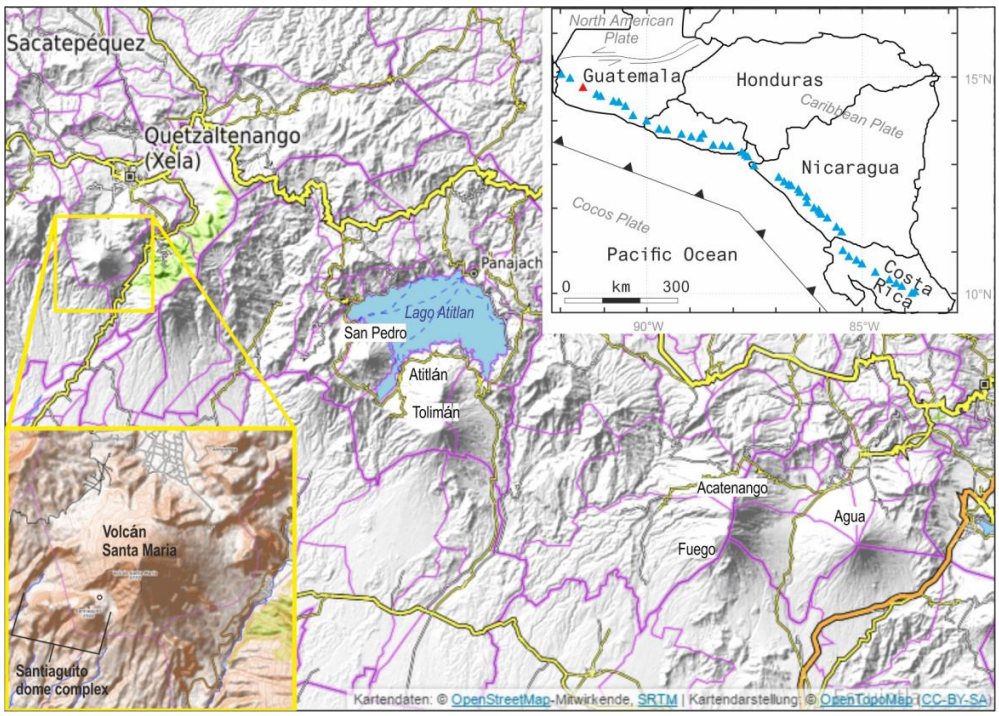

Figure 2.3 (previous page) *Location and tectonic setting of Santiaguito dome complex, together with other volcanoes forming the volcanic arc front in Guatemala, including the currently active Fuego. Right-hand inset shows the tectonic setting, with subduction of the Cocos plate beneath the Caribbean plate forming a parallel chain of volcanoes along the active front of the Central America volcanic arc. Santiaguito/ Santa Maria volcano is shown as a red triangle, with other major volcanoes shown as blue triangles. Bottom left inset shows a magnified view of Santa Maria and Santiaguito, with the outskirts of Quetzaltenango (Guatemala's second city) north of Santa Maria and the Santiaguito dome complex indicated. Map data from OpenStreetMap-Mitwirkende, SRTM | © OpenTopoMap (CC-BY-SA); Right inset compiled from several maps* (Carr et al. 2003; Escobar-Wolf et al. 2010; Scott et al. 2012).

The inception of dome-forming activity occurred in 1922 within the crater formed by the 1902 Plinian eruption of Santa Maria stratovolcano. Over the following 50 years, the ongoing eruption formed an arcuate complex of four lava domes (Figure 2.4). Activity was characterised by frequent small-moderate gas-and-ash explosions, effusion of viscous lava flows and extrusion of highly viscous lava lobes and spines (Rose 1972). This range of activity has been linked to decadal variations in extrusion rate at Santiaguito (Harris et al. 2003). Since the 1970s, activity has settled at the westernmost Caliente vent, which typically produces gas-and-ash explosions every 20-200 minutes, whilst simultaneously feeding lava flows that extend several kms down the southern flanks (Figure 2.4). Recent studies have shown a highly regular ~26 min cycle of inflation-deflation (Johnson et al. 2014) modelled from a source at ~300 m depth in the Caliente vent. Dome collapse has remained a chronic hazard throughout the eruption (Rose 1973), causing thousands of deaths in 1929 and continuing to threaten communities to the South. During the rainy season lahars also pose a significant hazard along drainage channels (Harris et al. 2006).

Figure 2.2. An overview of the Santiaguito dome complex, showing (l-r) Caliente, the active vent with lava flows, the spiny summits of El Mitad and El Monje, and the previously active dome of El Brujo. Around the base of El Brujo deposits from lahars form a wide boulder-strewn plain. Photo credit: Anthony Lamur

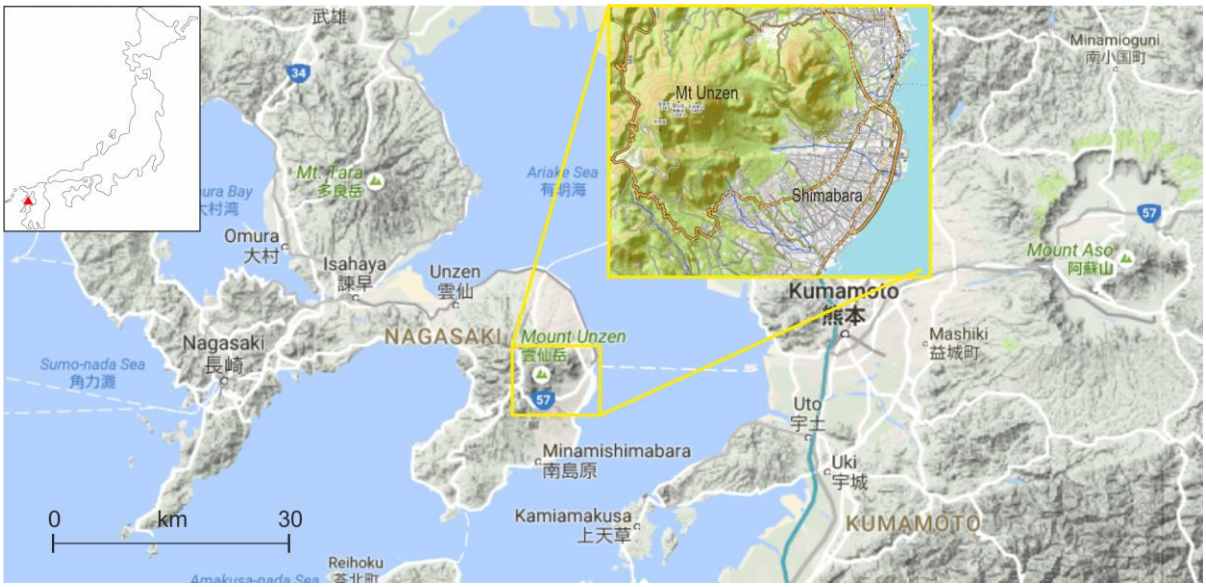

Figure 2.5 *Regional map of Mt Unzen, showing the proximity to Mt Aso caldera. Top left inset shows national setting, while r-h Inset shows a magnified view of the local setting (indicated on the regional map by a yellow box) showing proximity to Shimabara. Map data © Google, inset ©OpenTopoMap CC by SA*

2.2.2.2 Unzen (Fugendake) Japan 1991 - 1995 Dacite

A dome eruption commenced on 20 May 1991 following several months of phreatomagmatic activity, during which fresh magma rose in the conduit (Watanabe et al. 1999a). Dome growth occurred through the emplacement of highly viscous, overlapping lava lobes, causing instability of the summit dome and repeated episodes of collapse and pyroclastic flows throughout the first 15 months of eruption (Sato et al. 1992). A pyroclastic flow on 3 June 1991 killed 43 journalists and volcanologists observing the eruption near Shimabara (Figure 2.5). Effusion slowed from Dec 1992, before a second pulse of effusion began, continuing the pattern of lobe growth and collapse until November 1993. Dome growth then became increasingly endogenous from and the effusion rate decreased steadily until the end of the eruption (Nakada et al. 1999). Lobe-forming activity produced high-and low frequency shallow earthquakes (Umakoshi et al. 2008), however the final months of eruption, during which a lava spine was emplaced (Figure 2.6), were accompanied by rhythmic shallow earthquakes (Lamb et al. 2015b). In 2004-5 the feeder system was drilled under the ICDP programme (Nakada et al. 2005; Goto et al. 2008).

Figure 2.6. Aerial photograph taken from west of Mt, Unzen, seend to the centre-left of the image, with the 1994-95 spine creating a prominent shadow on the dome surface. The runout of collapse-related pyroclastic fow can be seen to the east, together with the levees and defences constructed to channel the flows away from built-up areas. Photo from Cities on Volcanoes 5 organising committee.

Figure 2.7. Setting of Montserrat within the Caribbean island arc formed by the subduction of the Atlantic plate beneath the Caribbean plate, forming the Puerto Rico Trench. Inset shows a magnified view of Montserrat (indicated by the yellow square in the regional map) with Soufrière Hills to the South of the Island and the evacuated capital to the west of the volcano. Inset map data © OpenTopoMap - CC by SA.

2.2.2.3 Soufrière Hills Volcano, Montserrat 1995 – 2013 Andesite

Dome growth began in November 1995, proceeding by emplacement of lava spines (Figure 2.8), megaspines and shear lobes (associated with varying extrusion rate) filling, collapsing and overtopping the summit crater and generating numerous pyroclastic flows from March 1996. During summer 1997 dome collapses to the west generated pyroclastic flows that reached the airport, killing 19, and subsequently inundated the evacuated capital of Montserrat, Plymouth (Figure 2.7, inset). The summit dome was destroyed and the conduit evacuated by large vulcanian to sub-Plinian explosions following the largest collapses, such as the Boxing Day 1997 event. Dome extrusion stalled in March 1998, ending the first of five periods of dome forming activity (Wadge et al. 2010). Extrusion resumed in November 1999. Dome growth during the second phase caused progressively larger dome collapses. Following an initial collapse removing the newly formed dome in March 2000, more rapid dome growth formed a larger dome until a hiatus in March 2001. In July 2001, a major collapse occurred to the East, after which rapid extrusion rebuilt the dome to an even greater height. The extrusive vent migrated considerably during extrusion, causing hazards on all sides of the volcano (Wadge et al. 2014). A catastrophic collapse occurred on 12 July 2003 following a 70-hour earthquake swarm (Figure 2.9). Most of the volcano collapsed into the sea over an 18 hour period, generating tsunamis and hydrovolcanic explosion where collapse deposits reached the coast (Herd et al. 2005). The

$2.1x10^6$ m3 collapse ended with a sequence of Vulcanian explosions, following which extrusion ceased until August 2005. Subsequent activity was typified by further lava dome growth and collapse (Wadge et al. 2014). Throughout the eruption, cyclic deformation signal were monitored over timescales from minutes to months (Costa et al. 2013).

Figure 2.8. Lava spine erupted in April 1996, showing smooth surfaces representing fault planes that extend into the conduit during emplacement. The spine is collapsing to the right of the picture forming a steep talus slope. Photo from Sparks et al. (2000)

Figure 2.9. Two views (left and right columns) showing Soufrière Hills volcano before (top) and after the dome collapse on the 12-13 July 2003. The dashed lines in the lower photos show the dome profile before the collapse (Herd et al. 2005).

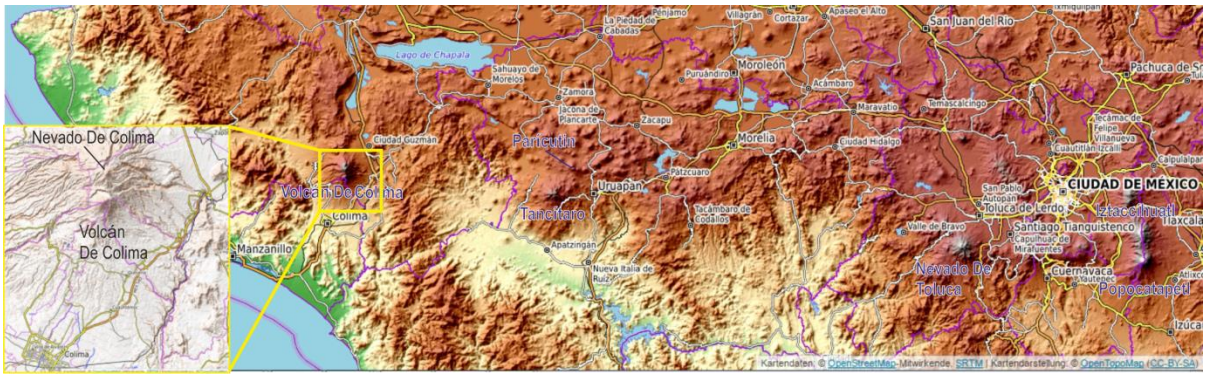

Figure 2.10. *Regional map showing the location of Volcán de Colima at the western edge of the Trans-Mexican volcanic belt, a chain of hundreds of volcanoes including Popocatépetl to the far east of the map. The inset shows a magnified view of the local area, with the nearby peak of Nevado de Colima hosting a permanent observatory and the city of Colima ~30 km to the SSW. Maps © OpenTopoMap - CC by SA.*

2.2.2.4 Volcán de Colima Mexico 1998 – present Andesite

Extrusion of a lava dome within the summit crater (3840 m) began at the start of the current phase of activity on 20 November 1998. Initially high extrusion rates caused the dome to overtop the crater within 24 hours, generating near-continuous pyroclastic flows down the southern flanks (Figure 2.10). Almost immediately dome emplacement transitioned in emplacement of a block-lava flow extending 3.8 km down the south and southwestern flanks by February 1999, when both effusion and dome building ceased (Navarro-Ochoa et al. 2002). Eruptive behaviour from this period was characterised by regular vulcanian explosions which destroyed the summit dome and associated pyroclastic flows. Endogenous dome growth restarted in May 1991, and extrusion in late 1991 included spine growth. Dome morphologies are symmetrical and relatively flat-topped (Figure 2.11). Activity waned by March, and restarted in 2003-2004 by a sequence of powerful Vulcanian explosions. A new dome appeared in September 2004, overtopping north and west crater rims and projecting lava flow up to 2.2 km (Savov et al. 2008). From late 2004 activity became dominantly explosive again, with 6 months of increasingly powerful explosive activity and associated pyroclastic flows during 2005 (Varley et al. 2010b). Activity from 2007 – 2011 proceeded by very slow endogeneous and exogenous dome growth restricted to the summit crater together with moderate Vulcanian explosions. New explosive activity began in December 2012, destroying the 2007-11 dome in January 2013 (Zobin et al. 2015b). New effusive activity then replaced the summit dome between Feb-November 2013. In 2015 powerful Vulcanian explosions destroyed the new dome and generated pyroclastic flows with runouts >10 km. Dome growth and lava flow emplacement took place during July-October,

disrupted by continuing explosive activity (Zobin et al. 2015a). A new lava dome was sighted on 19 Feb 2016.

Figure 2.11. Image looking north, showing Volcán de Colima (front left) with a breach in the crater wall providing the pathway for a lava flow. In the background the inactive peak of Nevado de Colima provides an overlook of the active volcano. Image from CIIV © Nick Varley

Figure 2.12. Two different dome structures – left shows a flat-topped viscous pancake-type dome filling the summit crater with prominent lava flow to the bottom left. Under slower extrusion rates, Colima forms steep-sided, pitted dome structure up to 60 m tall, overtopping the crater walls to the right f the picture. This type of dome is much more susceptible to collapse. Images © Nick Varley/CIIV

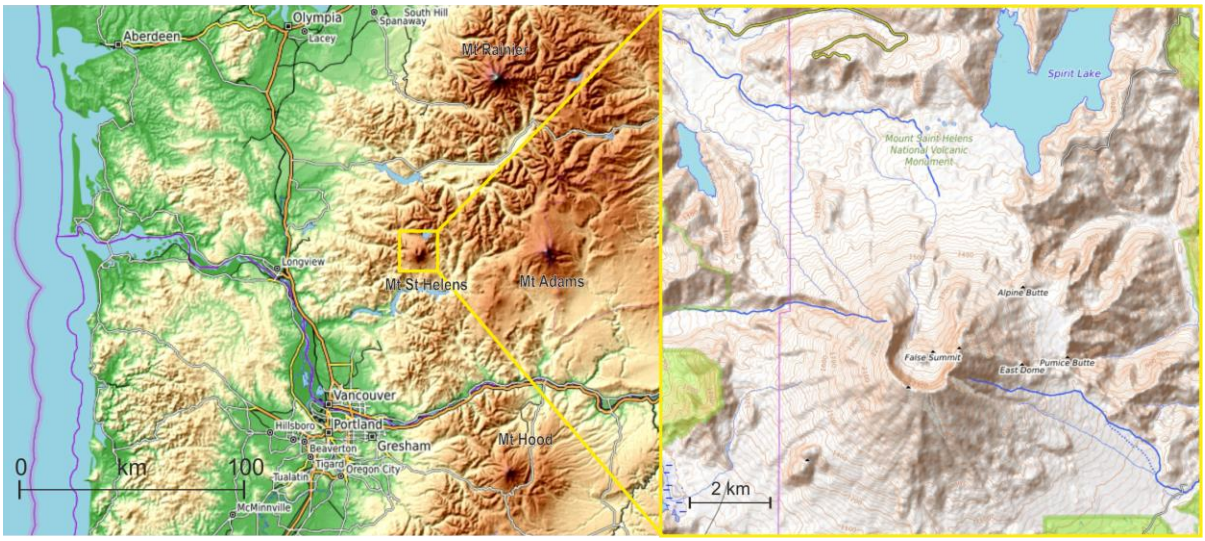

Figure 2.13. The regional setting (right) showing the location slightly seaward of the active front (Mt Hood, Mt Adams and Mt Rainier) in the Cascades; and local setting (left) of Mt St Helens, showing the prominent collapse scar and deep horseshoe shaped crater rim. Map data © OpenTopoMap CC by SA

2.2.2.5 Mount St Helens, USA 2004-2008 Andesite

The eruption began in September 2004 on the glacier-and-dome capped peak of Mt St Helens (2550 m, Figure 2.13). Endogenous growth and vent-clearing phreatic eruptions inflated the 1980 dome and uplifted the u-shaped Crater Glacier shortly before extrusion began with near-vertical spine growth in October 2004. The eruption as a whole was characterised by repeated emplacement and bulldozing of summit material by 8 successive spines with increasingly slow extrusion rate, filling the summit crater to the S and SW of the 1980s dome. The spines behaved as massive bodies extruded in a near solid state, with vent migration, crater walls and existing spines determining spine emplacement vectors (Figure 2.14, 2.13). In late 2004, the southerly emplacement of a large whaleback spine split Crater Glacier into east and west forks. Both glacial forks were compressed and thickened, but neither collapsed (Vallance et al. 2008). Thick bands of permeable cataclasite and fault gouge mantled planar spine surfaces, indicating fault-mediated emplacement (Pallister et al. 2013a; Gaunt et al. 2014). Evidence for frictional melting (pseudotachylyte) was found near the fault-plane of spine 7, indicating high thermal input during slip on spine-emplacing fault events (Kendrick et al. 2012). During the eruption, millions of small seismic events occurred repetitively, earning the name ‘drumbeat earthquakes’ and linked to the stick-slip dynamics of spine extrusion (Iverson et al. 2006; Kendrick et al. 2014b). Cyclic ‘sawtooth’ tilt signals were also detected, but over longer timescales than the ‘drumbeats’

Figure 2.12 View to the southeast with Mt Hood in the background, showing a prominent whaleback spine mantling the new dome in February 2005. The 1980's dome can be seen toward the front left of the picture, while to the right of the spine pressure ridges can be seen in the glacier arm. Photo - USGS

Figure 2.16. Prominent, smooth curving spine surface with arcuate subhorizontal unloading fractures indicating episodic growth. The spine is collapsing to the centre and right of the image. Photo - USGS

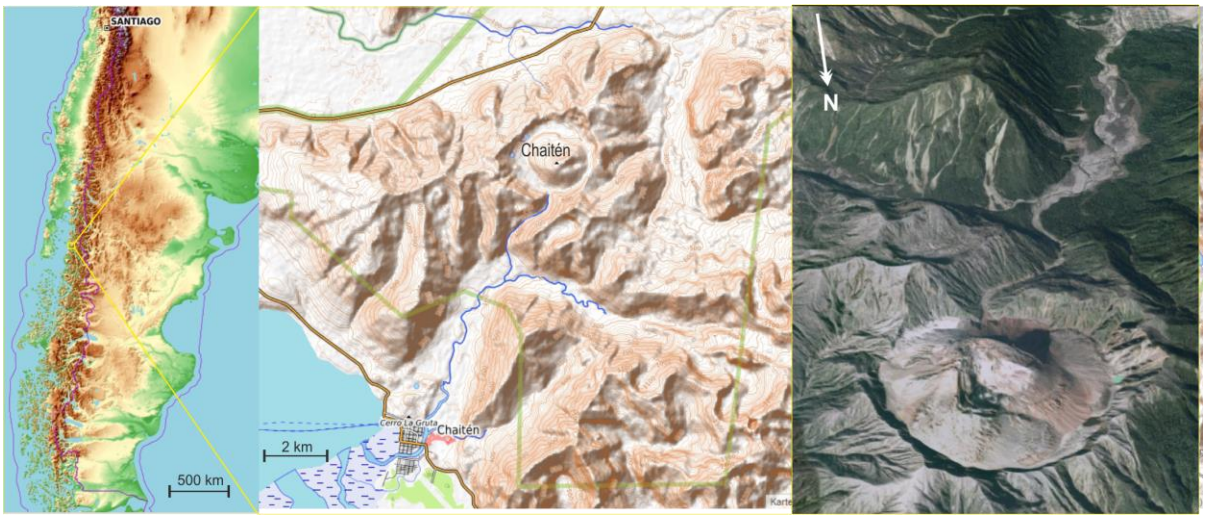

Figure 2.15. *Left to right: Location of Chaitén along the Southern volcanic zone of the Andean volcanic arc. Magnified view (shown as yellow box) showing historic caldera surrounding the new dome and the location of Chaitén town. Right panel shows pitted composite dome and view looking south towards Chaitén town. Map data © OpenTopoMap CC by SA and © Google*

2.2.2.6 Chaitén, Chile 2008-2010 Dacite

Following ascent of rhyolitic magma at rates of approximately 1 $m.s^{-1}$, Chaitén spontaneously erupted on 1 May 2008 with a VEI 4-5 explosion and a Plinian eruption column ascending to altitudes of 18-20 km (Castro and Dingwell 2009; Pallister et al. 2013b). Large eruptions continued during the first week of May (Figure 2.17), producing column-collapse pyroclastic flows, before several days of hybrid and low frequency earthquake heralded a transition to effusive activity (Major and Lara 2013). Several lava lobes, or coulees, were emplaced up through and around the prehistoric summit dome until September 2008, forming a composite lava dome of 0.5 km^3 (Figure 2.16). A prominent spine began to emerge in October 2008, together with endogenous dome growth until February 2009. On 19 February, extrusion was disrupted by overtopping and collapse of 10 % of the new dome, which generated directed blasts and pyroclastic density currents reaching within 3 km of Chaitén town. Following the collapse, effusive dome rebuilding transitioned into dominantly endogenous inflation of existing dome structures, steadily waning until early 2010. Repeated episodes of collapse continued until the end of the eruption (Pallister et al. 2013b). The rapid ascent of rhyolitic magma was attributed to moderate viscosities and high temperature (10^6-10^8 Pa.s, 800 °C) allowing fluidal rise of gas charged magma (Castro and Dingwell 2009). Evidence from tube pumices reveals the efficient degassing of magma through highly sheared vesicular regions near the conduit walls (Castro et

al. 2012b). During the initial explosive phase of the eruption, magmas were rich in volatiles, but through time, efficient degassing (Castro et al. 2008) favoured the transition to effusive, endogenous dome growth.

Figure 2.17. Photograph of powerful explosion and eruption column at Chaitén on May 26 2008, showing steep-sided dome, moat and caldera walls. Photo – J N Marso, USGS.

2.2.3. Cyclic and recurrent signals

Lava domes commonly exhibit cyclic eruptive behaviour. This translate into periodic variation in monitored geophysical (e.g. Neuberg et al. 2006) and geochemical (e.g. Edmonds and Herd 2007) signals. These cycles can occur over a wider range of timescales, and may be detected simultaneously over multiple monitoring techniques. While short cycles (<day) are often interpreted to represent fluctuations in stress caused by shallow magma ascent, such as the repetitive tilt cycles shown in Figure 2.18, longer cycles (>day) are usually resolved by invoking fluctuations within the magmatic plumbing system (Costa et al. 2013). At several spine-forming dome volcanoes, repetition of shallow signal has been linked to episodic, stick-slip extrusion of solidified magma (Iverson et al. 2006; Lensky et al. 2008; Costa et al. 2012; Lamb et al. 2015b), which may be modified by formation of frictional along shallow faults (Kendrick et al. 2014b; Hornby et al. 2015a). Cyclic signals may be detected throughout the seismic frequency range, and are also frequently observed in a range of geodetic and gas flux measurements (Christopher et al. 2014; Flower and Carn 2015).

Figure 2.18: Cyclic tilt recorded at Santiaguito over a 48h period. The red lines indicate explosions that occur following a period of inflation. Modified from Johnson et al. (2014)

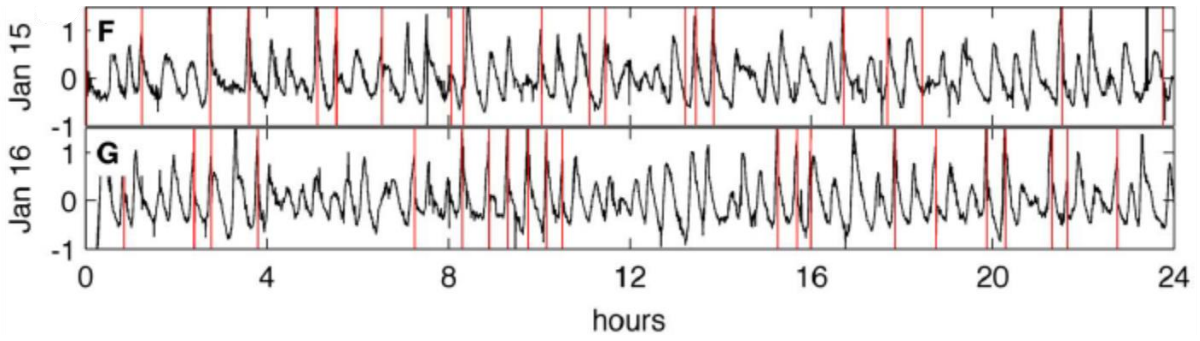

The cause for much eruptive cyclicity has been postulated to originate from a wide range of phenomena: permeable gas flow (e.g. Voight 1999; Michaut et al. 2009), stick-slip motion (Iverson 2008) conduit geometry and elasticity (Costa et al. 2007), pressurisation fluctuation in the magma reservoir (Christopher et al. 2014) and spatial variation in gas pressurisation and ascent rate of conduit magma (Lensky et al. 2008; Collombet 2009; Michaut et al. 2013; Cassidy et al. 2015).and spatial variation in gas pressurisation and ascent rate of conduit magma (Lensky et al. 2008; Collombet 2009; Michaut et al. 2013; Cassidy et al. 2015). In turn, these processes are strongly dependent upon the temporal evolution of porosity and permeability relationship within the volcanic edifice due to competing processes bubble growth and collapse and gas pathway formation and sealing (von Aulock et al. 2013; Vasseur et al. 2013; Ashwell et al. 2015; Heap et al. 2015a; Okumura et al. 2015; Kennedy et al. 2016). Comparisons between seismic patterns at a given timescale indicate a similarity in the driving mechanisms even at different volcanoes (Lamb et al. 2014); however, it remains that many observations are characteristic of a monitored volcano (Cashman and Biggs 2014).

2.3. Geophysical monitoring

Geophysical monitoring is an important tool to constrain the occurrence of subsurface processes, necessary to advance our understanding of the mechanisms acting during lava dome activity (see Section 2.2). Surficial activity and eruptive behaviour are often intrinsically linked to brittle processes occurring at within the upper 1-2 km depth within lava dome volcanoes. Such brittle activity can be monitored seismically, and correlate to acoustic signals produced experimentally on volcanic rocks (Benson et al. 2008). Seismic monitoring of dome volcanoes often reveal cyclic

variation (Voight 1999; Lamb et al. 2015b) during eruptions and patterns of increasing seismic event rate leading to explosions (Lavallée et al. 2008). Cyclic behaviour at lava dome volcanoes has been described using many monitoring techniques and it is attributed to the non-linear dynamics of magma ascent caused by competition between a wide range of processes, including crystallisation, gas exsolution, outgassing, viscous flow and fragmentation.

Lava dome eruptions produce a wide variety of measurable signals from both brittle and ductile deformation. Signals that are detected by geophysical monitoring instruments provide insight into otherwise inaccessible volcanic processes, however the signals themselves do not necessarily reveal how (the mechanisms and processes) they were produced: the value of geophysical data may depend on the interpretation of the signals, which is prone to error. An example of this comes from recent work showing that long period and hybrid seismic signals may reflect brittle fracture rather than fluid oscillation due slow rupture speeds of weak material and attenuation of the source signal through porous volcanic sediments (Harrington and Brodsky 2007; Bean et al. 2013; Eyre et al. 2015). The interpretation of tilt signals offer another example, as the characteristic sawtooth tilt patterns recorded at dome volcanoes may be interpreted either as inflation and deflation of the volcanic edifice (Johnson et al. 2014), or shear coupling between rising magma and the conduit walls (Green et al. 2006). Monitoring datasets provide an incomplete picture and it is often necessary to compare different monitoring datasets and evidence from other disciplines in order to better constrain volcanic processes. Multiparametric geophysical monitoring has revolutionised our understanding of volcanic systems within the last 25 years. Within these, the eruptions of Mt. Unzen, Soufrière Hills and Mt St Helens are case studies for modern monitoring campaigns. Within this section, I focus on seismic and infrasound monitoring of dome volcanoes, as these are methods I have employed, and simply introduce a range of other monitoring techniques at the end of the chapter.

2.3.1 Seismic signals

Lava dome eruptions are a rich source of seismic activity. Seismic signals may be broadly categorised by frequency and period, into short-period (SP), long-period (LP), very long period/ultra-long period (VLP/ULP), volcano-tectonic (VT) and tremor events. High-frequency events and some hybrid events (with SP onset and LP coda) have been argued to record brittle failure of magma/dome lava in response to stress (Harrington and Brodsky 2007; Umakoshi et

al. 2011). VLP and ULP seismic signals, with wavelengths from tens to hundreds of kms, are thought to indicate mass movement and inertial forces. As such, these signals have been used as a proxy for tilt, and may measure inflation and deflation of an edifice (Aoyama and Oshima 2008; Sanderson et al. 2010; Haney et al. 2013) or magmatic conduits (Lyons et al. 2016), or traction during pulsatory magma ascent (Ohminato et al. 2006). Tremor covers a wide frequency range, amplitude and duration, and can indicate hydrothermal interaction (Ohminato 2006), stick-slip ascent of magma (Dmitrieva et al. 2013) or wagging of the magma column (Jellinek and Bercovici 2011). Volcano-tectonic seismicity reflects local crustal readjustment to magma intrusion, including the generation of fractures associated with the propagation of dykes and sills below the volcano. These descriptions are illustrated in Figure 2.19, and introduce some of the diversity of seismic source interpretations in volcanic settings, where uncertainties propagate through incomplete information (e.g. earthquake source locations, seismic velocity structure) signal processing and difficulties in analogue simulations. However, with robust interpretation, seismic signals provide incomparable real-time evidence physical deformation and patterns of deformation that are essential for hazard mitigation and understanding of eruptive processes.

The source of long-period events garners significant debate. It has been argued that LP events result from the resonance of fluids. That may be fluid flowing in a crack (Ferrazzini and Aki 1987; Chouet 1988; Burlini et al. 2007; Benson et al. 2008; Matoza et al. 2015) or magma resonating following brittle failure in a conduit (Neuberg et al. 2006; Thomas and Neuberg 2012) . The origin or LP events is likely to change between volcanic systems, however they are often used as evidence for magma transport and to predict the onset of eruptions (Chouet and Matoza 2013) as well as a change in eruption style (Thomas and Neuberg 2012)

Seismic inversion is a powerful method to model the source characteristics (e.g. depth, volume, geometry) of seismic signals (Sanderson et al. 2010; Kim et al. 2014; Matoza et al. 2015), however this requires good knowledge of the seismic velocity structure of volcanoes and path effects, which are often difficult to accurately determine, therefore considerable error can arise. Wave path effects in poorly consolidated material can cause resonance and distort detected signals, even within long period signals, leading to poorly resolved source models (Bean et al. 2008). Most inversions model for an isotropically expanding point source (Mogi 1958) using a least-squares method, where the impulse response of the host material (the Green's functions) is calculated for each of the receiver component directions (Chouet and Matoza 2013). More recently, analysis of waveforms through cross-correlation and clustering of waveforms (Thelen et al. 2011) have allowed new techniques to track changes in repetitive earthquakes over time.

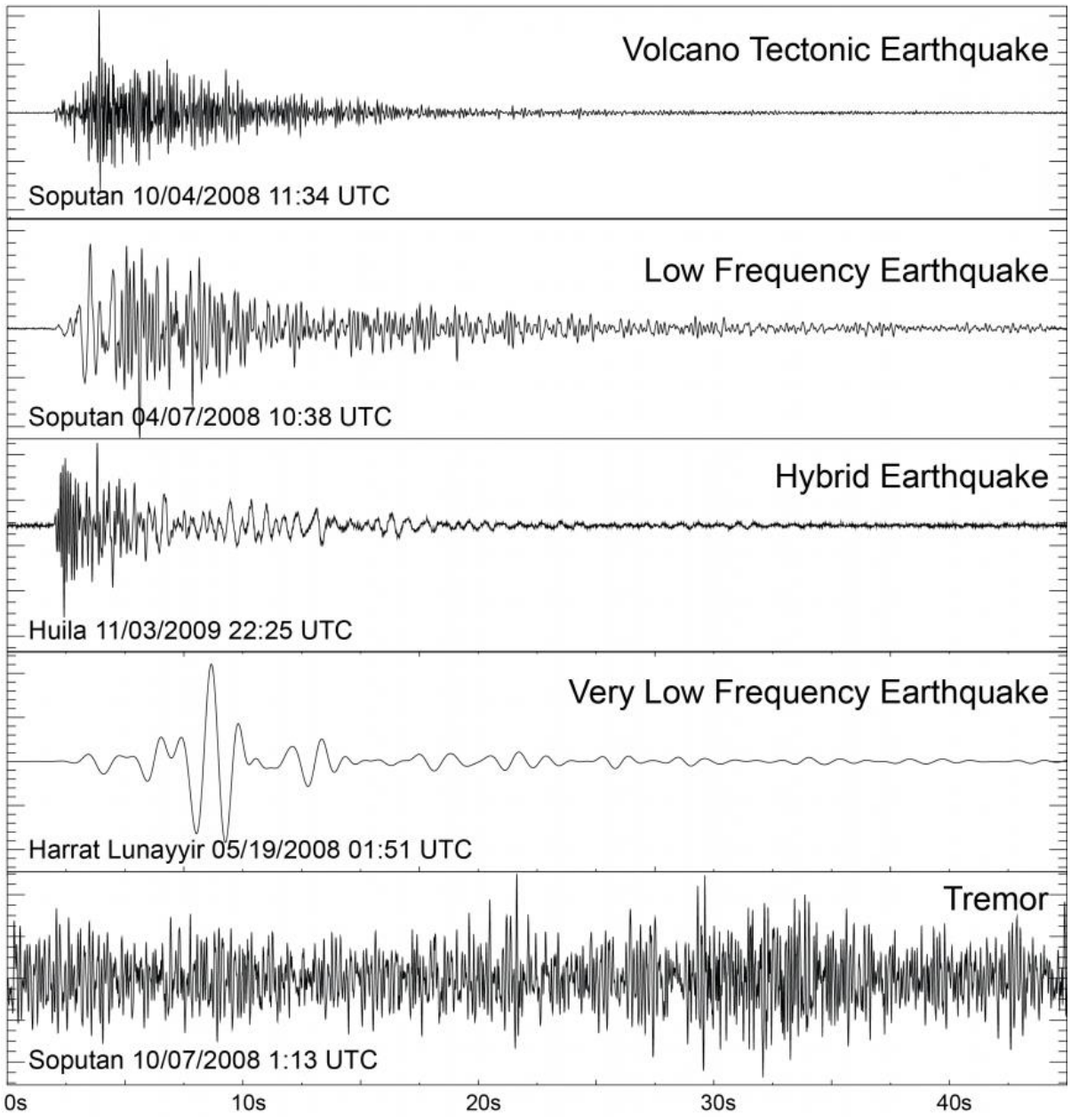

Figure 2.19.Typical waveforms of seismic events produced during volcanic unrest. Note that low frequency earthquakes correspond to LP earthquakes and very low frequency earthquakes correspond to VLP earthquakes in section 2.2.1. Modified from (Zoback et al. 2013)

Singular value decomposition is a method based upon standard matrix factorisation using data from the entire waveform, where a matrix containing vectors **M** can be described using a set of basic vectors **U** (input vector) and **V'** (output vector) and a set of non-negative invariable values $\sum$ that describe the magnitude of the transformation, in the relationship $M = U \sum V'$. In this instance, U is a matrix that gives the weight of each output basis vector. In clustered seismic

waveforms, this method relies on the magnitude of waveforms within a cluster varying significantly only in the first principal component. Relative trends in seismic moment and arrival time can be tracked across an eruption, or eruptive episode, shedding light on the evolution of long-lived and cyclic processes. In contrast, coda wave interferometry relies on the stationarity of scatterers and receiver to calculate the relative position of a source signal (De Angelis 2009), thereby tracking relative migration of sources without the need for waveform inversion (Lamb et al. 2015b).

2.3.2 Infrasound

Infrasound signals (air pressure waves) are produced by atmospheric disturbance, within the 0.2 – 20 Hz frequency band, recorded as the excess pressure detected within infrasound-sensitive microphones (Johnson and Ripepe 2011). Due to its sensitivity to atmospheric disturbances, infrasound is an effective tool for evaluating eruption magnitudes and mass flux (Kim et al. 2015; De Angelis et al. 2016); however this same sensitivity can detect unwanted signals, such as wind, surf, and severe weather, therefore installation and event detection are crucial in retrieving useful signals. Infrasound has been shown to be capable of tracking moving surface sources, however, due to the detection of infrasound as variation in air pressure, locating sources below the surface is a challenge. The advantage of the detection of atmospheric disturbances is the possibility to compare infrasound signals with visual monitoring data. Measurements of infrasound at erupting volcanoes have offered unique insights into the subaerial characterisation of volcanic processes. Infrasound wavelengths offer greater precision in source inversion than seismic signals, allowing differentiation and tracking of the pressurising sources, such as vent dynamics (Yamasato 1998) including rapid dome uplift (Johnson and Lees 2010), ash plumes (Lamb et al. 2015a), pyroclastic flows (Delle Donne et al. 2014), lahars (Johnson and Palma 2015) or rockfall (Johnson and Ronan 2015) during eruptions.

2.3.3. Tilt

Tilt signals record the deformation of the edifice itself, or the uplift and subsidence of regional crust due to magmatic activity and the inflation and deflation of pressure sources (Nishimura et al. 2012; Johnson et al. 2014; Hotta et al. 2016). Tiltmeters often record ground deformation in

two axes, with on axis aligned towards a volcanic source – positive changes in tilt in this axis record dome uplift or inflation, while negative tilt records deflation or subsidence. Tilt at lava dome volcanoes often shows cyclic behaviour, and sawtooth-shaped patterns of gradual inflation and rapid deflation (Anderson et al. 2010; Lyons et al. 2012), is thought to represent gas pressurisation and failure (slip or eruption) or a build-up and release of stress on the walls of a conduit (Green et al. 2006; Albino et al. 2011). Tiltmeters require very careful installation as they are highly sensitive and prone to drift and data clipping. In order to ensure instrument stability tiltmeters are often deployed in boreholes, however this can limit their use during difficult and inaccessible field sites, however tilt records have revealed characteristic cyclic deformation patterns at dome volcanoes that provide essential clues to subsurface deformation.

2.3.4 Other monitoring techniques

Local and regional deformation can be monitored by Global Positioning System (GPS) surveys (Nishi et al. 1999; Kohno et al. 2008), levelling surveys (Kohno et al. 2008) and other geodetic methods (Dvorak and Dzurisin 1997; Odbert et al. 2014). Regional deformation is often assessed by synthetic aperture radar interferometry (Wauthier et al. 2012; Ebmeier et al. 2012; Salzer et al. 2014), which detects changes in ground surface by comparing aerial (usually satellite or aircraft-borne) radar images with varying time. Ground surface measurements may also be taken using visible light by compiling photos or video footage to construct digital elevation models of volcanic features (James and Varley 2012; Farquharson et al. 2015b; Carr et al. 2016). These may be handheld or mounted onto manned or unmanned aerial vehicles, in order to obtain the required reference coverage. Unmanned aerial vehicles offer great mobility and ease of use, while autonomous flight has allowed unparalleled footage of hazardous activity (Williams 2013). Recently, use of unmanned aerial vehicles has become more common as greater availability and falling prices encourage their adoption as monitoring instruments. Doppler radar and groundSAR are effective means to evaluate the dynamics of dome surfaces and plumes during lava dome eruptions (Scharff et al. 2015).

2.4. Silicic magma rheology

Dome-forming magmas are complex suspensions containing solid (crystals), liquid (melt) and gaseous (gas bubbles) phases. Understanding the rheology of three-phase magmas is an important and topical challenge (Lavallée et al. 2007; Caricchi et al. 2007; Mueller et al. 2010; Cimarelli et al. 2011; Mader et al. 2013; Truby et al. 2015). Silicate liquids are viscoelastic bodies and generally exhibit a Newtonian rheology at low strain rates (i.e., the stress-to-strain rate relationship of the flow curve is linear and passes through the origin (Shaw 1969). At very high strain rate (or as they cool) magmas may undergo structural breakdown as they deform, resulting in non-Newtonian rheology (Dingwell and Webb 1989). The presence of crystals and/or bubbles in magmas further complicates this description (see Section 2.3.1 and 2.3.2).

Magma viscosity measurements are often challenging due to the extremely wide range of natural viscosities (over 15 orders of magnitude) and the limitations of sensitivity for each technique. Significant advances have been made over recent decades to expand our descriptions of the spectrum of magma types in nature. Viscosity can be measured using a range of methods depending on the viscosity to be measured. At low viscosities ($<10^5$ Pa s) the concentric cylinder method is often used (Dingwell 1991; Giordano et al. 2005; Chevrel et al. 2015)., as well as falling sphere viscometry (Vetere 2006; Whittington et al. 2009). High-viscosity measurements can be made using the fibre elongation method (Webb and Dingwell 1990a), micropenetration (Hess and Dingwell 1996) and torsion experiments (Caricchi et al. 2007). Applications of these various methods have provided us with a near-complete description of melt viscosity as a function of chemical composition, temperature, pressure and strain rate (Webb and Dingwell 1990b; Hess et al. 1996a; Hess and Dingwell 1996; Dingwell et al. 1996; Giordano et al. 2008; Di Genova et al. 2014; Lesher and Spera 2015).

The chemistry of magma varies widely in nature. In addition, magma undergoes dramatic chemicall and physical evolution during transport and eruption, resulting in substantial rheological changes (see 1.3.2. – 1.3.5.). Decompression forces crystallisation (Eichelberger 1995; Cichy et al. 2010; Chevrel et al. 2015) and volatile exsolution into bubbles (Lejeune et al. 1999; Melnik et al. 2005; Masotta et al. 2014), which may decouple from the magma and outgas at the Earth surface (Collombet 2009; Caricchi et al. 2011; Degruyter et al. 2012; Castro et al. 2012a). The first efforts to describe suspension rheology (Einstein 1906; Einstein 1911) and (Roscoe 1952) found that the addition of particles to a Newtonian liquid forms a suspension with a non-Newtonian rheology. At volcanoes, although both bubbles and crystals modify the viscosity of magma (e.g. Alidibirov et al. 1997; Truby et al. 2015). Thus, rheological contributions to volcanic processes are dynamic and difficult to quantify; yet they determine the

deformation mode and rate of many processes, and are essential to an understanding of magmatic behaviour.

2.4.1. Effects of suspended bubbles

Recent studies has focused on the rheological effects of suspended gas bubbles in melts (Manga and Rust; Saar et al). The effect of bubbles on suspension rheology are dependent upon the size, shape and fraction of the bubbles. For bubbles, the flow of the suspending liquid exerts viscous stresses that deform suspended bubbles due to competition between the liquid-gas surface tension (resisting deviations from a round bubble shape) and deforming stress. The degree of deformation of suspended bubbles in response to a constant flow stabilises over time. The timescale for equilibration following a change in applied stress from the suspending medium is termed the bubble relaxation time. The equilibrium deformation reached for a given strain rate is represented by the bubble capillary number,

$$Ca = \lambda \dot{\varepsilon}, \tag{2}$$

where λ is the bubble relaxation time and $\dot{\varepsilon}$ is the strain rate in the suspending medium (Manga et al. 1998; Truby et al. 2015). This relationship implies that when bubble geometries are preserved in magma or lava, shear rates can be calculated if melt viscosity and bubble surface tension are known (Rust et al. 2003). While bubbles are deforming (i.e. $t<\lambda$) the suspension rheology is continuously changing. The capillary number of bubbles determines their rheological significance with increasing volume fraction. At low capillary numbers (or low shear strain rates) bubbles remain relatively spherical and they have a positive contribution to the suspension shear stress (or viscosity). For higher capillary numbers (>1) addition of bubbles contributes to a decrease in suspension viscosity, due to the alignment of deformed bubbles in the direction of flow. This variability in the effect of bubbles contributes to a shear thinning rheology in areas of high strain (Manga et al. 1998; Mader et al. 2013; Truby et al. 2015). Complications to rheological modelling arise because natural flow processes commonly involve crystals, but also evolve towards heterogeneous distributions of suspended phases especially near flow boundaries and in non-Newtonian flow regimes. Such polydisperse bubble suspensions require size-dependent modelling of capillarity. In addition, all bubble bearing suspensions are viscoelastic, with elastic behaviour increasing with bubble volume fraction (Truby et al. 2015).

It is important to stress that magma ascent is dependent on the suspended bubble fraction – bubble nucleation decreases magma density, driving buoyant ascent. The bubble nucleation rate is limited by diffusion of volatile species (e.g. water, SO_2) between the melt and bubbles, and the competition between surface tension (proportional to bubble diameter) with increasing melt viscosity during magma ascent (von Aulock et al. 2013; Burgisser and Degruyter 2015). Magma ascent causes melt oversaturation, thereby increasing bubble formation and growth and further increasing magma ascent rate. The bubble volume fraction will continue to increase until a percolation threshold is reached, whereby interconnected bubbles form a permeable network and fluids can freely escape the system. As magmas outgas and bubbles coalescence, foamed magma may collapse and densify (Nakamura et al. 2008; Takeuchi et al. 2009; Castro et al. 2012a). Additionally, magma deformation becomes increasingly elastic at higher porosities (Namiki and Manga 2008; Heap et al. 2015b; Truby et al. 2015) through the fracturing and fragmentation of pores under an applied stress. If internal stresses exceed the tensile strength of bubble walls bubbles will fracture and fragment, causing the propagation of a pressure differential that may induce deepening fragmentation of bubbly magma (Alidibirov and Dingwell 2000). The relationship between porosity and permeability during outgassing determines the degree of bulk densification and explosivity of the magma during shallow gas loss (Blower 2001; Farquharson et al. 2015a; Wadsworth et al. 2016). High magma permeability during magma densification is measured or inferred at many lava dome volcanoes (Mueller et al. 2004). These observations may be due to a high micro-crack density (Heap et al. 2015a), outgassing through interconnected bubble networks (Okumura et al. 2009) or highly fractured conduit margins (Marti et al. 1999; Landi et al. 2004; Nakamura et al. 2008; Gaunt et al. 2014). Recent experimental work subjecting pumice samples to isostatic pressures and temperatures relevant for shallow (<1.5 km depths) volcanic conditions has also shown that the surface tension leads to a pore size reduction whilst maintaining high permeability, potentially giving rise to permeable and dense lavas at shallow depths, rather than forming an im permeable 'plug' (Kennedy et al. 2016). Textural evidence for repeating fracture and healing cycles at conduit margins may explain the low explosivity of protracted silicic lava dome eruptions through enhanced degassing (Tuffen et al. 2003; Castro et al. 2012b; Castro et al. 2014; Cabrera et al. 2015).

2.4.2. Effects of suspended crystals

Crystals, as well as xenoliths, contribute to the solid phases present in magmatic suspensions. Crystallisation takes place due to changes in pressure, temperature and/or the loss of dissolved volatiles (e.g. Martel and Schmidt 2003). Many magmatic crystal populations are bimodal, as phenocrysts grow over long periods during storage in magma reservoirs, and relatively small crystals (microlites) form rapidly during ascent and eruption. The size, shape (Figure 2.20) and chemistry of microlites therefore provide a record of magma ascent (Noguchi et al. 2008; Genareau et al. 2009; Cichy et al. 2010) and very shallow residence (i.e. <2 km depth). The rate of crystallisation depends on the diffusivity of element and volatiles from the melt and is inversely proportional to the viscosity of the melt phase, and the degree of ascent-driven crystallisation (either through decompression or undercooling) can vary widely, producing crystal-free obsidian in the extreme case (Calder et al. 2015).

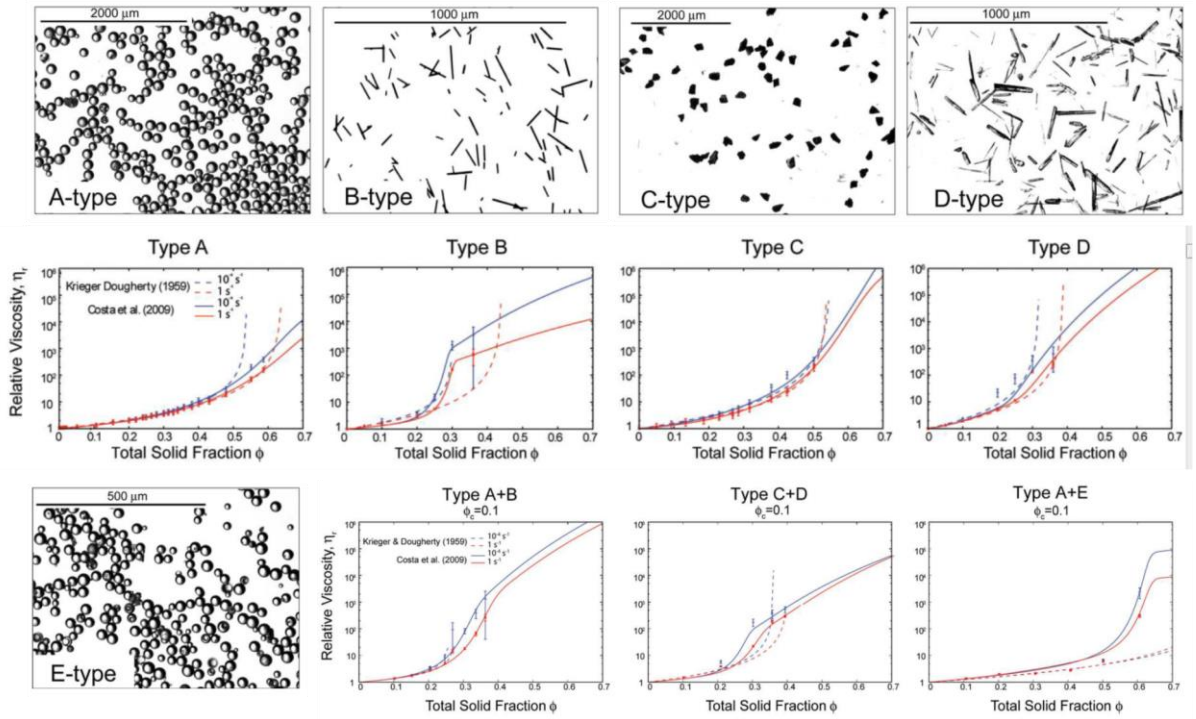

Figure 2.20 The effects different particle shapes on suspension viscosity (relative to a crystal-free melt) with increasing solid fraction, from spheres (A), fibres (B), angular grit (C) and crystal lathes (D). Relative viscosity values are shown together with fitting curves from the viscosity models of (Costa et al. 2009) in solid lines and (Krieger and Dougherty 1959) in dashed lines at strain rates of 10^{-4} (blue lines) and 1 s^{-1} (red lines). The relative viscosity of bimodal mixtures of particles are shown in the bottom row, including bimodal sizes (Type A + Type E). Modified from (Cimarelli et al. 2011)

Rheologically, the addition of crystals to a magmatic suspension acts to increase the viscosity. Microlite crystallisation can significantly increase the viscosity of dome lavas (Lejeune and Richet 1995; Caricchi et al. 2007; Chevrel et al. 2015), and is attributed to generating shallow over-pressurisation (Stix et al. 1997; Sparks 1997) and inhibiting magma effusion. Crystal bearing magmas generally adopt a non-Newtonian rheology and exhibit shear thinning (Lavallée et al. 2007; Caricchi et al. 2007; Kendrick et al. 2013a).or in certain cases shear thickening behaviour (Mader et al. 2013) depending upon the volume and orientation of axisymmetric crystals and the degree of coupling between solid and liquid phases.

As crystal volume fraction increases, the suspension rheology becomes increasingly dictated by the solid fraction as neighbouring crystals interact and inhibit particle motion. The maximum packing fraction; which is determined by the aspect ratio, surface roughness and size distribution of the suspended particles (Mueller et al. 2011; Cimarelli et al. 2011; Truby et al. 2015); represents the point at which a network of interacting suspended particles deforms elastically to an applied stress. This can give rise to a suspension with a yield stress, as particles deform elastically then fail, fragment and allow flow to occur. The maximum packing fraction occurs at lower concentrations for particles with higher aspect ratio, and can vary between 0.3 – 0.7. As suspended particle fractions increase beyond the maximum packing fraction, the suspension rheology adopts a singular non-Newtonian rheology (Lavallée et al., 2007). The dominance of shear thinning in magmatic suspension favours the localisation of strain near the conduit margin (Lavallée et al. 2013) – a phenomenon which promotes stress concentration and may prompt brittle processes (Lavallée et al. 2007; Kendrick et al. 2013a; Hornby et al. 2015a).

2.4.3. Modelling and calculation of magma viscosity

The calculation of three-phase magma viscosity is complex (Mader et al. 2013; Truby et al. 2015), however significant advances have been made in understanding the rheology of volcanic melts and the effects on viscosity imposed by suspended phases and variations in strain rate. Most calculations of magma viscosity first calculate single-phase melt viscosity then calculate the relative viscosity caused by either bubble or crystals suspension and strain rate. The calculation of single-phase melt viscosity depend upon the chemical composition of the melt. Most calculations use as a basis the Vogel-Fulcher-Tamann equation (Fulcher 1925):

$$log\eta = \mathrm{A} + \frac{B}{\mathrm{T(K)} - \mathrm{C}} \quad (2)$$

where A, B and C are variables related to the intrinsic behaviour of silicate melts. Work over the past few decades (Hess and Dingwell 1996; Hess et al. 1996b; Dingwell et al. 2000; Giordano et al. 2005; Giordano et al. 2008) has helped to constrain the effects of oxides, volatiles, temperature and the glass transition on melt viscosity. A substantial compilation of silicate melt chemical composition and viscosity was undertaken by Giordano et al. (2008), which allowed the effect of common oxides on the VFT parameters B and C (Equation 2) to be constrained, while A has been shown represent the high-temperature limit for viscosity, which may be taken as a constant. Each oxide for a measured melt composition is recalculated to obtain molar % and assigned a multiplier, the sign and magnitude of which are determined by the effect on viscosity – this has been shown to be valid over a wide range of melt compositions (Figure 2.21).

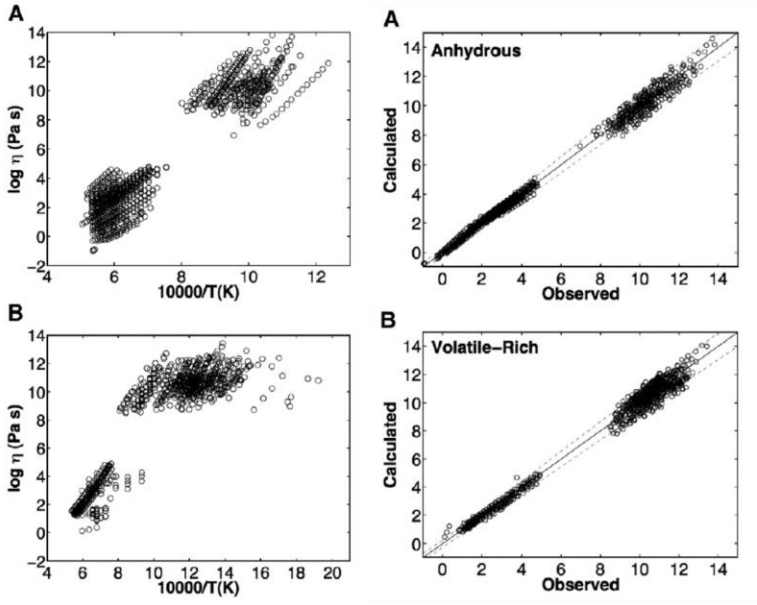

Figure 2,19. Left-hand panels show the range of different viscosity measurements that were used to calibrate the GRD viscosity model, while the right-hand panels show the fit between measured and calculated viscosity. The relative values of the oxides used to calculate their effect on melt viscosity are shown in the table below. Figures and table from (Giordano et al. 2008)

Table 1
Coefficients for calculation of VFT parameters *B* and *C* [*A* = −4.55 (±0.21)[a]] from melt compositions expressed as mol% oxides

	Oxides	Values		Oxides	Values
b_1	SiO_2+TiO_2	159.6 (7)	c_1	SiO_2	2.75 (0.4)
b_2	Al_2O_3	−173.3 (22)	c_2	TA[c]	15.7 (1.6)
b_3	$FeO(T)+MnO+P_2O_5$	72.1 (14)	c_3	FM[d]	8.3 (0.5)
b_4	MgO	75.7 (13)	c_4	CaO	10.2 (0.7)
b_5	CaO	−39.0 (9)	c_5	NK[e]	−12.3 (1.3)
b_6	Na_2O+V[b]	−84.1 (13)	c_6	ln(1+V)	−99.5 (4)
b_7	$V+\ln(1+H_2O)$	141.5 (19)	c_{11}	$(Al_2O_3+FM+CaO-P_2O_5)*(NK+V)$	0.30 (0.04)
b_{11}	$(SiO_2+TiO_2)*(FM)$	−2.43 (0.3)			
b_{12}	$(SiO_2+TA+P_2O_5)*(NK+H_2O)$	−0.91 (0.3)			
b_{13}	$(Al_2O_3)*(NK)$	17.6 (1.8)			

[a] Numbers in brackets indicate 95% confidence limits on values of model coefficients.
[b] Sum of $H_2O+F_2O_{-1}$.
[c] Sum of $TiO_2+Al_2O_3$.
[d] Sum of $FeO(T)+MnO+MgO$.
[e] Sum of Na_2O+K_2O.

The effects of crystal fraction and strain rate on melt viscosity have been constrained empirically (Hess et al. 2007; Caricchi et al. 2007; Robert et al. 2008) and led to the formation of fitting parameters to match measurements by Caricchi et. al. (2007) and formulation of a model to describe relative viscosity based upon these parameters (Costa et al. 2009). The dependence of the three semi-empirical parameters on strain rate and (Figure 2.23) has been modelled (Costa et al. 2009) allowing a full semi-empirical model for relative viscosity to be applied. The maximum packing fraction has been empirically constrained (Mueller et al. 2011) for varying particle shape (Figure 2.22.) and more recent models allow for solely observational/analytical determinations of relative viscosity (Mader et al. 2013).

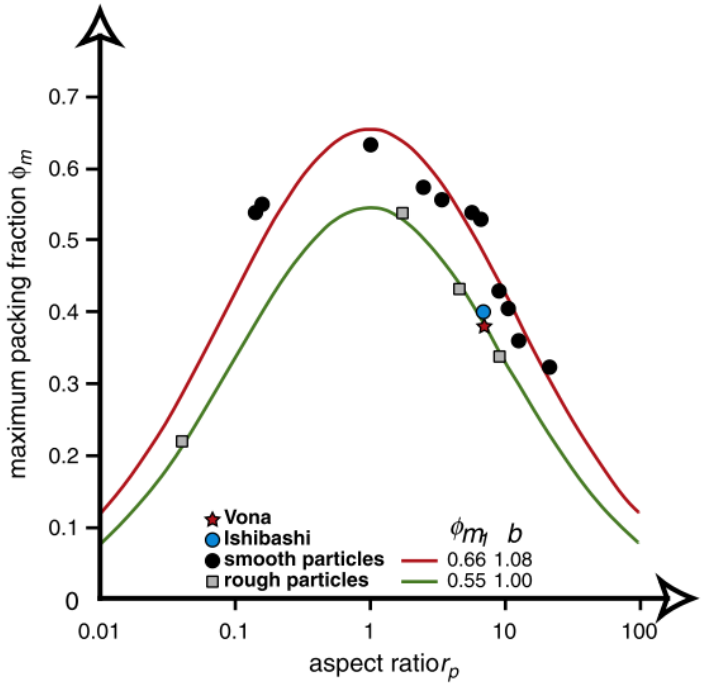

Figure 2.22. *The effect of particle aspect ratio (x-axis) and particle shape (rough particles - grey squares; smooth particles – black dots) on the maximum packing fraction ϕ_m, shown on the y-axis. The data has been fit with axisymmetric curves for rough (green) and smooth (red) particle for aspect ratios from 0.01 to 100* (Mueller et al. 2011).

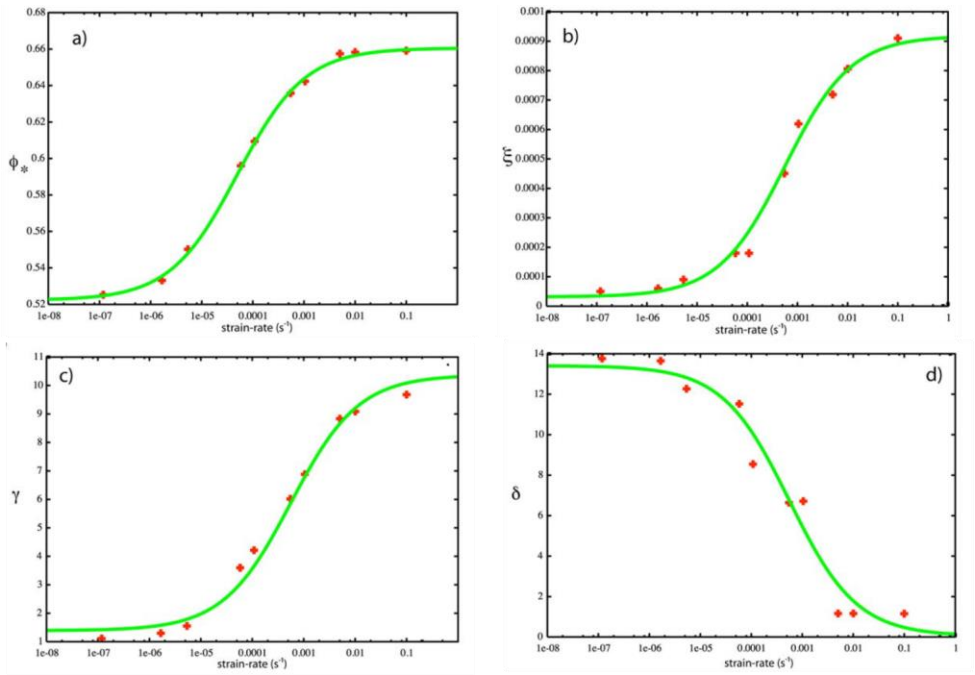

Figure 2.23. The dependence on strain rate of the semi-empirical fitting parameters defined by Caricchi et al. (2007) *allowing a full relative viscosity model to be described by Costa et al.* (2009).

2.4.4. Glass kinetics and the glass transition

2.4.5. Silicic melts are viscoelasticity bodies that exhibit a glass transition. The glass transition defines the regime for which a melt behaves viscously like a liquid or elastically like a solid. The glass transition is the structural change in a silicate melt from a dominantly viscous material to a rigid structure. Silicate melt may cross the glass transition and rigidify via changes in chemistry, temperature or strain rate, and may cause rapid transitions from ductile to elastic behaviour. The glass transition is a kinetic phenomenon that can be described as a measure of the ability of the melt to structurally reorganise sufficiently quickly to relax, or dissipate an applied stress. If not, the stress is stored within a rigid silicate framework and responds elastically. The glass transition (T_g) of a melt, with a given chemistry, is defined by a timescale of observation (or a deformation rate) and temperature (and thus viscosity). The glass transition is thus a kinetic phenomenon where molten silicate melts may undergo sudden changes from liquid-like to solid-like behaviour. As the glass transition is chemistry dependent, water loss during decompression may induce drastic rheological shifts in erupting magma. At low water and high silica contents (as often

found in magmas at dome volcanoes) small variations in water have a pronounced, non-linear effect on viscosity (Dingwell et al. 1996; Whittington et al. 2009). Measurements of the water content of natural melts are challenging, however approaches include Fourier transform infrared spectroscopy (von Aulock et al. 2014), Karl-Fischer titration (Giordano et al. 2005; Okumura et al. 2015) and Raman spectroscopy (Di Genova et al. 2015).

Flow to failure and beyond

The rheology of dome lavas becomes increasingly brittle at as magma ascends, especially in the last few kms of ascent. As described above, this may be due to a combination of increased bubble volume fraction, increased particle fraction and, importantly, volatile loss and rheological stiffening of the melt phase. The transition in rheology from ductile flow to elastic, brittle deformation may occur under varying stress and strain states at dome volcanoes, but is an inevitable consequence of silicic magma ascent. Dome volcanoes express this transition in a range of behaviour, from shear and tensile fracture development (Tuffen et al. 2008; Okumura et al. 2009; De Angelis and Henton 2011; Benson et al. 2012) to magma faulting and seismic slip (Johnson et al. 2008; Pallister et al. 2013; Kendrick et al. 2014a) and explosive fragmentation (Carn et al. 2009; Varley et al. 2010; Cole et al. 2014). These are not mutually exclusive processes, and one may trigger (Lavallée et al. 2015a) or defuse (Castro et al. 2012b) another; but it is clear that the onset of brittle deformation has a fundamental role on the observed activity and relevant hazards during lava dome eruptions. Variation in the glass transition temperature can be observed as changes in the timescale of structural relaxation (viscous accommodation of a stress state) either by increasing the observation period (or decreasing strain rate) at a fixed temperature, or by changing the temperature for a fixed observation timespan (Dingwell 1996; Dingwell 2006). Therefore, deformation behaviour can vary between viscous and brittle at temperature and strain rate conditions approaching to the glass transition interval (see Figure 2.24). The glass transition interval is intimately linked to the viscosity and strain rate via the Maxwell's (Maxwell 1867) viscoelastic law,

$$\tau = \frac{\eta_s}{G}, \qquad (1)$$

where τ is the relaxation timescale (inversely proportional to the strain rate), η_s is the shear viscosity and G the shear modulus at infinite frequency. Dingwell and Webb (1989) showed that the G may be approximated as 10^{10} Pa across a wide variety of silicate melt compositions and is invariable relative to changes in shear viscosity, and that brittle behaviour takes place at

deformation approximately two orders of magnitude above than the relaxation time. This allows simple formulation of the rheological transition between viscous flow and failure with strain rate and magma vicosity,

$$\dot{\varepsilon} = 10^{8} \eta_s^{-1} . \qquad (3)$$

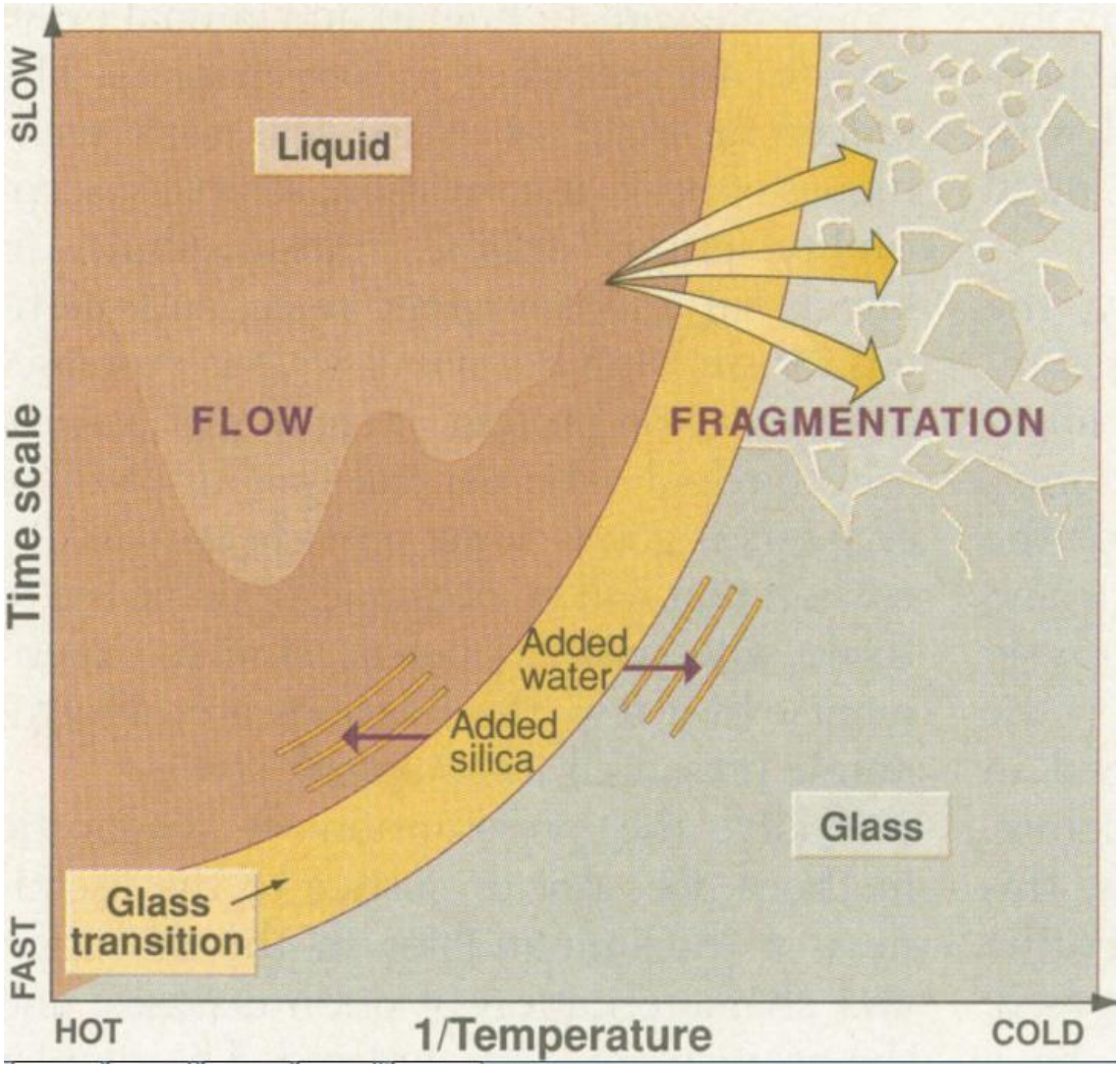

Figure 2.24. The glass transition interval with varying temperature and timescale, showing how the glass transition curve would shift with increasing silica and water in the silicate melt. This shows that the behaviour of melt is dependent on both temperature and strain rate, and that changes in melt chemistry can significantly shift the glass transition – therefore loss of water can provoke dramatic increases in the glass transition temperature. The yellow arrows demonstrate that if the glass transition interval is crossed melt will accumulate stress and will fail and fragment for large strains. Figure from Dingwell (1996).

Although much is known of the glass transition in silicate liquids, very little is known as to the effect of the presence of crystals and bubbles on the failure of magma – a topic investigated further in **Section 2.3.4.**

2.5. Rock fracture

Fracturing of rock under confined and unconfined conditions has been an area of intense study for many years (Paterson and Wong 2005). Early efforts focused on an understanding of the strength and failure criterion of shallow crustal rocks to inform geoengineering applications. As such, great research effort has gone into characterisation of the failure of sandstone, granite and limestone, and standardised rock deformation testing methods have been developed (Ulusay 2015). Decades of investigation into the brittle deformation of rocks have revealed a diversity of behaviour during elastic failure, dependent upon rock sample properties (texture, geometry, porosity, pore fluids), deformation conditions (rate, temperature) and sample confinement (uniaxial to triaxial) (Paterson and Wong 2005). Under confined experimental conditions the pore fluid pressure within rock samples can be varied, and the effective pressure on the sample is the difference between confining pressure and pore pressure. Under low confinement and unconfined experimental conditions rock failure is always dilatant, and fractures may propagate in shear and tension. Within highly confined conditions, the failure of porous material commonly occurs in compaction, associated with cataclastic loss of porosity and permeability (David et al. 1994; Wong et al. 1997; Heap et al. 2015a); Application of rock mechanical methods to an understanding of volcanic materials has recently encouraged a more mechanistic understanding of rock and magma failure and crack propagation under diverse volcanological deformation conditions. Of especial interest to failure in dome rock are the effects of elevated temperature, pore pressure, and the time dependence of material failure (Kilburn and Voight 1998; Smith et al. 2009; Lavallée et al. 2013; Farquharson et al. 2016a). Viscoelastic magmas show a propensity for transitions in deformation mode, therefore an understanding of such mechanical behaviour and failure at the brittle-ductile transition is essential (Paterson 2001; Wong and Baud 2012; Evans et al. 2013).

2.5.1. Failure modes in uniaxial and triaxial tests

Rock deformation in the brittle field has been the dominant focus of rock physics research (Paterson and Wong 2005). A key concept during brittle behaviour has been defining the criteria for rock failure under experimental conditions (Handin 1969). During (unconfined) uniaxial compressive strength (UCS) experiments, macroscopic dilation during failure initiates macroscale rupture in shear. However, within (confined) triaxial experiments cataclastic compaction of pore spaces may cause shear strain to focus within cataclastic bands and encourage granular reorganisation and further compaction (Mair et al. 2000; Wong et al. 2001). Pore pressure acts against confining pressure in triaxial experiments and therefore decreases the effective pressure, resulting in increasingly dilatant behaviour. During experiments conducted under triaxial conditions, dilatant and macroscopic shear fractures are induced as pore pressure approaches confining pressure (Farquharson et al. 2016a). These fracture modes are visually represented in classic experiment by Paterson (1958) shown in Figure 2.25 From this, it can be seen that increased pore pressure reduces the mechanical strength of rocks, by increasing the susceptibility to macroscopic, dilatant failure (Sammis and Ashby 1986; Bruno and Nakagawa 1991; Heap et al. 2015b).

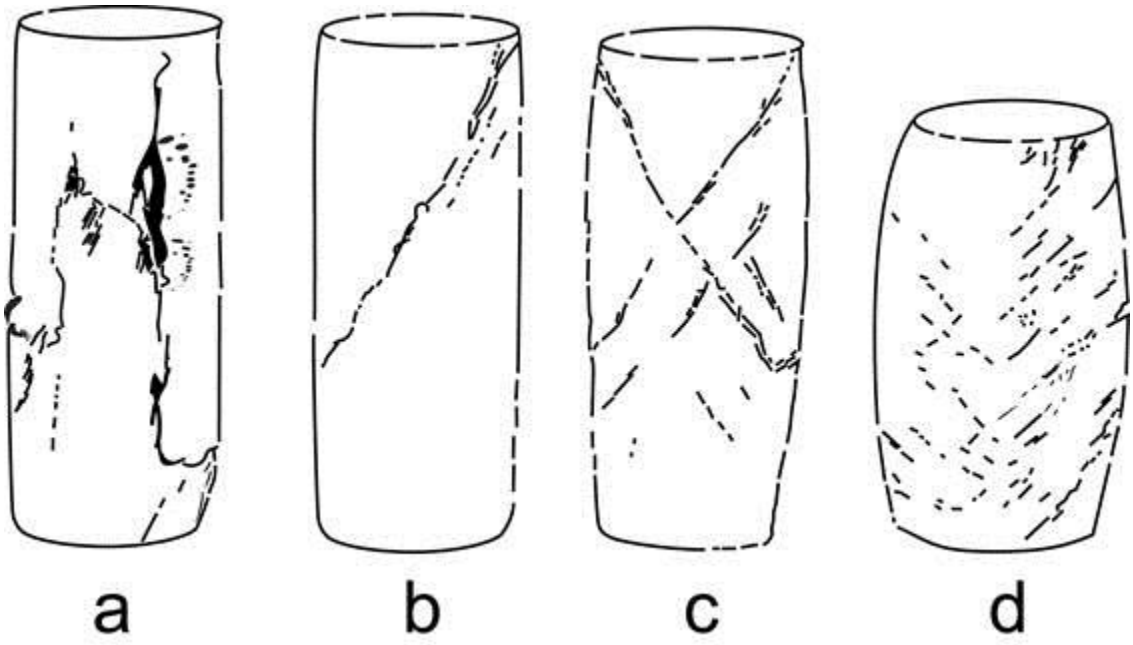

Figure 2.25 showing the change in fracture modes as confining pressure in increased in a triaxial apparatus, from tensile cracks (a) to shear fracture (b) conjugate shear fractures and barrelling (c) to highly dispersed conjugate fracture and significant barrelling (d). Figure from (Paterson 1958).

During experiments varying deformation modes may be detected through changes in stress and strain. Elastic strain accommodation is represented by a linear increase in both measures. The Young's modulus of a rock can be calculated from $\frac{\delta stress}{\delta strain}$ during elastic deformation. The onset of failure takes place through the initiation of micro-cracks, a process that can be monitored through the acoustic emissions from deforming rocks (Lockner 1993; Burlini et al. 2007). Within unconfined experiments, the point at which micro-cracks begin to be detected (the initiation of inelastic strain) may be seen as an inflection within the stress-strain curve, which is denoted as C' (Wong et al. 1997). The increase in acoustic energy with time follows a power law as micro-cracks grow and coalesce during increasing damage and localisation, allowing forward modelling of the timescale to macroscopic failure following the onset of acoustic emissions (Meredith et al. 1990; Vasseur et al. 2015). This technique has been successfully applied to a wide range of rocks in the laboratory, and to failure at volcanoes (Smith et al. 2007; Lavallée et al. 2008; Bell et al. 2011; Arámbula-Mendoza et al. 2011). During highly confined experiments, the onset of shear-enhanced compaction also has an attendant deviation from a linear relationship between differential stress and strain. This threshold in confined experiments on granular rock is denoted C*, and is also defined by the initiation of acoustic emissions due to inelastic pore compaction (Wong et al. 1997; Heap et al. 2014a; Farquharson et al. 2016a).

2.5.2. Rock strength in the brittle field

The behaviour of material following the onset of elastic damage is dependent upon the deformation regime. In UCS tests, progressive weakening of rock occurs as micro-cracks propagate and connect, indicative of an increasing localisation of damage into larger fractures. At a critical micro-crack density or connectivity, a macroscopic crack propagates through remaining intact rock causing a rapid drop in stress (Rudnicki and Rice 1975; Paterson and Wong 2005). This manifests as strain hardening (i.e., increasing curvature of the stress-strain curve) due to damage accumulation upon loading until dramatic stress drop upon failure. The stress at which a rock undergoes macroscopic failure, or the peak stress achieved during unconfined experiments is the rock strength, which is a function of physical and experimental properties. Heterogeneity in rocks provides locations for stress concentration and micro-crack initiation, therefore increasingly heterogeneous rocks weaken earlier, and propagation of inelastic damage may lower the rock strength (Mahabadi et al. 2014; Vasseur et al. 2015). Rock

strength typically decreases with increasing porosity due to shortening of fracture propagation paths, however this depends on the nature of the porosity: a sample with pore space composed of micro-cracks will fail at lower stress than a more porous sample with rounded bubbles (Heap et al. 2010; Kendrick et al. 2013b; Heap et al. 2014b). Faster deformation rates allow less time for micro-crack growth and damage localisation, and therefore rock strength and stress drop upon failure are higher. Thus, rock strength is also dependent upon deformation rate, as the development (or degree) of inelastic deformation prior to failure is time-dependent (Wawersik and Fairhurst 1970; Paterson and Wong 2005; Brantut et al. 2014). Finally, the strength of rock in compression is 10-20 times higher than in tension (Li and Wong 2013), therefore sample geometry, loading configuration and the orientation of principal stress axes have significant implications for rock strength (Mahabadi et al. 2010; Li et al. 2011; Perras and Diederichs 2014). For example, in the Brazilian disc test (ISRM 1978), core samples are compressed axially across their circular faces, leading to similar values of compression and tension at the centre of the circular profile; in this case the rock always fails in tension and the rock tensile strength may be indirectly measured (Perras and Diederichs 2014).

In contrast, during confined experiments, rocks maintain significant strength following brittle failure. Cataclastic compaction of pore spaces increasingly localises strain to inelastically deformed regions, until all deformation imposed by differential stress is accommodated through inelastic shear, granular flow and compaction (Wong et al. 1997; Wong et al. 2001; Wong and Baud 2012). This is indicated by increasing strain per stress increment following C*, followed by a renewed sublinear relationship between stress and strain, with characteristically decreasing differential stress during increasing strain. The degree of differential stress reduction following failure relates to the degree of compaction, which is controlled by the effective pressure (Paterson and Wong 2005). The maximum differential stress reached during confined experiments (the rock strength) increases with higher effective pressures, up to a threshold where compactant deformation begins to occur at lower differential stress. This indicates that confined rock strength follows a parabolic trend with increasing effective pressure, defined as the Mohr-Coulomb envelope (Handin 1969; Wong and Baud 2012). The accommodation of increasing strain in a compactant regime commonly results in barrelling of rock samples due to shear strain during granular flow of cataclastic bands.

2.5.3. Micromechanical models

In shallow volcanic conduits, where low confining pressure and high pore pressure may develop, dilatant failure modes are generally expected. Dilatant failure is induced within rock through the initiation, propagation and coalescence of tensile micro-cracks (Rudnicki and Rice 1975). The micromechanical propagation of micro-cracks is described by two dominant models: the pore emanated crack model (Sammis and Ashby 1986) and the sliding wing-crack model (Ashby and Sammis 1990). The pore emanated crack model (Sammis and Ashby 1986) describes circular vesicles in a homogeneous medium that act as stress concentrators. Tensile micro-cracks propagate from the vesicle parallel to an applied stress, (from the regions experiencing greatest tension during deformation of the vesicle). Once micro-cracks formed in this way reach a critical length they can interact and coalesce, leading to macroscopic failure (Heap et al. 2014b). Catastrophic dilation occurs when the stress at a crack tip reaches the critical stress intensity K_{IC} (Meredith and Atkinson 1983) also known as the fracture toughness, upon which the crack propagates parallel to the maximum principal stress at speeds approaching the speeds of sound. However, in experiments on rocks with high pre-existing micro-crack density the pore-emanated crack model is ineffective, and micro-fractures propagate by a sliding wing-crack model (Ashby and Sammis 1990). Within this model, a set of micro-cracks undergo shear-induced slip during application of differential stress when the frictional resistance on the crack is exceeded. The crack tips act to concentrate tensile stress during slip, and once the critical stress intensity at the crack tips is overcome, the micro-crack propagates from both crack tips in a direction parallel to the maximum principal stress (Heap et al. 2014a). These micromechanical are illustrated in Figure 2.26, showing the principal stress axes, induced deformation and micro-crack propagation for the sliding wing crack model (A) and the pore-emanated crack model (B).

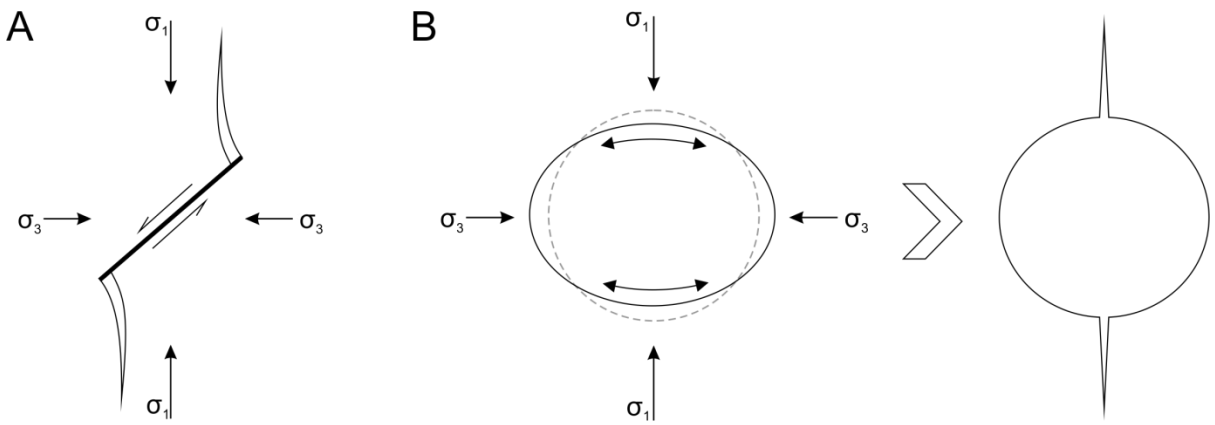

Figure 2.26 *Simplified representation of the wing crack model (A) and pore-emanated crack model (B). The sense of slip on an existing microcrack is shown by ski arrows. Microcracks propagate from the crack tips, towards the principal stress axes. In panel B, deformation of a pore from an initial shape (shown as a dashed line) increases tensile stress perpendicular to the principal stress axes at the pore wall (shown as twin-arrowed lines), leading to propagation of microcracks parallel to the principal stress axes (shown at the far right). After Paterson and Wong* (2005) *and Sammis and Ashby* (1986).

2.5.4. Stretching the brittle field – high temperature deformation and strain-to-failure

Rock deformation experiments conducted at increasingly high temperatures show a tendency to both brittle and viscous deformation modes. The mechanisms triggering fracture development may be similar (Mogi 1971; Paterson and Wong 2005), but the time-dependency of fracturing can greatly increase (Meredith and Atkinson 1985; Kilburn and Voight 1998; Liu and Xu 2015). The contributions of elastic and viscous deformation modes near the brittle-ductile transition is strongly dependent on temperature and strain rate (Rocchi et al. 2003; Balme et al. 2004), and elements of both deformation modes are found (Duclosi and Paquet 1991; Smith et al. 2011; Evans et al. 2013). As viscous forces are more effective at stress dissipation, non-linearity in stress-strain curves may not indicate brittle damage, but the viscous relaxation timescale in response to stress. Where this is accompanied by brittle damage, the propagation of fractures is highly time dependent (Kilburn and Voight 1998; Nara and Kaneko 2005; Smith et al. 2009), and crack tips are often blunted (Meredith and Atkinson 1985). As such, damage is more efficiently dispersed, and brittle fractures can maintain lower aspect ratios (greater dilation). During experiments with greater viscous behaviour deformation is more distributed (ductile) and

a greater total strain may be accommodated within the sample prior to efficient localisation and macro-scale fracture propagation to failure (Paterson and Wong 2005). In rock mechanics, the nominal rock strength in the ductile field is simply the stress recorded at 10% strain, however this does not allow for failure at greater strains. One effective way to quantify the degree of viscous stress accommodation is to compare the total axial strain prior to failure under varying temperature and strain rate conditions.

2.5.5. High-temperature uniaxial press at the University of Liverpool

The experimental volcanology laboratory at the University of Liverpool hosts a retrofitted Instron 8862 uniaxial press fitted with a water cooled Severn Thermal Solutions three-zone split-tube furnace capable of sample temperatures up to 1000 °C (Figure 2.27). The press has a servo-driven single-screw electromechanical actuator capable of producing constant, programmed or oscillating deformation rates spanning >5 orders of magnitude. The load cell has a maximum capacity of 100 kN and the piston accommodate samples up to 100 mm height and 60 mm diameter. At room temperature the apparatus can be fitted with acoustic microphones to detect acoustic emissions during deformation and a radial extensometer to measure deformation normal to compression for calculation of Young's modulus or Brazilian tensile stress. Experimental data is transferred using the high data-rate 8800 digital controller and test data is configured using either Bluehill 3 or WaveMatrix. During high-temperature experiments, sample temperature is recorded using a K-type thermocouple inserted into the furnace. Prior to experiments, sample porosity is measured using a He-pycnometer from Micromeritics. The volume displaced by a sample within a chamber of known volume can be compared to the external dimensions of the same to calculate the connected porosity. Once rock samples are prepared, measured and characterised, the apparatus can be used to measure either the Brazilian tensile strength of rock samples using the sample orientation shown in the centre panel of Figure 2.27, or the uniaxial compressive strength of the sample, using the orientation shown in the right-hand panel of Figure 2.27. Under high-temperature uniaxial conditions, the apparent viscosity of a sample can also be measures, by applying the Gent equation during steady flow of the sample under load. This technique has been calibrated and validated using similar apparatus at LMU Munich (Hess et al. 2007).

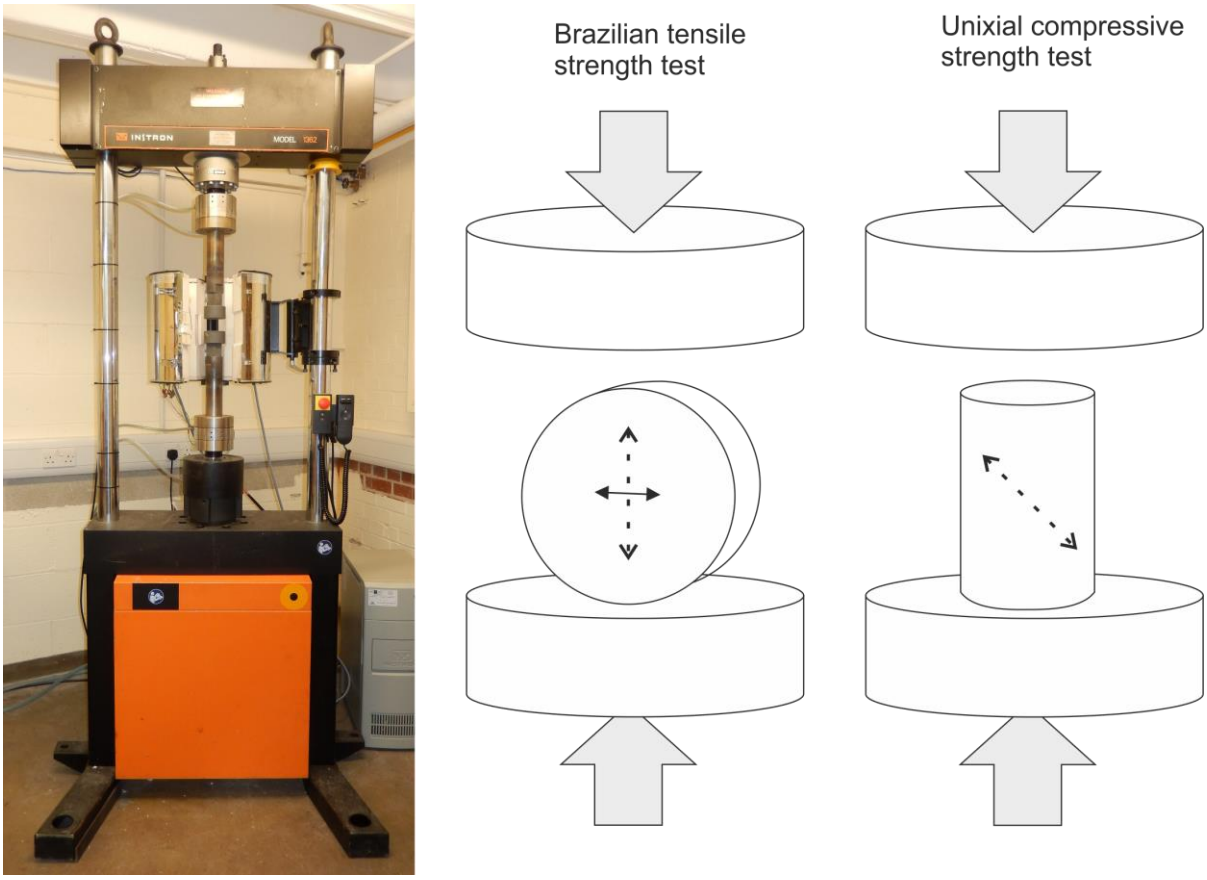

Figure 2.27 Instron model 8862 servo-driven uniaxial press apparatus in the experimental volcanology laboratory with 100 kN load cell, and a water-cooled three-zone split-tube furnace (Severn Thermal Solutions) capable of temperatures up to 1000 °C. This uniaxial rig is designed to test the tensile and compressive strength of volcanic materials at high temperature using Brazil test (B) and UCS tests (C). The sample configuration is shown with the expected fracture orientiation (dashed arrow) and maximum tensile stress in the Brazil test (solid arrow In panel B). The direction of deformation (i.e. compression) during the experiments is shown by the large grey arrows.

2.6. Faulting, friction and fragmentation

Studies of faulting and friction have a basis in rock mechanics, where the relationship of friction with normal stress (Byerlee 1978), and mechanics of faulting at low slip rate have been effectively modelled (Dieterich 1978; Ruina 1983; Dieterich and Kilgore 1994; Marone 1998a). Earthquake researchers extended the study of faulting to high velocities in order to evaluate

frictional processes at natural slip rates (Magloughlin and Spray 1992; Shimamoto and Tsutsumi 1994; Mizoguchi et al. 2007). This revealed discrepancies with rate and state friction models, and revealed a propensity for frictional heating to cause remelting of fault rocks at or adjacent to the fault plane and generate pseudotachylyte (Shand and Shand 1916; Sibson 1975; Spray 2010). Psuedotachylyte forms due to total or partial remelting of fault rocks during slip. Due to the high strain rates and fluid mobility during faulting, together with rapid cooling rates pseudotachylytes are often emplaced as glassy veins describing the fault plane. Further descriptions of pseudotachylytes are contained in Chapter 2.5.2. The properties of pseudotachylyte at crustal depths were found to be lubricating relative to rock surfaces (Spray 2005; Di Toro et al. 2011), helping to explain observations of efficient stress drop during earthquakes.

Faulting within lava dome volcanoes has been recognised to an increasing degree in recent years (Tuffen and Dingwell 2004; Neuberg et al. 2006; Cashman et al. 2008; Dmitrieva et al. 2013; Lavallée et al. 2015a). The ascent of viscous magma generates shearing forces that are widely recognised to result in shear failure and faulting within the shallow conduit (Lensky et al. 2008; Weinberg and Regenauer-Lieb 2010; De Angelis and Henton 2011; Okumura et al. 2015). In addition, the extrusion of coherent bodies, such as spines and whaleback lobes, takes place along shallow fault planes that experience repeated slip events (Iverson et al. 2006; Pallister et al. 2013; Lamb et al. 2015b) and can generate sufficient heat to locally melt rock at or near the slip plane to form pseudotachylyte (Kendrick et al. 2012; Plail et al. 2014). Recently, researchers have applied high velocity faulting experiments to volcanologically relevant scenarios (Lavallée et al. 2012b; Lavallée et al. 2014; Violay et al. 2014), revealing that under shallow conditions (<1 km) volcanic pseudotachylytes may have higher friction coefficients than bare rock surfaces. These observations may control the cyclic and repetitive extrusion dynamics found at many lava domes (Kendrick et al. 2014b).

2.6.1. Rate and state friction

The friction coefficient is defined as the ratio of shear stress to normal stress on a fault plane. Early data compilation has shown that the static friction coefficient (i.e., the shear resistance to normal stress ratio of a rock prior to faulting) for most intact rocks at crustal depths is 0.7 – 0.85 (Byerlee 1978). Experiments producing multiple slip events after varying hold times have shown that static friction is time dependent (Dieterich and Kilgore 1994). They demonstrated an

increase in asperity contact area over time, which may explain observation of fault strengthening with increasing contact time (Wang and Scholz 1994; Marone 1998b). The use of a static value for friction fails to describe the observed frictional behaviour during faulting in laboratory experiments however. Rate and state dependent friction laws have been formulated to describe the variation in frictional behaviour during faulting (Dieterich 1979; Ruina 1983). The rate dependency describes a rapid change in the frictional resistance in response to varying slip rate. Increasing the slip rate will increase the dynamic friction coefficient and vice versa. The rate dependency of friction is modified a time-dependent effect during faulting, during which the dynamic friction evolves toward a new state over time. This effect trends in the opposite direction to the rate effect on friction and can be modelled as the evolution of a state variable (θ) from the initial state of asperity contacts to a new state (see Figure 2.28). The empirically determined rate-dependent change in dynamic friction is termed *a*. The change in friction from this new state to a new stable state during ongoing slip is termed *b*. A material is considered rate strengthening if a-b is positive for an increase in slip velocity, and rate weakening if it is negative. The distance over which the dynamic friction coefficient decays to the initial friction value (in the case of rate weakening behaviour) is the slip weakening distance (D_c) shown in Figure 2.28. The constitutive rate and state friction law can be written as

$$\mu = \mu_0 + a \ln\left(\frac{V}{V_0}\right) + b \ln\left(\frac{V_0 \theta}{D_c}\right), \qquad (3)$$

where V_0 is an initial reference velocity, V is slip velocity, μ is the friction and μ_0 is the steady state friction coefficient at V_0. Rate weakening behaviour, typical of crustal rocks, instigates slip instability and rapid displacement on faults, generating earthquakes. Rate and state friction laws have been demonstrated to explain a diverse range of seismic behaviour, including stick-slip, seismic coupling and aftershock phenomena (Marone 1998a; Scholz 1998).

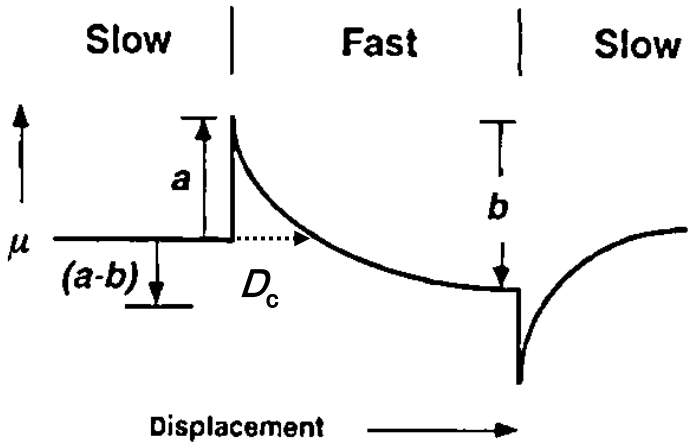

Figure 2.26. *The direct velocity (arrow marked 'a') and the time-dependent state effects (arrow 'b') on dynamic friction demonstrated for a rate weakening scenario (a-b is negative). The opposite excursion of the rate effect is shown for positive and negative changes in velocity The dynamic friction recovers the initial value if velocity is reduced back to the initial rate. The slip weakening distance (D_c) is shown as a dotted line. Figure modified from Scholz* (Scholz 1998).

2.6.2. High velocity friction: natural and experimental fault textures

Experimentalists attempting to replicate fault slip at high, natural slip rates realised that frictional behaviour under these conditions does not follow the rate and state friction formulation. Rather the production of frictional melt under high slip zone temperatures modified the frictional behaviour considerably (Magloughlin and Spray 1992; Tsutsumi and Shimamoto 1997a). Frictional melt textures produced in the laboratory were very similar in many respects to those exposed in natural fault zones, helping to confirm the origin of natural pseudotachylyte textures, a matter of considerable debate (Sibson 1975; Shimamoto and Nagahama 1992; Spray 1995). Natural faults zones are generally found to exhibit increasing damage towards the fault core (Faulkner et al. 2003; Wibberley et al. 2008). Damage within the fault zone is cataclastic and increasingly fine grained towards the fault surface. Fault surfaces themselves are very narrow relative to fault length, and movement is generally localised within one or several narrow zones, often hosting fine clastic gouge showing evidence for granular redistibution during fault movement. Natural fault gouges are often relatively impervious compared to surrounding damage within the fault zone (Mizoguchi et al. 2008). Pseudotachylytes are highly susceptible to alteration, recrystallization and overprinting, therefore preservation at fault zones may be

considered uncommon (Kirkpatrick and Rowe 2013); where pseudotachylyte is found it is often present in very narrow bands (sub-mm to cms) indicating extreme strain localisation during faulting; Offshooting veins indicate high pressurisation within the fault zone during slip and lead to development of tensile fractures adjacent to the main fault plane (Di Toro 2006). Pseudotachylytes are often anastomosing or branching and may be associated with a narrow zone showing intense cataclasis. Pseudotachylyte-bearing fault textures show evidence for highly disequilibrium melting, controlled by interaction between cataclasis and selective melting of minerals dependent on the mineralogy of the host rocks (Maddock 1992; Griffith et al. 2008). Natural pseudotachylytes contain numerous angular and subrounded fragments derived from wall rocks; the degree of rounding and the melt fraction within the pseudotachylyte may be representative of the degree of fault motion (Warr and van der Pluijm 2005; Pittarello et al. 2008). Experimentally produced pseudotachylytes reveal a range of textures similar to natural examples. The propensity for flash-melting at asperity contacts (Goldsby and Tullis 2011) and extreme temperature gradients during faulting often leave their trace in textural observations disequilibium melting, where phases with the lowest fusion points are the first to melt (Spray 1992; Shimamoto and Lin 1994). Where high-velocity friction experiments are rapidly terminated unmixed filaments of heterogeneous melt may be preserved within the pseudotachylyte (Lavallée et al. 2015a). The presence of both viscous and brittle deformation within frictional melts can be observed, both at the boundaries of melt zones, where thermal breakdown, or fusion, textures may be seen, and within the melt, where crystal and groundmass particles are entrained, occasionally showing evidence for grain size sorting. As such, brittle behaviour in frictional melt hosting slip zones may be common, and the presence of coeval pseudotachylyte and fault breccia hint toward the possibility of brittle fragmentation of frictional melts during natural faulting (Ray 1999; Kim et al. 2010). It is not known whether thermal pressurisation of faults is a significant contributor to fault strength in shallow volcanc environments, however would make an interesting avenue for research. Experimental investigations of slip on volcanic fault gouge have revealed strong slip weakening behaviour and the localisation of slip onto narrow planes within the gouge. The degree to which brittle processes at the boundaries and within frictional melts contribute to the frictional resistance requires further investigation. In silicate-rich rocks, pseudotachylytes may exhibit behaviour controlled by rheology neat the glass transition (Lavallée et al. 2015b). Frictional melts may be two- or three-phase suspensions (Spray 1993; Kendrick et al. 2014a); frictional melts formed from typical dome rocks are three phase silicate fluids that exhibit a non-Arrhenian temperature dependence on viscosity (Lavallée et al. 2012b). The recent observation that frictional heating

and an attendant drop in viscosity within frictional melts triggers exsolution of volatiles into bubbles, has sparked a renewed consideration of the role of frictional heating within volcanic conduits (Lavallée et al. 2015a) and the triggers for magma fragmentation in the conduit.

2.6.3. HVR apparatus at University of Liverpool

In March 2014, the experimental volcanology group at the University of Liverpool received a new-generation apparatus to test low-to-high velocity friction during faulting in and around volcanoes (Figure 2.29). The apparatus was designed and constructed by Marui, Japan, in consultation with Toshi Shimamoto, the designer of the first-generation HVR apparatus (Shimamoto and Tsutsumi 1994). This HVR apparatus was custom-designed to accommodate a single-zone split- tube furnace allowing the first high velocity rotary friction experiments at high initial temperatures - natural conditions in volcanic settings. The apparatus has a geared motor capable of replicating a wide range of fault displacement behaviour, from creep (mm/year displacement) to seismogenic faulting and frictional melt generation (m/s). The apparatus continuously measures the normal stress between a pair of cores and the torque generated during sliding, in addition to the shortening measured by an external extensometer. From the normal stress and torque, the shear stress and friction can be easily calculated. Direct observations are also made by visual and thermal camera, allowing heat and power output to be analysed, and detecting the onset and evolution of frictional melting, if present. In addition to bare rock surfaces, the sample setup can be adapted to accommodate fault gouge between two sample cores by using a close-fitting Teflon ring around the slip zone. This apparatus enables the full spectrum of shallow faulting conditions to be simulated, from fast to slow, cold to hot, on faults that are gouge laden, melt laden or between bare rock surfaces. The natural condition that is not easily satisfied by high-velocity frictional apparatus is confining pressure on the slip zone, however in shallow volcanic environments this constraint is less important than in tectonic settings. A broad overview of the apparatus, sample setup and features is given in Figure 2.29 and the accompanying caption.

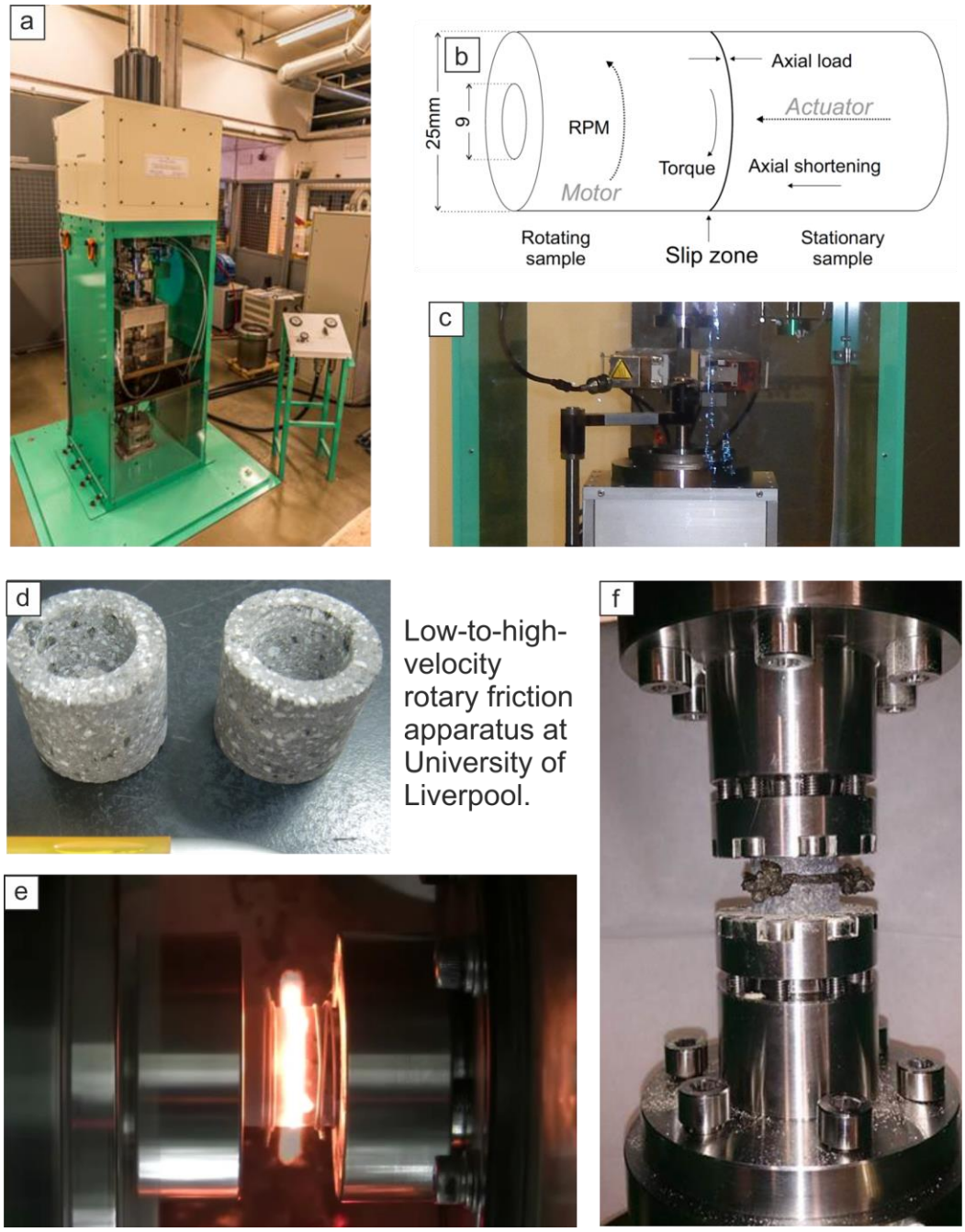

Figure 2.29. Detail of the Low-to-High-Velocity Rotary friction apparatus at the University of Liverpool, showing a) an overview, with the standalone control panel to the right of the apparatus. The apparatus has a geared rotary motor (at the top) capable of experimental faulting speeds from mm/year (creep) to m/s and an air-driven actuator applying normal stress between hollow rock cores (see panel b). During experiments, torque, axial load and axial shortening are measured. This apparatus is uniquely set up to accommodate a split-tube furnace, c). This is capable of producing sample temperatures up to 1100 °C prior to faulting. Samples are typically 25 mm diameter hollowed cores in order to reduce the gradient in slip rate across the

contact surface (d). The low-temperature sample holders are hydraulic, and are shown in e) during an experiment producing frictional melt between the sample cores. A larger set of low-temperature sample holders can accommodate samples up to 40mm diameter, allowing faster slip rates and stronger samples. An experiment conducted with high-temperature sample holders is show in f), where frictional melt can be seen extruding from the slip zone on both sides of the sample.

2.6.4. Fragmentation

Volcanoes are renowned for their capacity to erupt explosively and generate plumes of gas and ash into the atmosphere. Explosive activity occurs for almost all magma compositions and eruption types. Lava dome eruptions feature explosive activity in the vast majority of cases (Sparks 1997), and explosive eruptions may range from Vulcanian and phreatomagmatic explosions (Volcanic explosivity index (VEI) 1 to 4) to Plinian (VEI 5-7) magnitudes (Bluth and Rose 2004; Major and Lara 2013). Magmatic fragmentation can occur in several ways. Fragmentation is generally described to be triggered by the expansion of gas in bubbles causing tensile stresses sufficient to fracture the bubble walls. This may be produced due to accumulation of gas pressure or due to rapid decompression, which cause a high pressure gradient with the resultant effect of fragmentation. Decompression fragmentation has been extensively studied in shock tube apparatuses for several decades (Mader et al. 1994; Alidibirov and Dingwell 1996; Spieler et al. 2004; Koyaguchi and Mitani 2005; Kueppers et al. 2006; Alatorre-Ibargüengoitia et al. 2010; Arciniega-Ceballos et al. 2014), and the decompression threshold necessary to initiate fragmentation has been shown to be a function of permeability (Mueller et al. 2008) and crystallinity (Spina et al. 2016). Alternatively, the interaction of magma with of external volatile species such as water (generally termed molten fuel-coolant interaction and often encountered via a hydrothermal system) causes flash steaming. The rapid volume increase associated with this transition causes the thermomechanical strain to surrounding magma that may effectively fragment magma and cause powerful phreatomagmatic explosions (Wohletz 1983; Barberi et al. 1989; Büttner et al. 2006; Autin-Erickson et al. 2008). Fragmentation is thought to propagate within magma either as a rarefaction wave (Woods 1995; Koyaguchi and Mitani 2005) or a shock wave (Alidibirov and Dingwell 2000; Lavallée et al. 2012a). Fragmentation also occurs during fracturing (Clayton 2009; Kennedy and Russell 2012), fault slip (gouge and cataclasis) (Marone and Scholz 1989; Cashman et al. 2008; Hirose et al. 2012; Lavallée et al. 2015a; Lavallée et al. 2015b), abrasion (Freundt and Schmincke 1992; Dufek and Manga 2008; Mueller

et al. 2014) and milling (Campbell et al. 2013) within lava dome volcanoes. Due to the highly brittle behaviour of dome lavas, the production of ash manifests in almost every deformation event, and the sources of ash may be more diverse than for low-viscosity magmas which may be restricted to magmatic fragmentation (Dingwell et al. 2012).

2.6.5. The fragmentation threshold

The ability to simulate volcanic fragmentation events using a shock tube apparatus has spurred the understanding of decompression-triggered fragmentation. Seminal works have highlighted the critical effects of bubble overpressure and outgassing efficiency on the explosive potential of magma (Dingwell 1996; Mueller et al. 2008). A shock tube apparatus is composed of a large, low pressure tank, a high-pressure steel autoclave where a sample is enclosed, and a pressurisation system using diaphragms which open at a given differential pressure (Alidibirov and Dingwell 1996; Spieler et al. 2004). Pore pressure can be increased within the autoclave up to the threshold pressure of the diaphragm, when the diaphragm punctures. At this point a shock wave is generated upwards into the low pressure tank and a rarefaction wave propagates downwards through the sample in the autoclave. As the rarefaction wave passes through the sample, pressure stored within pores in the sample is released at a rate dependent on the pressure differential and the flow rate of the trapped fluid. The ability of a rock sample to outgas during rapid decompression depends upon the initial porosity and permeability (see Figure 2.30) within the sample, as this determines the flow rate (or pressure decay rate) under the imposed decompression (Spieler et al. 2004; Mueller et al. 2008). During shock tube experiments the imposed conditions can be carefully controlled (up to 50 MPa confining pressure and sample temperature up to 850 °C), the fragmentation process can be visually monitored and the entire particle distribution is preserved. This technique has therefore proved to be exceptionally useful in forensic determinations of the explosive behaviour of porous materials (Kueppers et al. 2006; Alatorre-Ibargüengoitia et al. 2010; McGuinness et al. 2012; Perugini and Kueppers 2012; Cimarelli et al. 2013). Ongoing comparisons between natural ash and experimentally produced particles will continue to contribute to our understanding of fragmentation phenomena at volcanoes.

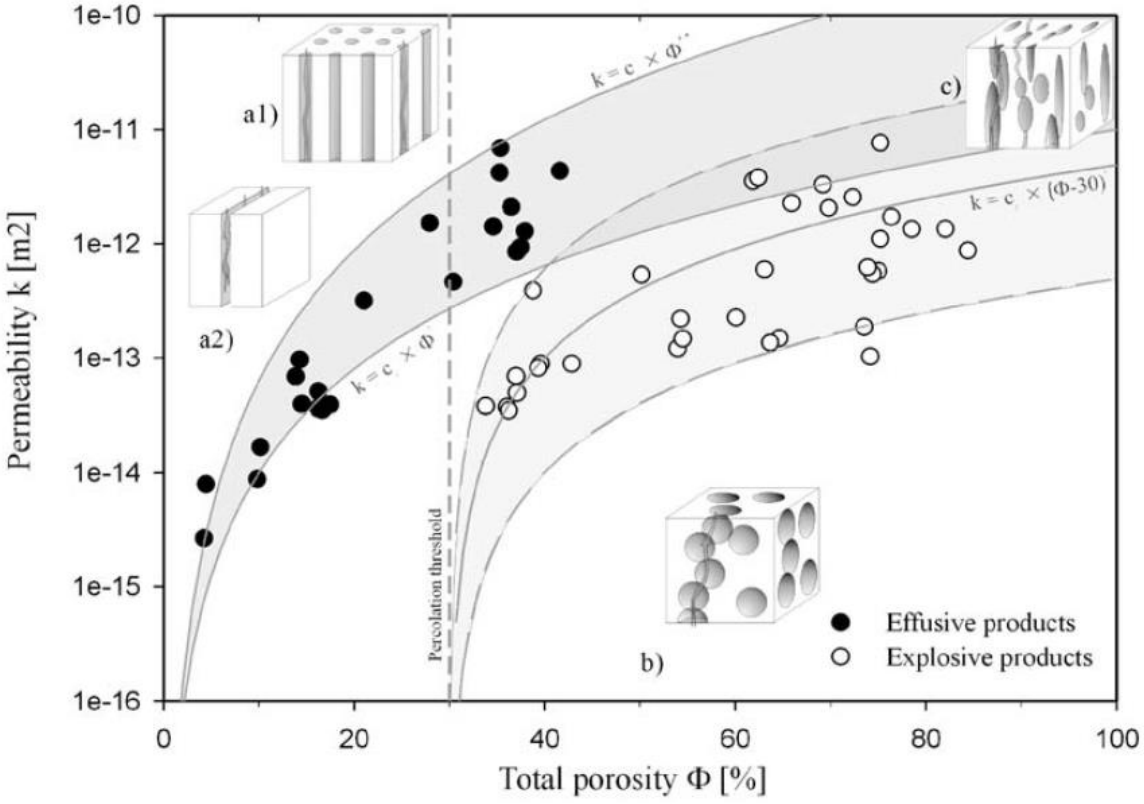

Figure 2.30. Porosity and permeability relationships of effusive and explosive products showing two separate trends. Porosity was measured using He-pycnometry and permeability by unsteady-state shock tube experiments where samples did not fragment and permeability was measured by a setup with a pair of transducers that measured the pressure decay in gas below the sample following instantaneous decompression in the upper chamber.For effusive products, capillary tube or fracture-flow models for degassing describe the spread in data (indicated in a1 and a2); For explosive products at 30 – 80% porosity (above the percolation threshold) porosity-permeability relationships fall within fully-penetrable sphere percolation models (shown in inset b), while a hybrid model may apply to very high porosity and permeability products. The overlap in data between effusive and explosive products indicates that fractures or intense shearing may defuse porous magmas, even above the percolation threshold. Figure from Mueller et al. (2004).

2.6.6. Particle analysis methods: QEMSCAN imaging and image processing

The programmed collection of microanalytical data to assign mineralogy and phases bears the general description 'automated mineralogy'. Automated mineralogy techniques use a particular set of measurements (physical and/or chemical) to classify phases within a sample – this may be a simple as discriminating a single mineral, ore or phase within a bulk sample, to classifying all phases within a material. The development of automated mineralogy methods since the 1970s was spurred by the mining and resources industry in order the rapidly analyse materials for commercial assessment and replace laborious manual processing of SEM images and microphotographs (Gottlieb et al. 2000). As such, most modern automated mineralogy techniques have been developed commercially for industrial applications and have been relatively poorly exploited for academic research within the geosciences (Pirrie et al. 2004; Haberlah et al. 2011). QEMSCAN® is an automated mineralogy technique that uses SEM-EDX (Scanning Electron Microscope – Energy Dispersive X-ray) measurements to assign phases within a material and produce a false-colour phase map of the sample. One of the significant advantages of QEMSCAN analysis is high-speed mapping of samples to rapidly provide large datasets resolved at high resolution. QEMSCAN® is particularly effective in PMA (particle mineralogical analysis) mapping mode, providing a size-sorted image output and a range of standard particle size, distribution and shape analyses using proprietary software.

The system employs a combination of SEM BSE (Back-scattered electron) signal and EDS X-ray data to automatically analyse a sample at a micron scale, producing thousands or millions of chemical analysis points in a map, with a selection of four measurement modes (Haberlah et al. 2011). In PMA mode, backscatter electron signals are used to map the occurrence of non-overlapping particles from background within a polished stub or thin section, and omitting other particles from further analysis, thereby improving mapping speeds and allowing for particle size and shape analyses and image sorting. Each isolated particle in a mapping region is measured in a grid, with each measurement step producing a pixel defining the resolution of the output image (Figure 2.31). Each analysis point or pixel records an X-ray that is used to assign mineralogy from the chemical elemental spectrum, by comparison to a database that is customised using *a priori* information on the expected assemblage for a sample type. The EDX spectrum for each measurement point is analysed in real time by a Species Identification Protocol (SIP) consisting of background subtraction, thresholding, windowing, overlap correction and calculation of peak

ratios to determine element spectral lines (Gottlieb et al. 2000) and compare against a mineral database. These data are compared to the database using a hierarchical system that compares against the most likely and most abundant phases first, and considers variations in BSE intensity and element ratios where EDX data do not provide a firm or unique match.

Figure 2.31. A QEMSCAN® apparatus with four EDS detectors is shown, together with the step-by-step measurement protocol running left-to-right along the top row and phase assignment protocol (left-to-right along the bottom row). Images ©FEI Company.

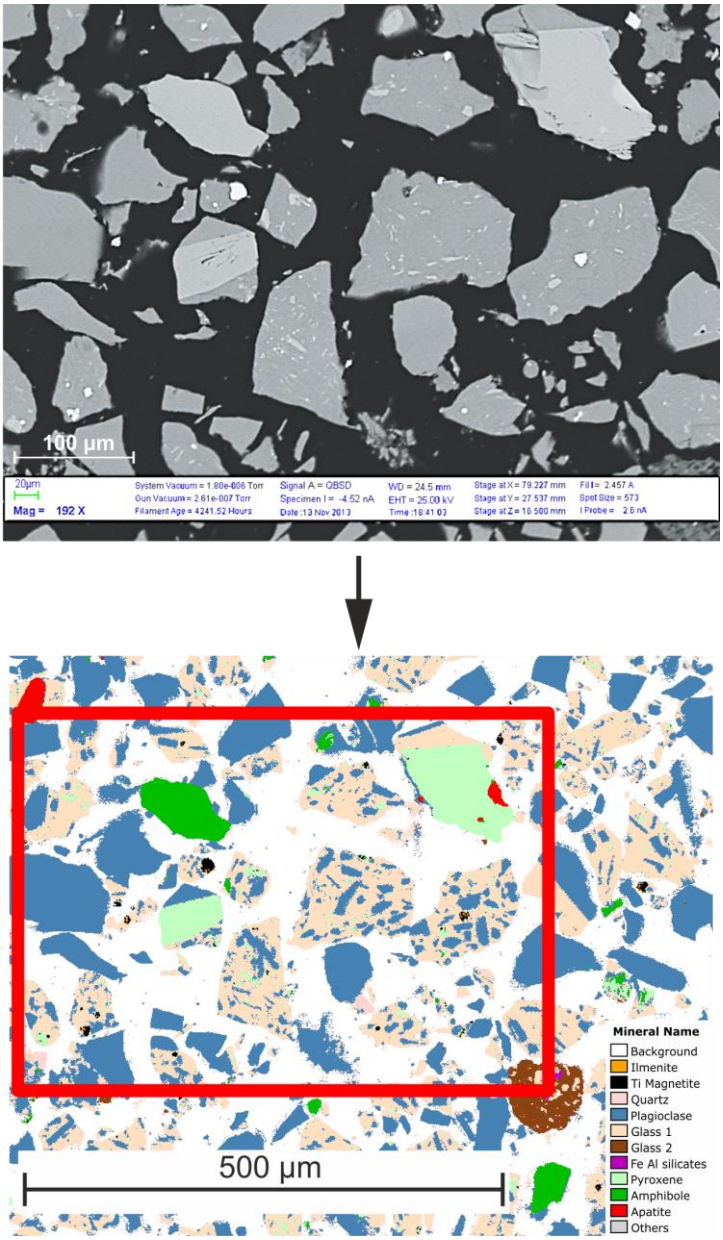

Figure 2.32. SEM BSE image (top) and corresponding area shown by red box analysed using QEMSCAN® PMA (bottom). Notice the variations in greyscale (backscatter electron intensity) corresponding to different phases, and the similarity in shade between plagioclase feldspar and glass, the two most abundant phases.

Multiple (2 or 4) EDS detectors are used in tandem and the EDX pre-amplifiers are optimised to rapidly measure x-rays, improving measurement time, however each pixel is typically restricted to 3% approx. elemental detection limit per analysis point due to the rapid mapping speed. This restricts the capability to measure minor elemental constituents of some minerals, occasionally obscuring distinctive minor element ratios (Rollinson et al. 2011). Therefore, the mapping speed must be balanced by the necessity to provide representative sampling. EDS resolution is limited

by the x-ray generation volume, which is typically 1-2 µm in diameter and depth and the measurement step-size, which provides a lower limit for the resolution of particles and phases. In addition, x-ray spectra do not detect differences in the concentration of light elements (e.g. H) and have limited detection of C and O. For unusual minerals (Rollinson et al. 2011) or phases (e.g. volcanic glass), electron microprobe (EPMA) and x-ray diffraction measurement data can be used to expand or constrain the SIP database, as accurate phase classification requires confidence in the validity of the SIP. However, with sufficient preparatory work, QEMSCAN® provides highly efficient and robust phase mapping and a versatile image output.

QEMSCAN image outputs can be readily analysed using freely available software such as ImageJ to determine particle size distribution, phase size distribution, distribution of phases within particles and particle and phase shape descriptions. The size-sorted particles and phase-limited palette in the image output allow for easy per-particle analysis. Thresholds can be applied to discriminate phase populations within each image (Figure 2.33). In practise, this is easier using image manipulation software like Adobe Photoshop or Gimp rather than ImageJ. The single phase images from a QEMSCAN® image output can be interrogated individually or loaded into ImageJ as an image stack by selecting File>Import>Image sequence and selecting the first image in a folder. This enables total phase fractions to be quickly measured and keeps all phases in a sample together for ease of measurement. Separate phase images can be converted to binary and set to scale to allow measure functions in ImageJ.

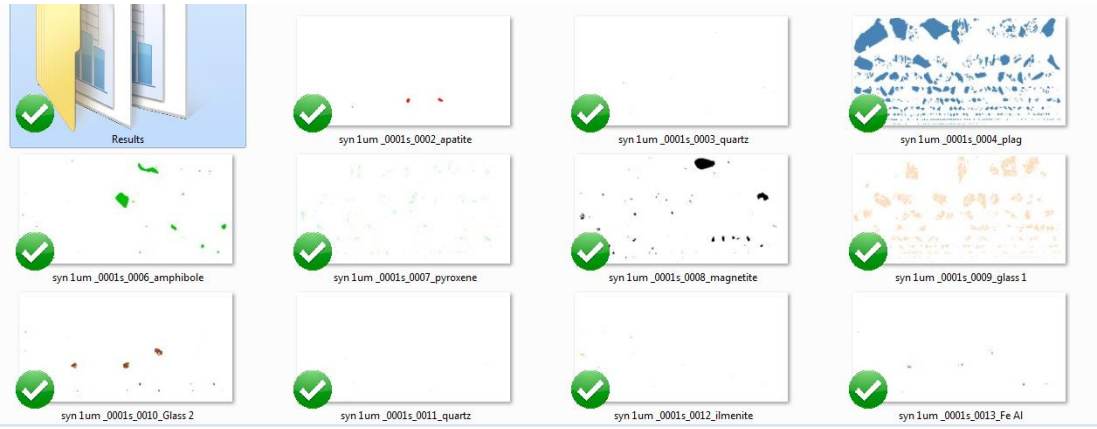

Figure 2.33. An example of phase-resolved images from a composite QEMSCAN® image

The outline of particles (Figure 2.34) can be retrieved by loading two full-colour QEMSCAN® output images and converting one to binary, then using Process>Binary>Fill Holes/Outline to create a black outline of each particle. This can then be used to measure the fraction of phases

present at particle boundaries (using the Process>Image Calculator>AND operation to create a full-colour outline) or as a mask to measure the per-particle fraction of each phase (figure 2.34). In order to do this, each particle must be classified as a region of interest (ROI) by ticking 'Add to Manager' in the Analyze>Analyze Particles tool, then selecting the stacked phase images and selecting Image>Overlay>From ROI Manager. This then allows the phase fraction for each particle to be calculated, allowing size-sensitive variations to be detected.

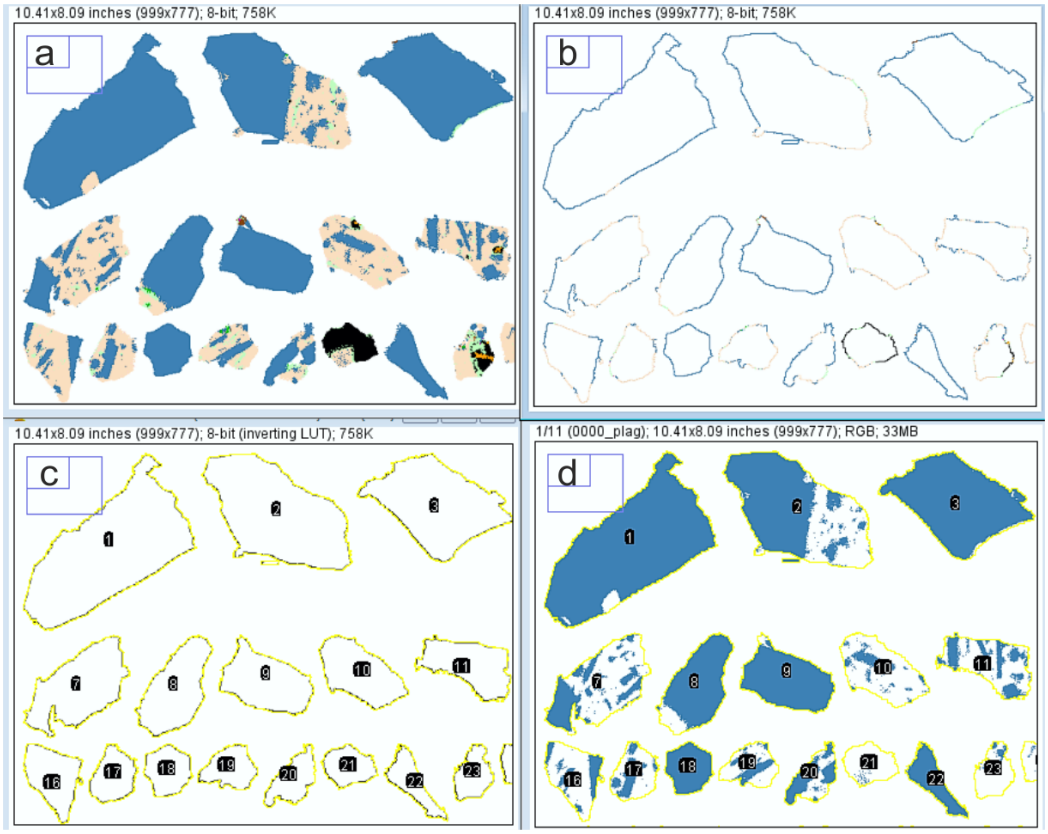

Figure 2.34 a. Unmodified QEMSCAN® output file – 12-colour tiff bitmap. b) Outlines of particles shown in part a), showing distribution of mineralogy. c) Each particle set as a region of interest and selected (in yellow). d) Regions of interest applied as a mask to a phase image stack, showing plagioclase distribution within total particle shape and size. All images were produced using ImageJ.

Chapter Three

Spine growth and seismogenic friction at Mt Unzen, Japan

Preface

This study explores the emplacement of lava spines, a spectacular representation of brittle faulting at lava dome volcanoes. However, this study expands on a purely brittle description of faulting to describe the likelihood and rheological consequences of frictional melting production during slip in volcanic environments. Many of the key themes within the thesis are first introduced in this chapter: transitions between viscous and brittle deformation, the integration of geophysical and experimental data and the focus on macro-scale mechanics driving volcanic deformation. Fault friction was investigated using state-of-the-art high velocity rotary shear apparatuses in Japan and Liverpool, and constraints on the magnitude and rate of slip were estimated from analysis of seismic and visual monitoring data during the episode of spine growth. This study was published in the Journal of Geophysical Research in 2015. The seismic analysis proved particularly interesting and fruitful, spurring a standalone study (Lamb et al. 2015c) published in the same year.

Within this paper all work was my own, with the exception of the primary seismic dataset, provided by K. Umakoshi with assistance from T. Miwa, seismic signal processing and analysis conducted by S. De Angelis and O. Lamb and field photographs taken by Y. Lavallée and J. Kendrick. Access and support for specific facilities and apparatus are also recognised in the author list (HVR apparatus provided through T. Hirose; Electron microprobe access provided through D. Dingwell and microanalytical support from F. von Aulock and S. Henton De Angelis) together with discussions and comments from all co-authors.

Spine growth and seismogenic faulting at Mt. Unzen, Japan

Abstract

The concluding episode of activity during the recent eruption of Mt. Unzen (October 1994 to February 1995) was characterised by incremental spine extrusion, accompanied by seismicity. Analysis of the seismic record reveals the occurrence of two dominant long-period event families associated with a repeating, non-destructive source mechanism, which we attribute to magma failure and fault-controlled ascent. We obtain constraints on the slip rate and distance of faulting events within these families. That analysis is complemented by an experimental thermo-mechanical investigation of fault friction in Mt. Unzen dacitic dome rock using a rotary-shear apparatus at variable slip rates and normal stresses. A power density threshold is found at 0.3 $MW.m^{-2}$, above which frictional melt forms and controls the shear resistance to slip, inducing a deviation from Byerlee's frictional law. Homogenised experimentally-generated pseudotachylytes have a similar final chemistry, thickness and crystal content, facilitating the construction of a rheological model for particle suspensions. This is compared to the viscosity constrained from the experimental data, to assess the viscous control on fault dynamics. The onset of frictional melt formation during spine growth is constrained to depths below 300 m for an average slip event. This combination of experimental data, viscosity modeling and seismic analysis offers a new description of material response during conduit plug flow and spine growth, showing that volcanic pseudotachylyte may commonly form and modify fault friction during faulting of dome rock. This model furthers our understanding of faulting and seismicity during lava dome formation and is applicable to other eruption modes.

3.1. Introduction

Lava dome eruptions are one of the most hazardous forms of volcanic activity. Dome destabilization may generate block-and-ash flows as well as catastrophic explosive eruptions. Magma ascent during dome eruptions has been described as cyclic at timescales of seconds to years (Voight 1999; Sparks 2000; Harris et al. 2003; Costa et al. 2013; Lamb et al. 2014); where longer timescales are attributed to variations in the magmatic system and shorter timescales are generally believed to reflect shallow conduit processes, including the rheological stability of magma. Careful monitoring of lava domes is thus central to mitigating the risk posed by their activity. Seismic monitoring in particular has revealed that magma transport in dome-building eruptions is a rich source of earthquakes, and analysis has revealed the importance of discerning the frequency and period of earthquakes emanating from the uppermost (<3 km) edifice (Chouet and Matoza 2013). Many studies have attempted to describe the source mechanisms underlying these signals: high-frequency and hybrid seismic signals have been interpreted to originate from magma fracturing processes (Harrington and Brodsky 2007; Umakoshi et al. 2011; De Angelis and Henton 2011), whilst shallow long-period (LP) seismicity has been associated with resonance of fluid in the conduit (Neuberg et al. 2006; Thomas and Neuberg 2012), or in a crack (Chouet 1988; Burlini et al. 2007; Maryanto et al. 2008; Benson et al. 2008). A recent study, employing proximal seismometer networks, has proposed that LP events may also be caused by slow-rupture of weak volcanic materials (Bean et al. 2013).

Lava dome eruptions at Mt. Unzen (Japan), Mount St. Helens (USA), Soufrière Hills volcano (Montserrat), Volcán De Colima (Mexico) and Santiaguito dome complex (Guatemala) have all been characterised by cyclic behaviour (Neuberg et al. 2006; Iverson et al. 2006; Umakoshi et al. 2008; Lamb et al. 2014; Johnson et al. 2014). The seismic signals emitted contain a characteristic sequence of waveform families with event counts that emerge and decay in a near-sinusoidal fashion, simultaneous with cycles of tilt. Seismic output often increases during inflation and decreases following rapid deflation, once a threshold is reached, after which the cycles begin again (*e.g.,* Neuberg et al. 2006). The threshold in question has been modeled to reflect friction along faults that form at the conduit margin as magma releases the stress accumulated during inflation by fracturing, leading to the pulsatory extrusion of spines (Neuberg et al. 2006; Iverson et al. 2006; Lensky et al. 2008; Massol and Jaupart 2009; Scharff et al. 2014). Spines are dense, degassed and high-viscosity magma plugs, extruded as coherent bodies bounded by marginal fault zones (Cashman et al. 2008; Pallister et al. 2013). Gas pressurization beneath the plug has

commonly been cited as the driving force for fracture propagation (Voight 1999; Johnson et al. 2008; Massol and Jaupart 2009; Lyons et al. 2012) and the mechanical contribution from magma failure and slip events (Lavallée et al. 2011; Thomas and Neuberg 2012; Chouet and Matoza 2013; Kendrick et al. 2014b) outgassing pulses (Voight 1999; Waite et al. 2008; Massol and Jaupart 2009; Collinson and Neuberg 2012; Michaut et al. 2013) and wall rock elasticity (Costa et al. 2007; Costa et al. 2012) have been proposed to contribute to short term cyclicity in monitored geophysical and geochemical signals.

Evidence from field, experimental and numerical studies show that strain localization in magmas can control ascent dynamics in a volcanic conduit. During ascent, magma undergoing localised strain near the conduit margin may yield to brittle failure (Yamasato 1998; Goto 1999; Tuffen and Dingwell 2004; Lensky et al. 2008; De Angelis and Henton 2011; Okumura et al. 2013) and slip (Thomas and Neuberg 2012; Lavallée et al. 2013; Kendrick et al. 2014b). Rheologically, the presence of multiple phases in magma (liquids, crystals, gas bubbles) partitions the applied stress, and, as strain rate across a conduit of ascending magma varies non-linearly, shear thinning favors strain localization at the conduit margin (Caricchi et al. 2007; Okumura et al. 2013; Lavallée et al. 2013). Extensive strain and high strain rates in this area may lead to seismogenic magma failure (Lavallée et al. 2008; Cordonnier et al. 2009), marking the onset of friction-controlled ascent (Kendrick et al. 2014b). These two scenarios for magma ascent are illustrated in the upper and lower parts of the conceptual model in Figure 1. The processes and criteria attendant on magma failure have been the subject of several experimental (Alidibirov and Dingwell 1996; Dingwell 1996; Gonnermann and Manga 2003; Rust et al. 2004; Spieler et al. 2004; Okumura et al. 2010; Cordonnier et al. 2012a; Costa et al. 2012; Lavallée et al. 2012a) and numerical (Costa et al. 2007; Hale and Wadge 2008; Collinson and Neuberg 2012) studies, but knowledge of the frictional properties of volcanic fault rocks is more scarce (Moore et al. 2008; Kennedy et al. 2009; Lavallée et al. 2012b; Lavallée et al. 2014; Violay et al. 2014; Kendrick et al. 2014a) and thus our ability to interpret the geophysical signals that accompany volcanic unrest remains insufficient.

3.1.1. Fault friction

The process of fault slip has been extensively studied in earthquake physics in past decades (Sibson 1975; Spray 1992; Tsutsumi and Shimamoto 1997b; Di Toro 2006; Beeler et al. 2008; Faulkner et al. 2011; Hirose et al. 2012; Chang et al. 2012). At low slip velocities rock friction

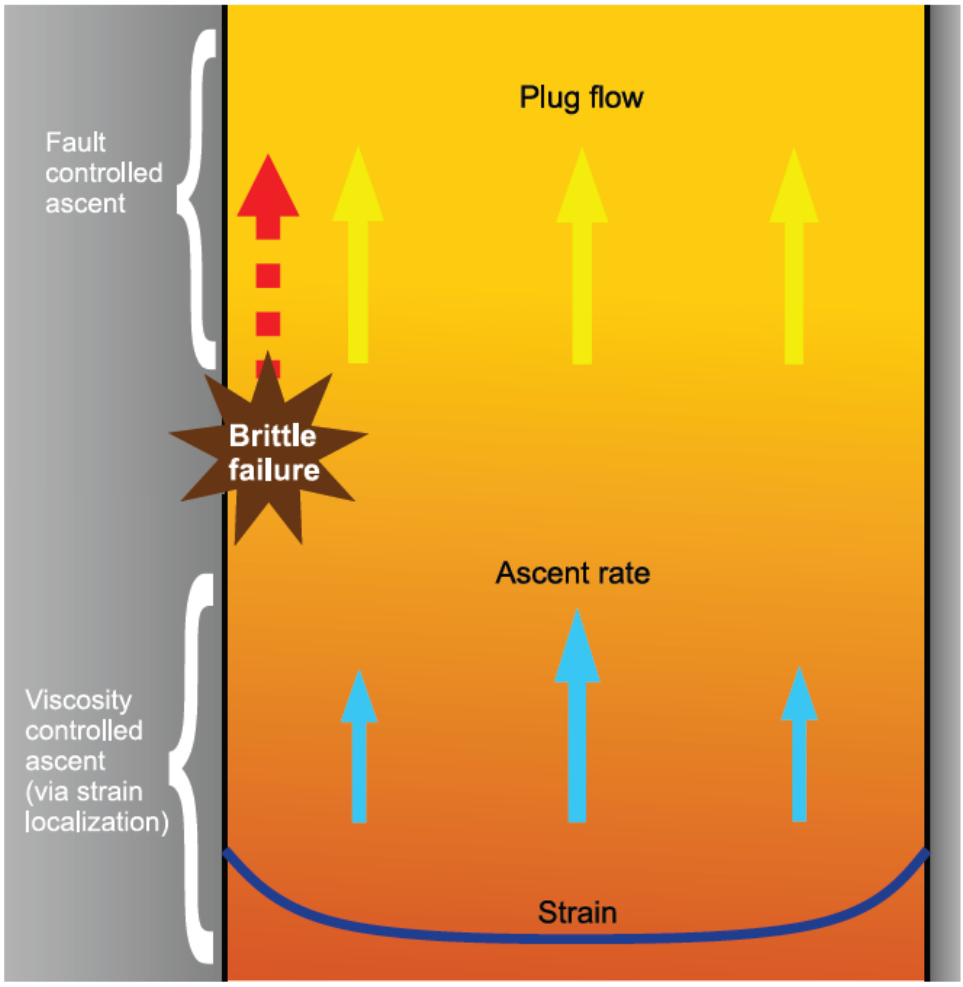

Figure 1: *Conceptual model of magma ascent within a shallow conduit cross-section. Arrows represent relative magma ascent rate across the conduit, blue arrows showing faster rates toward the centre of the conduit, and yellow arrows showing plug flow during marginal faulting events. Strain localization of viscously ascending magma at the conduit walls is shown in the lower half of the figure as friction inhibits flow at the conduit walls, localizing strain (thick blue line). This may force magma to fail and slip can occur near to the conduit walls, causing a transition from viscosity- to fault-controlled ascent as illustrated in the center of the figure. Above this point magma moves as a solid plug and slip dynamics are governed by friction along the slip interface.*

measurements have led to the conception of rate- and state-dependent friction laws (Dieterich 1978; Ruina 1983; Dieterich and Kilgore 1994), and for normal stress <200 MPa (*i.e.,* shallow crustal conditions), the relationship between shear stress (τ) and normal stress (σ_n) is well described by Byerlee's empirical friction law (Byerlee 1978):

$$\tau = 0.85\sigma_n \qquad (1).$$

At high slip velocities, however, the shear resistance to slip exhibits a strong departure from this relationship, which has generally been attributed to flash heating due to the conversion of mechanical work into heat (Spray 1992; Goldsby and Tullis 2011). Slip at high power densities (the product of slip rate and shear stress) may generate sufficient heat to induce frictional melting in silicate rocks – a process preserved in the geologic record in the form of pseudotachylyte (Shand and Shand 1916; Sibson 1975). In cases where a fault hosts gouge material, mineral decomposition and strain localization at high slip rate have also been shown to provide low friction coefficients (Mizoguchi et al. 2009; Di Toro et al. 2011; Hirose et al. 2012; Lavallée et al. 2014).

Friction in volcanic conduits and during spine extrusion, is especially important for the final stage of magma ascent in the uppermost ~1-2 km (Kennedy et al. 2009; Pallister et al. 2013), and shows a dependence on velocity and normal stress. Experiments have shown that failure, followed by slip at low power density, engenders comminution and cataclastic ash generation (Kennedy and Russell 2012). Ascent mechanics of the spine may be influenced by incorporation of fragmented ash and breccia in the fault surface at shallow depths due to low normal stresses (Kendrick et al. 2012). The frictional properties of volcanic ash have been experimentally determined at low- to high-slip velocities. At low slip rate (10^{-6}-10^{-3} $m.s^{-1}$) faults bearing volcanic ash gouge change from rate-weakening to rate-strengthening (Moore et al. 2008) and exhibit strain-hardening (Kennedy and Russell 2012). A recent study of high-velocity, rotary-shear (HVR) experiments on volcanic ash gouge from different volcanoes (including Mt. Unzen) has extended the description of ash gouge friction (at ambient temperature), providing a frictional law to constrain rate-weakening behaviour at a range of slip velocities of up to 1.3 $m.s^{-1}$ and normal stresses of up to 2.5 MPa (Lavallée et al. 2014). In ash gouge experiments, high temperatures may be achieved, possibly prompting rapid viscous sintering, which raises the question of the longevity of (particulate) volcanic ash in conduit slip zones (Kolzenburg and Russell 2014; Bizzarri 2014).

Field and experimental evidence have suggested that faulting during dome eruptions may commonly result in frictional melting even over short slip distances, owing to the high temperatures (and low fusion temperatures) of dome lavas in the magmatic column (Kendrick et al. 2014a; Kendrick et al. 2014b). Rotary shear experiments have helped shape our understanding of frictional melt, its rheology and role during energetic seismogenic faulting. At high slip rates, rapid and intense heat generation achieves temperatures in excess of the fusion temperature of some, or all of the mineral phases, to form a melt (Shimamoto and Lin 1994; Di

Toro 2006; Spray 2010). The rheology of silicate melts is very well described in terms of composition, temperature, strain rate (Webb and Dingwell 1990b; Hess et al. 1996a; Hess and Dingwell 1996; Hess et al. 1996b; Dingwell et al. 1996; Giordano et al. 2008) and, to some extent, in terms of crystal and vesicle fraction (Lejeune et al. 1999; Lavallée et al. 2007; Caricchi et al. 2007; Mueller et al. 2011; Cimarelli et al. 2011; Cordonnier et al. 2012a; Mader et al. 2013; Truby et al. 2015); yet, its control on fault friction has received little attention (Bowden and Persson 1961; Spray 1993; Fialko and Khazan 2005; Nielsen et al. 2008; Sone and Shimamoto 2009; Violay et al. 2014). Lavallée et al. [2012] stated that volcanic frictional melts have a non-Arrhenian temperature dependent viscosity and, at volcanically relevant strain rates, display a small component of shear thinning behaviour. Under tectonic conditions it has been observed that frictional melt lubricates the fault plane (Spray 2005; Di Toro 2006; Di Toro et al. 2011; Brown and Fialko 2012), however, studies have revealed high shear resistances induced by the presence of frictional melt at low normal stresses, that suggest they may act as an adhesive (or viscous brake) to slip (Fialko 2004; Koizumi et al. 2004). This is particularly important in shallow volcanic settings where it provides an additional rheological contribution to fault slip instability, and may control the stick-slip phenomenon that produces drumbeat seismicity during magma ascent (Kendrick et al. 2014b). The significance of frictional melting in shallow volcanic processes requires further study. Here we have expanded and constrained the application of frictional properties to lava dome eruptions by combining seismic analysis, experiments, and rheological modeling to evaluate the role of fault processes during spine extrusion in 1994-1995 at Mt. Unzen.

3.1.2. Spine growth at Mt. Unzen

Mt. Unzen underwent a protracted period of dome growth between 1991 and 1995 (Nakada et al. 1999). In less than 4 years, 2.1 x 10^8 m^3 of magma (dense rock equivalent)
was erupted at discharge rates of 0.1 - 4 x 10^5 $m^3.day^{-1}$, equivalent to ascent rates of 0.008 – 0.13 $m.s^{-1}$ (Venezky and Rutherford 1999; Noguchi et al. 2008; Cichy et al. 2010). The eruption was punctuated by two distinct phases of spine growth, at the onset of the eruption (20–21 May 1991) when extrusion rate was at its highest, and at the end of the eruption (mid-Oct. 1994 and mid-Feb. 1995) when spine growth was measured at an average of 0.8 $m.day^{-1}$ (Yamashina et al. 1999). The late spine extrusion was accompanied by 40-60 hour inflation/deflation cycles and vigorous seismic swarms at depths generally shallower than 0.5 km (Yamashina et al. 1999; Umakoshi et al. 2008), constrained to originate from pressure fluctuations at 0.7-1.3 km depth

(Hendrasto et al. 1997; Kohno et al. 2008). The final spine grew to a total of 150 m wide, 30 m deep and 40 m high (Nakada et al. 1999), preserving a record of the deformation mechanisms

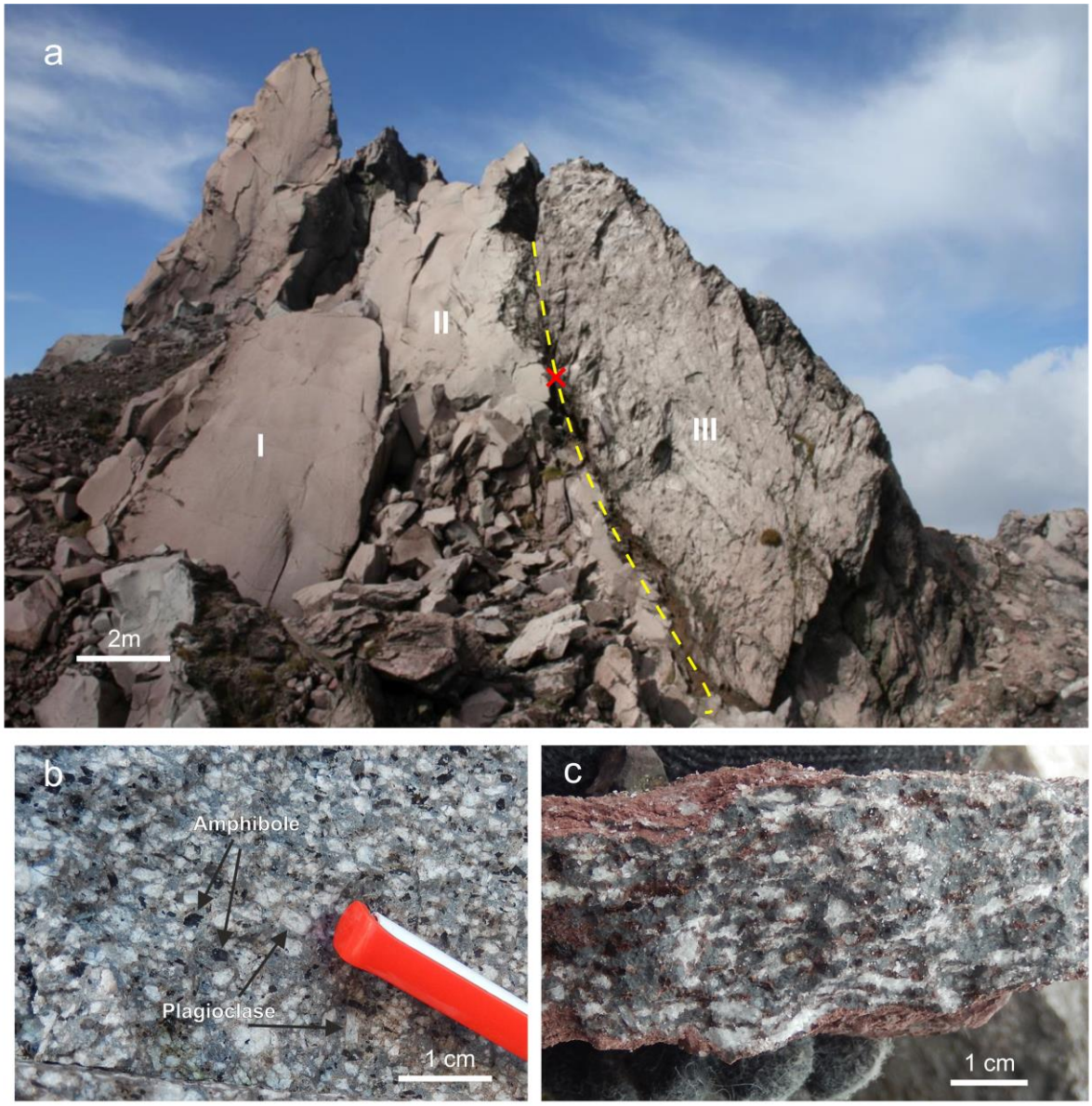

Figure 2: *a) The relict 1994-95 spine at Mt. Unzen volcano, showing a range of deformation types, including: (I) a viscously sheared spine interior showing cavitation structures (Smith et al. 2001) and grading of macroscopic fractures increasing in number towards (II) an intensely sheared block showing the textural record of viscous to brittle deformation bounded to the right by the core of the fault zone (dashed line) and (III) fault breccia consisting of large blocks and sintered fragmented ash and gouge which has become welded to, and extruded with the spine; b) Undeformed rock specimen from Mt. Unzen dome, showing large, euhedral, phenocrysts of plagioclase and amphibole, and smaller Fe-Ti oxides set into a rhyolitic interstitial glass; c) Deformed rock specimen from the fault zone (marked with a red cross on main photo), showing intense shearing of plagioclase phenocrysts and loss of amphibole phenocrysts.*

acting during magma ascent. A structural survey of the relict spine (Smith et al. 2001) exposed a range of ductile and brittle deformation structures, including shear zones with complex dilational structures (contributing to the permeable network), sintered breccia, and shear zones hosting cataclasite (Figure 2a). Close examination of the fault zone compared to the undeformed lava core (Figure 2b), reveals a heavily damaged rock, with sheared plagioclase crystals and few visible amphibole fragments (Figure 2c).

The dome and spine material is dacitic (65 ±1.5 wt. % SiO_2) and contains 24-35 vol. % phenocrysts, dominantly plagioclase, amphibole, and biotite together with iron-titanium oxides and quartz in a groundmass containing 40 ±10 vol. % microlites within a peraluminous rhyolitic interstitial glass containing ca. 78 wt. % SiO_2 (Nakada and Motomura 1999; Almberg et al. 2008; Cordonnier et al. 2009). The interstitial glass transition (estimated on the basis of a viscosity of 10^{12} Pa.s) is constrained to 759 °C using the chemical composition in the viscosity model of Giordano et al. (2008). Note that the glass transition is higher when considering heating rates and strain rates as high as those presented in this study (*e.g.,* Lavallée et al. 2012b) and would approximate values some 200-250 °C higher at heating rates of ca. 300-400 °C.s^{-1} (c.f., Gottsmann and Dingwell 2001).

3.2. Methods

3.2.1 Seismic analysis of fault friction at Mt. Unzen

We analyzed the continuous seismic records from one station (FG1) for the period October 1st 1994 – February 28th 1995 using the GISMO MATLAB suite (Figure 4) (Reyes and West 2011) and performed single-station detection (SSD) on the data using a short-term average/long-term average (STA/LTA) algorithm. Seismic station FG1 (Figure 3) was chosen as the best candidate for use as a master station in SSD due to its consistent operation and its proximity (~0.6 km) to the lava dome (Umakoshi et al. 2008). Event rates, peak amplitude and frequency index (*FI*) metrics were used to characterise identified seismic events. Event rates were computed on an hourly basis by counting the events that fall within hour-long bins. Peak amplitude was determined from the highest absolute value of demeaned event waveform data. *FI* is a spectral ratio defined as:

$$FI = \log_{10}\left[\frac{mean(A_{upper})}{mean(A_{lower})}\right] \quad (2),$$

which was designed to provide a consistent classification of seismic events (Buurman and West 2010). This method uses the ratio of the mean spectral amplitude in two predefined spectral bands, A_{upper} and A_{lower}, to describe the relative partitioning of energy at high and low frequencies for a given event. To identify earthquake clusters (families of events with similar waveforms, also known as multiplets) from the series of SSD events, we used a cross-correlation technique with a hierarchical clustering scheme. This scheme was successfully employed to detect clusters at Augustine (Buurman and West 2010) and Redoubt (Ketner and Power 2013) volcanoes.

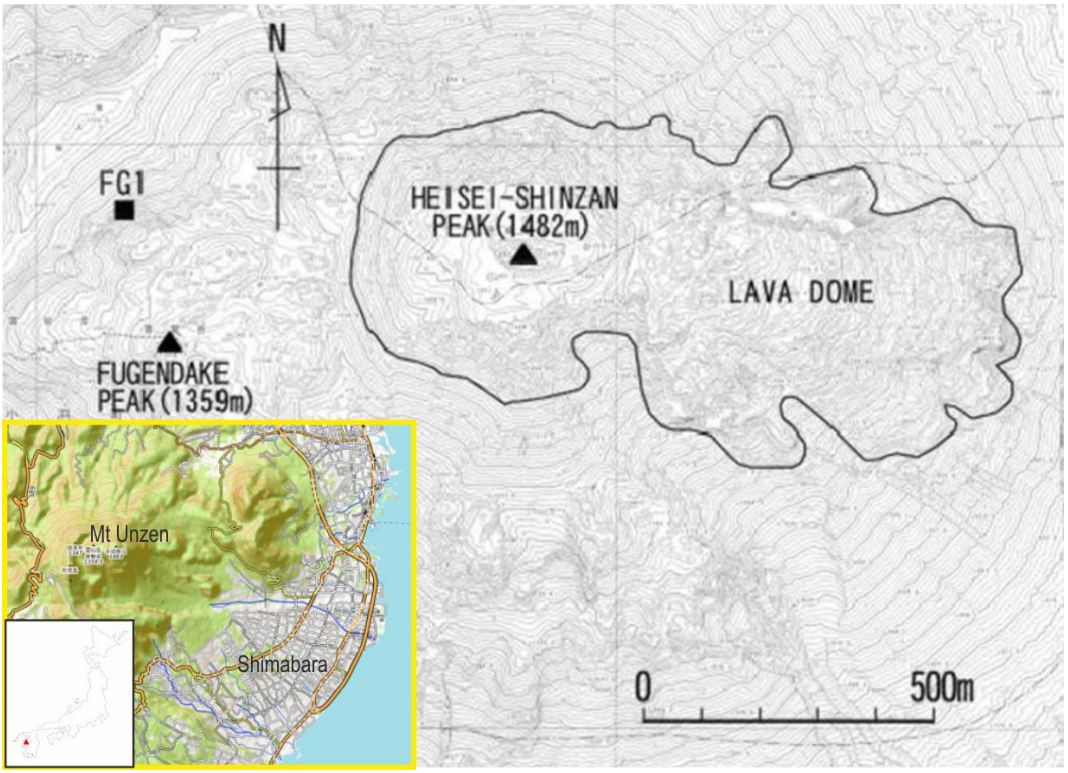

Figure 3. Overview map, showing the extent of the 1991-95 lava dome and the location of the FG1 seismic station, modified from Umakoshi et al (2008). The spine was emplaced on the Heisei-Shinzan peak, near to the black triangle. Insets shows the local and national setting of Mt. Unzen – source Topomapapp CC

To be successfully included in a cluster, an event must have a minimum mean correlation value of 0.8 with all the other events in the cluster. A threshold of five events was used to define the minimum number needed to compose a cluster. Source durations were estimated from manual picking of the *P*-wave pulse duration for each event (Figure 4c). Estimates of average fault slip velocity were obtained from measurements of average source duration and slip distance per event. In order to estimate the average slip distance associated with a single seismic event we considered the total event count for clusters over two periods in early November 1994 (assuming

that all these events originated from faulting along spine walls during extrusion; see discussion in **Section 3.4.2**) during which vertical spine extrusion was recorded using time-differential spectroscopy and theodolite surveys (Japanese Meteorological Association 1995; Yamashina et al. 1999).

3.2.2. Fault friction experiments

The frictional properties of Mt. Unzen dacite were investigated using two low- to high-velocity rotary shear (HVR) apparatuses. The sample block was collected from a block and ash flow deposit during a field campaign in 2008, and has mineralogy akin to that described in Nakada and Motomura (1999) and Almberg et al. (2008), with <40 vol. % glass, a density of 2505 kg.m^{-3} and contains ~13 vol. % porosity as measured by a Micromeritics He-Pycnometer. The HVR set-ups use a concentric sample geometry and are capable of rotation rates from ~1 rotation per year up to 1500 rotations per minute (rpm) and applied normal force up to 10 kN (Shimamoto and Lin 1994; Tsutsumi and Shimamoto 1997a). In this study, high slip rate (>0.4 m.s^{-1}) tests were performed with the first-generation HVR at the Kochi/JAMSTEC Core Center (Japan) and low slip rate (<0.4 m.s^{-1}) tests were performed with the second-generation HVR at the University of Liverpool (UK). We prepared hollow cylindrical samples with 25 mm outer diameter and 10 mm inner diameter to create a ~7.5 mm wide annular contact surface; this minimises the effect of variable shear resistance produced by a gradient in strain rate (see Figure 5a). Displacement rate was calculated using an equivalent rotational rate, V_e (m.s^{-1}), defined such that $\tau V_e S$ gives the rate of total frictional work (where τ is shear stress and S is the fault area), assuming constant shear stress across the fault surface (after Shimamoto and Tsutsumi 1994):

$$V_e = \frac{4\pi R(D_o^2 + D_i D_o + D_i^2)}{3D_o + D_i} \quad (3)$$

where R is the revolution rate (s^{-1}), and D_o and D_i are the samples' outer and inner diameters, respectively. We conducted the HVR experiments at six slip rates (0.001, 0.01, 0.1, 0.4, 1.0 and 1.45 m.s^{-1}) and five normal stresses (0.4, 1.0, 2.0, 3.0 and 3.5 MPa) for a total of 20 m of slip. A full list of experiments is contained in Table 3.1. During the experiments the shear stress, normal stress and shortening were recorded at 500 Hz. Prior to high slip rate tests the sliding surfaces were ground parallel over ~200 revolutions at 0.1 MPa and 0.1 m.s^{-1}, and each sample was bound with aluminum wire to reduce the tendency for fracturing by thermal expansion during

experiments at high load. Axial stresses >3.5 MPa led to failure at the onset of rotation as high torque, thermal fracturing (Ohtomo and Shimamoto 1994) and high initial fracture density of the samples (*e.g.,* Cordonnier et al. 2009) caused the sample strength to be overwhelmed. The experiments were recorded with optical and infrared thermographic cameras throughout the experiment. For experiments in Kochi/JAMSTEC Core Center, we employed a H2406 NEC\Avio thermographic infrared camera with 90 μm pixel size at 30 frames per second and analyzed the images using InfReC Thermography Studio. For the experiments in Liverpool, we used a FLIR X6000sc thermographic infrared camera and analyzed the images using the FLIR IR Max software package. For all thermal videos the maximum pixel temperature was tracked through time, as a lower bound for temperature along the slip zone. It is important to note that the monitored surface temperatures slightly underestimate the actual temperatures generated along the slip interface inside the samples (see **Section 3.3.5**).

3.2.3 Frictional melt structure, chemistry and rheology

The frictional melt layers that solidified into glassy pseudotachylytes were examined using optical microscopy on thin sections cut tangentially to the sample annulus. The fraction, size and aspect ratio of the comminuted crystalline phases were measured by converting cross-polarised photomicrographs (using a Leica 2500P microscope under transmitted light at 10x zoom) of the center of each slip zone into binary images using the open source software ImageJ. We assigned cumulative crystal fragment area by aspect ratio bins to determine the crystal size distribution within the pseudotachylytes. The thickness of melt layers is required to calculate strain rates, but thickness cannot be estimated directly during a test, and we revert to measuring the average thickness of the solidified glass layers as a proxy, although this represents a minimum value as a certain amount of melt may have been extruded upon cooling at the end of the test (*e.g.,* Hirose and Shimamoto 2005).

Chemical analysis and imaging were performed using a Cameca SX100 electron microprobe. Measurements were made on polished thin sections prepared from 8 post-experimental samples (see Table 2). For the homogenised slip zones we conducted measurements using a 10 μm defocused beam with 15 kV accelerating voltage and 5 nA sample current. For each thin section ~30 points were chosen on the glass of the experimentally generated pseudotachylyte: near the center of each thin section and away from crystals. However, for sample 3758 (with low melt

generation), 12 additional measurements were performed under shortened acquisition time with a focused beam. In order to assess and thereby minimise the potential loss of alkalis we compared analyses made with focused and defocused beams. The water content present in the glass was estimated through measurement of thermogravimetric weight loss using a simultaneous thermo-analyzer (Netzsch STA Jupiter 449 F1 with a resolution of 25 ng). The change in mass of a 0.19 g sample of glass produced from experiment HVR 3376 (1.45 $m.s^{-1}$ at 3 MPa) was measured during heating in an argon atmosphere to 1150 °C at 10 $°C.min^{-1}$ with a dwell time of 180 min.

The temperature dependence of viscosity of the frictional melt was calculated using mean major element compositions and volatile content of the pseudotachylyte glass as inputs into the melt viscosity model developed by Giordano et al. (2008). The apparent viscosity of the frictional melt suspension was estimated using the strain rate dependent rheological model for magma suspensions of Costa et al. (2009) with fitting parameters solved from the experimental data of Caricchi et al. (2007). Maximum packing fraction of the clast population was estimated using the aspect ratio distribution within the model of Mueller et al. (2011). Minimum and maximum values of strain rate (as described by the slip rate and minimum and maximum solidified melt thickness across the sample contact area) and crystal content were considered. We estimated the mechanical importance of frictional melt viscosity by comparing modeled values of apparent viscosity to viscosity experimentally determined via the steady state shear stress to strain rate ratio (see also Violay et al. 2014).

3.3. Results

3.3.1. Seismicity during spine growth

Spine extrusion at Mt. Unzen was accompanied by vigorous seismic activity (Figure 4a). Clear cyclic patterns in seismicity can be seen in the early part of the record (13 October to 15 November 1994) where peaks in event count are separated by approximately 48-hour periods. Cross correlation of all the events in this period found 29 clusters of 5 to 481 events (see Figure

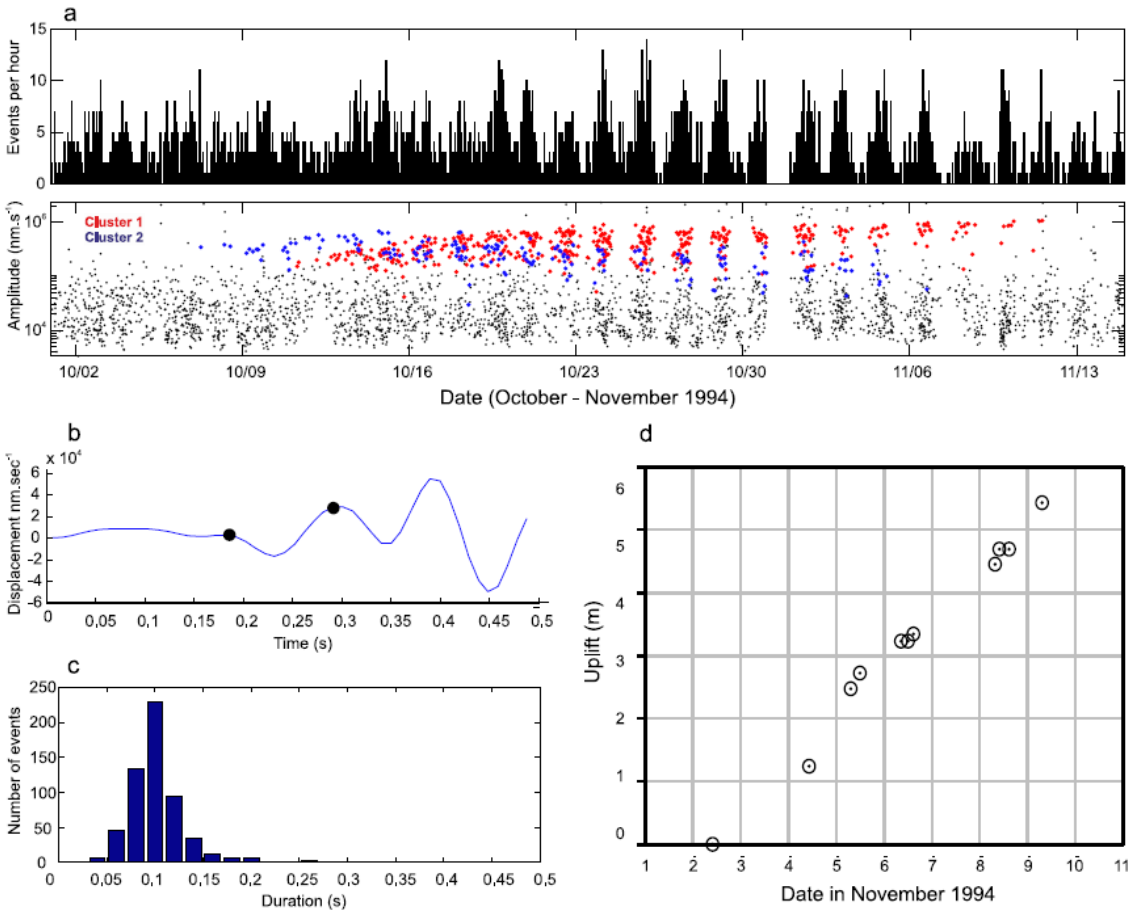

Figure 4: *Geophysical data showing a) hourly counts (above) and amplitude (below) for all seismic events from 1 October to the 15 November 1994. A periodicity in event count peaks emerges on 15 October. We highlight the clustering of two waveform families (multiplets of five or more events with very similar waveforms) marked in red (cluster 1) and blue dots (cluster 2); b) P-wave pulse duration taken from the first arrival of the average waveform for the clustered events, from the point of maximum curvature to the peak where the acceleration gradient falls again to zero; c) Histogram of P-wave pulse durations for all events in families 1 and 2 (binned with 0.02 s intervals); d) Uplift of the spine between 11 am on 2 and 11:00 am on 9 November 1994 from time-differential stereoscopic measurements, adapted from Yamashina et al.* (1999)

3a, 3b). The two largest clusters (cluster 1, containing 481 events and cluster 2, containing 187 events) contain 73% of all clustered events from 1 October to 15 November (Figure 4b) and

coincided with the emergence of the spine and onset of cyclicity in earthquake occurrence rates. Cluster 2 began several days before visible extrusion of the spine in mid-October, and was characterised by repetitive bursts of seismic activity until 5 November. Cluster 1 contains the majority of seismic events throughout this period, showing near-continuous activity until 20 October, before evolving into a repetitive pattern of periodic bursts in concert with cluster 2 (Figure 4b). Events in cluster 1 show steadily increasing amplitudes up to mid-November, distinct from non-clustered events (Figure 4b). These results point to a non-destructive and repetitive source mechanism for the clustered seismic events in the early period of spine growth. The distinct increase in amplitude suggests an increasing fault plane area or a shallowing source during spine extrusion. Seismic activity decreased after mid-November and was associated with a drop in extrusion rate until activity ceased in February 1995. During the period from 11:00 am on 2 November to 11:00 am on 9 November, 61 seismic events from clusters 1 and 2 occurred concurrently with observed uplift of 5.43 m, indicating an average slip distance of 8.9 cm per event (Figure 4e). The *P*-wave pulse durations of earthquakes in cluster 1 and 2, shown in Figure 4d, average at 0.118 s and show a strong bunching around this value; hence, this average value is suitably robust for our calculations (Figure 4c). These measurements indicate that average slip rate of the clustered events was 0.75 $m.s^{-1}$, a rate similar to that constrained for other spine extrusions (Kendrick et al. 2012; Kendrick et al. 2014b).

3.3.2. High-velocity rotary shear experiments

Shear experiments performed to assess the frictional properties of Mt. Unzen dome material have shown that at low slip rates (<0.4 $m.s^{-1}$) and normal applied stress (<0.4 MPa) rock-rock friction takes place and cataclastic gouge forms within the slip zone, and that at higher slip rates and normal applied stresses melting ensues along the slip interface (Table 1). Rock-rock friction is characterised by an initial peak in shear stress, followed by a rapid decrease (see data for ≤0.4 MPa normal stress in Figure 5a and Figure 6. Beyond this brief weakening stage, the shear stress stabilises. During experiments which triggered frictional melting, the shear resistance further evolves, showing a progressive increase in shear stress. Visible growth of a melt layer across the entire slip zone corresponds with a second, higher, peak in shear resistance. The melt layer subsequently thickens and melt begins to be expelled due to centrifugal force

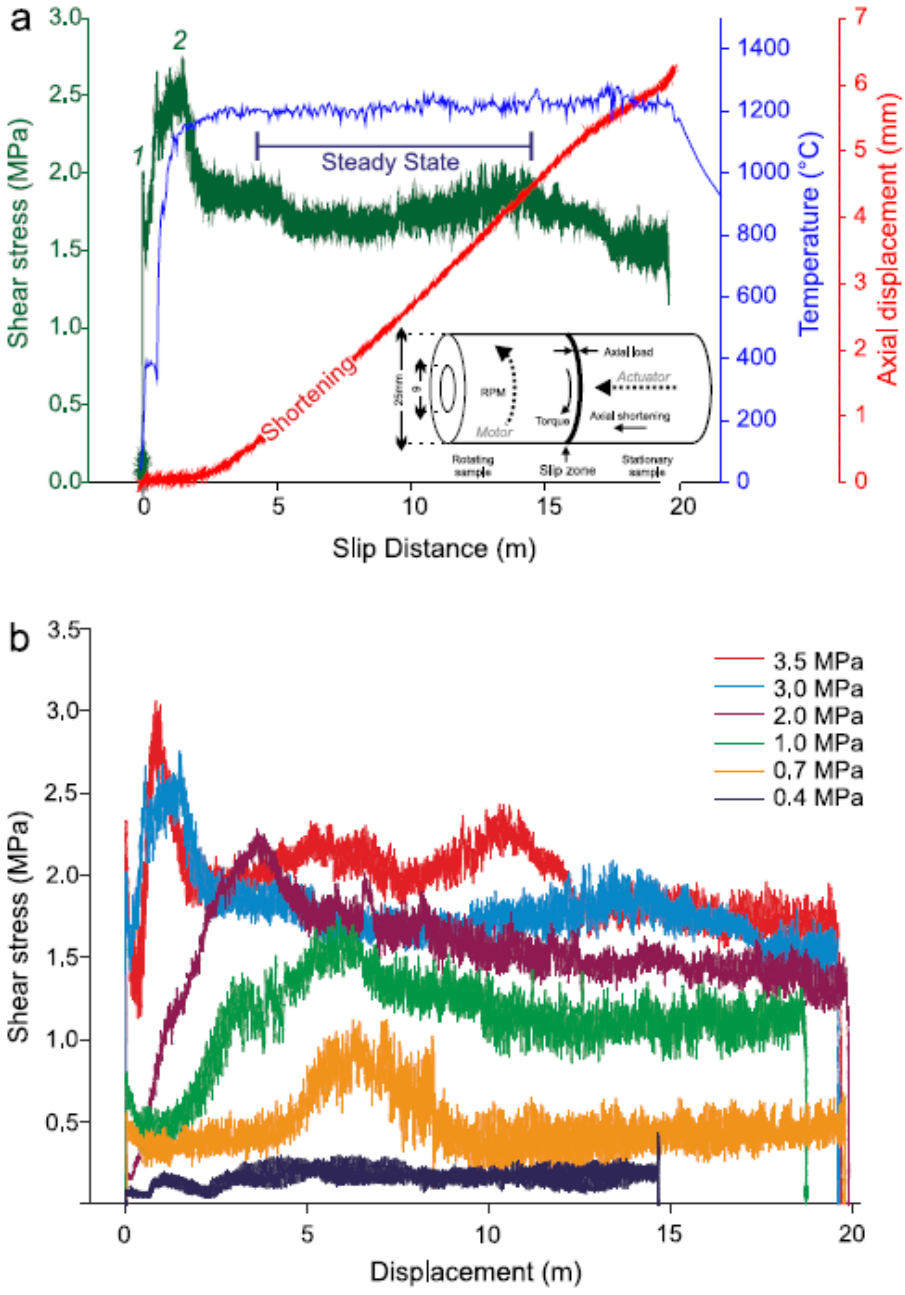

Figure 5: *a) Characteristic mechanical data monitored during a high-velocity rotary-shear experiment undergoing frictional melting, from experiment 3376 (conducted at 1.45 m.s^{-1} and 3.0 MPa). The first and second peaks referred to in the results are labeled 1 and 2. Note stabilization of temperature, shear stress and shortening rate during steady state slip. The inset details the sample setup, showing the directions of applied forces and measurements (modified from Hirose and Shimamoto 2005); b) The mechanical data for all experiments conducted at 1.45 m.s^{-1} slip rate reveal a systematic increase in shear resistance with applied normal stress. For the data at an applied stress of 0.4 MPa, no second peak in shear stress was observed and the applied slip dynamics did not induce frictional melting.*

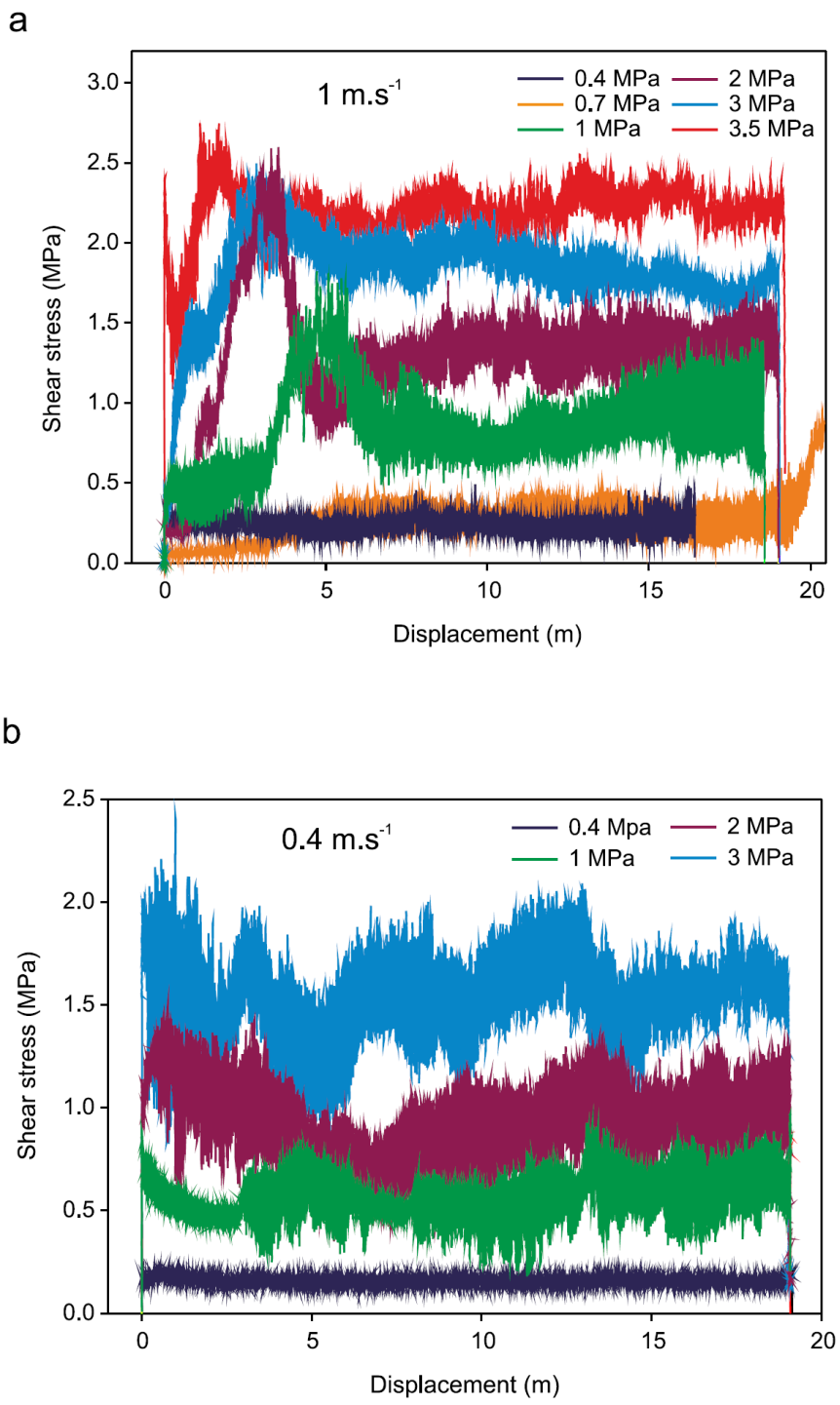

Figure 6. a) The mechanical data for all experiments conducted at 1.0 m.s^{-1} slip rate reveal a systematic increase in shear resistance with applied normal stress. For the data at an applied stress of 0.4 MPa, no second peak in shear stress was observed and the applied slip dynamics did not induce frictional melting, while slip at 0.7 MPa produced frictional melt at 20 m slip distance. b) The mechanical data for all experiments conducted at 0.4 m.s^{-1} slip rate reveal a systematic increase in shear resistance with applied normal stress without any mechanical evidence of frictional melting.

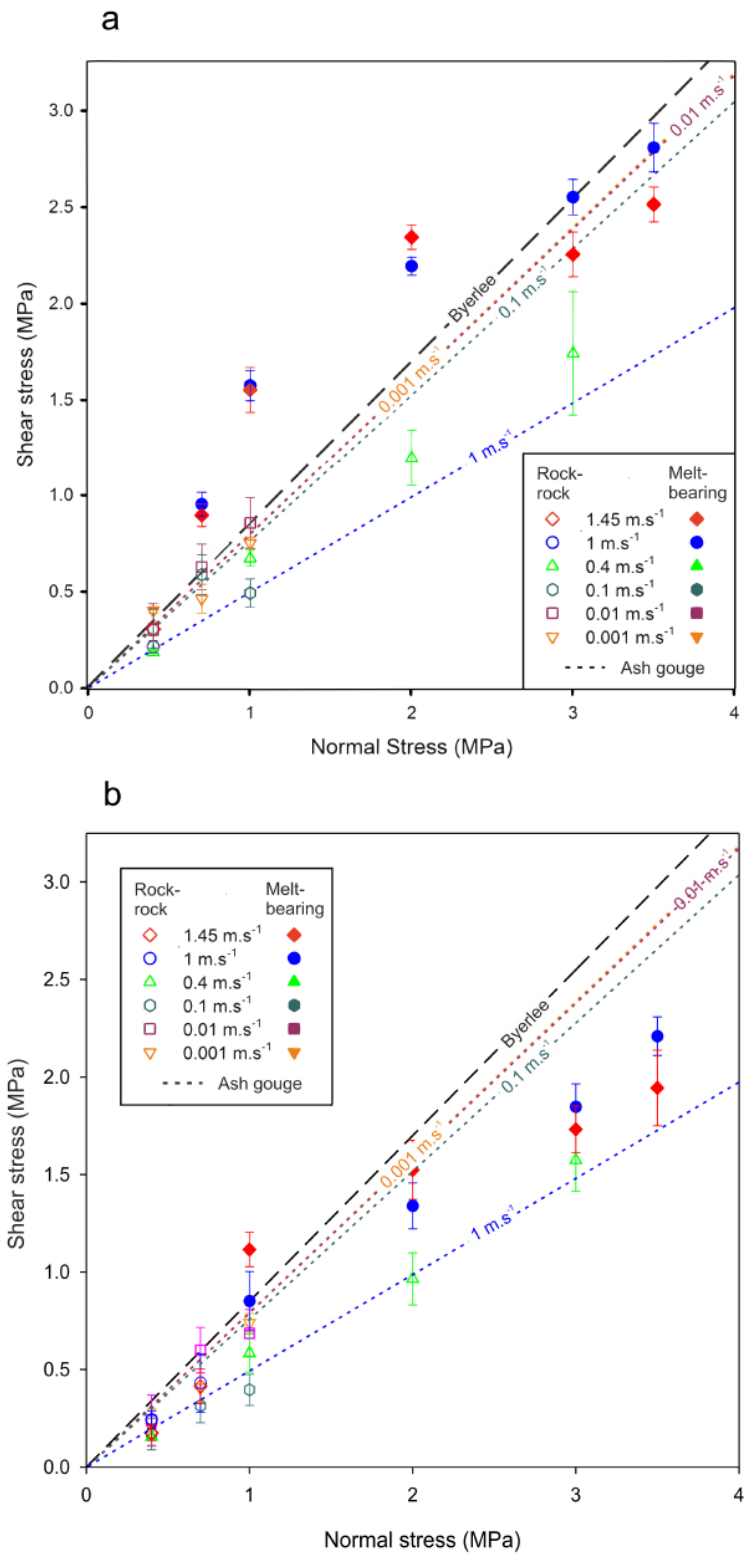

Figure 7. *Shear resistance in rock-on-rock and melt-bearing faults. The dataset highlights a) the peaks and b) the steady state shear stress monitored during slip for all experiments. The data is plotted together with Byerlee's law for rock friction (black dashes) as well as the empirically modeled frictional response of Mt. Unzen ash gouge as a function of slip rate shown as colored dotted lines;* (Lavallée et al. 2014)

Table 1: *Summary of experimental conditions together with mechanical, thermal and axial shortening data measured during the experimental runs. The values of shear stress at steady state refer to equilibrated values after complete melting. The melt zone width is an estimated average value for the entire slip zone.*

Experiment No.	Equivalent slip rate V_e ($m.s^{-1}$)	Normal stress σ_n (MPa)	Max shear stress σ_p (MPa)	Steady state shear σ_{ss} (MPa)	Max recorded temperature (°C)	Total slip distance (m)	Melt zone width *w* (μm)[a]	Strain rate $\dot{\varepsilon}$ (s^{-1})	Melt zne crystal fraction φ	Melt zone crystal aspect ratio[b] R_p	Melt viscosity[c] η_m (log Pa.s)	Mean power density Ω_p ($MW.m^{-2}$)	Viscosity measured by HVR[d] η_{HVR} (log Pa.s)
3375	1.450	0.4	0.212	0.175	259.0	14.7	-	-	-	-	-	0.236	-
3758	1.450	0.7	0.950	0.413	969.4	19.8	100	1.5E+04	0.20	1.6; 2	2.82	0.804	1.82
3373	1.450	1.0	1.573	1.115	1281.6	18.7	100	1.5E+04	0.08	-	2.95	1.249	2.04
3755	1.450	2.0	2.192	1.524	1285.6	19.9	100	1.5E+04	-	-	2.88	1.611	2.18
3376	1.450	3.0	2.549	1.732	1284.2	19.6	150	9.7E+03	0.12	-	2.85	3.039	2.42
3384	1.450	3.5	2.806	1.944	1286.7	19.7	100	1.5E+04	0.09	-	2.96	2.941	2.29
3378	1.000	0.4	0.303	0.243	532.3	16.4	-	-	-	-	-	0.245	-
3757	1.000	0.7	0.893	0.432	1117.8	21.3	-	-	-	-	-	0.354	-
3365	1.000	1.0	1.550	0.851	1156.6	18.6	-	-	-	-	-	0.778	-
3359	1.000	2.0	2.342	1.339	1264.3	19.0	150	6.7E+03	0.16	1.5; 2.2	2.75	1.160	2.55
3370	1.000	3.0	2.253	1.847	1267.0	19.0	100	1.0E+04	0.08	-	2.81	2.086	2.35
3382	1.000	3.5	2.512	2.209	1268.6	19.2	150	6.7E+03	0.22	1.4; 1.8	2.95	1.630	2.58
3379	0.400	0.4	0.183	0.155	193.6	19.1	-	-	-	-	-	0.064	-
3369	0.400	1.0	0.669	0.584	650.8	19.1	-	-	-	-	-	0.221	-
3363	0.400	2.0	1.195	0.965	1128.1	19.1	-	-	-	-	-	0.366	-
3372	0.400	3.0	1.794	1.574	1187.3	19.0	150	2.7E+03	0.18	1.4; 2	-	0.593	2.83
0046	0.001	0.4	0.400	0.205	-	1.4	-	-	-	-	-	-	-
0047	0.010	0.4	0.300	0.238	-	7.1	-	-	-	-	-	-	-
0048	0.100	0.4	0.305	0.169	-	21.5	-	-	-	-	-	-	-
0049	0.001	0.7	0.461	0.407	-	1.4	-	-	-	-	-	-	-
0051	0.010	0.7	0.625	0.599	-	7.1	-	-	-	-	-	-	-
0052	0.100	0.7	0.586	0.315	-	14.2	-	-	-	-	-	-	-
0053	0.001	1.0	0.780	0.739	-	1.4	-	-	-	-	-	-	-
0056	0.010	1.0	0.854	0.686	-	7.1	-	-	-	-	-	-	-
0054	0.100	1.0	0.490	0.396	-	6.2	-	-	-	-	-	-	-

[a] *Average solidified melt zone width estimated from photomicrographs – a lower bound for melt zone width during steady state slip (see methods)*

[b] *Bin size 0.2 determined by mean normalised to area fraction; for bimodal aspect ratio distribution both values are given.and*

[c] *Melt viscosity values are quoted for a single temperature (1300 °C) predicted using the model of Giordano et al. (2008)*

[d] *Viscosity calculated as shear stress/strain rate mechanically measured in the HVR tests for steady state conditions.*

and axial load, causing axial shortening (Figure 5a). In the process, the shear stress decreases to a steady state as equilibrium is reached between melt production and expulsion (*e.g.,* Hirose and Shimamoto 2005). Thermal monitoring during the friction experiments showed that heating of the slip zone increases rapidly, reaching rates of up to 1000 °C.s^{-1} and achieving melt temperatures of 1180-1290 °C during mechanical steady state (Figure 5a). Normal stress and slip distance exhibit important controls on the shear resistance imposed by the rock or melt (Figures 5b, 6*)*.

The cumulative dataset for all experiments is plotted in shear stress to normal stress space for the monitored peak (Figure 7a) and steady state (Figure 7b) shear stresses. Byerlee's frictional law (Equation 1) is accompanied by modeled curves of the dependence of both slip rate (V_e) and normal stress (σ_n) on the shear resistance (τ) using the relationship $\tau = 0.8e^{-0.42Ve} \cdot \sigma_n$ (where 0.42 is a coefficient with units s.m^{-1}) empirically constrained for Mt. Unzen ash gouge (Lavallée et al. 2014). Both peak and steady state shear resistance increase systematically with normal stress as predicted by Byerlee's friction law, although a considerable deviation from a linear relationship in peak shear stress is induced by high slip rates and importantly, the generation of frictional melt along the slip surface. We note that the peak in shear stress can be extremely high (inducing a state where $\sigma_n/\tau>1$) when a melt layer first forms. Peak shear resistance remains particularly high during the steady state slip at low normal stresses (<3 MPa), where melt plausibly acts as a brake (*e.g.,* Kendrick et al. 2014b); for higher normal stress, the shear stress tends to fall to values below those predicted by Byerlee's law, implying that frictional melt acts as a lubricant to slip compared to the internal friction of intact rocks (Di Toro 2006). Lubrication within the steady state reduces the normal stress dependence on friction compared to Byerlee, but not to the extent demonstrated in previous studies on crustal rocks (Di Toro 2006; Nielsen et al. 2008). It should also be noted that an increase in slip rate (for a given applied normal stress) does not necessarily lead to a decrease in shear stress as would be expected from the non-Newtonian, shear-thinning rheology of the multiphase melts produced by friction (Lavallée et al. 2012b).

The combined effect of slip rate (Equation 2) and applied normal stress on the resultant friction coefficient is assessed by analyzing the mean power density (Ω_p) produced in the experiments, as follows

$$\Omega_p = V_e \tau_p \qquad (4)$$

where τ_p is the average shear stress (Di Toro et al. 2011) and V_e is the equivalent velocity. For the purpose of this analysis, where melting occurred the mean power density was calculated from the average shear stress from the onset of slip to peak shear stress due to melting, whereas for experiments without melting the average shear stress of the full data was used. The slip distance

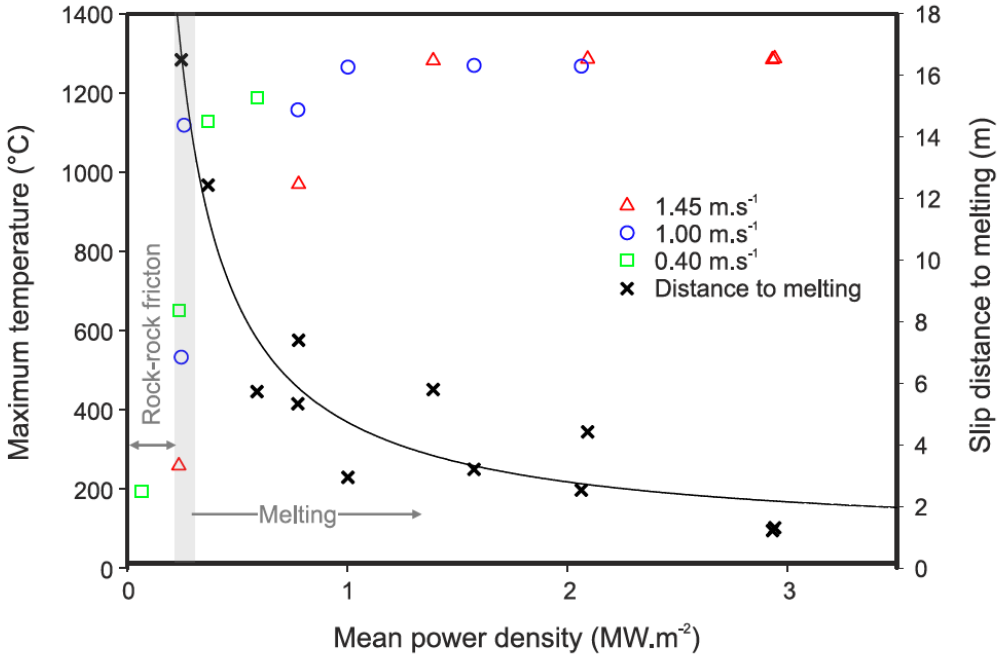

***Figure 8**. Thermal budget and melting propensity during HVR friction experiments. The data shows that at Ω_p >0.3 MW.m^{-2} the maximum temperature monitored reaches a plateau, which coincides with observations of frictional melting on the fault plane. Experiments with Ω_p <0.3 MW.m^{-2} did not achieve temperatures sufficient for melting on the slip plane. The total slip required to achieve frictional melting decreases nonlinearly with increasing mean power density (solid line shows best fit to the data).*

required to generate a complete melt layer along the slip zone decreased as normal stress and/or slip rate increased (Figures 5b, 8). As such, the mean power density becomes a more informative measure of the conditions prompting melting. At the lowest mean power densities (<0.3 MW.m^{-2}) frictional melting did not occur. Experiments with mean power density of 0.3 to 1 MW.m^{-2} reached temperatures sufficiently high to induce melting over slip of a few meters (Figure 8). Experiments with higher power density ≥1 MW.m^{-2} reached higher maximum temperatures of ~1285 °C with near-instantaneous melt production (Figure 8). We note that the maximum temperature during steady state slip on melt-hosting slip zones remained constant, independent of imposed conditions – an observation which facilitates a rheological description of fault slip dynamics.

3.3.3. Microstructural analysis of experimental products

Thin sections from experimental samples that developed a frictional melt layer were prepared for optical and geochemical analyses. The frictional melt layers (solidified into glasses) exhibit a distinct change in texture from the surrounding protolith; the pseudotachylyte glass hosts crystal

fragments (primarily of plagioclase) with a lower aspect ratio and smaller size than in the host rock. Importantly, amphiboles are not present in these layers. The thickness of the solidified melt zones ranges from 75-300 μm, but does not vary systematically with experimental conditions, and can differ by >100 μm across a given sample. The characteristics of the rock-melt boundary as well as of the pseudotachylyte layer itself reveal a dependence on the local mineral assemblage. The boundary is generally defined by relatively straight margins, though a few irregular embayments likely result from existing heterogeneities in the host rock. This is particularly enhanced by the presence of large amphibole phenocrysts (up to 5 mm diameter), which preferentially decompose along the melt-rock interface (Figure 10a). The boundary observed in our experimental products is not as sharp as those observed in holocrystalline rocks (Hirose and Shimamoto 2003; Hirose and Shimamoto 2005) and we note the progressive alignment of microlites near the slip plane, associated with viscous remobilization (Figure 10b) as local temperatures are sufficient to exceed the glass transition of the neighboring groundmass glass without inducing melting (see **Section 3.4.1**). Crystal fragments in the experimental pseudotachylytes are generally angular, suggesting the occurrence of cataclasis and short periods of interaction with the melt (Bizzarri 2014). The crystal fragments are dominated by plagioclase, while ferromagnesian oxide minerals are scarcer than in the host rock and amphibole is not seen: observations that indicate preferential melting of amphibole and ferromagnesian minerals.

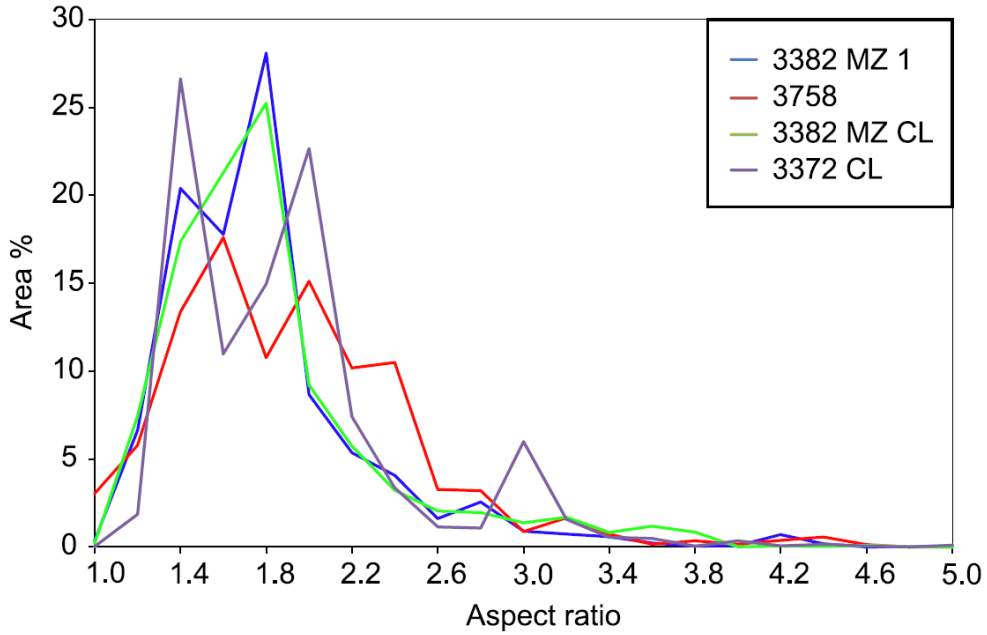

Figure 9. Selected aspect ratio distributions of suspended clasts within melt zones as a whole (MZ) or the center of each melt zone (CL). Polarized photomicrographs were analyzed with ImageJ software and binned at intervals of 0.2 according to aspect ratio. The aspect ratio appears weakly bimodal, with peaks around 1.4 and 1.8, with no apparent difference across the melt zone or between samples.

Particle size distribution was estimated on between 480 and 3314 suspended crystal fragments for each experimentally produced pseudotachylyte layer (Figure 9). The layers contain between 8 – 22 vol. % particles with local variation reaching >5 vol. % (see Table 1). Cumulative particle size (binned by aspect ratio) show that the particle shape distribution is weakly bimodal, with aspect ratio peaks at approximately 1.6 and 2.0 (Figure 9).

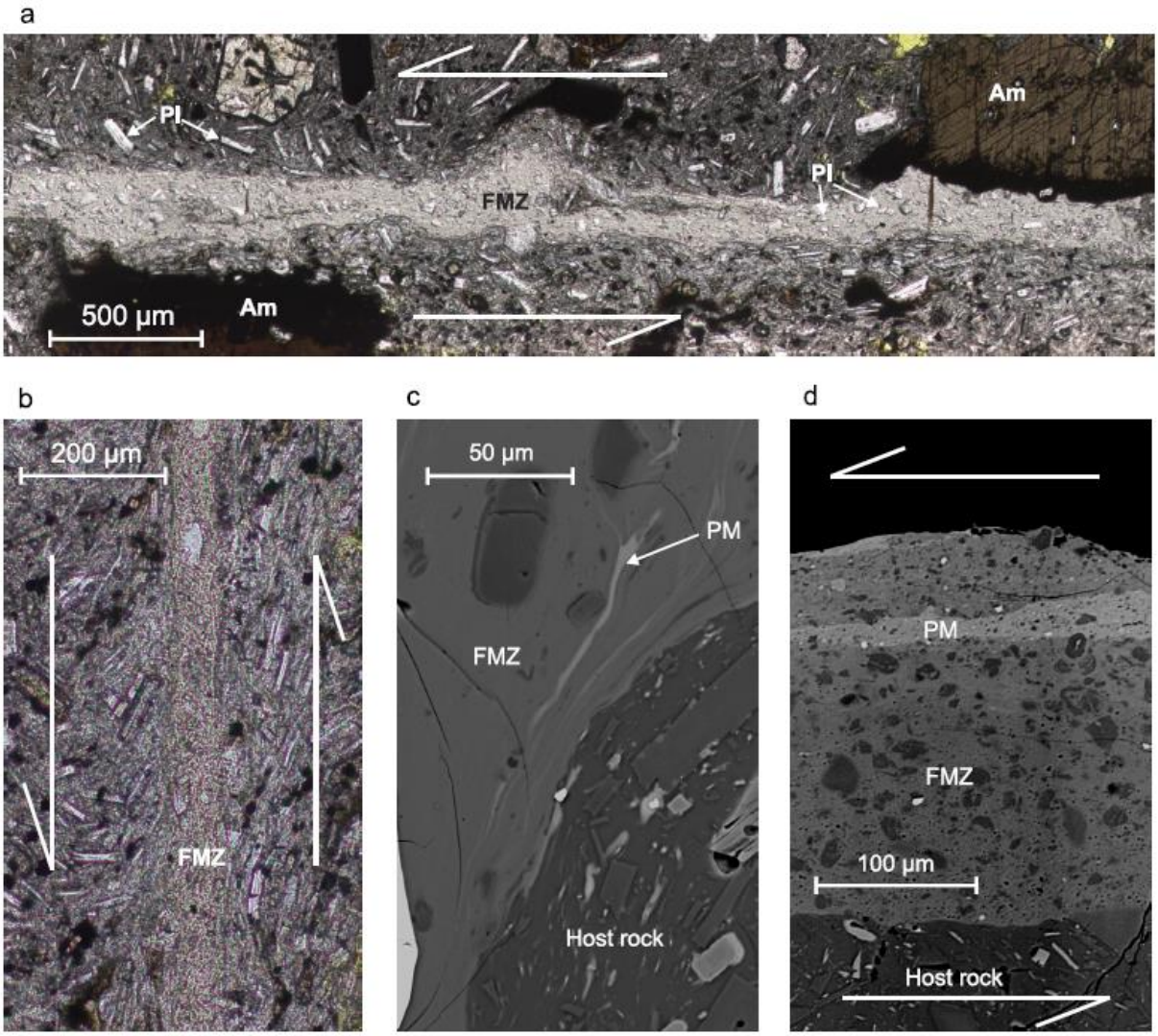

Figure 10. *Microtextural characteristics of frictional melt zones; a) Photomicrograph of a typical frictional melt zone (FMZ) from experiment 3376 (conducted at 1.45 m.s^{-1} and 3 MPa) showing suspended angular plagioclase fragments (Pl) and amphibole phenocrysts (Am). The edge of the melt zone exhibits an embayment (in the middle) and a dark rim along the amphibole suggestive of thermal breakdown; b) Close-up image from experiment 3373 (1.45 m.s^{-1} and 1 MPa normal stress) showing crystal rotation in the host rock along the outer margin of the frictional melt layer due to viscous remobilization in areas where temperatures exceed the glass transition. Arrows indicate the direction of slip; c) SEM image showing an inhomogenised melt filament due to selective amphibole melting (light grey) inside the main frictional melt zone (darker grey) from experiment 3359 conducted at 1.0 m.s^{-1} and 2.0 MPa; d) SEM image of melt zone in sample 3758 (1.45 m.s^{-1}, 0.7 MPa), showing a protomelt (PM) within a crystal-rich frictional melt zone.*

Scanning electron microscope (SEM) analysis reveals chemical and physical homogenization of the frictional melt solidified at the end of the experiments. All but one experimental pseudotachylyte (experiment 3758, at 1.45 $m.s^{-1}$ and 0.7 MPa, which did not reach a steady stateafter melting) show a near-homogeneous suspension with minor chemical heterogeneities, seen in the grey-scale exhibited by the interstitial glass, and the presence of small pores near the rock-melt boundaries (Figure 10c). The pseudotachylyte from sample 3758 shows a range of suspended clast sizes, iron content and thickness (Figure 10d): a thin layer of protomelt (*i.e.,* an inhomogeneous melt band resulting from single crystal melting) containing smaller crystal fragments is surrounded by a thicker, homogeneous, solidified melt zone. The groundmass of the host rock in this experiment does not show evidence for viscous remobilization (Figure 10d), as seen in other samples, suggesting that the host-rock in this particular example did not surpass the glass transition temperature and strain was localised in the protomelt along the inner slip interface only.

3.3.4. Geochemistry of frictional melt

Electron microprobe analysis reveals that these experimentally produced frictional melts have similar compositions, with the exception of the aforementioned heterogeneous pseudotachylyte produced in sample 3758 (Table 1). This single heterogeneous product has substantially lower SiO_2 and Al_2O_3, and higher MgO and FeO contents: differences suggesting selective melting of amphiboles and ferromagnesian minerals (Table 2). The volatile content of the pseudotachylyte glass is low (0.1 wt. %) as ascertained by simultaneous thermo-analysis, which shows no detectable weight loss (Figure 11) up to 1150 °C (0.1% relative mass increase is likely due to iron oxidation) concordant with water analysis of the bulk rock of ~0.1-0.2 wt. % (Kusakabe et al. 1999; Nakada and Motomura 1999; Noguchi et al. 2008).

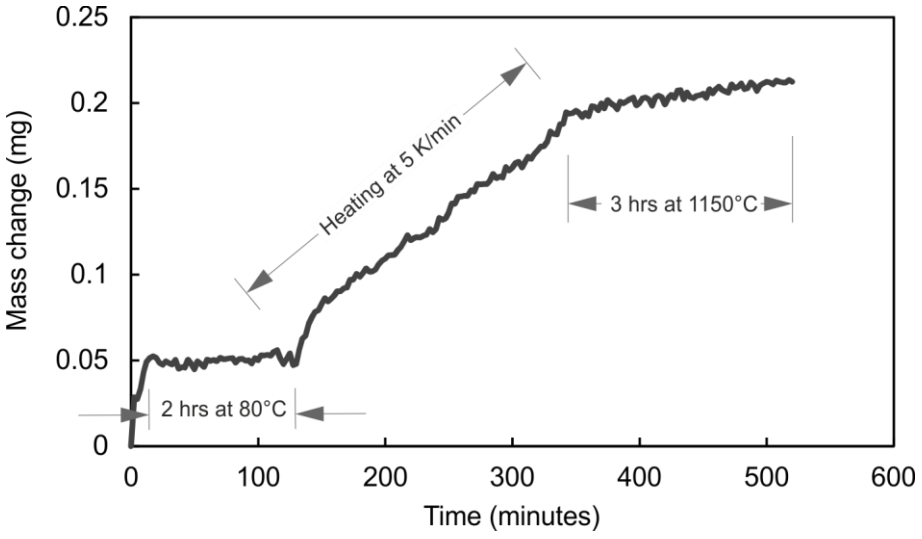

Figure 11. TGA data showing weight change at high temperature. No weight loss associated with water loss is measured. Minor weight gain is likely due to oxidation (e.g. of iron).

3.3.5. Rheological analysis of frictional melt

An accurate description of the rheological impact of frictional melt on fault slip behaviour requires a detailed description of the viscosity of the melt. The temperature-dependent viscosity range of the frictional melts, calculated based on their chemical composition and using a melt-viscosity model (Giordano et al. 2008), shows little variation (Figure 12). Viscosities derived from this model fall between 10^3-$10^{3.5}$,Pa.s, however these are likely slightly overestimated, because of underestimated temperatures due to cooling of melt at the sample exterior. Notably, the calculated viscosity of the inhomogenised melt from experiment 3758 (see Figure 10c) is significantly lower than the other "homogenised" frictional melts. The rate-dependent apparent viscosities of the frictional melt suspension were constrained for the sample-specific crystal fraction and strain rate estimates in the solidified melt zones (Table 1), using the semi-empirical model of, and fitting parameters within, Costa et al. (2009). A maximum packing fraction of 0.55 was estimated from the model of Mueller et al. (2011) using an aspect ratio of 1.8 (Figure 9). The low crystal fraction (Table 1) caused only a slight increase in the apparent viscosity of the multiphase frictional melt of $<10^{0.4}$ Pa.s.

The mechanical data can be used to estimate the viscosity of frictional melt during torsion experiments (*e.g.,* Caricchi et al. 2007; Violay et al. 2014). Here, by dividing the monitored shear resistance (at steady state) by the calculated strain rate we obtain a narrow range of apparent viscosity for the frictional melt (η_{HVR}; Figure 12). These values are a lower bound for viscosity, as thickness of the melt may be underestimated due to continued extrusion of melt at the end of the experiment. The obtained viscosity range is compared with the temperature dependence of the modeled viscosity to derive the range of temperatures likely to be found in the slip zone ($T_{HVR} \approx$ 1320-1590 °C). We find the temperatures constrained from the mechanical data are 50-300 °C higher than those monitored using the thermographic camera (T_m) on the surface of the expelled melt (Figure 12); there are discrepancies of ~0.2 to 1 order of magnitude between the values of viscosity estimated from the mechanical data (η_{HVR}) and the values estimated using the monitored temperature (η_m). We note that in this rheological analysis, viscous remobilization of the host rock was not considered; however the presence of glass-bearing wall rocks has been argued to facilitate viscous coupling to the frictional melt, increasing the shear resistance during faulting events, which could serve to hinder slip (Lavallée et al. 2012b; Violay et al. 2014; Kendrick et al. 2014b)

Table 2. Electron microprobe measurements showing major oxide compositions from experimental frictional melts (3359 – 3758). The geochemical data is complemented by measurements on interstitial glass in the host rock[2] and X-ray fluorescence (XRF) analysis of the bulk rock chemistry. Results shown are mean values for (n) number of measurements. All iron - FeO(T) is considered as FeO for the microprobe measurements and as Fe_2O_3 for the XRF measurements.

	Interstitial glass composition of experimental pseudotachylyte										Starting material	
	3359	3370	3373	3376	3382	3384	3755	3758	3758ii main[a]	3758 protomelt[a]	2007B bulk rock	Interstitial glass[b]
SiO2	64.98	64.21	65.86	64.70	65.80	64.77	65.47	64.58	62.41	51.20	63.87	78.34
TiO_2	-	-	-	-	-	-	-	-	-	-	0.66	0.43
Al_2O_3	15.02	16.30	14.86	15.20	14.77	17.11	14.94	16.38	15.41	10.95	16.54	11.88
FeO(T)	5.44	4.64	5.03	5.01	4.92	4.16	5.22	4.90	6.48	12.40	5.07	0.84
MnO	-	-	-	-	-	-	-	-	-	-	0.11	0.03
MgO	3.78	3.30	3.34	3.37	3.27	2.57	3.36	3.14	4.41	10.66	2.72	0.09
CaO	5.48	5.44	4.66	5.31	5.08	5.53	5.07	5.78	6.39	9.67	5.39	0.49
Na_2O	3.30	3.60	3.32	3.35	3.33	3.77	3.39	3.45	3.15	1.96	3.55	3.06
K_2O	2.38	2.35	2.70	2.36	2.42	2.19	2.47	2.20	2.10	1.22	2.24	4.79
P_2O_5	0.22	0.15	0.16	0.15	0.17	0.14	0.18	0.19	0.19	0.24	0.17	0.02
H_2O[c]	0.10	0.10	0.10	0.10	0.10	0.10	0.10	0.10	0.10	0.10	0.03	-
F_2O_{-1}	0.00	0.00	0.00	0.00	0.00	0.00	0.00	0.00	0.00	0.00	-	-
Totals	100.59	99.99	99.94	99.45	99.76	100.24	100.10	100.61	100.54	98.30	100.34	99.97
n	20	22	29	29	28	25	22	18	4	4	1	11

[a] Measurement with focused beam

[b] Electron microprobe analysis by Cordonnier et al. (2009)

[c] Wt. % water estimated based on previously published measurements (Kusakabe et al. 1999; Nakada and Motomura 1999; Noguchi et al. 2008)

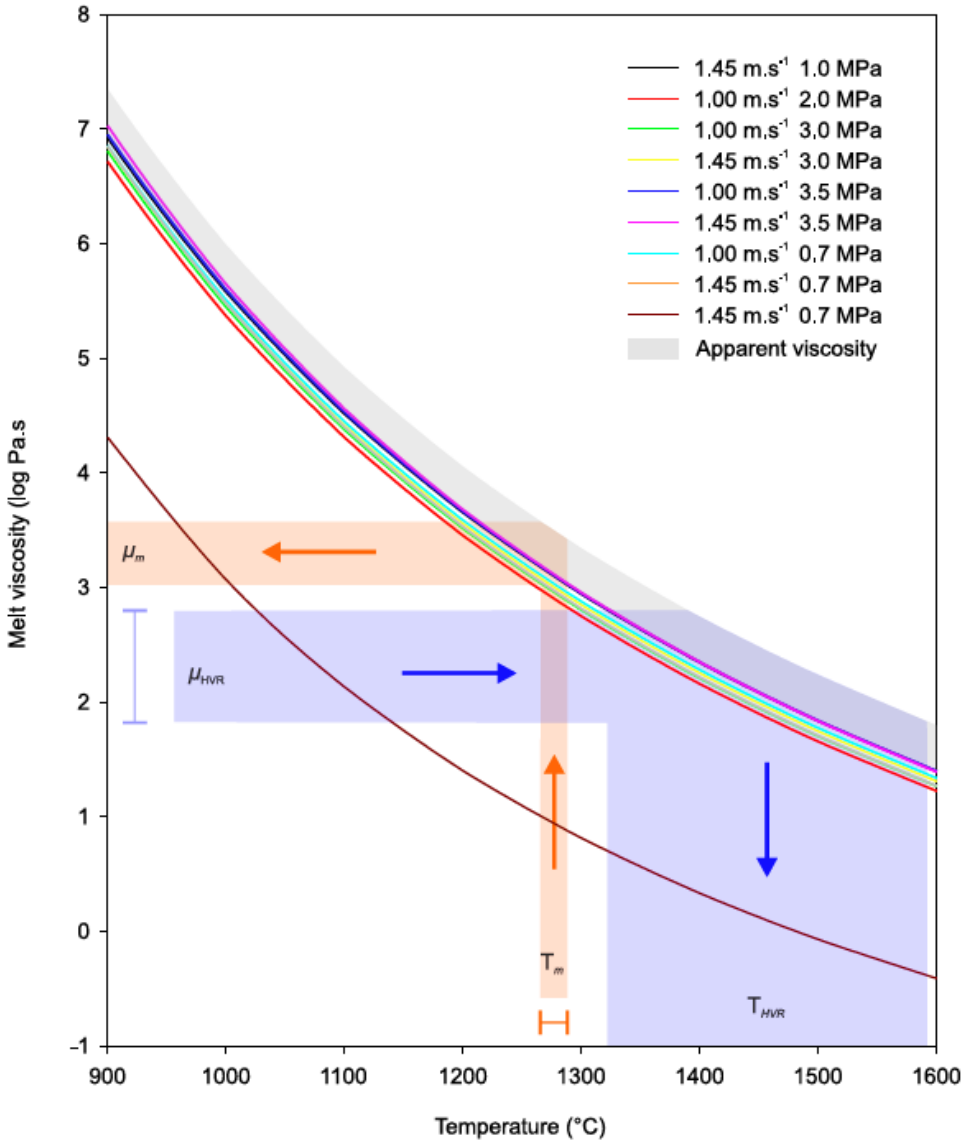

Figure 12: *Temperature dependence of melt viscosity calculated from the model of Giordano et al. (2008) for nine frictional melt compositions (see Table 1). The apparent viscosities of the frictional melt suspension (grey band) were calculated considering the crystal fraction and strain rate following the method of Costa et al.* (2009). *We used a maximum packing fraction of 0.55, estimated from the model of Mueller et al. (2011), and empirical fitting parameters derived by Costa et al.* (2009) *from the experimental data of Caricchi et al. (2007). The modeled apparent viscosity (μ_m) of experimental frictional melts can be constrained from the monitored slip zone temperatures, as indicated by the red arrows. This is compared to the viscosity range mechanically constrained from the steady state regime in the HVR tests (μ_{HVR}), which corresponds to a greater temperature range as defined from the intersection with the apparent, suggesting that experimental temperatures (T_{HVR}) reach 1360-1600 °C; this is higher than the maximum monitored temperatures (T_m), which on their own would suggest higher apparent viscosities (μ_m) during fault slip events.*

3.4. Interpretation and discussion

3.4.1. Fault-friction: melting, viscous braking and remobilization

Here we have constrained spine extrusion at Mt. Unzen to be a fault-driven eruptive process whereby the evolution of the volcanic rocks involved in fault slip is complex. Fault friction of Mt. Unzen dacite falls into the following two regimes: at low mean power densities (*i.e.*, low normal stress and/or slip velocities) slip occurs in the rock-rock regime; above 0.3 $MW.m^{-2}$ the rock-rock slip regime is overprinted by a rheological control on slip when frictional melt forms, accompanied by viscous remobilization of interstitial glass in the adjacent rock. This observation comes with the caveat that power density is an empirical measurement; it determines the thermal energy produced (Equation 4, Figure 8), however the temperature of the slip zone depends on the ratio of thermal energy produced to that lost. This depends on the sample properties and geometry, as well as the design and thermal properties of the apparatus. Our key finding, therefore, is a well-constrained threshold in Ω_p over which the slip regime switches from rock-rock to viscous-dominated dynamics. Observations consistent with frictional melting during dome eruptions, and especially spine growth (Kendrick et al. 2012; Plail et al. 2014; Kendrick et al. 2014a; Kendrick et al. 2014b), are facilitated by the high temperatures in volcanic conduits (Lavallée et al. 2012b). At Mt. Unzen, groundmass crystallization temperatures have been constrained to 850-870 °C (Venezky and Rutherford 1999) and 860-910 °C (Saito and Ishikawa 2012) by Fe-Ti oxide re-equilibration temperatures, giving estimated eruptive temperatures ~800 °C (Goto 1999). This suggests that fault slip producing as little as 300 °C increase may push slip zone temperatures in excess of 1100 °C, and so it appears inevitable that frictional melting and viscous remobilization must be incorporated in dome eruption models.

The friction experiments presented here underline the strong affinity of volcanic rocks for rheological changes due to heat generated through faulting events. Melting occurs due to the very high temperatures achieved along the slip surface, whereas viscous remobilization initiates in the surrounding host at moderate temperatures (above the glass transition temperature, varying between 759 – 1010 °C due to the range of heating rates generated in these experiments), and its extent normal to the slip surface increases as frictional heat dissipates laterally. Such a complex process and associated rheological profile likely play an integral role in

strain localization during slip events. The ability of glass to remobilise at moderate temperatures may have important implications during faulting in nature, as a slip event may be able to release enough heat to the surrounding rocks/magma to remobilise larger zones than the localised slip plane. Remobilised areas (Figure 10b) will exhibit high viscosities and non-Newtonian rheology (due to the abundance of microlites and long structural relaxation timescales at moderate temperatures above the glass transition interval), which may induce non-linearity in shear strain and thus affect the dynamics of magma ascent. Distributed strain partitioning has been observed near the margin of spines (Figure 2) and is commonly attributed to strain experienced by magma in ascent up to the point of failure (Smith et al. 2001; Pallister et al. 2013); yet the results here are consistent with a scenario in which strain localization also takes place in the slip-dominated region above the locus of shear-induced failure.

Our experiments on dacite affirm previous claims that frictional melting is a highly disequilibrium process (Spray 1993; Shimamoto and Lin 1994). Early melting initiates in minerals with the lowest melting temperatures at very high heating rates (here 10^2 to 10^3 °C.s^{-1}).The generation of protomelts from selective melting of crystals with the lowest melting temperatures suggests that, in the HVR experiments, transient changes in melt composition (*e.g.,* Spray 1993) as well as the evolving contact along the rock-rock to melt-rock surface (*e.g.,* Hirose and Shimamoto 2005) may contribute to changes in shear stress on the slip zone (Figure 5a). Observations of irregular rock-melt boundaries and small crystal fragments in the solidified melt zones suggest that the preferential melting of amphiboles and subsequent spreading of the melt layer may enhance the suspension of plagioclase fragments in the melt (Figure 10d).

The rheology of frictional melt in the steady state regime appears to be well-constrained, as the temperature-dependent melt viscosity is found to be very consistent irrespective of slip conditions (if melting has reached equilibrium with the imposed slip dynamics). The apparent viscosity on the slip zone is also described via the slip rate and clast content; yet, the relatively low suspended clast content (8-22 vol. %) induces only a minor apparent viscosity offset of <0.5 log units (using the model of Costa et al. (2009). The viscosities calculated from the mechanical data in this study are 1-2 orders of magnitude lower than the modeled viscosities (see Table 1), an opposite trend to that found in (Violay et al. 2014), where apparent viscosity measurements were one order of magnitude higher for glassy basalts, however the absence of water-bearing minerals within this basalt may cause a very different mechanical response. The offset in viscosity measurements in our study may be attributed to one or more of a) an underestimation on the order of 50-100 °C in measured temperature; b) overestimation of strain rate due to partitioning of strain in viscously

remobilised groundmass [*e.g.,* Violay et al., 2014] and due to melt zone thinning from post-experiment melt extrusion upon solidification; and c) deformation occurring in the brittle regime within the frictional melt.

The analysis presented here portrays a regime in which frictional melting leads to a non-linear rheological (and hence slip) response, with important implications for spine eruption dynamics. The mechanical control of fault processes in spine growth is likely to be complex as locally fluctuating stress conditions and temperature evolve. In a rock-rock fault regime (low-temperature), we observe a linear normal to shear stress relationship for experiments at low slip rates in accordance with Byerlee's frictional law (Equation 1). Slip is found to be rate weakening, falling further below Byerlee's law with increasing strain rates. In a high-temperature, melt-hosting fault regime, slip rapidly evolves from gouge production to preferential melting of low melting temperature crystals to production of a mature (chemically mixed), steady state melt zone; such changes lead to transient rheology. The mechanical response of frictional melt is highly dependent on the normal stress; while in tectonic settings frictional melt may offer a lubricating effect (*i.e.*, impart lower resistance than the internal friction of rocks as stated by Byerlee), in shallow volcanic scenarios low normal stress conditions mean the peak shear stress induced by production of frictional melt can exceed the internal friction of rocks predicted by Byerlee's law, and impose a viscous brake (Koizumi et al. 2004; Fialko and Khazan 2005; Kendrick et al. 2014b).

The contrasting properties of rock-rock and melt-bearing slip zones suggest fault dynamics in an ascending magmatic column are highly unstable and lead us to conclude that spine extrusion may be hindered when frictional melt forms at the conduit margin. These ascent dynamics may encourage unsteady faulting events (and associated periodic geophysical signals), as a higher shear stress must be generated to overcome the melt-enhanced shear resistance. Thus the variable frictional properties of volcanic rocks (with or without melting) may have an important role in regulating stick-slip behaviour and promote unstable spine extrusion (Kendrick et al. 2014a) providing a feedback to the cyclic deformation patterns seen at Mt. Unzen and other dome-building volcanoes.

3.4.2. Frictional controls on seismogenic spine extrusion

The October 1994 to Feb 1995 extrusion of a spine at Mt. Unzen volcano was monitored by seismic, tilt and stereoscopic techniques (Yamashina et al. 1999; Umakoshi et al. 2008). A

mechanistic interpretation of these signals requires consideration of the slip mechanics at work in the shallow conduit. Spine extrusion rates from 2–9 November 1994 averaged 0.8 m.day^{-1} and cycles in the seismic and tilt data, similar to those measured at Soufrière Hills volcano (Voight 1999), suggest pulsatory dynamics where the ascent and extrusion of the spine occurred through incremental slip along an intact plug with minimal strain in its core.

We analyzed the seismic data to provide a constraint on the slip conditions at Mt. Unzen and apply our experimental findings to the monitored eruption dynamics during spine growth. The regular ~48 h cyclicity in seismic event counts (Figures 4a, b) indicates a process whereby pressure build-up in the conduit, that leads to inflation, is released by seismogenic fault slip events along the margin of the ascending plug (Yamashina et al. 1999). Our analysis of the seismic record revealed the importance of two dominant clusters of earthquakes found to take place in periodic cycles. The timing of these cycles shows a strong correlation with peaks in tilt and total event count, from which we conclude that seismogenic slip events represent the dominant mechanism of uplift during spine growth. The non-destructive source character of the seismicity and similarity of the waveforms suggest a common process occurring within a similar location, from which we surmise that their source mechanism is most likely the brittle failure and slip of magma near the conduit walls at shallow depths (Yamasato 1998; Varley et al. 2010; De Angelis and Henton 2011; Thomas and Neuberg 2012; Bean et al. 2013).

We used our seismic analysis to estimate slip zone properties during spine growth. We find an average slip distance of individual events of 8.9 cm, slip velocity of 0.75 m.s^{-1} and a faulting depth shallower than 700 m below the dome surface (Japanese Meteorological Association 1994; Umakoshi et al. 2008). From this depth range we constrain the stress normal to the fault plane using values of the horizontal stress, σ_h) as estimated from the lithostatic stress (σ_l) via Sheorey (1994) with E in GPa and z in meters:

$$\frac{\sigma_h}{\sigma_l} = 0.25 + 7E\left(0.001 + z^{-1}\right), \qquad (5),$$

where the wallrock elastic modulus (E), is estimated at 10 GPa [Uhira et al., 1995], and z is the depth of interest (0-700 m) providing us with $\sigma_h = 0.42\sigma_l$. Note that the elastic modulus of the magmatic column may differ slightly prior to slip events, but we assume that its elastic response upon faulting at high slip rate, would contribute to a value similar to that of a rock (c.f., Lavallée

et al. 2015). In our calculation, we use a mean density (ρ) of 2505 kg.m^{-3} (measured by He-pycnometry) to constrain stress normal to the fault plane.

In order to solve the problem of heat transfer during slip events (prior to melting), we use the 1-D calculation for temperature change at negligible distance from a heat source (*i.e.,* a slip zone of 0-thickness) derived by Carlslaw and Jaeger (1959):

$$\Delta T = \frac{q\sqrt{t}}{C_p \rho \sqrt{\pi k}} \qquad (6),$$

where heat capacity (C_p) is estimated at 1000 J.kg^{-1}.K^{-1} at 900 °C, thermal diffusivity (k) is estimated at 0.7 mm^2.s^{-1} (Nishimura et al. 2005; Cordonnier et al. 2012b), time (t) is constrained by dividing the average slip distance by the slip velocity constrained from the seismicity, and the heat flux (q) is defined as $q = \mu\sigma_n V_e$, in which the coefficient of friction (μ) is set to 0.85 to constrain heat generated from the onset of a slip event at low normal stresses (c.f., Byerlee 1978). The results of these calculations are illustrated in Figure 13, showing the temperature increase plotted against conduit depths for an average slip event. We set a threshold temperature for the onset of frictional melting at 1100 °C and an initial conduit temperature of 800 °C. This suggests that frictional melting may be viable during fault slip events deeper than 500 m. At shallower depth, we expect that insufficient heat would be produced to melt the rocks by friction: however, enough heat may be generated to viscously remobilise the interstitial glass in these rocks (Figure 13). Considering this thermal budget of fault slip events we conclude that it is highly likely that spine extrusion mechanics were modified by viscous forces associated with viscous remobilization and melting during ascent.

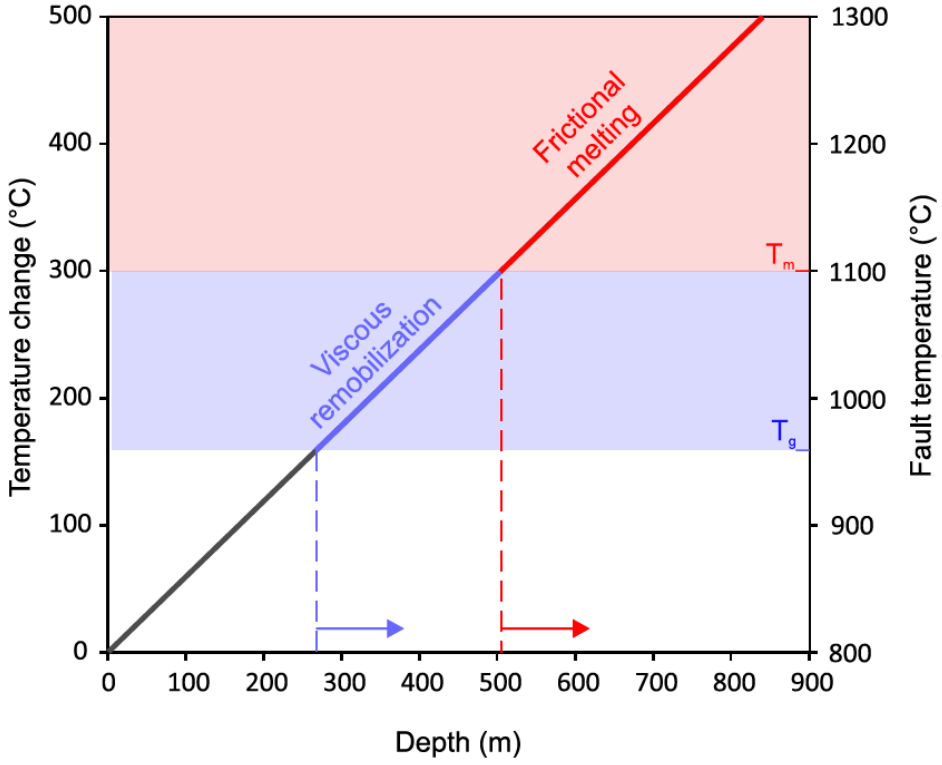

Figure 13: *Heat generated by fault friction of an average slip event at Mt. Unzen at varying depth. The left axis shows change in temperature calculated from the equation of Carlslaw and Jaeger (1959), from an initial conduit temperature of 800 °C. The right axis shows the fault zone temperature. Normal stress on the fault plane is calculated from the lithostatic stress using the equations of Sheorey (1994), providing a fault temperature to depth relationship (bold line). Viscous remobilization above T_g is constrained to temperatures >960 °C (blue field) and we highlight a threshold temperature of 1100 °C, above which frictional melt forms (pink field). Blue and red dashed lines constrain the minimum depths at which an average fault event during spine extrusion at Mt. Unzen results in viscous remobilization and frictional melt formation respectively, with arrows indicating these processes are active at greater depths.*

3.4.3. Fault friction beyond melting

Magma ascent is driven by buoyancy, and during spine-building episodes is regulated by internal frictional processes. Although the present findings highlight the effect of frictional melting and suggest that it may be a common and important process to be considered, we wish to emphasise that we do not believe that it is the mechanism that controls magma ascent in the entirety of the

shallow region for which fault friction influences the eruptive behaviour. Field studies have documented the presence of shear zones bordered by fault planes which bear cataclasite, volcanic ash gouge and breccia near conduit margins (*e.g.,* Smith et al. 2001; Watts et al. 2002; Kennedy and Russell 2012; Kendrick et al. 2012; Pallister et al. 2013). These result from frictional processes and rapid thermal expansion and stress drops during eruptive activity that lead to fragmentation (*e.g.,* Alidibirov and Dingwell 1996; Büttner et al. 2006; Lavallée et al. 2012a; Lavallée et al. 2014a). Gouge and polymict breccia found during drilling of the conduit within the intercontinental drilling program are evidence for repeated fragmentation events in the conduit at Mt. Unzen (Goto et al. 2008) As such, the rheological contribution of frictional melt on slip dynamics must be further combined with the frictional properties of gouge material (*e.g.,* Moore et al. 2008; Lavallée et al. 2014a). The study by Lavallée et al. (2014) measured the frictional properties of Mt. Unzen ash gouge, which was found to abide by a simple relationship between normal stress and slip rate (Figure 7a). Energy partitioning into surface creation and granular flow reduce the heat budget in ash-gouge bearing fault planes, which may inhibit further melting along the slip interface (Lavallée et al. 2014).

The mechanics of slip during spine extrusion at Mt. Unzen are likely variably controlled by frictional melt or gouge within the slip interface at the conduit margin. Our study provides a strong geophysical and thermomechanical argument for the formation of volcanic pseudotachylyte at shallow depths. In addition, we describe the rheology of frictional melt laden fault zones and their potential impact on shallow conduit fault mechanics. Mechanical consideration of fault slip processes have wider implications as frictional melt generation can occur at lava domes during extrusion (Kendrick et al. 2012; Plail et al. 2014; Kendrick et al. 2014a), block-and-ash flows (Grunewald et al. 2000; Schwarzkopf et al. 2001), during large sector collapse (Legros et al. 2000) and along caldera-subsidence faults (Spray 1997; Kokelaar 2007). Future efforts to further constrain fault slip characteristics will afford a better description of volcanic processes, ranging from conduit dynamics to edifice stability and friction-based flow processes, thus contributing to a more accurate assessment of hazards during volcanic crises.

3.5. Conclusion

Fault friction processes regulating the 1994-95 spine growth, during the 1991-1995 dome eruption at Mt. Unzen, have been investigated using combined seismic analysis and

experimental simulations. The seismic record shows the occurrence of clusters of recurring waveforms, revealing a repetitive, cyclic seismic source. These low frequency earthquakes are interpreted to represent repeated faulting events associated with ascent of a plug and extrusion of a lava spine.

Low- to high-velocity rotary shear (HVR) experiments were conducted on Mt. Unzen dacite to constrain the mechanics of fault friction and the character of the slip zone. The experiments show that at mean power densities <0.3 $MW.m^{-2}$ friction takes place along a rock-on-rock slip interface, inducing cataclasis along the fault. Beyond this mean power density threshold, frictional melt forms along the slip interface and temperature dissipation causes viscous remobilization surrounding the fault zone. Close examination of the experimentally generated frictional melt (cooled to pseudotachylyte) indicates a disequilibrium melting process that delivers an unstable shear stress evolution. Subsequent slip ultimately homogenises the chemistry of the frictional melt, which then exerts a viscous control on the slip zone, which is both normal stress and slip rate dependent. Application of our findings to Mt. Unzen spine growth suggests that during average faulting events at depths below 500 m in the conduit frictional melt may form and act as a viscous brake. At depths below 270 m viscous remobilization is likely in the glass bearing host rock, whereas at shallower depths the cataclastic production of gouge material may lubricate the slip zone. These conflicting effects may limit the propensity of magma to achieve steady state slip conditions during ascent, thereby regulating the seismogenic process of dome growth.

Chapter Four

Tensile fracturing of shallow magma at Santiaguito volcano, Guatemala

Preface

Experimental observations such as those described in Chapter 3, showing the propensity for frictional melting during faulting in volcanic environments, has led to novel studies on the contribution of frictional melt to stick-slip magma extrusion (Kendrick et al. 2014b) and fragmentation (Appendix A). In the latter scenario, the propagation of tensile fractures leads to magma failure and slip (via increasing localisation of damage), which in turn leads to frictional melting, thermal vesiculation and fragmentation, triggering a Vulcanian explosion.

In this study I take a step further back, to investigate the tensile fracturing as the trigger for magma failure and subsequent faulting that leads to Vulcanian explosions at Santiaguito Volcano, Guatemala. The timescales of deformation leading to explosions are constrained from cyclic tilt recorded at the active Caliente vent. Long lived and self-similar tilt cycles define a 5-6 minute period of increasing tilt (apparent inflation) prior to explosions. I have conducted uniaxial deformation experiments using a Brazilian tensile strength test configuration to examine the development of tensile fractures and the criterion for tensile failure under high (magmatic) temperatures.

All work in this Chapter is my own, except for the analysis of very long period/ultra long period seismicity presented in Figure 2 panels A and B, which was conducted by S. De Angelis.

Tensile fracturing of shallow magma at Santiaguito volcano, Guatemala

Abstract

Gas- and ash explosions at Santiaguito volcano, Guatemala, occur through arcuate fractures in the active Caliente dome at regular 20-200 minute intervals. Infrasound, ground deformation and seismic monitoring have helped constrain a stable, repeatable source and intensity for these explosions, believed to result from thermo-mechanical processes (melting and vesiculation) during rapid faulting following ~5 minute constant edifice inflation (Lavallée et al. 2015a). Observation of fault processes at Santiaguito suggest a strong shear component, but we surmise that fault propagation proceeds from the development of tensile fractures due to the volumetric strain exerted by a pressurising gas source at these shallow depths. Here, we assess whether tensile fractures propagate from the top-down or bottom-up. Brazilian tensile strength tests were conducted on Caliente dome lavas with a porosity range of 3-30%, at radial strain rates of 10^{-3}, 10^{-4}, and 10^{-5} s^{-1}, and temperatures of 25, 750 and 800 °C. Across the expected conduit temperature range (750-800 °C) the dome material becomes highly sensitive to strain rate, showing a range of responses from brittle to viscous, where the magnitude of strain-to-failure shows a non-linear increase at slower strain rates, indicating an increase in viscous deformation. We use this information to constrain the timescales for fracture propagation in different temperature-strain rate scenarios. We conclude that fractures are likely to propagate upward following viscoelastic deformation during the inflation cycle at Santiaguito, shedding light on the processes leading to Vulcanian explosions at active lava domes.

4.1. Introduction

The processes triggering "Vulcanian" gas-and-ash explosions at active lava dome remain widely debated as competing hypotheses exist at both all-encompassing (Chouet et al. 2005) and volcano-specific (Hall et al. 2015) scales. Commonly, the explosive event is suggested to result from the ascent of a fresh batch of bubbly magma in the shallow conduit (Michaut et al. 2009; Cassidy et al. 2015), a period of relative sealing and gas pressure accumulation (Wright et al. 2007; Nishimura et al. 2012), or the development of fractures along the margins of a volcanic conduit by shear failure during ascent of highly viscous magma (Tuffen et al. 2003; Lensky et al. 2008). A general agreement for such activity is in the need for fracturing parts of the dome, both during fragmentation and to permit the ejection of ash-laden plumes from within the dome. A detailed investigation of the tensile strength of dome rocks under magmatic temperatures and monitored deformation rates is therefore germane to an understanding of explosive processes at lava dome volcanoes.

4.1.1. Geophysical signals accompanying Vulcanian activity

In recent years, several very well monitored dome eruptions have provided a rich geophysical record that is rapidly changing our view of their eruption mechanisms. The integration of seismic and tilt signals has proven a helpful tool to track pressure evolution during dome eruptions (Chouet and Matoza 2013; Johnson et al. 2014; Thomas and Neuberg 2014). Seismicity provides evidence for magma fracturing (Neuberg et al. 2006; Bean et al. 2013) and gas fluxing (Chouet 1988) during transitions to explosive activity. Proximal monitoring of tilt signals at various dome volcanoes can identify shallow (<500 m) inflation for several minutes prior to explosions (Nishimura et al. 2012; Lyons et al. 2012; Johnson et al. 2014), suggesting pressurisation of shallow magma due to gas fluxing (Michaut et al. 2013; Johnson et al. 2014) magma ascent and wallrock traction (Green et al. 2006; Albino et al. 2011).

4.1.2. Santiaguito volcano

Santiaguito volcano is located in the Western Highlands of Guatemala, at the Northern end of the Central American volcanic arc stretching from Guatemala to Panama. The volcanic arc

parallels the trench formed from the subduction of the Cocos plate, and consists of hundreds of volcanoes along the active front, as well as dozens of monogenetic back-arc volcanoes (Carr et al. 2003; Walker et al. 2011). Figure 4.1 shows the tectonic setting and location of Santiaguito volcano, together with other major volcanic centres in Guatemala. Santiaguito dome

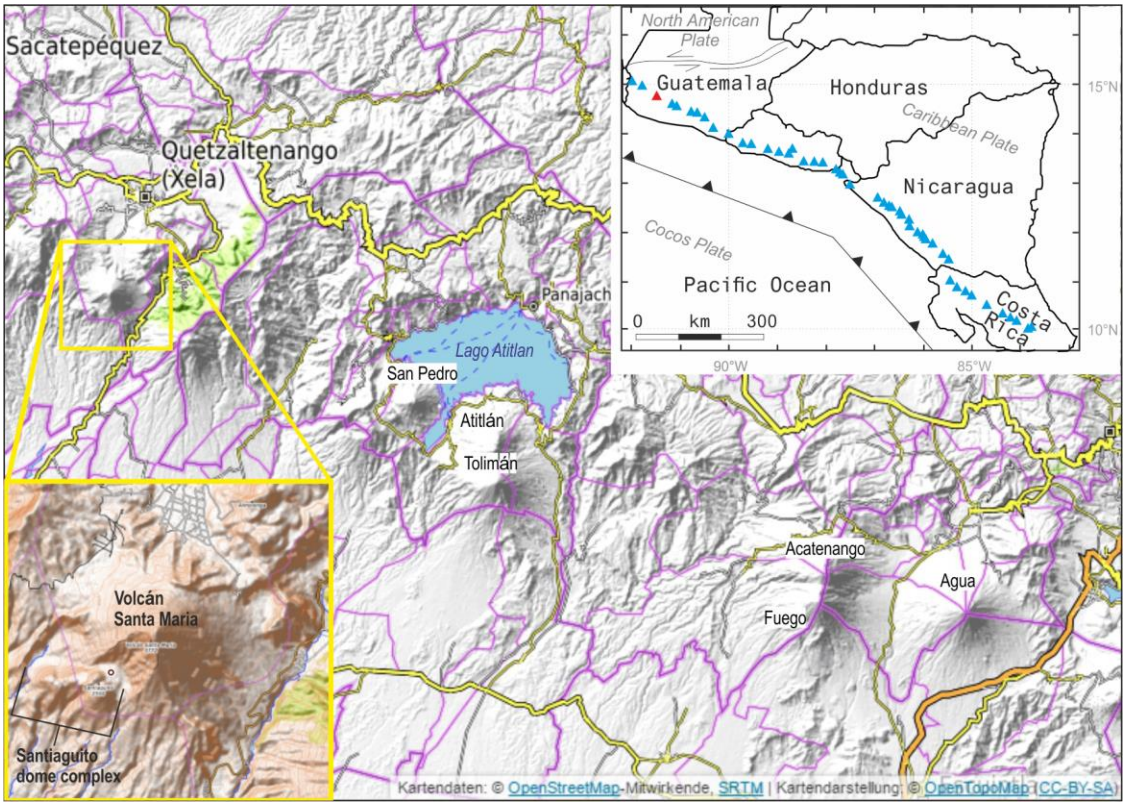

Figure 4.1. Location and tectonic setting of Santiaguito dome complex, together with other volcanoes forming the volcanic arc front in Guatemala, including the currently active Fuego. Right-hand inset shows the tectonic setting, with subduction of the Cocos plate beneath the Caribbean plate forming a parallel chain of volcanoes along the active front of the Central America volcanic arc. Santiaguito/Santa Maria volcano is shown as a red triangle, with other major volcanoes shown as blue triangles. Bottom left inset shows a magnified view of Santa Maria and Santiaguito, with the outskirts of Quetzaltenango (Guatemala's second city) north of Santa Maria and the Santiaguito dome complex indicated. Map data from OpenStreetMap-Mitwirkende, SRTM | © OpenTopoMap (CC-BY-SA); Right inset compiled from several maps (Carr et al. 2003; Escobar-Wolf et al. 2010; Scott et al. 2012).

complex (bottom-left inset in Figure 4.1) has formed since 1922 in the collapse scar formed following a Plinian eruption of Santa Maria volcano in 1902. Activity at Santiaguito has shown cyclicity in effusion rate and explosivity, but has remained active almost 100 years; since the 1970s activity has been predominantly Vulcanian, with small to moderate ash-poor eruptions

occurring every 20-200 minutes together with effusion of lava flows (Harris et al. 2003). This repetitive explosive activity is accompanied by apparent inflation-deflation cycles, as monitored by long-period seismic and tilt signals (Sanderson et al. 2010; Johnson et al. 2014). Inflation at Santiaguito results in either an outgassing event or a gas-and-ash explosion (Johnson et al. 2014). The latter outcome is accompanied by inflation and deflation at a higher rate and magnitude as well as by the occurrence of a very-long period seismic event (Lavallée et al. 2015a). Monitoring of the dome surface during explosions and observations of dome blocks and erupted volcanic ash suggests the occurrence of shear fracturing during the explosive events (Holland et al. 2011; Scharff et al. 2014; Lavallée et al. 2015a) an argument used by Lavallée et al. (2015a) to invoke the occurrence of friction-driven thermal vesiculation leading to explosive eruptions. Cyclic inflation-deflation cycles monitored at Santiaguito have been modelled to result from a Mogi source at approximately 300 m depth and postulated to result from gas pressurisation of a shallow reservoir (Johnson et al. 2014). Outgassing of this pressurised region necessitates the creation of highly permeable pathways – a process achieved by fracturing of the overlying material. Observations between 2012 and 2015 show that the shallow dome structure in the Caliente vent remains mostly intact during explosions, and magma effusion continuously feeds lava flows that descend the south and southeast flanks (Figure 4.2). Consistently low eruption magnitudes and plume volumes at Santiaguito (Sahetapy-Engel et al. 2008; Scharff et al. 2014) indicate open-vent activity and a non-destructive mechanism for depressurisation – indeed, results from Lavallée et al. (2015a) demonstrate that depressurisation more commonly occurred via passive outgassing than explosion. The shallow magmatic system resides in a delicate, yet repeatable, balance between dominant pressurisation, fracturing events and outgassing regimes, where the rate and timescale of inflation ultimately determines the eruptive style.

4.1.2 Tensile fracture mechanics

A common element to dome eruption models is the requirement for brittle failure of shallow magma (Lavallée et al. 2012a). The explosion itself requires magmatic fragmentation (Dingwell 1996); in addition, ascent-driven rupture of magma where strain localises (e.g., Papale 1999) lead to the development of shear and tensile fracture networks at the margins of the conduit (e.g. Tuffen et al. 2003; Massol and Jaupart 2009); finally, lava may break in tension due to low effective pressure (i.e., low confining pressure and high pore pressure (Farquharson et al. 2016a) as well as due to the action of progressive cooling of the dome carapace (e.g. Wadge et al. 2009;

Suzuki-Kamata et al. 2009). In all of these cases (even for the development of shear zones), failure always initiates in tension (Paterson and Wong 2005). But do fractures propagate upward to the surface or downward from the surface into the shallow conduit? This question may be crucial to the development of pressure in the magmatic column. In volcanology, but for the study of material fragmentation by pore overpressure (e.g. Romano et al. 1996; Spieler et al. 2004), the mechanics of silicic volcanic rocks and magma in tension has received little attention, despite longstanding recognition of their paucity and significance (Self et al. 1979). Indirect tensile strength tests, or Brazilian tests, are most commonly employed in rock physics to study material failure in tension (Li and Wong 2013). The tests, generally conducted under low and invariable strain rate and at low temperature, provide evidence for material strength decreasing with porosity and with a tensile strength at least 10 times weaker than in compression (Paterson and Wong 2005; Perras and Diederichs 2014). However, the typical test conditions do not encompass the conditions experienced by magma during deformation in the volcanic conduit, which takes place at high temperature and at widely varying rates; these may result in brittle failure as well as in viscous flow. Herein, we address this important data gap by testing the behaviour of rocks and magma from Santiaguito volcano at conditions simulating natural conduit temperatures and strain rates to constrain whether tensile fractures propagate upward or downward at the apex of the tilt cycles that accompany gas emission or gas-and-ash explosions.

4.2. Experimental setup and data collection

4.2.1. Geophysical signals at Santiaguito volcano

During 2014, the University of Liverpool deployed a network of seismometers and infrasound microphones around Santiaguito volcano. We analyse very-long period (VLP) seismic signals (600-30 s) from a Trillium compact broadband seismometer at station LB05, ~500 m NW and 200 m below the active Caliente vent at Santiaguito (Figure 4.2). Following interpretation in recent studies (Johnson et al. 2009; Johnson et al. 2014), we use the horizontal component of VLP signals to recover ground tilt, assuming elastic radiation of strain from a Mogi-type volumetric source. Infrasound was recorded using an iTem broadband infrasound microphone also installed at station LS05, and converted to air pressure variations.

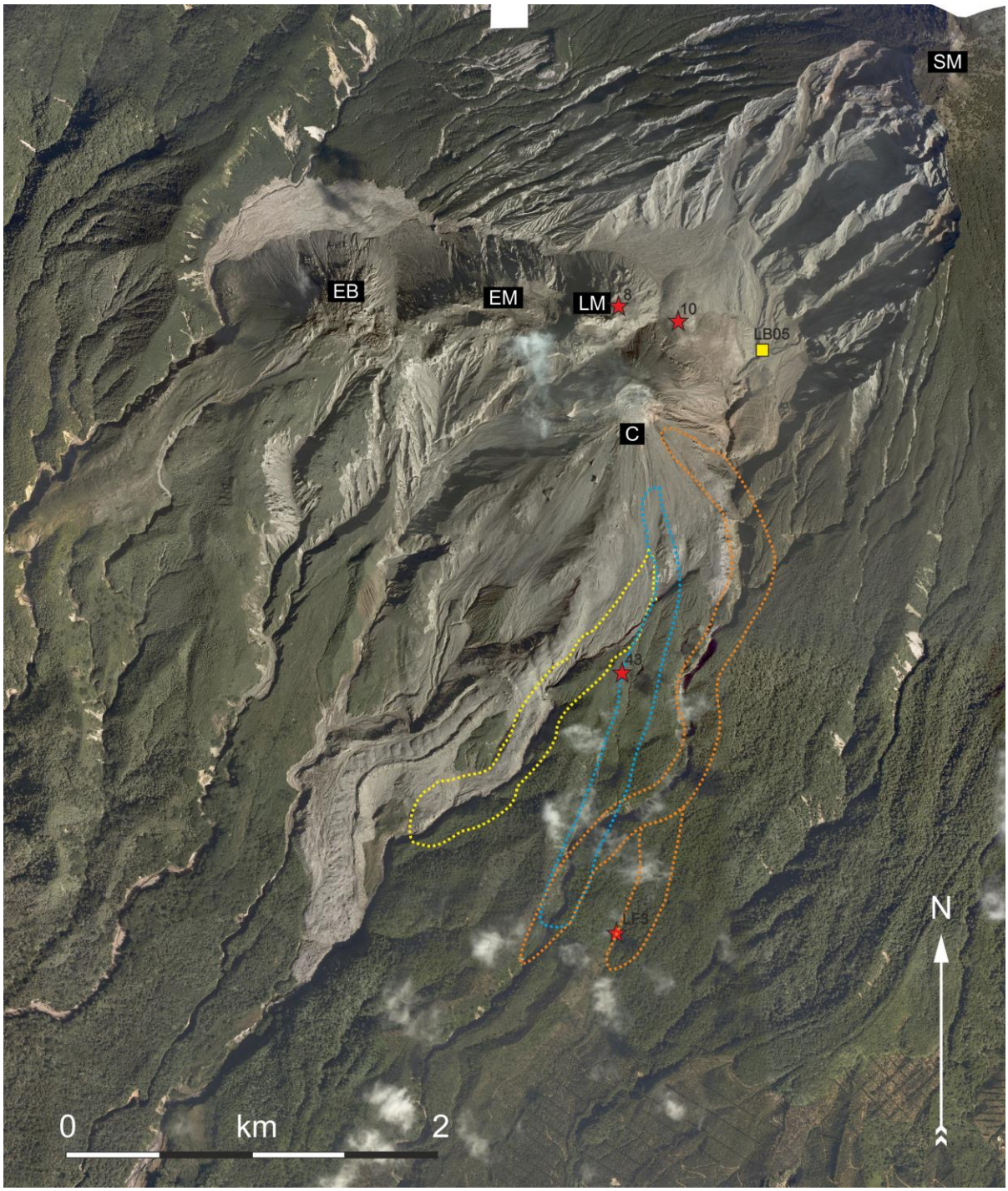

Figure 4.2. High-resolution satellite imagery showing Santiaguito dome complex (EB – El Brujo; EM – El Monje; LM – La Mitad; C – Caliente) and Santa Maria (SM), together with the extent of recent lava flows to the South, marked in dashed lines (2010 flow – yellow; 2012 flow – blue; 2014-15 flow – orange), the rock sample locations (shown as red stars with the sample number (omitting SG prefix) adjacent and the location of the seismic station LB05 shown as a yellow square. Sample SG13 was collected from a pyroclastic flow deposit 2 km south of the lava flow fronts.

Table 4.1 *Sample location, porosity and componentry (measured from photomicrographs using ImageJ) together with the softening temperature measured by dilatometry.*

Sample	Type	Location	Core porosity %	Pheno-crysts (total)	Average phenocryst aspect ratio	Softening temperature (°C)
SG8	Bomb	La Mitad	11.5 - 12.5	29%	1.74	1045
SG10	Bomb	Base of Caliente	23.2 - 26.0	36%	1.55	740
SG43	2012 lava flow	Finca El Faro	8.6 - 10.6	--	–	748
SGLF3	2014 lava flow	Finca San Jose Patzulin	6.1 - 7.7	37%	1.62	784
SGPF13	Glassy block	Finca El Faro	2.2 - 4.7	30%	2.04	786

Table 4.2 *Electron microprobe measurements of groundmass glass from sample SGLF3 (average of four measurements)*

SiO_2	TiO_2	Al_2O_3	FeO(T)	MnO	MgO	CaO	Na_2O	K_2O	P2O5	H_2O*	F_2O_{-1}	Total
77.98	0.61	11.46	1.61	0.02	0.06	0.43	4.17	3.93	0.09	0.10	0.00	100.46

*H_2O content estimated at 0.1% (lava flow samples assumed to be fully degassed).

4.2.2. Material

Five pristine dome rock and lava samples were collected during field campaigns in 2012 and 2014 at the active Caliente dome. Sampling locating are shown in Figure 4.2 and Table 4.1, together with the sample code. Lava flow samples (SG43 and SGLF3) were collected from the base of the flow levees, while bombs (SG8 and SG10) and the block collected from pyroclastic flow (SGPF13) have travelled a considerable distance from the source. The rocks are dacites with similar interstitial glass chemistry (see Table 4.2) and mineralogical assemblage but they vary in porosity, as determined by He-pycnometry. The mineralogical assemblage is dominated by plagioclase feldspar, consisting of ~50 wt.%, with ~6% Mg-pyroxene and 2% amphibole and minor Ti-magnetite, Ilmenite and crystalline silica (Hornby et al., In prep., Scott et al. 2013). Analysis of photomicrographs using ImageJ show phenocrysts forming 29-37% area % of the samples, with average aspect ratios of 1.8±0.25. The remainder is formed of a rhyolitic (78% SiO_2) groundmass glass (Table 2; Scott et al. 2013); this suggests a microlite population of ~15-

20 % in the groundmass glass. Details of the sample type and location, together with the total area fraction of phenocrysts and the porosity of cores from each sample are shown in Table 1.

4.2.3. Softening temperature determination

To constrain the flow temperature regime of these lavas, we measured the softening temperature, using a Netzsch TMA 402F1 Hyperion thermo-mechanical analyser. For these tests, we prepared 6 mm x 5 mm cores of each sample; each core was axially loaded in a piston assembly, under a load of 3N (±0.01mN) and heated at 3 °C/min whilst monitoring length change at a resolution of ±0.125 nm. The softening point was constrained as the temperature for which the sample no longer thermally expanded upon heating, but rather deformed under the imposed load by a strain of 0.25%.

4.2.4. Brazilian tensile tests

For Brazilian tensile testing, the rocks were cored into discs 39.8 ±0.1 mm diameter and cut parallel to 20 ± 1 mm thickness, giving a contact area:diameter ratio of 0.5, as suggested by Lin et al. (2016). Prior to testing, core sample porosities were measured by He-pycnometry (Table 3). Brazilian tensile strength tests were conducted using an Instron 1362 servo-driven uniaxial press with a 100 kN load cell. The press was fitted with a three-stage split- furnace from Severn Thermal Solutions, capable of temperatures ≤1000 °C. The samples were loaded sideways, with the disc edge against the platens of the press. During high-temperature tests, samples were heated to target temperatures of 750 and 800 °C at 3 °C/min and left to thermally equilibrate over a period of ~1 hr; sample temperature was monitored using a K-type thermocouple. Experiments were conducted at compressional displacement rates of 0.04, 0.004, and 0.0004 $mm.s^{-1}$, (equivalent to diametral strain rates of 10^{-3}, 10^{-4} and 10^{-5} s^{-1}), thus imposing a tensile stress on the sample interior. During the test, the applied stress was monitored by a load cell at 100 Hz until sample failure or, until ~2% axial strain when material exhibited viscous-dominated deformation. The tensile strength (σ_t) was calculated as follows:

$$\sigma_t = \frac{2P}{\pi D h}, \qquad (1)$$

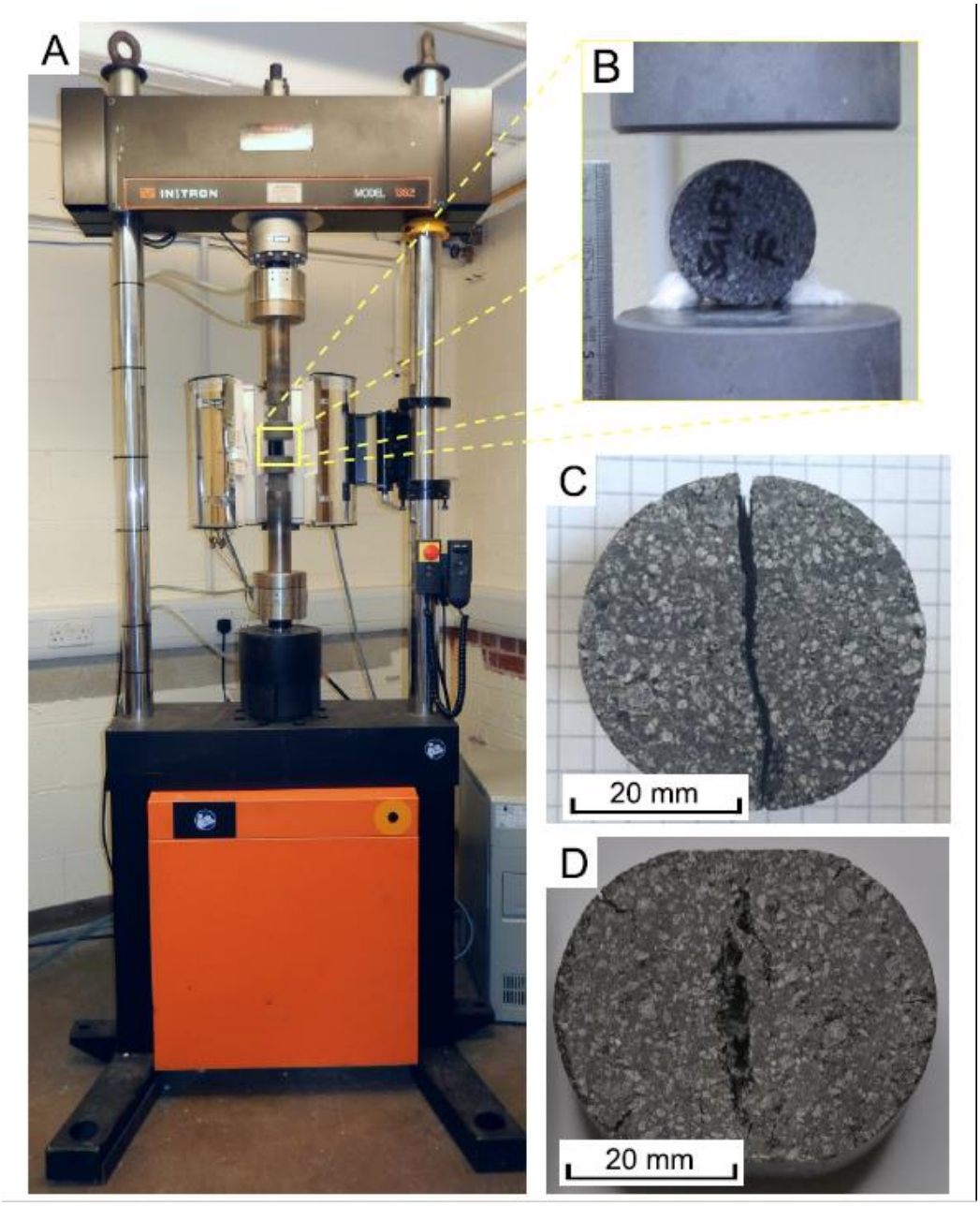

Figure 4.3: *(A) Photograph of Instron uniaxial press with 100 kN load cell and split-tube furnace from Severn Thermal Solutions used to conduct Brazilian tensile strength tests; (B) sample setup (inset) used during the Brazilian experiments; (C) Post-experiment sample deformed fully in the brittle regime at 800 °C and strain rate of* 10^{-3} s^{-1}*. Note the imposed deformation appears to be accommodated solely within the fracture, which extends almost linearly across the sample; (D) Post-experiment sample (SGPG13) deformed at high temperature (800 °C) and a strain rate of* 10^{-5} s^{-1}*, showing a mixture of ductile (viscous) deformation (evidence from the flattening of the upper and lower part of the samples that were in contact with the piston of the press) as well as brittle deformation evidenced by the tear observed in the centre of the sample.*

Rock sample and core (A-S)	T_{exp} °C	Width, w (mm)	Diameter, D (mm)	Porosity (%)	Compressive strain rate (s^{-1})	Peak tensile stress (MPa)*	Strain to failure
SG8D	25	19.88	39.82	11.66	10^-4	4.46	0.00566
SG8B	25	22.30	39.79	12.2	10^-4	4.50	0.00608
SG43D	25	18.99	39.80	9.1	10^-4	4.66	0.00561
SG10 A	25	21.16	39.74	24.69	10^-4	2.63	0.00497
SG10 D	25	22.77	39.83	24.33	10^-4	3.19	0.00496
SG43F	25	22.41	39.81	9.33	10^-4	3.86	0.00522
SGLF3 C	25	20.20	39.76	7.05	10^-4	4.93	0.00546
SGLF3 D	25	20.33	39.79	7.05	10^-4	4.73	0.00474
SGPF13F	25	18.71	39.8	3.12	10^-4	5.68	0.00625
SGPF13B	25	18.43	39.75	2.91	10^-4	5.05	0.00619
SG8A	25	19.48	39.83	11.82	10^-5	3.53	0.00517
SG8C	25	20.78	39.82	11.96	10^-5	3.73	0.00494
SG43B	25	20.27	39.80	9.55	10^-5	4.20	0.00528
SG43A	25	19.78	39.84	9.35	10^-5	3.92	0.00524
SG10 E	25	20.20	39.82	25.24	10^-5	2.96	0.00537
SG10 C	25	18.01	39.82	25.14	10^-5	2.52	0.00423
SGLF3 M	25	20.43	39.8	7.07	10^-5	4.31	0.00493
SGLF3 E	25	20.55	39.79	7.01	10^-5	4.16	0.0047
SGPF13A	25	20.25	39.8	4.72	10^-5	4.51	0.00558
SGPF13D	25	19.15	39.76	3.27	10^-5	4.95	0.00588
SG43E	748.5	19.45	39.79	8.62	10^-5	6.17	0.00371
SG8H	744.9	20.85	39.8	12.54	10^-5	4.82	0.00372
SG10 L	763.6	20.54	39.8	23.29	10^-5	3.02	0.0108
SG10 B	743.9	19.59	39.81	25.96	10^-5	3.37	0.00809
SG8E	757.6	22.84	39.8	11.83	10^-5	4.66	0.00304
SGLF3_L	744.6	20.60	39.82	6.71	10^-5	5.05	0.00441
SGPF13 E	758.5	19.99	39.78	3.88	10^-5	4.87	0.00426
SG10 F	752.9	20.5	39.81	24.25	10^-4	5.22	0.00342
SG8J	755.3	18.74	39.80	12.83	10^-4	5.58	0.00373
SG43K	752.4	20.77	39.80	9.85	10^-4	4.72	0.00300
SG10 G	752.8	20.68	39.80	23.24	10^-4	4.92	0.00369
SG43 L	755.6	20.47	39.80	10.31	10^-4	6.22	0.00442
SGPF13 I	763.3	20.94	39.74	2.22	10^-4	5.08	0.0041
SGPF13 L	745.2	20.31	39.78	3.07	10^-4	4.80	0.00342
SGLF3 F	742.6	21.36	39.77	7.25	10^-4	5.31	0.00323
SG10S	762	20.00	39.81	24.10	10^-3	4.33	0.00389
SGLF3 G	758.7	19.74	39.76	7.28	10^-3	5.34	0.0032
SGPF13 K	741.1	20.30	39.77	2.25	10^-3	5.84	0.0032
SG10 H	804.5	17.99	39.79	23.35	10^-4	4.97	0.0139
SG43P	788.8	20.26	39.81	10.8	10^-4	6.15	0.0032
SGLF3 P	792.6	20.88	39.80	6.10	10^-4	5.42	0.00344
SGPF13G	812.6	21.59	39.79	2.60	10^-4	6.21	0.00726
SG10 J	796.4	21.31	39.79	24.25	10^-5	5.36	0.01137
SGLF3 H	791.6	20.55	39.76	6.67	10^-5	5.07	0.00914
SG10 N	795.9	19.45	39.81	24.60	10^-5	1.32	0.0248†
SGPF13 C	796.5	20.48	39.76	2.98	10^-5	4.03	0.0256†
SG10 K	791.2	22.19	39.77	23.75	10^-3	5.77	0.00256
SGLF3 N	812.8	20.15	39.79	7.67	10^-3	5.85	0.00333
SGPF13 J	789.2	20.16	39.78	3.00	10^-3	6.00	0.00339

* Tensile strength calculated as $2F/\pi \cdot D \cdot w$ where F is the compressive force on the sample in N (see discussion in Li and Wong (2013)

† failure not reached during experiments – deformation stopped at the indicated strain

Table 3 *Sample properties and experimental results for all Brazilian disc tests*.

where P is the applied force at failure (N), D is the sample diameter (m) and h is sample height (m), following standard procedures (ISRM 1978). Displacement was recorded along the vertical diametrical axis of the sample and is used as a relative measure for tensile strain during testing (under the assumption of invariable Poisson's ratios between samples and experiments). In order to avoid confusion with tensile strain (as measured horizontally at the centre of the circular sample surface) we refer to these strain measurements as axial strain.

4.2.5. Uniaxial compressive strength tests

A set of uniaxial compressive strength tests was conducted under the same strain rate and temperature bounds to constrain the elastic and viscous properties of the dome rock. Sample cores were prepared to 20 mm diameter and 40 mm height. The tests were conducted in an Instron 1362 servo-driven uniaxial press with a 100 kN load cell. The press was fitted with a three-stage split- furnace from Severn Thermal Solutions, capable of temperatures ≤1000 °C. The Young's modulus was calculated during experiments exhibiting brittle, elastic behaviour. During experiments where deformation was accommodated by viscous flow (showing constant stress under continuous deformation), we calculated the apparent viscosity (η_{app}) of the core sample using the Gent equation (Gent 1960), following previous calibrations for volcanic samples (Hess et al. 2007; Robert et al. 2008):

$$\eta_{app} = \frac{2\pi F h^5}{3V\dot{\varepsilon}(2\pi h^3 + V)}, \qquad (2)$$

where F is the force in N during flow, h and V the height in m and volume in m^3 of the sample. The post-experimental dimensions and volume of a viscously deformed sample were carefully measured to determine the Poisson's ratio for a given temperature and strain rate condition (Table 4).

Table 4 *Properties and results from all UCS tests conducted on cores from sample SGLF3*

Sample core	Diameter (mm)	Height (mm)	Strain rate (s^{-1})	Temp. (ºC)	UCS (MPa)	Strain to failure	Apparent viscosity (Pa s)	Young's modulus (GPa)
SGLF3C C	20.10	39.60	10-5	811.5	41.00	0.03424 *	$10^{10.72}$	-
SGLF3C D	20.11	41.11	10-5	760.2	92.144	0.0221	$10^{11.09}$	9.7
SGLF3C E	20.09	39.88	10-3	761	133.78	0.00676	-	21.1
SGLF3C F	20.09	37.57	10-3	803.3	110.05	0.00946	-	14.1

4.2.6. Rotary shear experiments

Rotary shear experiments were conducted to determine the frictional properties during faulting events. We prepared 26 mm diameter by 30 mm height cores from Caliente dome rocks. Half these cores were left solid whilst the other half were drilled concentrically to achieve an annulus of 8 mm thickness and an inner diameter of 9 mm. Each annulus was paired with a solid core sample to minimise the range of slip rate across the annular surface of contact during a test. After careful preparation to ensure opposing core faces were parallel, pairs of cores were loaded into a high-velocity rotary shear (HVR) apparatus so that a normal stress was applied against the flat end of the annular and solid cores. Further details of the experimental methodology and sample loading geometry can be found in Hornby et al. (2015b). We conducted experiments at natural faulting conditions of 1-1.45 $m.s^{-1}$ slip rate and applied normal stresses of 0.4-6 MPa, as determined for faulting events coeval with explosions at Caliente lava dome (Johnson et al. 2008).During a test, the torque and axial shortening (due to radial ejection of frictional melt from the unconfined slip zone) were monitored at 500 Hz and the slip zone temperature was monitored at 30 Hz using a NEC Avio infrared thermographic camera.

4.3. Results

4.3.1. Geophysical monitoring

Analysis of the VLP signals recorded proximally over 4 months (from November 2014) show highly similar, repetitive tilt cycles (Figure 4.4). The radial tilt and air pressure variations over a 6 hour period on 29/11/14 and a 5 hour period on 04/04/14 are presented in Figure 4A and B respectively. Figure 4A shows 11 tilt cycles and 7 spikes in infrasound pressure coincident with sudden, rapid negative tilt (i.e., radial tilt changing towards the edifice), which we observed to generate a small gas-and-ash explosion. Figure 4B shows 9 cycles of positive-to-negative tilt, all of which are associated with an explosive event. Taking a closer look into a typical tilt cycle (Figure 4C), we observe a linear increase over ~5 minutes; following the tilt maximum, we note a rapid (<60 s) negative tilt episode, often coincident with a spike in infrasound air pressure, before a period of slower negative tilt over a period of ~15 minutes. These observations, including the timescale of each tilt cycle, conform with those made by Johnson et al.(2014) and analysis presented in Lavallée et al. (2015a), whereby 222 stacked tilt cycles recorded over 5 days reveal near-identical patterns and timescales, and show that faster rates of positive tilt culminate

in explosions. From this geophysical analysis, we constrain a 5-6 minutes characteristic timescale of positive tilt at a constant rate leading to a gas-and-ash explosion; here, we relate this timescale to the period of stress accumulation in the magmatic column and use it to constrain the strain rate experienced by magma leading to either gas emission or rupture, fragmentation and explosive events.

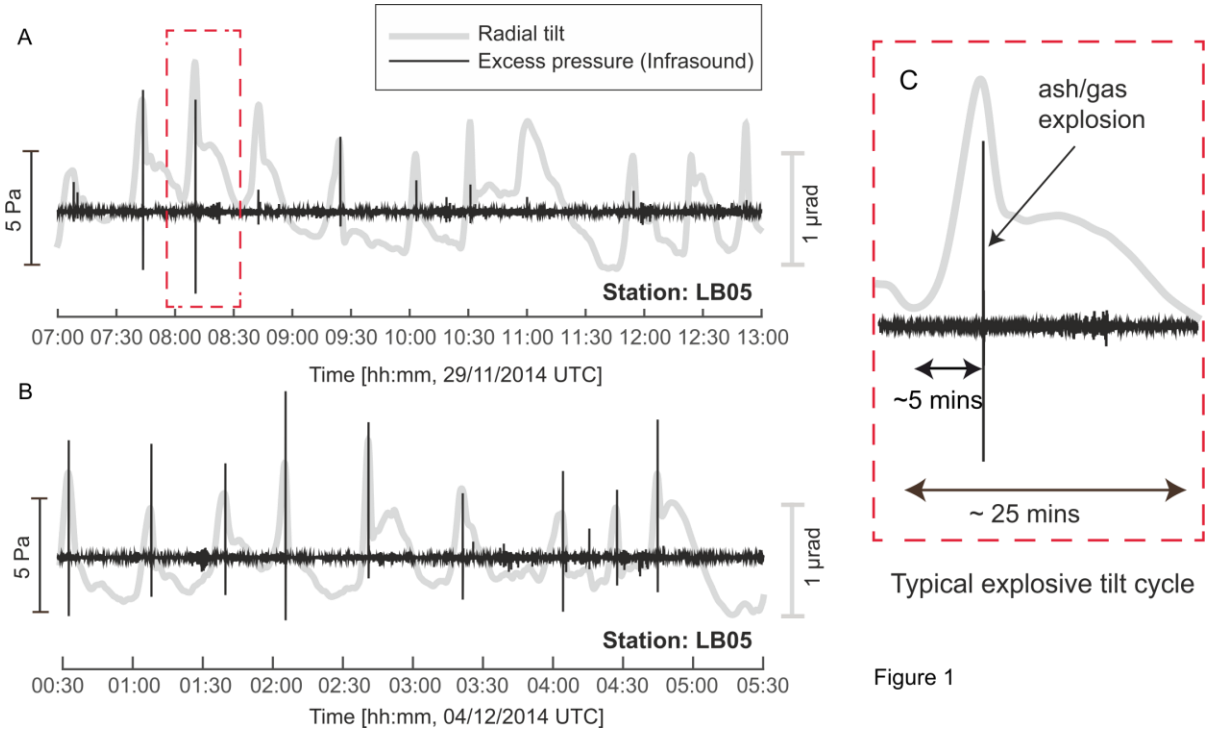

Figure 4.4. *A 6-hour record from 29 November 2014 (A) and a 5-hour record from 04 April 2015 (B) showing radial tilt calculated from very long period seismic signals (thick grey line, right hand y-axis) and infrasound (black line, left-y-axis) monitored at station LB05, ~500 m from the active Caliente vent at Santiaguito. (C) Magnified inflation-deflation cycle and infrasound pulse, circled in part A. Note the timescale for inflation here is ~5mins, in agreement with independently monitored inflation timescales* (Johnson et al. 2014; Lavallée et al. 2015a).

4.3.2. Tensile strength tests

Brazilian tensile tests were conducted on dacitic dome rocks with 2.5% - 25% porosity. The experimental apparatus is illustrated in Figure 4.3A, with sample configuration shown in Figure 2B. Macro-scale changes in deformation behaviour can be seen between experiments under solely brittle deformation (Figure 4.3C) and those for which extensive viscous deformation took place whilst magma tore apart (Figure 4.3D). [Note that in the latter scenarios, the stress

monitored does not reflect the real tensile stress experienced by the sample as the upper and lower part of the cylindrical sample underwent deformation; this however indicates the temperature and strain rate conditions at which magma begins to partially relax the applied stress.]

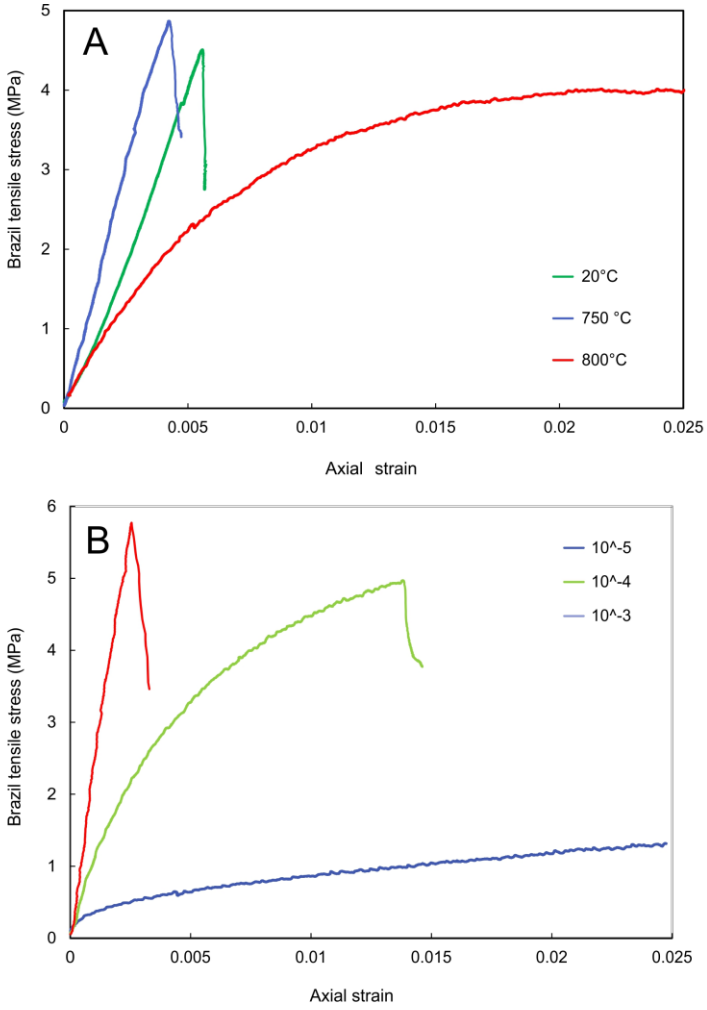

Figure 4.5. *(A) The mechanical data for three experiments on samples cored from SGPF13 with 2.5-3% porosity, conducted at strain rate of 10^{-5} s^{-1} with varying temperatures of 20, 750 and 800 °C presented in green, blue and red lines respectively. The test at 800 °C produced non-linear mechanical data due to a significant component viscous deformation in the sample; (B) The mechanical data for three experiments conducted at 800 °C on samples cored from SG10 with 24-25% porosity, with strain rate varying between 10^{-5} s^{-1}, 10^{-4} s^{-1}, and 10^{-3} s^{-1} presented in red, green and blue lines respectively.*

Typical mechanical data for tests at room temperature and at high temperature is shown in Figure 4.5A; a shift from elastic to partially viscous deformation with decreasing strain rate at a

constant temperature can be seen in Figure 4.5B. The data presented in Figure 4.5 presents the most significant changes in the deformation behaviour and attendant mechanical data under the range of test conditions.

The results for all 49 Brazilian disc experiments are presented in Table 1 and plotted against porosity in Figure 4.6, which shows that tensile strength (maximum tensile stress before sample failure) decreases with increasing sample porosity. This trend is clearest for room-temperature (RT) experiments (Figure 4.6A). Samples deformed at high temperatures record higher tensile strength than their rock counterparts (for a given porosity) – an observation also made during testing of Mount Saint Helens dacite (Smith et al. 2011).

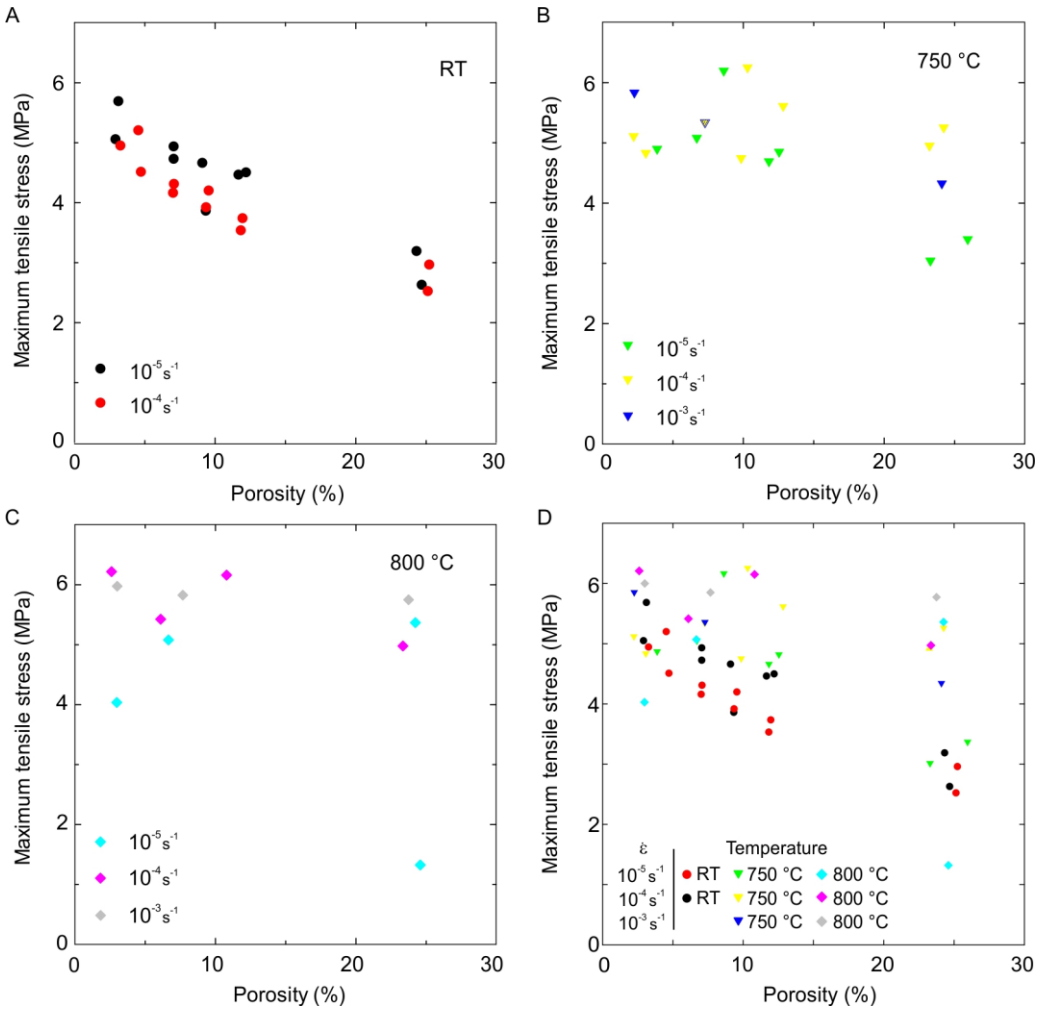

Figure 4.6 *The peak tensile stress during Brazilian disc tests are presented against sample porosity for all samples (A). Room temperature results are shown as circles. Note the decreasing tensile strength with increasing porosity, and that most high-temperature tests show greater tensile strength than room*

temperature for a given porosity. These results are separated into tests at (B) room temperature; (C) 750 °C; and (D) 800 °C, to help distinguish trends across different testing conditions.

Experiments conducted at 750 °C (Figure 4.6B) show a shallower trend of weakening with increasing porosity than at room temperature, and more scatter in the results, however samples at 25% porosity deformed at the slowest rate, 10^{-5} s^{-1}, plot below this trend (these experiments underwent a degree of viscous deformation during the experiments and therefore the monitored stresses are not true tensile stress). At 800 °C (Figure 4.6C), the porosity-related weakening trend diminished further; however two samples (of 3 and 25% porosity) accumulated very little stress during deformation at 10^{-5} s^{-1} owing to high degree of viscous dissipation (as seen by the non-linearity of stress accumulation in the mechanical data; see Figure 4.5). These results point toward a strongly rate-sensitive weakening of Santiaguito dome rock at (near-)eruptive temperatures. We explore this weakening further by comparing the total axial strain accommodated by samples prior to failure (from here on referred to as 'strain to failure') with the tensile strength (Figure 4.7A). This highlights the narrow range (0.02-0.06) of strain to failure for deformation under fully brittle conditions, irrespective of porosity or strain rate. Within this cluster of brittle behaviour, experiments at higher temperatures show lower strain to failure, but higher tensile strength, implying higher Young's moduli. Test conditions for which the strain to failure exceeded 0.06 resulted in progressive decrease in monitored peak stresses (Figure 4.7A); this only occurs for those samples deformed at high temperature and low strain rate. The control of strain rate on strain to failure is further displayed in Figure 5B - this effect is accentuated with temperature (Figure 4.7 C-E; note the change in scale of the strain to failure axis in 4.7E). At 800 °C, all deformation tests at 10^{-5} s^{-1} underwent strain to failure in excess of 0.08, and two samples reached a plateau in tensile stress and did not achieve failure in 20% strain, indicating that deformation was being accommodated viscously. Within the strain rate to strain domain (Figure 4.7 D-E) we explore the timescales and rates of failure measured by geophysical observations at Santiaguito (i.e., the positive tilt timescale prior to explosions), using the concept that stress accumulation represents the time to failure, which can be constrained by the ratio of strain to failure to strain rate. We plot the time to failure curves for 5 and 6 minutes (red curves) and define the region where these curves intersect the upper and lower strain to failure bounds (grey lines) of the suite of experiments having undergone failure in tension (shaded in grey). This exercise brackets the viable strain-rates experienced by the magma prior to failure and an

ensuing explosive event at Santiaguito to 7×10^{-6} to 3×10^{-5} s^{-1} at 750 °C and 1.5×10^{-5} to 6.5×10^{-5} s^{-1} for a magmatic temperature of 800 °C.

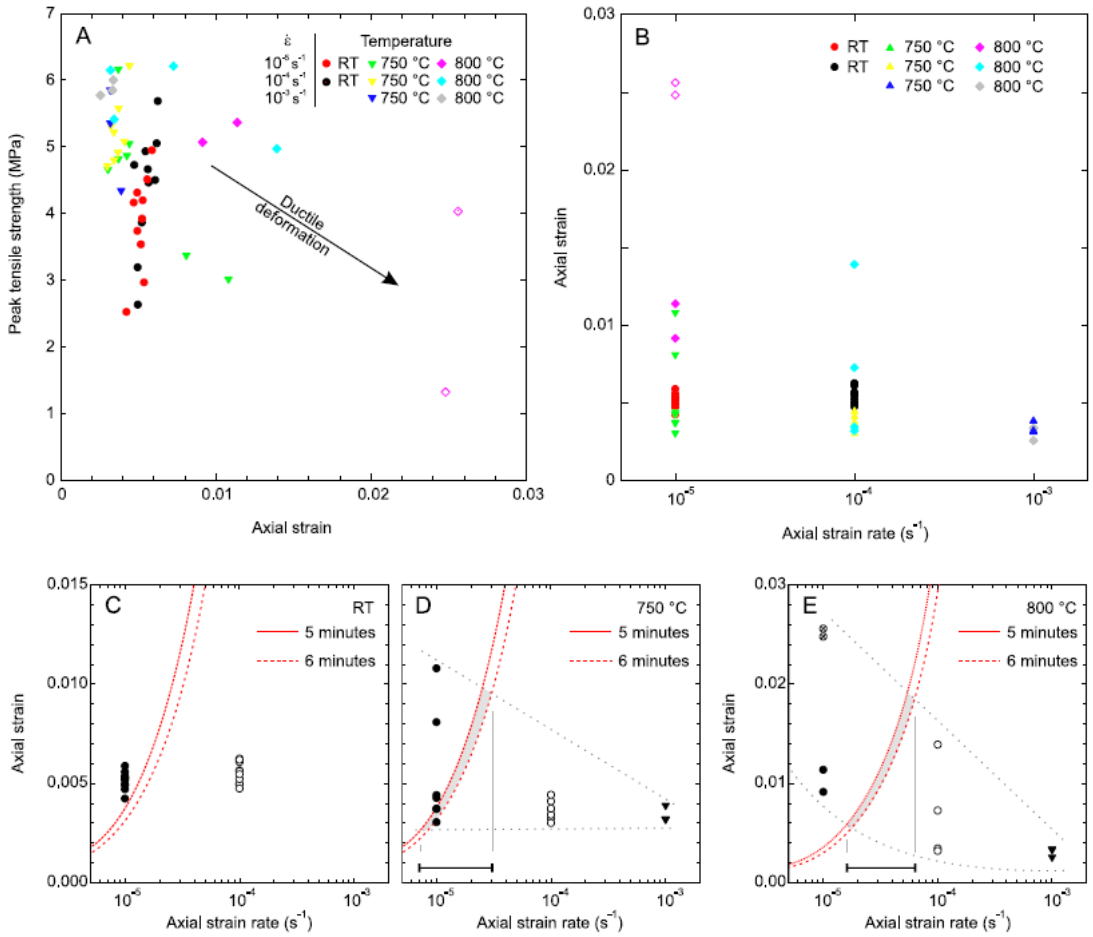

Figure 4.7: *(A) the tensile strength resolved in all experiments is plotted against the axial strain to failure. Most tests show a narrow range of strain to failure (0.002-0.006) indicating fully elastic loading prior to brittle failure. Certain tests at high temperature show greater strain to failure and lower tensile strength, indicating increasing ductile (viscous) component of deformation leading to failure (although some samples did not reach failure at the slowest applied axial strain rate). We assess the importance of geophysical constraints in timescales of deformation by plotting strain rate against strain to failure. (B) Strain to failure is plotted against strain rate, highlighting how strain to failure decreases with an increase in strain rate; this effect is not visible for rocks at ambient temperature (C), but prevails at (D) 750 °C and (E) 800 °C. By dividing the strain to failure by the strain rate we can estimate the time to failure of the samples deformed under a range of deformation conditions; at Santiaguito, the tilt signal constrains stress accumulation to 5-6 minutes (this is plotted as red dotted lines). We constrain the strain rate range leading to failure (grey dotted*

lines) within this monitored failure timescale (red dotted lines), shown as a black scale bar along the x-axis in panels D and E. Note that increasing strain rates are required to cause brittle failure at higher temperature. Note that there is some variability between samples deformed under the same conditions (B-E).

4.3.3. Magma rheology: viscosity and failure mode

Uniaxial compressive strength tests were conducted at 760 and 810 °C and strain rates of 10^{-3} s^{-1} and 10^{-5} s^{-1}. Both experiments at 10^{-3} s^{-1} exhibited a fully brittle elastic response, however at 10^{-5} s^{-1} the magma underwent deformation exhibiting both brittle and ductile modes; at 760 °C, magma failed after 2.7% strain whereas at 810 °C magma underwent viscous deformation without failure (Figure 4.8). We used the mechanical data from experiments at 10^{-5} s^{-1} to calculate apparent viscosities of $10^{11.09}$ and $10^{10.72}$ Pa s, using equation *(2)*, for temperatures of 760 and 810 °C, respectively (Table 2). [Note that the viscosity of the interstitial melt phase of sample SGLF3 was also estimated using chemical composition as input parameters in the GRD viscosity calculator, at $10^{10.96}$ and $10^{10.01}$ Pa s at 760 and 810 °C, respectively (Table 3)].

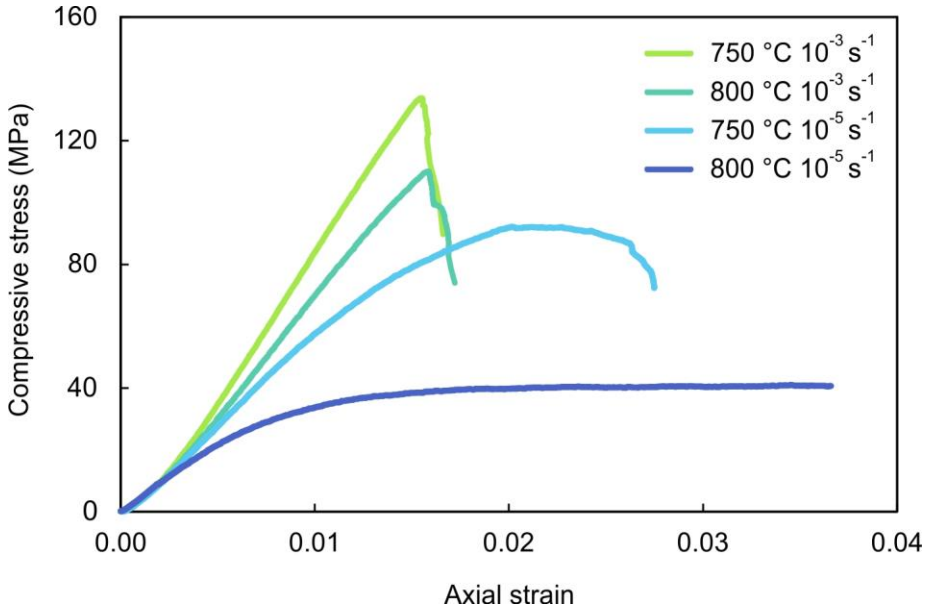

Figure 4.8 *Mechanical data of high-temperature uniaxial compressive strength tests. Tests conducted at a strain rate of 10^{-5} s^{-1} exhibit viscous deformation represented by the non-linearity of the curves, and at the highest temperature the sample flows (i.e., the stress reaches a plateau while strain increases). At the faster strain rate (10^{-3} s^{-1}) the samples deform under dominantly brittle, elastic conditions denoted by linear increases in stress and strain, rapid onset of failure and large associated stress drop.*

4.3.4. Frictional properties of dome rocks

We investigate the effects of plug pistoning experimentally using a high-velocity rotary shear (HVR) apparatus. We conducted experiments on blocks from the Caliente vent and from the 2014 lava flow. HVR experiments were conducted under slip rate (1 and 1.45 $m.s^{-1}$) and normal stress (0.7-6 MPa; equivalent to ~35-300 m depth) conditions representative of those monitored at Santiaguito (Johnson et al. 2008; Johnson et al. 2014; Lavallée et al. 2015a). Under such conditions, rock-rock friction produced substantial heat, resulting in melting of the rock cores adjacent to the slip zone after slip distances ranging from 1 to 45 m, depending on the slip rate (Figure 4.9) normal stress and experimental variablility (Figure 4.10).

The results from experiments on dome rock show that the shear resistance of melt-bearing slip zone does not follow a linear relationship with normal stress, and produces a higher shear resistance than Byerlee's friction rule (Byerlee 1978) under low normal stress conditions (Figure 4.11) – an observation leading to the concept of a melt 'brake' to shallow slip at lava dome volcanoes (Kendrick et al. 2014b). Normal stresses greater than 4 MPa decreases friction toward a lubrication effect, as found in tectonic regimes (Di Toro et al. 2011), therefore an important nonlinear depth-dependence exists for faults in dome eruption settings (Hornby et al. 2015b). Our experiments on Santiaguito dome rock show that formation of frictional melt acts as a brake to slip at normal stresses <4 MPa, equivalent to ~150 m depth. Heating rates from high temperature friction experiments at 1 $m.s^{-1}$ indicate that temperatures sufficient for melting (e.g. 1050 °C) would occur during 0.5 m slip events (Lavallée et al. 2015a).

4.4. Discussion

Changes in radial tilt during eruptive episodes have often been argued for as evidence of varying magma pressure in subsurface reservoirs (Mogi 1958), gas-driven inflation and deflation of the edifice (Nishimura et al. 2012; Johnson et al. 2014) or changes in shear stress between ascending magma and edifice rock (e.g. Green et al. 2006; Albino et al. 2011). Due to the shallow inflation source (<300 m depth), small explosions, continuous effusion and high viscosity of Santiaguito magma, cyclic recharge of magma into a reservoir is highly unlikely. Discerning between gas-driven inflation and shear coupling between ascending magma and conduit walls is challenging,

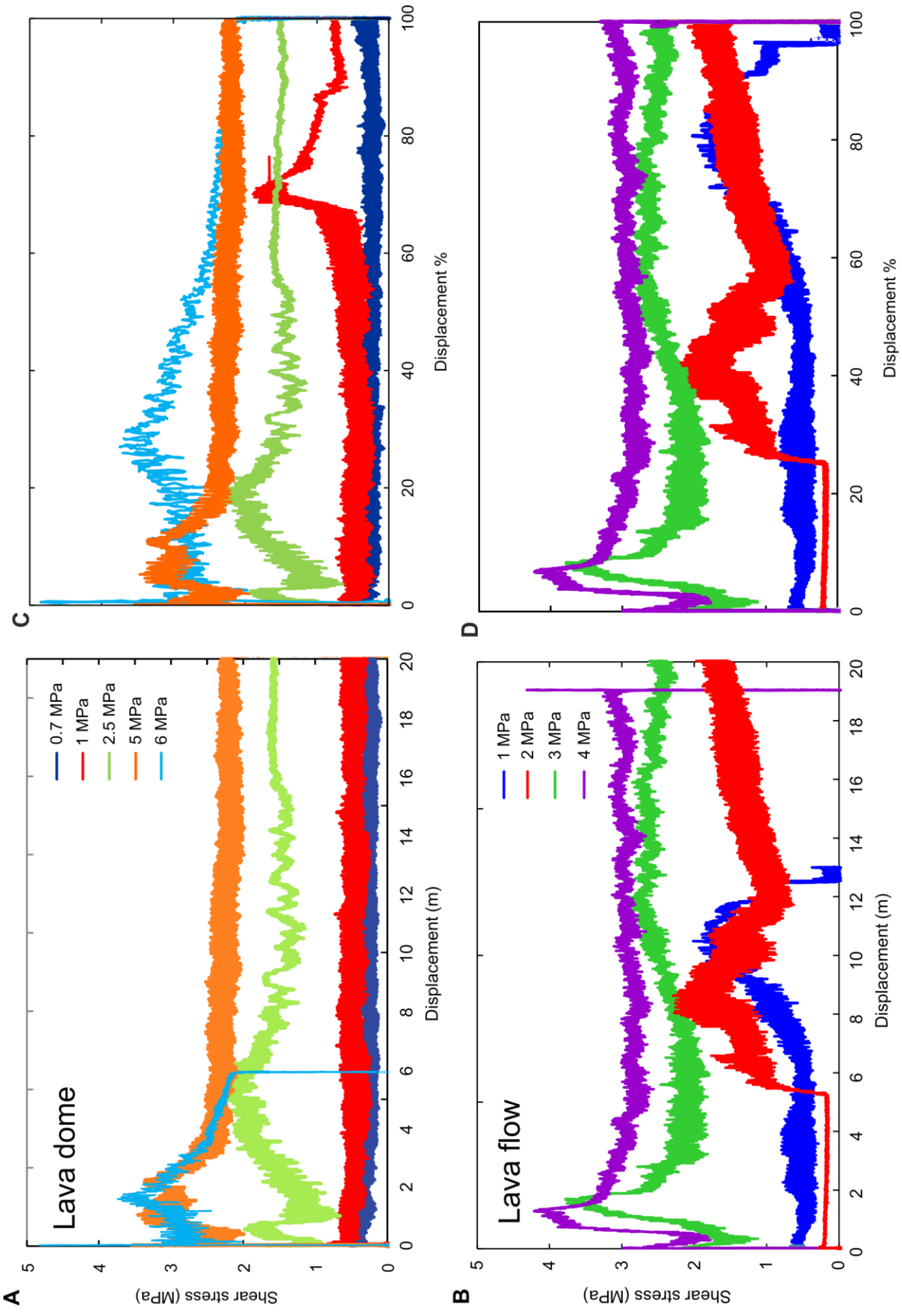
A
Lava dome
0.7 MPa
1 MPa
2.5 MPa
5 MPa
6 MPa
Shear stress (MPa)
Displacement (m)
B
Lava flow
1 MPa
2 MPa
3 MPa
4 MPa
Shear stress (MPa)
Displacement (m)
C
Displacement %
D
Displacement %

Figure 4.9 (previous page): *Shear stress against displacement curves for high velocity friction experiments conducted at 1 m.s^{-1} slip rate and varying normal stress for (A) Caliente dome rock and (B) Caliente lava flow rock core samples. An initial spike in friction represents the static friction on the incipient fault. Shear stress subsequently falls, before increasing again toward a broader peak. This second peak represents the melting of phases in the rock along the fault plane due to rapid heating, and the peak coincides with establishment of a full layer of melt across the slip interface. From this point onward, the shear resistance decreases and establish a new steady shear stress, as melt lubricates (and is ejected from) the fault interface.*

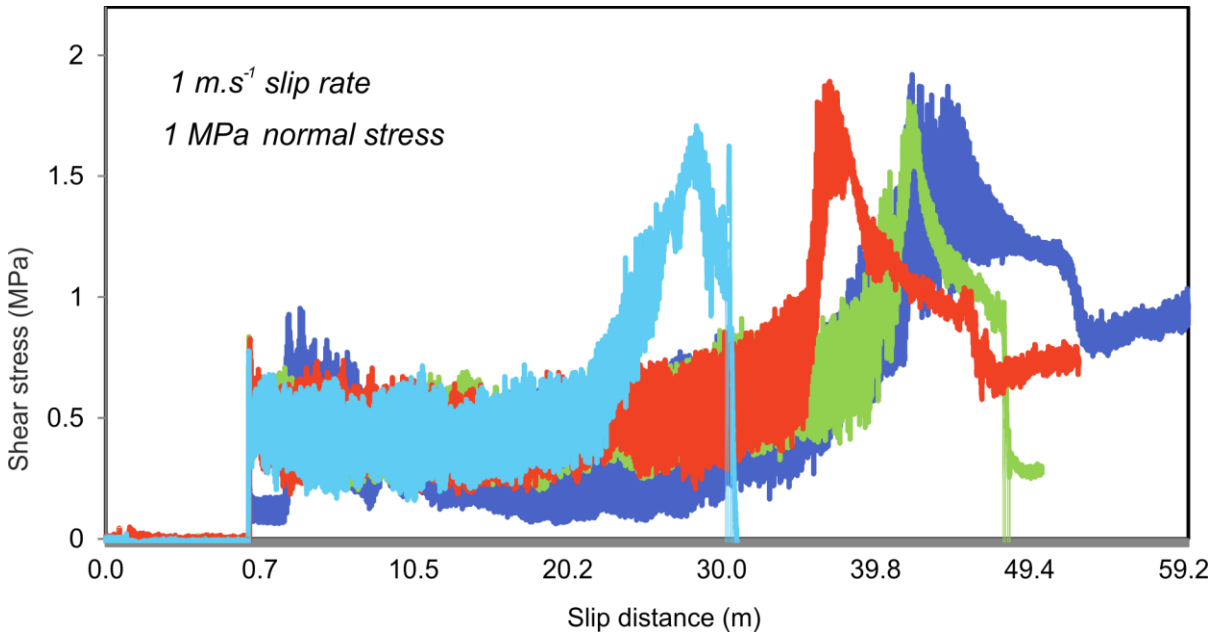

Figure 4.10. *Repeated experiments at the same slip rate and normal stress conditions show similar values for peak shear stress (1.85±0.15 MPa) however, more significant variation in slip distance required to form a frictional melt (from 28 to 42 m). The shape of the peak in shear stress caused by frictional melting, and a sudden decrease in shear stress found 8-10 m after the peak in shear stress in the red and blue curves is similar, and the characteristically long slip prior to melting is shown to be replicated.*

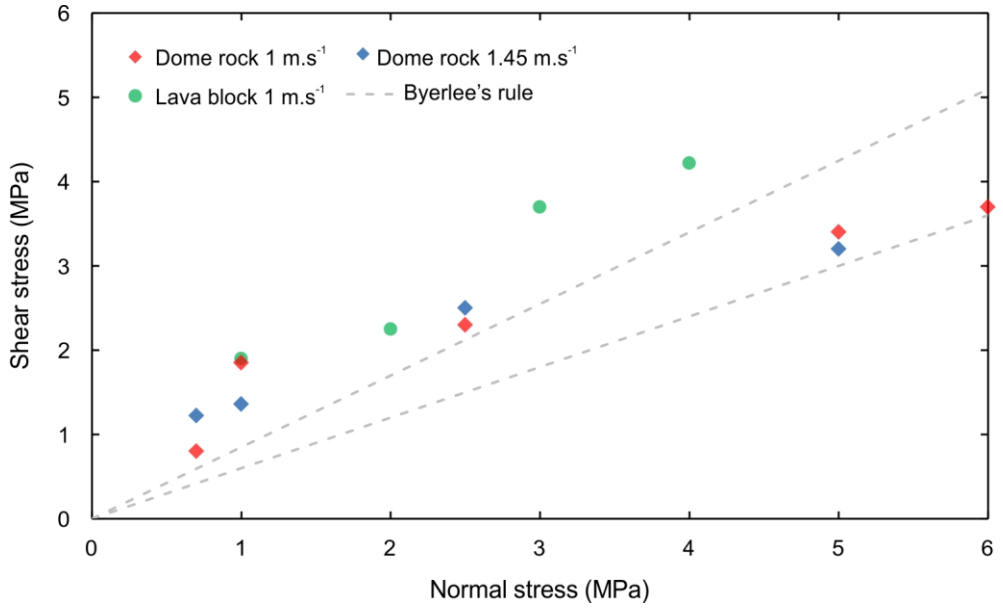

Figure 4.11 *A comparison of peak shear stress values with varying normal stress and slip rate. The shear resistance induced by the presence of frictional melt exceeds those produced by rock-rock friction (Byerlee's friction law, marked by dashed lines) when normal stress is lower than 4 MPa, indicating that frictional melt would act as a brake to slip at shallow depths. The lava block may produce slightly higher shear stresses than the dome rock, however the variation in rate from 1 to 1.45 m.s^{-1} appears to have little effect on the resultant shear resistance*.

and both have been argued for at Santiaguito (Holland et al. 2011; Scharff et al. 2014; Johnson et al. 2014). It is important to stress that failure in tension is highly likely during gas pressurisation (Alidibirov and Dingwell 1996) and strain localisation and conduit shearing scenarios (Massol and Jaupart 2009), especially if there is a change in geometry in the shallow conduit. However, several lines of evidence indicate that gas overpressures do not act to trigger vulcanian explosions at Santiaguito. Observations of SO_2 outgassing fluxes do not significantly vary during pre- and post-eruptive episodes and show poor correlation with eruption magnitudes (Rodríguez et al. 2004; Holland et al. 2011). Additionally, Okumura and Sasaki (2014) estimated that the permeability reduction timescale of fractures present during explosions at Santiaguito is at least one order of magnitude longer than the eruption interval, suggesting that gas overpressures sufficient to exceed the tensile strength of magma could not develop in the shallow edifice. Finally, volcanic ash particles emitted during the explosions are dense and blocky, with few small, well-rounded vesicles (Hornby et al. In Review), indicating that the erupted material had a low bubble number density and did not fail due to bulk bubble overpressures. Therefore, it is

likely that shear stress provides an essential contribution to the triggering of explosions and the cyclic monitored tilt patterns. This could operate by coupling (Green et al. 2006) and shear failure of magma during strain localisation along conduit walls (Neuberg et al. 2006; Holland et al. 2011). A recent model (Lavallée et al. 2015a) argues for explosion triggering via magma failure and subsequent slip-induced vesiculation (see **Section 4.5**), a sequence of events that is supported by textural evidence (Hornby et al. In Review).

During fracture processes at magmatic temperatures near to the brittle-ductile transition, crack tips become more blunted and subcritical crack propagation is likely to become more important (e.g. Meredith and Atkinson 1983; Atkinson and Meredith 1987), perhaps aided by stress corrosion in the interstitial melt/glass (Ciccotti 2009). Such time-dependence of ductile deformation has been inferred at other dome volcanoes, including Montserrat (Kilburn and Voight 1998), Mount Saint Helens (Denlinger 1990; Smith et al. 2007) and Unzen (Smith et al. 2001), and given the low effusion rate and the results of our high-temperature experiments, appears likely to operate to some extent at Santiaguito. Evidence for incremental and time-dependent fracture propagation is present in the crenulated fracture path propagating between crystals and void spaces in our samples (cf. Maire et al. 2016), and widening of existing fractures seen in samples deformed at high temperature and low strain rate (Figure 4.4D, Figure 4.12A-B). In fluid-saturated and high-temperature environments such as at persistently degassing dome volcanoes, sub-critical crack growth may perhaps influence the timescales of fracture propagation and monitored deformation rates under deformation conditions close to the brittle-ductile transition.

4.5. Interpretation

4.5.1. Brittle processes in magma

The mechanical experiments conducted here highlight the importance of constraining temperature and strain rate in our description of magma behaviour at eruptive conditions. Whereas porosity does not hold such a high influence on the behaviour of magma (compared to that of rocks), we find that an increase in strain rate lowers the strain to failure and results in a higher tensile strength. Under low strain rate conditions, stress is dissipated viscously and strain becomes more widely distributed (i.e., ductile) across the sample. As ductility increases, the propagation of a fracture becomes increasingly time-dependent (at higher temperature and lower

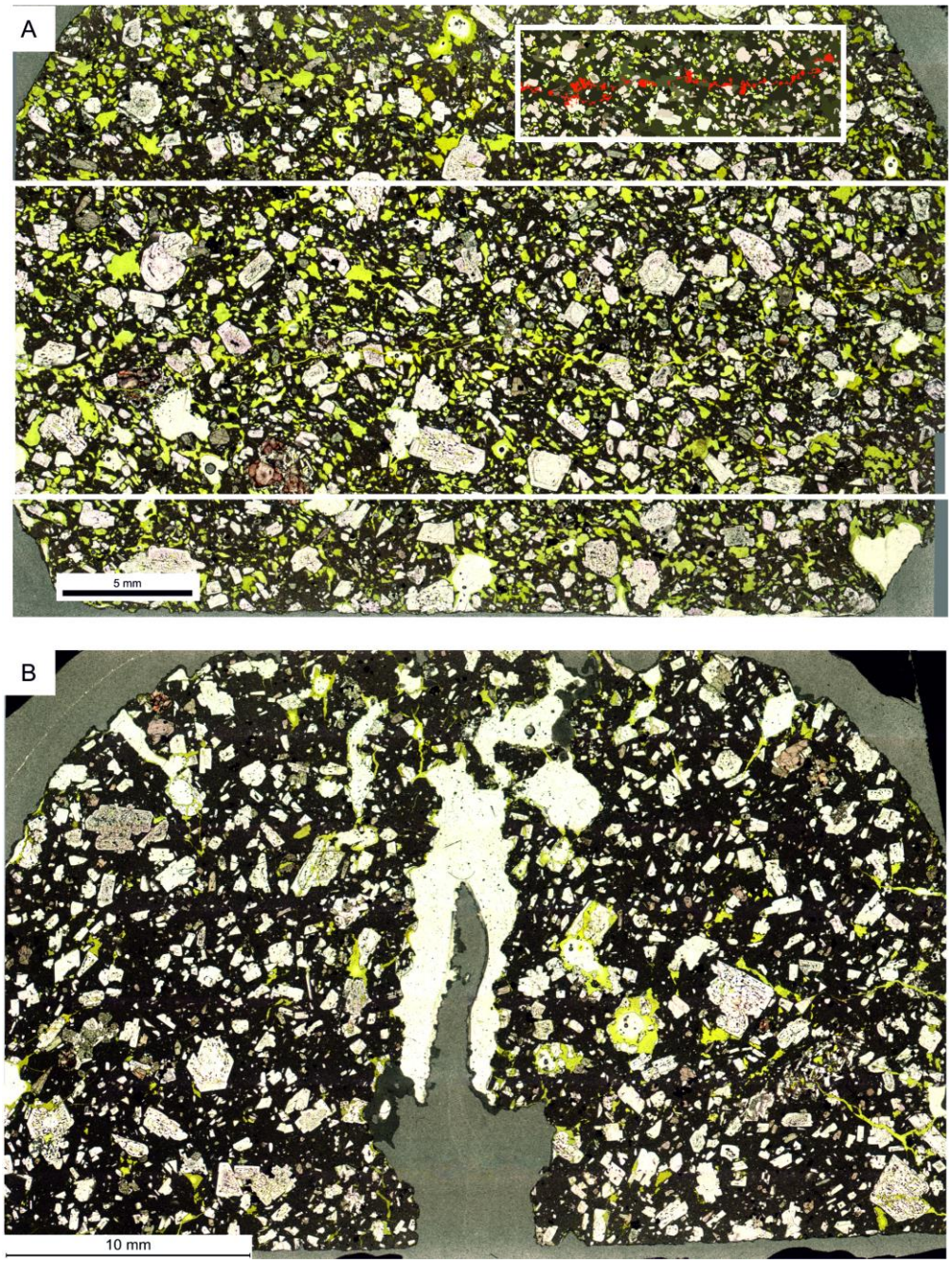

Figure 4.12 *(A) Photomicrograph showing detail of tensile fracture propagating through sample SG10J (25% porosity; see Table 1 for experimental conditions). Thin sections have been impregnated with fluorescent epoxy so that voids show as yellow. Notice the presence of conjugate and en echelon fractures, and the tendency for fractures to deviate toward vesicles and crystal; (B) Post-experiment sample SGPF13 (Brazilian experiment conducted at 800 $^{\circ}$C and 10^{-5} s^{-1}) showing detail of the irregular, crenulated fracture boundaries that develop incrementally from crystal to crystal. Radial fractures propagating inwards from the right-hand boundary of the sample are more localised (and appear more spontaneous).*

strain rates). Our choice of temperature is somewhat conservative, and therefore we expect deformation leading to fracture at 300 m depth at Santiaguito to exhibit a degree of ductility that leads to propagation under time-dependent conditions. The upper part of the dome is prone to undergo cooling to the atmosphere, as such we expect magma to exhibit different brittle/ductile proportion in their mechanical behaviour at different depths.

The apparent viscosity calculation used here were based on calibrations with silicate glasses and prior experimental work (e.g. Hess et al. 2007; Lavallée et al. 2007), using a uniaxial press apparatus developed at LMU Munich; the similarity in design between the apparatuses, and the strength of the calibration, suggests that this formula is valid for the test apparatus used here. The apparent viscosity we measure at 860 °C is at the lower end of the viscosity bracketed ($10^{10.26}$-$10^{12.26}$ Pa.s^{-1}) for ascent-driven shear fracture [previously calculated assuming a shear strength of 10^6 to 10^8 Pa (Holland et al. 2011). The shear strain rates constrained at Santiaguito from effusion rate and SO2 fluxes are $10^{-4.08}$ – $10^{-4.26}$ s^{-1}, comfortably bracketed by the range of strain rates used in our experiments. However, shear fracture remains feasible, especially when considering variations in magma ascent rate generated by heterogeneous porosity and permeability structures within lava dome volcanoes (Michaut et al. 2013; Cassidy et al. 2015; Farquharson et al. 2016b).

4.5.2. Rheological controls on eruption at Santiaguito

Magma deformation at Santiaguito encompasses both the ductile and brittle regime. The experimental findings presented here support this view and highlights the strong temperature- and time-dependent behaviour of magma at eruptive conditions. We have constrained the magma deformation behaviour likely to exist during the 5-6 minute cycle of inflation recorded by tiltmeters. The (upper and perhaps marginal) portions of the lava dome at moderate temperature of 750 °C, are expected to undergo failure in tension if sustained strain rates reach and exceed ca. 7×10^{-6}-3×10^{-5} s^{-1}. The hotter portion of the lava dome (e.g., at 800 °C) requires higher strain rates of 1.5×10^{-5}-6×10^{-5} s^{-1} to succumb to failure. Such temperature- and time-dependent tensile fracturing behaviour may favour the propagation of tensile fractures downward as well as upward depending on the conditions and profile of stress accumulation in the shallow magmatic column. If strain from a pressure source is radiated elastically, then lower sustained strain rates are required for brittle fractures to propagate downwards within cooler

material in the overlying plug or at the conduit boundaries. Yet, we do not expect solely (elastic) brittle deformation in the magmatic column (at least not across the range of eruptive behaviour observed at Santiaguito); in cases where we consider viscous deformation (sustained at strain rates up to 8.5 times faster in magma at 800 vs 750 °C), we expect that tensile fractures are most likely to occur proximally to a stress source, which would require such fractures to propagate upwards to initiate an explosion. We anticipate that upon formation of a tensile fault, any differential residual stress would be dissipated by slip along the fault. During vulcanian explosions the dome surface rises and falls by 0.5 m in 1 s, (Johnson et al. 2008) indicating the faulting and slip of conduit magma at velocities >1 $m.s^{-1}$. Previous work has shown that slip of a magma plug is controlled by frictional properties at the slip interfaces (Lavallée et al. 2012b; Kendrick et al. 2014b; Hornby et al. 2015b), and that slip generates rapid temperature increases sufficient to induce melting as well as local vesiculation in the fault zone during dome pistoning at Santiaguito (Lavallée et al. 2015a). Lavallée and co-authors (2015) argue that the pore pressure developed in the shallow magmatic column is insufficient to trigger fragmentation, but local tensile failure only, and in turn present a model in which local thermal vesiculation along fault zones, generates the pore pressure capable to trigger (what they refer to as) a 'sacrificial' fragmentation. Thermal vesiculation may pose a significant source of weakening even for a few centimetres of slip (Kendrick et al. 2014b; Hornby et al. 2015b). Such slip conditions may occur during shear failure events near the conduit margins and between blocks in the dome carapace. This sacrificial fragmentation is argued to stabilise the dome structure over recurrent tilt cycles. Volcanic ash produced in such a cataclastic and thermal-driven fashion erupts in pulsatory manner (e.g., Scharff et al, 2014) and creates ash with a distinct mineralogical signature (Hornby et al., In Review).

4.6. Conclusion

Here, geophysical observations and laboratory experiments are combined to describe the eruptive behaviour at Santiaguito. Analysis of tilt signals indicates that gas emission events as well as vulcanian explosions are preceded by a 5-6 minute inflation period, which we argue to correspond to the period of stress accumulation (elastic energy storing) in the magmatic column. Experimentally, we find that the tensile strength of dome lava is sensitive to strain rate and temperature, as brittle deformation becomes important at higher strain rates and lower temperature. Our results suggest that tensile fracture is highly likely during shallow deformation

at Santiaguito under a range of realistic conditions. Strain rates exceeding ~7×10^{-6} and 1.5×10^{-5} s^{-1} are expected to result in magma failure in tension at 750 and 850 °C, respectively, within the 5-6 minute tilt cycle at Santiaguito. This temperature- and time-dependent mechanical response of lava is used to argue that tensile fractures are more likely to propagate upwards from an inflating volumetric source in the shallow magmatic column. Following fracture propagation, we expect that the dissipation of remaining energy occurs via faulting along the fracture plane. Experimentally, we find that under the slip, stress and temperature conditions at Santiaguito, faulting will lead to melting (as well as vesiculation) of adjacent rock/magma, which may support the recent model suggesting that moderate Vulcanian explosions are caused by sacrificial fragmentation along faults developed through the tilt cycle. Our findings highlight the need to better constrain the temperature and strain rate profile in shallow magma as the rate of stress accumulation dictates fracturing dynamics and eruptive style at Santiaguito volcano.

These are lower bounds of strain rate leading to explosion over the measured 5-6 min inflation cycles, as the interaction of multiple fractures experiencing subcritical fracture growth may be required to trigger a rapid decompression event. Stress corrosion may determine the timescales of fracture development during ductile deformation, however further experimental work is needed to describe the propagation mechanisms during subcritical crack propagation. Estimations of the strain rate and temperature within the dome prior to explosions are vital in determining deformation mode and fragmentation mechanisms. Our results indicate the viability of thermal vesiculation during conduit faulting as a mechanism for rapid local weakening of magma leading to fragmentation, presenting a hybrid model between decompression and shear failure modes.

Chapter Five

Characterization of volcanic ash particles produced at Santiaguito volcano, Guatemala: QEMSCAN® insights into fragmentation mechanisms

Preface

In the previous chapter, tensile fracturing was explored as a deformation trigger for explosive eruptions at Santiaguito. Here, the nature of fragmentation events themselves are investigated by studying volcanic ash samples deposited close to the active vent at Santiaguito. Ash particles produced at Santiaguito are dense and blocky, and little research has been done to constrain the mechanisms for formation of volcanic ash at lava dome volcanoes.

Here, a thoroughly novel methodology is proposed to constrain and discriminate between the fragmentation mechanisms producing ash during explosive eruptions and dome collapse events, using QEMSCAN® particle mineralogical analysis to analyse the distribution of mineral and glass phases in ash particles.

The work presented here is my own, except for the QEMSCAN® imaging and preparation of thin sections and stubs containing Santiaguito ash, which was conducted by G. Rollinson and A. Butcher at the Camborne School of Mines.

Characterization of volcanic ash particles at Santiaguito volcano, Guatemala: QEMSCAN® insights into fragmentation mechanisms

Abstract

The physical and mineralogical properties of volcanic ash provide evidence for magmatic conditions leading to, during and following fragmentation. Here, we use novel characterisation methods to explore the textural fingerprint of fragmentation processes during varying volcanic activity at Santiaguito volcano, Guatemala. We compare two ash samples collected 500 m from the active vent: one deposited following Vulcanian explosions on 13 November 2012 and the other after a dome collapse with associated pyroclastic density currents on 28 November 2012. The ash particles from both samples appear blocky and poorly vesicular under scanning electron microscope (SEM). Particle size analyses show a unimodal size distribution of ash particles associated with dome collapse, whereas the ash derived from a Vulcanian explosion exhibits a more complex distribution. We employ QEMSCAN particle mineralogical analysis (PMA), an SEM-based automated mineralogy technique that rapidly produces micron-scale images showing the distribution of minerals and glass in thousands of ash particles from each sample. We use image analysis to isolate phases and measure size-dependent variation in ash particle properties, finding that ash produced by the Vulcanian explosion contains a greater total fraction of glass and is preferentially bordered by plagioclase, indicating the focusing of fracture propagation in crystals during magmatic fragmentation. Conversely, ash generated during dome collapse shows a greater distribution of interstitial glass at particle boundaries over most of the particle size range, suggesting that fragmentation processes favour fracturing in the glass phase at coarse grain sizes. This novel characterisation protocol permits new lines of study into the links between particle properties and conduit fragmentation triggers and processes, furthering the understanding of lava dome eruptions and associated hazards. We discuss potential applications of QEMSCAN PMA of volcanic ash for timely assessment of hazards to aviation and respiratory health and encourage further development of the technique within volcanology.

5.1. Introduction

5.1.1. Background

1.1 Background

The production of volcanic ash, defined as airborne particles (<2 mm diameter), is a near-ubiquitous phenomena at active volcanoes (Cas and Wright 1987). The size, composition, dispersal and sedimentation of ash pose a range of hazards to respiratory health, the natural environment, infrastructure and aircraft activity (Wilson et al. 2015; Song et al. 2016). Volcanic ash is the product of fragmentation, and is inevitable, irrespective of the failure modes and mechanisms at play across a broad spectrum of eruptive activity. Once rock and magma is fragmented, particle interaction during subsequent transport in pyroclast-laden flows can modify and create ash-sized particles (Freundt and Schmincke 1992; Dufek and Manga 2008). This final category includes particles produced by milling and abrasion (Kueppers et al. 2012; Mueller et al. 2014) and attrition (Lavallée et al. 2014).

Ash deposits are commonly described by their size distribution, morphology, composition, componentry, and spatial extent, and can be modified by from grain-size sensitive fragmentation, aggregation and sorting processes prior to deposition (Walker 1971; Wohletz et al. 1989; Mueller et al. 2016). An important tool in constraining the processes of formation, entrainment and transport is the deconvolution of GSD curves (Wohletz et al. 1989; Evans et al. 2009) into subpopulations representing separate transport and fragmentation processes. However, any single ash sample represents an apparent grain size distribution for a given set of eruptive and meteorological conditions and an estimation of the total GSD is necessary to fully interpret the GSD (Bonadonna and Houghton 2005; Rose et al. 2008). The initial, or triggering fragmentation mechanism, and the degree of in-transit particle modification can also be assessed by particle shape measurements (Maria and Carey 2007; Caballero et al. 2012). Although a wide range of measures and nomenclature may be applied, a rigorous set of shape descriptors has emerged in recent literature [e.g. *Heilbronner and Barrett*, 2014; *Liu et al.*, 2015]. Vulcanian activity produces ash particles with characteristics of both decompression, shear failure and hydrovolcanic fragmentation mechanisms (Heiken and Wohletz 1987; Miwa et al. 2013; Lavallée et al. 2015a). Failure and wear mechanisms are of particular importance in dense, highly viscous dome lavas,

where brittle deformation and slip in areas of strain localization can regulate eruptive behavior at shallow depths (Kendrick et al. 2012; Lavallée et al. 2015a; Hornby et al. 2015b). *Rowe et al* (2008) present evidence that ash collected during the 2004-2005 explosive activity at Mount St. Helens was sourced primarily from faulting, fracturing and abrasion of a quasi-solidified viscous magma can be an abundant source of ash and highlight the similarity of ash particle shapes and composition with those of ash derived from rock-falls.

Only a handful of studies have investigated the distribution or abundance of mineral and glass phases within ash particles with respect to fragmentation mechanisms. *Bayhurst et al.* (1994) used SEM-EDS to map the phase and size distribution in ash retrieved from a Boeing 747 following the eruption of Redoubt, deriving a hydrovolcanic fragmentation source from the ash properties. Plagioclase feldspar is the dominant crystalline phase in andesitic or dacitic eruptive products and appears to play an important role during fragmentation and deposition. A study by *Riley et al.* (2003) showed that the characteristic size of plagioclase feldspar crystals modified the grain size distribution of the ash and *Bonadonna et al.* (2002) found an increased fraction of plagioclase feldspar in Vulcanian (plume-derived) compared to flow-derived ashfall deposits, attributed to segregation of coarser and denser crystal-rich particles within pyroclastic density current (PDC) deposits (Sparks and Walker 1977; Horwell et al. 2001). A recent experimental comparison of particle characteristics has recently provided comparative data on particle attributed during primary (decompression) fragmentation and milling (Jones et al. 2016). Changes in ash particle componentry and glass chemistry were used in a study by *Cassidy et al.* (2015) to infer variations in magma ascent rate that determine eruptive behavior. Finally, the presence of interstitial glass requires consideration with regard to kinetic processes and fracture mechanisms (Dürig and Zimanowski 2012; Lavallée et al. 2015b). Here, we use a novel analysis protocol combining the componentry of volcanic ash to the size and shape distribution to shed new light on the mechanisms operating during Vulcanian explosions and dome collapse events at Santiaguito volcano in Guatemala.

5.1.2. Santiaguito dome complex, Guatemala

The Santiaguito volcanic complex, in Guatemala, consists of a chain of four dacitic lava domes, formed along a fracture at the base of a sector-collapse scarp associated with the 1902 Plinian eruption of Santa Maria stratovolcano (Rose 1972; Escobar-Wolf et al. 2010; Andrews 2014). Following a hiatus of 20 years, the Santiaguito dome complex initiated a dome-forming eruption in 1922 and has been continuously active since. The Caliente dome is the earliest active structure as well as the only vent that has shown near-continuous discharge of lava interspersed by regular Vulcanian explosions throughout the eruptive history. Today, the almost hourly generation of gas-and-ash clouds (see Figure 5.1a-b) and the episodic occurrence of PDCs associated with dome collapse are the greatest hazards to surrounding communities (Bluth and Rose 2002) and aviation (Song et al. 2014). Large dome collapse events have most recently taken place in September 2015, May 2014, August 2013 and November 2012, and can generate PDCs >6 km in length, reaching nearby communities and plantations. These events produce abundant airborne ash particles as seen in photos from the 28 November 2012 event shown in Figure 5.1c-f.

The Vulcanian explosions occur at regular intervals of 20-120 minutes and typically produce discreet ash-rich bursts generally following gas-rich emissions (Figure 5.1 a-b), which evolve into small (500-1000 m) ash-poor plumes (Bluth and Rose 2004; Scharff et al. 2014). Data from recent geophysical deployments involving seismometers and infrasound microphones installed proximal to the active vent show that the ascending magma undergoes highly self-similar processes producing consistent and regular, ~25-minute, inflation/deflation cycles, which lead to either gas release or gas-and-ash explosions, which preserve the dome structure (Johnson et al. 2014). The source of deformation has been postulated as cyclic pressurization of a gas pocket at ≤300 m depth (Johnson et al. 2014) or shear-induced failure and faulting at the conduit boundaries (Bluth and Rose 2004; Holland et al. 2011; Scharff et al. 2014). Recently, Lavallée et al. (2015a) have suggested a new mechanism, whereby inferred fault friction causes rapid heat input, leading to thermal-driven water exsolution and vesiculation of heated magma. Such vesiculation reduces the strength of magma at shallow depths and initiates failure and fragmentation expelling ash along multiple active faults that allows movement during inflation/deflation cycles and enables the central portion of the dome to remain intact. This sacrificial fragmentation mechanism would regulate the stability of the dome during its growth cycles (Lavallée et al. 2015a). Here, we characterization the volcanic ash produced from a Vulcanian explosion and a dome collapse event to compare the mechanisms and products of fragmentation processes at this incessantly active dome-building volcano.

Figure 5.1: (a) *The Caliente vent at the Santiaguito dome complex in Guatemala, showing gas venting from an arcuate fracture and ash from a separate fracture set associated with Vulcanian eruptions. The dome surface is approximately 200 m in diameter;* ***(b)*** *Vulcanian explosive activity including a small pyroclastic flow and the separation of gas- and ash-rich plumes at the onset of explosion. Photos (a) and (b) record the same explosion from 9 November 2012;* ***(c)*** *The ash cloud following a partial dome collapse on the southern flank of the Caliente vent on 28 November 2012;* ***(d)*** *Ashfall obscuring the sun near the campsite 900 m NW of the Caliente vent, 3 hours within the 6-hour long dome collapse event;* ***(e-f)*** *Photos taken from the Santiaguito volcano observatory (OVSAN), situated 3.5 km South of the Caliente vent, before and after the dome collapse. The area of the dome that collapsed and path for subsequent pyroclastic flows is indicated in part* ***(e)*** *by a yellow dashed line;* ***(f)*** *shows the dome on November 29th, following the collapse event. Photographs (e-f) courtesy of J. Cornejo and Á. Rojas (INSIVUMEH-OVSAN).*

5.2. Materials and methods

5.2.1 Ash collection

Ash samples were collected 15 days apart ~500 m North from the active Caliente vent during a field campaign in November 2012. The ash samples were collected by laying clean canvas sheets on the ground prior to eruptive activity. After ash settling, we used a paintbrush to collect the particles into sealable sample containers. The sheets were carefully cleaned between each collection, thus providing ash samples linked to individual eruptive events. This study compares two samples. The first was collected at 09:00 (local time) on 13 November, during typical gas-and-ash venting associated with Vulcanian activity; The second sample was collected at 10:30 on the 28 November following the deposition of ash initiated by the collapse of a subaerial lava lobe/flow, on the southern-western edge of the Caliente dome, and subsequent generation of strong pyroclastic density currents (Figure 5.1e-f). The Guatemalan monitoring agency, INSIVUMEH, reported strong pyroclastic flows on the southern flanks of Caliente, ash clouds rising 3.5 km and ashfall up to 70 km from the vent (Chigna et al. 2012). Visibility at the collection site was reduced to ca. 10 m during the heaviest ashfall (Figure 5.1d) and the canvas sheet was covered by ~10 mm of ash. The Caliente vent was obscured by airborne ash for approximately six hours. These two samples, deposited following a Vulcanian explosion (termed hereafter sample VE) and dome collapse (sample DC) respectively, are used to compare the characteristics of volcanic airfall ash generated by Vulcanian explosions and dome collapse events at Santiaguito..

5.2.3 Ash sample analysis

Grain size analyses were performed in a Coulter LS230 laser diffraction grain size analyzer, following the methods described in Blott et al. (2004). We deconvoluted the resulting GSD curves into subpopulations (modified gamma curves generated from skewed lognormal distributions) using DECOLOG 5.1 software (Borselli and Sarocchi 2015) to integrate subpopulations with negative skewness. Deconvoluted subpopulations and stacked (modeled) GSD curves are shown in Table 5.2.

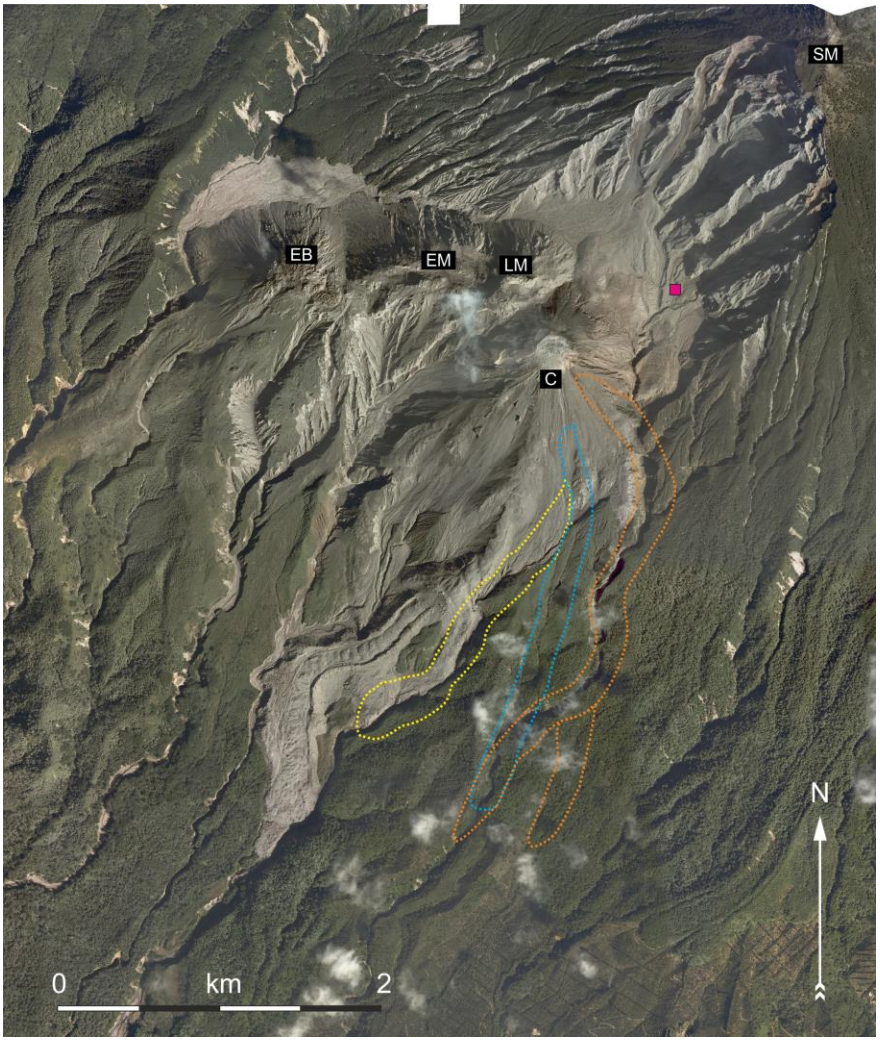

Figure 5.2. The sampling location of the ash is shown as a pink square NE of the Caliente vent (marked C). Both Vulcanian explosion ash and dome collapse ash were collected at this location. The path of the dome collapse followed the path of the lava flow shown in blue. The sampling location is approximately 600 m from the active Caliente vent and is protected by the Santa Maria collapse scarp from strong winds.

Table 5.1: *QEMSCAN® identification criteria and range of possible mineral matches within each mineral category, applied during particle mineralogical analysis (PMA). Significant manual checks and comparisons with external data, including EPMA measurements of interstitial glass, were conducted before phase assignment was finalized.*

Mineral Category	**Mineral Description**
Plagioclase feldspar	Plagioclase feldspars: phases with Ca,Al,Si,O.
Glass	Any phase with K,Al,Si,O (including orthoclase/microcline/sanidine) and Na,Al,Si,O (albite).
Pyroxene	Any phase with Mg,Fe Si, such as olivine, serpentine group and orthopyroxenes
Amphibole	Any phase with Ca,Mg,Fe,Si, (with or without Al) such as hornblende, tremolite, augite, actinolite.
Ti Magnetite	Any phase with Fe,O and low Ti. May include other Fe oxides such as magnetite, hematite, goethite.
Quartz	Quartz and other silica minerals/ polymorphs.
Ilmenite	Any phase with Fe,Ti,O.
Apatite	Any phase with Ca,P,O.
Others	Any other mineral not included above. These may include Fe sulphides, Cu-Fe-sulphides, kaolinite/ halloysite/ dickite, chlorite, and phases with Fe-Al-Si (±Mg).
Background	All resin related/edge effects.

Textural & mineralogical analysis of the volcanic ash samples was conducted using scanning electron microscope photomicrographs, and images with data acquired by QEMSCAN®, which is an automated SEM-EDS system for compositional mineral/phase mapping and was originally designed in the late 1970s for the mining industry (Gottlieb et al. 2000). Since then, it has been used within research and has been successfully applied to many types of projects and samples (Pirrie et al. 2004; Martin et al. 2009; McLeod et al. 2016; Namkung et al. 2016). The system employs a combination of SEM BSE signal and EDS X-ray

data to automatically analyse a sample at a micron scale, producing thousands or millions of chemical analysis points in a map, with a selection of four measurement modes (Haberlah et al. 2011). Each analysis point or pixel records an X-ray that is used to determine mineralogy from the chemical elemental data, compared against a database that is customised to characterise a sample type. Advantages and limitations of the technique are discussed in Chapter 2.5.5 and Rollinson et al. 2011. These include the rapid and automated mapping of samples on a micron scale to provide superior data of many samples types, but is limited to a 3% approx. elemental detection limit per analysis point due to the rapid speed it operates at and it still has the usual SEM-EDS limitations.

For this study, Particle Mineralogical Analysis (PMA) mode was conducted at a resolution of 2 microns, mapping approx. 4000 particles from each polished block that contained the ash samples, and this analysis was manually checked by comparison with a 1 micron resolution fieldscan map that contained approx. 300 particles for each ash sample. Particle morphologies were thus mapped at 1 micron resolution. Eleven minerals/phases were assigned according to criteria detailed in Table 5.1. Manual checks, including addition of electron probe microanalysis (EPMA) measurements of groundmass glass to the phase database, were conducted to assist accurate phase assignment. Mineral/phase assignment criteria agree well with the componentry found in other studies (Rose 1972; Scott et al. 2013), however some phases remain unclear, such as 'Glass 2 (Al,Si,O phase)' and 'Fe Al silicates' and 'Others'. Although a future study may further illuminate these phases, here we exclude them from interpretation as they altogether comprise <2% of the total mineralogy. We produced one particle-size sorted PMA image for each technique to create two images per ash sample. The images comprised 621 and 2141 ash particles for sample 13N, and 408 and 628 particles for sample 28N, at 1 μm and 2 μm resolution respectively. Additionally, unpolished stubs, each containing 11554 to 13340 ash particles were prepared for QEMSCAN PMA analysis at a 2 μm resolution. This latter analysis was used to

measure the size distribution of particles and phases. Each image was output as a 12 color, 8-bit tiff file at an identical resolution to the corresponding QEMSCAN® analysis, to ensure validity of the image analysis.

The QEMSCAN® PMA images were converted to separate phase maps using color thresholds in Adobe Photoshop and maintaining the same color scheme as the original PMA images. In order to analyze per-particle phase distribution we created region-of-interest (ROI) masks in ImageJ over each particle before analysis of both total and boundary phase image stacks (created from single slices for each isolated phase (see extended discussion and figures in chapter 2.5.5) These phase maps were converted to binary images in ImageJ. From these binaries, the X-Y co-ordinates of each individual particle were extracted using the Jazy XY export macro for ImageJ and smoothed at 0.25 pixels using the Scasmo Fortran script to remove pixelation stepping that occurs in binary images. Shape analysis was then carried out with the iShapes Fortran script which produced multiple particle dimensions and shape factor descriptors for each particle. These tools are available from the University of Basel (https://earth.unibas.ch/micro) and development of the software and image analysis techniques used here are described in detail in Heilbronner and Barrett (2014). In addition we produced separate phase maps for intra-particle crystals (i.e. those entirely within the crystal boundary) and whole-particle crystals in order to compare size and shape distributions between intact (intra particle) and modified (whole particle) minerals for each sample. For all analyses, particles smaller than 10 μm^2 for 1 μm PMA scans and 20 μm^2 for 2 μm PMA scans were removed before analysis, in order to mitigate pixel resolution distortions. Analysis of phases was conducted in ImageJ, in particular using overlay masks and the ColorCounter plugin, on both separate and composite color phase maps.

5.3. Results

5.3.1. Petrographic description of volcanic ash

Volcanic ash erupted at Santiaguito is made up of phenocrysts of plagioclase, amphibole, titanomagnetite and pyroxene in a groundmass of rhyolitic glass hosting plagioclase and minor mafic microlites (see also Scott et al. 2013). Backscatter electron images taken on a scanning electron microscope (SEM) show a range of petrological textures. Qualitatively, most particles appear dense, blocky and angular with low aspect ratio and no evidence for smooth concave

margins, which would indicate the pre-fragmentation presence of large vesicles (see Figure 5.3a). Vesicles are rare and are generally small (<30 μm) and rounded (Figure 5.3b), and not necessarily distributed along particle boundaries, as is the case for the ash generated during Strombolian or Plinian explosive eruptions (e.g. Lautze and Houghton 2007). The ash textires, sizes and shapes appear similar under SEM for both samples (Figure 5.3c): groundmass is glassy and hosts tabular microlites, 5-10 μm in length, although large phenocrysts are common, and ash particles may be monocrystalline. Phenocrysts of amphibole (Figure 3d) commonly show recrystallised rims (Scott et al. 2013), suggestive of disequilibrium conditions (e.g. De Angelis et al. 2015). The mineralogical assemblages of both ash samples, generated by a Vulcanian event and by a dome collapse event, show qualitative similarities. In **Section 5.3.5**, we quantify the distribution of phases using QEMSCAN® analysis

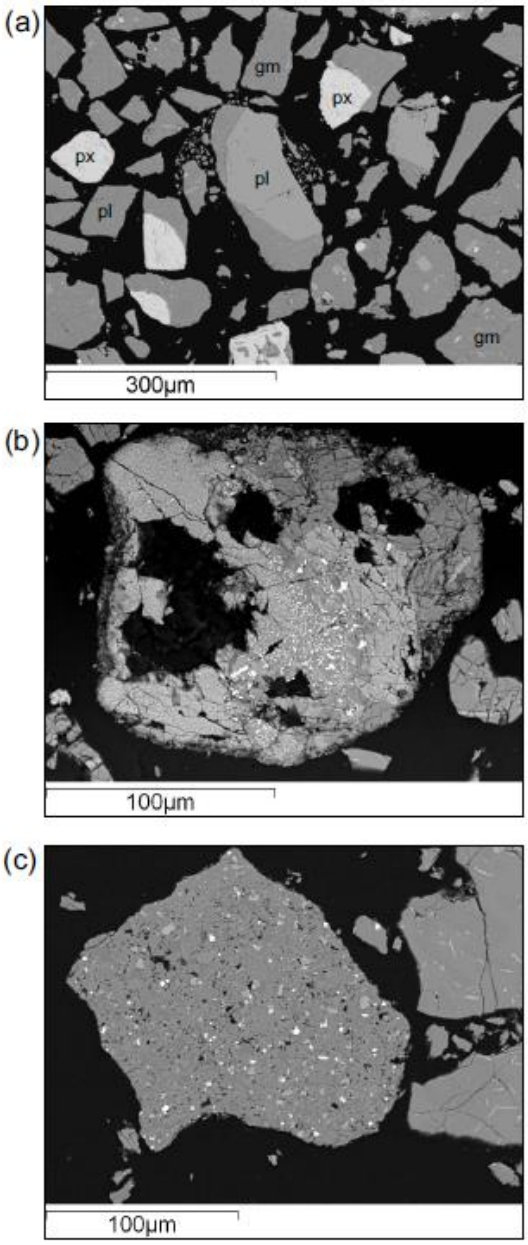

Figure 3. *(a) Typical ash particles from sample VE, generated by Vulcanian activity at Santiaguito, shown as photomicrographs. Note the blocky, dense particle shapes and the lack of vesicles. pl=plagioclase, px=pyroxene, gm=groundmass (glass and microlites). To the far left are examples of single-phase (pl or px) dominated particles; (b) A single ash particle bearing textural evidence for low pressure/high temperature breakdown rims on amphibole phenocrysts* (De Angelis et al. 2015) *This is the most common disequilibrium texture found in the Santiaguito ash samples; (c) Less commonly, ash particles contain textural evidence for repeated fragmentation and healing (or sintering); this example is from sample VE.*

5.3.2 Grain size analysis

Coulter laser grain size granulometry results reveal an asymmetric GSD for both ash samples (Figure 5.4a). The ash from the Vulcanian event (VE) has a minimum grain size of ~0.4 μm, a mode of 30 μm, and a maximum grain size of 800 μm; the ash from the dome collapse event (DC) exhibits the same minimum grain size, but a mode of 50 μm and a maximum grain size of 150 μm. Closer examination reveals that the DC sample is relatively enriched in the finest grain sizes (<5 μm) and depleted in grain sizes >100 μm. The GSD curve for sample DC decreases smoothly from the modal peak whereas the curve for VE appears relatively convoluted at grain sizes >150 μm. Both samples show a similar flattened tail at the finest sizes, showing enrichment of fine ash particles. The DECOLOG GSD deconvolution results are replotted as the probability density function against grain size for the observed curve, subpopulations and stacked curves (Figure 5.4b-c and Table 1). Sample DC shows a dominant subpopulation comprising ~94% of the modelled curve, and a subpopulation focused in the sub-5 μm range which is absent from sample VE. In contrast, sample VE shows a more complex GSD curve, described by a large subpopulation (68%) with lesser subpopulations describing main portion of the curve (20-200 μm). The stacked subpopulation curve traces the observed GSDs well, with two exceptions. For sample VE the fit does not describe fluctuations at coarsest grain sizes (>150 μm), whereas the fit for sample DC does not fully capture the observed distribution at the finest grain sizes (<5 μm). The fractal dimension of the GSD (in a frequency-grain size domain) was calculated for the main grain size range of 1-100 μm and showed similar *d*-values (or slopes) of 1.88 and 1.95 for samples VE and DC, respectively (Figure 5.5).

5.3.3. Particle shape analysis

The shape of individual particles can be described by the defect area (ΔA) and excess perimeter (ΔP) from a convex hull containing the particle of interest (Figure 5.6). This method combines several shape descriptors, and is less prone to assumptions in shape description than many others shape factors (Heilbronner and Barrett 2014). The parameters ΔA and ΔP are identified in the inset in Figure 5.6b and described in further detail in Heilbronner and Barrett (2014) and Liu et al. (2015). Both samples show increasing ΔA and ΔP with increasing grain size (Figure 5.6) and values clustered below 30% for ΔA and 15% for ΔP for each ash sample, indicating relatively simple, dense particle shapes. Sample DC shows smaller increases in both parameters with increasing particle area than sample VE, indicating increasingly simple, rounder particle shapes at coarse grain sizes.

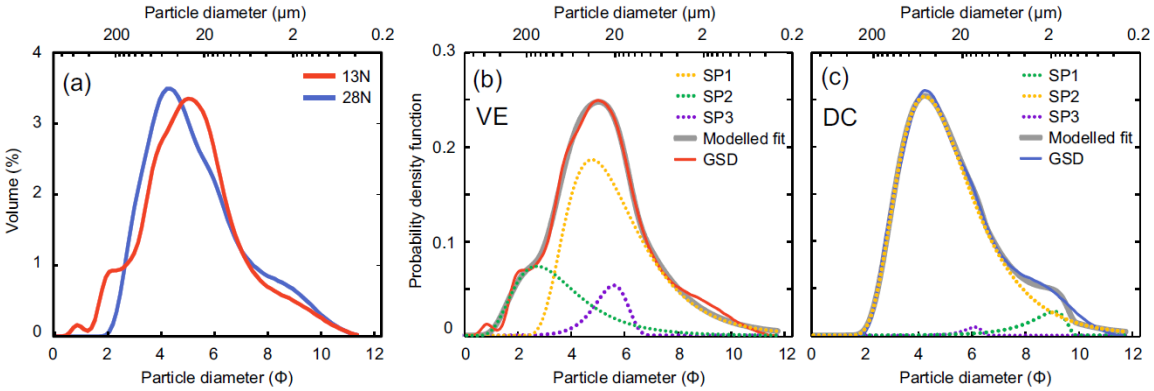

Figure 5.4. *(a) Results of Coulter laser diffraction grain size distribution measurements, showing an increased proportion of fine grain sizes (<10 μm) in sample DC (blue line) and a more complex distribution at grain sizes >100 μm for sample VE (red line); (b-c) Deconvolution of the GSD curves (solid purple lines) into three weighted log-normal subpopulations (sp1-sp3) using DECOLOG software and plotted as the probability density function (PDF) against grain size for sample VE (b) and sample DC (c). Stacked subpopulations are shown as a thick grey line. Subpopulations sp1, sp2 and sp3 are shown as colored dotted lines (see key for details) and their relative weighting is shown in Table 1, allowing interpretation of disruption and transport events on the total grain size distribution* (Wohletz et al. 1989).

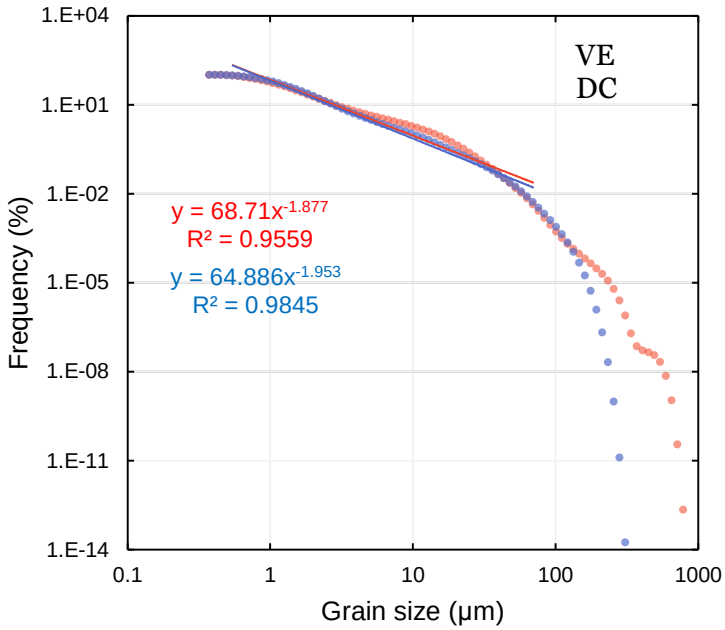

Figure 5.5: *Converting volume % to frequency % (assuming spherical grains) for sample VE and DC (red and blue dots respectively) allows the fractal dimension, or D-value, of the grain size distribution to be calculated (the negative exponent of the linear fit). The analysed portion, chosen due to increasingly non-linear fit for coarse and fine grain sizes, is shown as red and blue lines and spans less than 3 orders of magnitude, therefore the GSD does not show a strong fractal distribution, and the calculated D-values are very similar (see* ***Table 1****).*

***Table 5.2**: GSD properties for both Coulter particle analyser and DECOLOG deconvolution results.*

	VE		DC	
	Coulter GSD	Decoplot	Coulter GSD	Decoplot
Mean	5.18	5.23	5.30	5.33
Median (Md_Φ)	5.05	5.06	4.95	4.95
Sorting (δ)	1.83	1.96	1.81	1.92
Skewness	0.46	-0.02	0.77	0.06
Kurtosis	3.24	3.07	3.01	2.99
sp1 weighting (%)	-	67.80	-	94.50
sp2 weighting (%)	-	23.80	-	4.70
sp3 weighting (%)	-	8.40	-	0.80
Fractal dimension (d-value)	1.877	-	1.953	-

All results are given in units of *phi* ($\Phi = -\log_2 D$) where D = particle diameter in mm.

Observed values from resampled Coulter particle analysis results by geometric method of moments (MonteCarlo Method) using DECOLOG 5.1 software.

Statistics for subcomponents (sp1-sp3) calculated using DECOLOG 5.1 (Borselli and Sarocchi 2015)

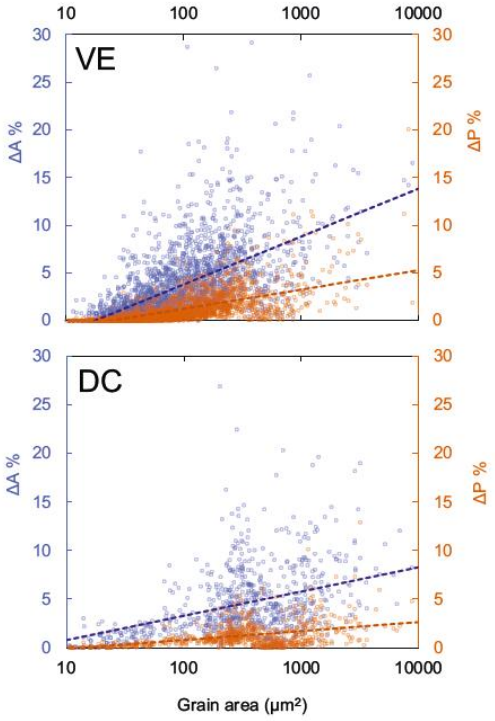

***Figure 5.6:** The variation in defect area (ΔA) and excess perimeter (ΔP) with grain size for every particle within the image analysis for (a) ash sample VE and (b) ash sample DC. ΔA and ΔP are visually described in the inset in part (b) showing a particle shape with perimeter P and area A (top) enclosed by a convex hull shown in green (bottom). The difference in area (ΔA) and perimeter (ΔP) to the convex hull are labelled. The dashed lines show the linear regression for the ΔA (blue) and ΔP (orange) data respectively.*

5.3.5. Textural contributions to size and shape

We produced one particle-size sorted PMA image for each technique and analyzed 3 QEMSCAN® output images per ash sample – PMA analysis on polished blocks at 1 μm and 2 μm and on sprinkle mount stubs at 1 μm step size. The images analyzed for sample VE comprised 459 and 1723 ash particles for 1 and 2 μm resolution polished blocks (Figure 5.7 and 5.8) and 3345 particles from the sprinkle mount stub (Figure 5.9), giving 5527 particles in total. For sample DC we analyzed 406 and 1053 particles for polished blocks at 1 μm and 2 μm resolution (Figure 10 and 11, respectively), and 1514 particles from the sprinkle mount stub (Figure 12), producing a total sample size of 2973 ash particles. Each image was output as a 12 color, 8-bit tiff file at an identical resolution to the corresponding QEMSCAN® analysis..

An example QEMSCAN® image output is shown in Figure 5.13a. Eight phases (plus a few unrecognised and labelled as "others") were assigned during the automated PMA procedure according to criteria summarized in Table 5.1. Stacked phase maps (Figure 5.13b) and boundary phase maps (Figure 5.13d) were created for three QEMSCAN® images each from the VE and DC ash samples, using ImageJ to analyze the phase distribution of the ash particles (see Chapter 2.5.5). The fraction of each phase in the ash particles as well as the relative abundance of each phase at particle boundaries has been quantified for both ash samples (Figure 5.13). The fractions of plagioclase and glass vary considerably between samples, with particles generated by dome collapse (DC) containing 3.8% less glass and 1.5% more plagioclase; this sample DC further shows 4.6% more glass and 3% less plagioclase at the particle boundaries than the Vulcanian ash sample VE. The distribution of phases within a sample is shown by presenting the difference between the overall area fraction and the boundary fraction for each phase (Figure 5.14), where positive values indicate a preferential distribution at particle boundaries, and vice versa. The greatest variations in distribution are found in sample DC, which has a 5% decrease in plagioclase feldspar and 5% increase in glass at the particle boundaries compared to the total abundance. Sample VE shows <1% variation in the distribution of these phases, and all other phases show relatively modest variations in both samples. We constrain the size-dependence of these phase variations at particle boundaries by measuring the phase fraction and boundary phase fraction for each particle analyzed in the study. The results are arranged into 24 bins of increasing particle area, and the average phase abundance within each bin is plotted against the median particle area within the bin (Figure 5.14). From this analysis it is clear that variations in total abundance and boundary abundance of phases are closely linked, and that phase distributions are size-dependent for both samples. Most phases show relatively minor size

dependence; the main differences between each ash sample are in the fraction and distribution of glass and plagioclase (Figure 10). The Vulcanian ash sample VE shows relatively constant plagioclase and glass fractions as a function of particle size; the largest variations appear linked with grain sizes larger than 2000 μm^2, owing to few particles present in this size range as seen in the GSD inset (Figure 10a, c). For the dominant grain sizes, we observe negligible differences in the distribution of these phases in the particles or at the particles' margin. In contrast the dome collapse ash sample DC has an increasing fraction of plagioclase and a decreasing fraction of glass with grain size increase (Figure 10b-d). The latter is especially noticeable below 100 μm^2 where we see the predominance of glass in ash particles.

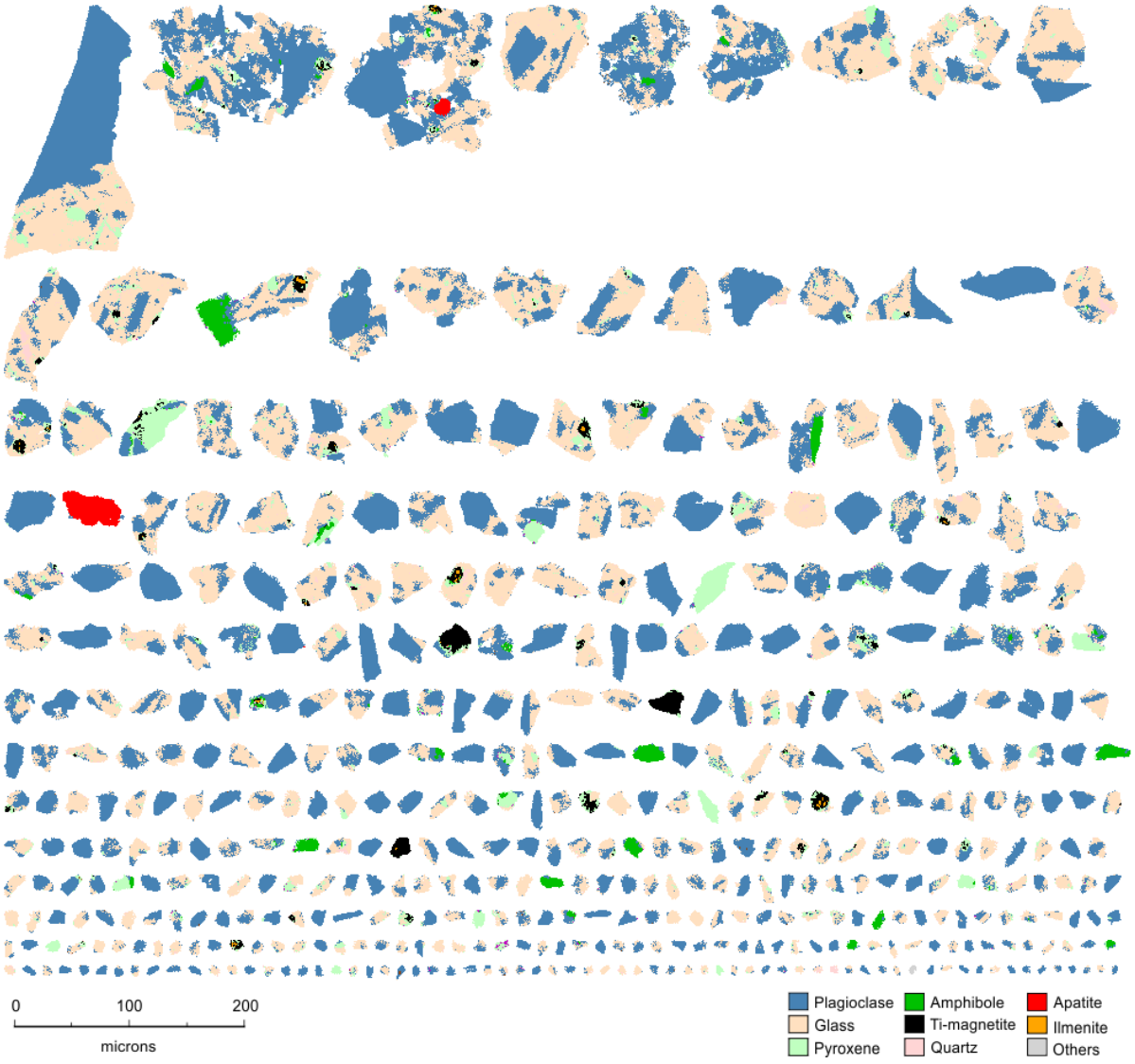

Figure 5.7. *QEMSCAN® PMA image output for sample VE (polished section) at 1 μm resolution (1 pixel = 1 μm^2). T Any colors not included in the key represent minor phases (altogether comprising <2% total phase area) and are included in 'Others' in all analyses.*

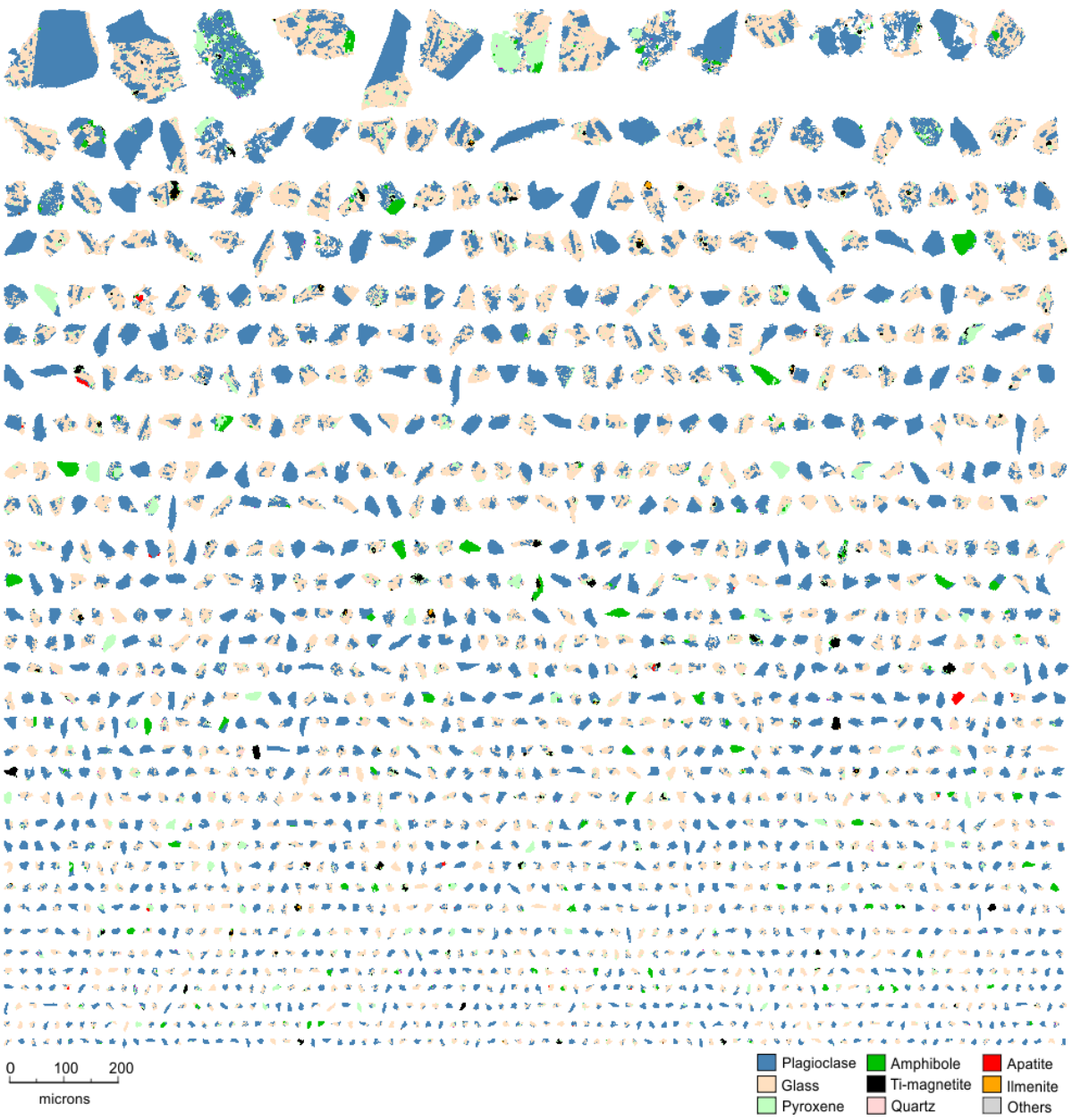

Figure 5.8. *QEMSCAN® PMA image output for sample VE (polished section) at 2 µm resolution (1 pixel = 4 µm^2). Any colors not included in the key represent minor phases (altogether comprising <2% total phase area) and are included in 'Others' in all analyses.*

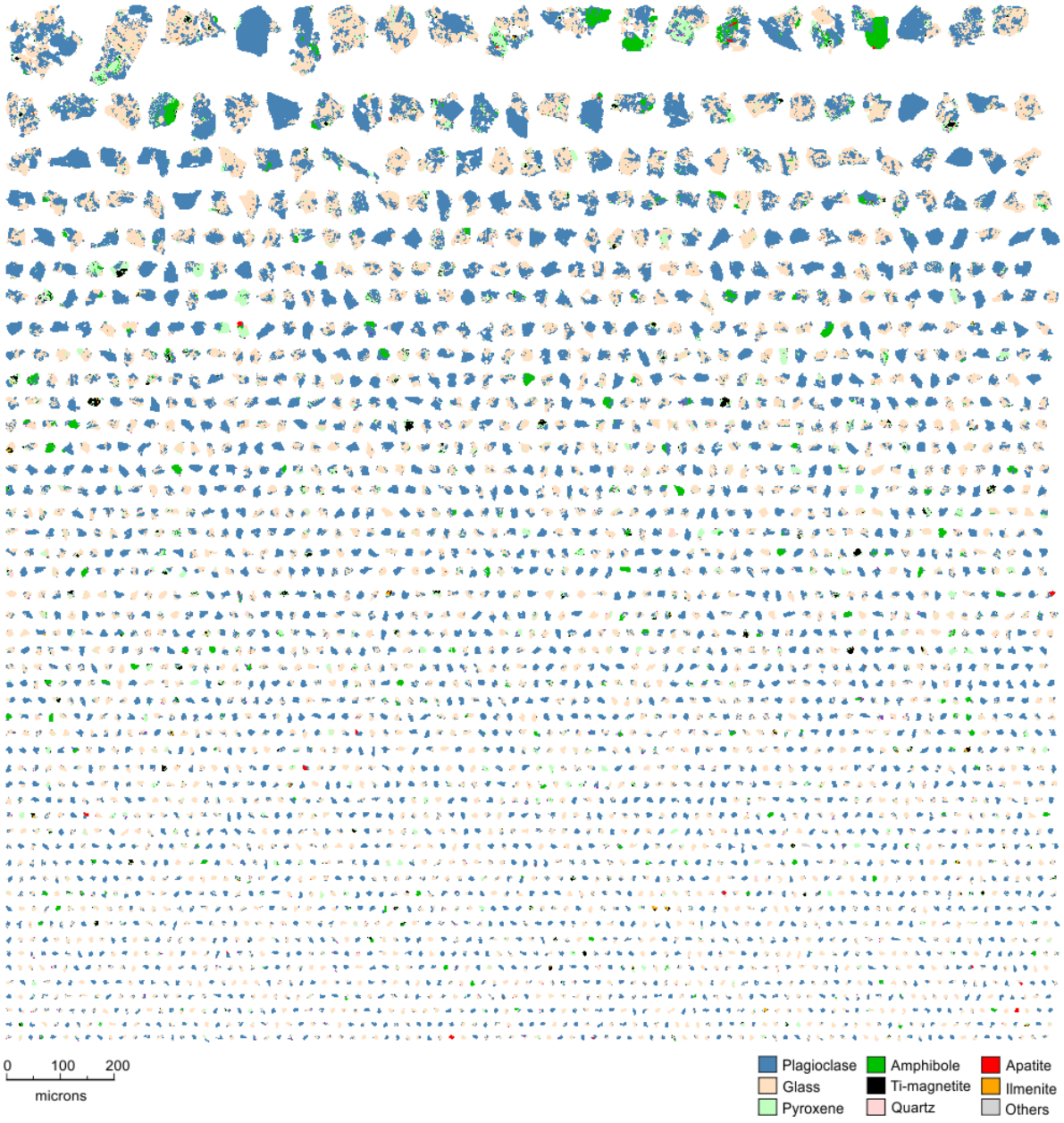

Figure 5.9. *QEMSCAN® PMA image output for sample VE (unpolished stub) at 2 µm resolution (1 pixel = 4 µm^2). Any colors not included in the key represent minor phases (altogether comprising <2% total phase area) and are included in 'Others' in all analyses.*

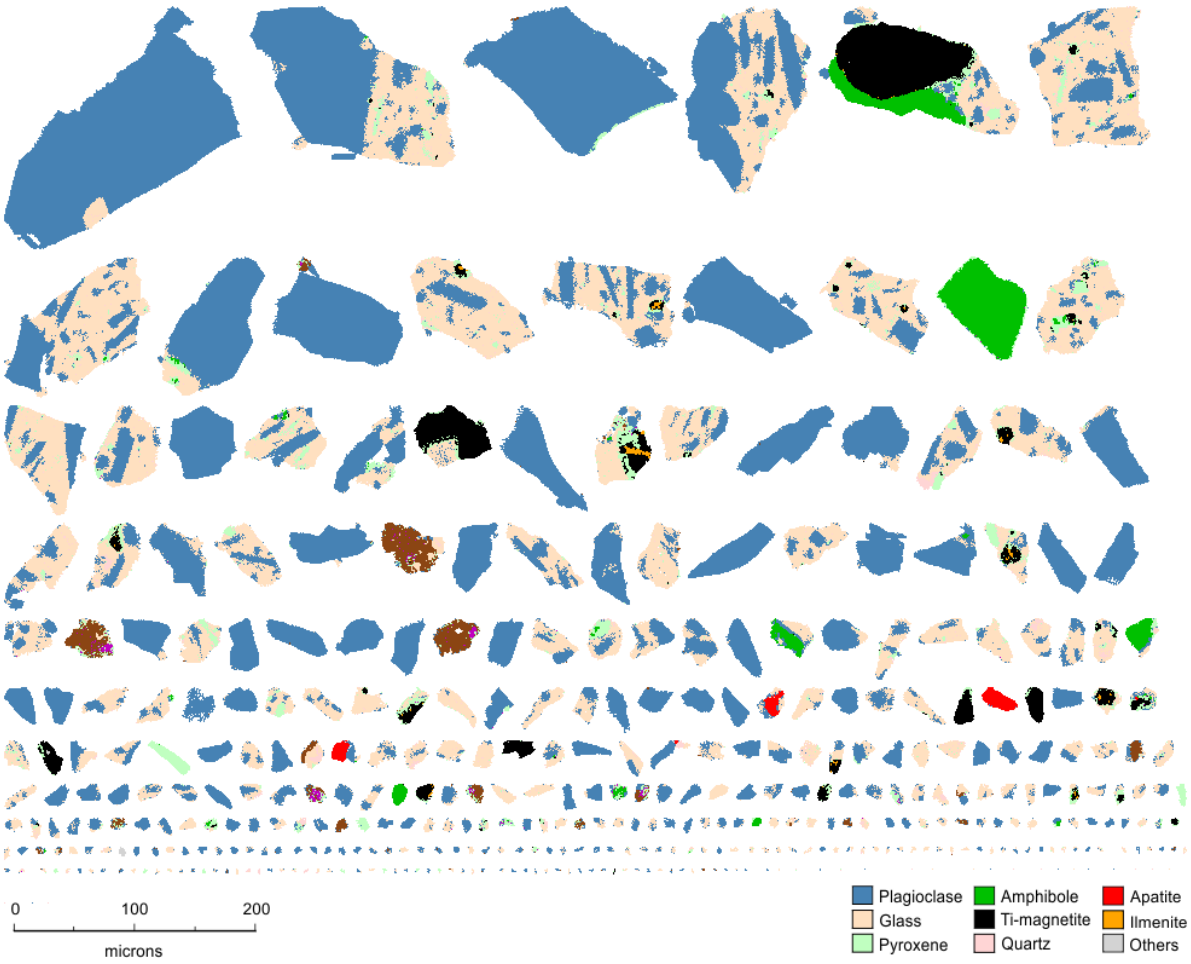

Figure 5.10. *QEMSCAN® PMA image output for sample DC (polished section) at 1 μm resolution (1 pixel = 1 μm^2). Any colors not included in the key represent minor phases (altogether comprising <2% total phase area) and are included in 'Others' in all analyses.*

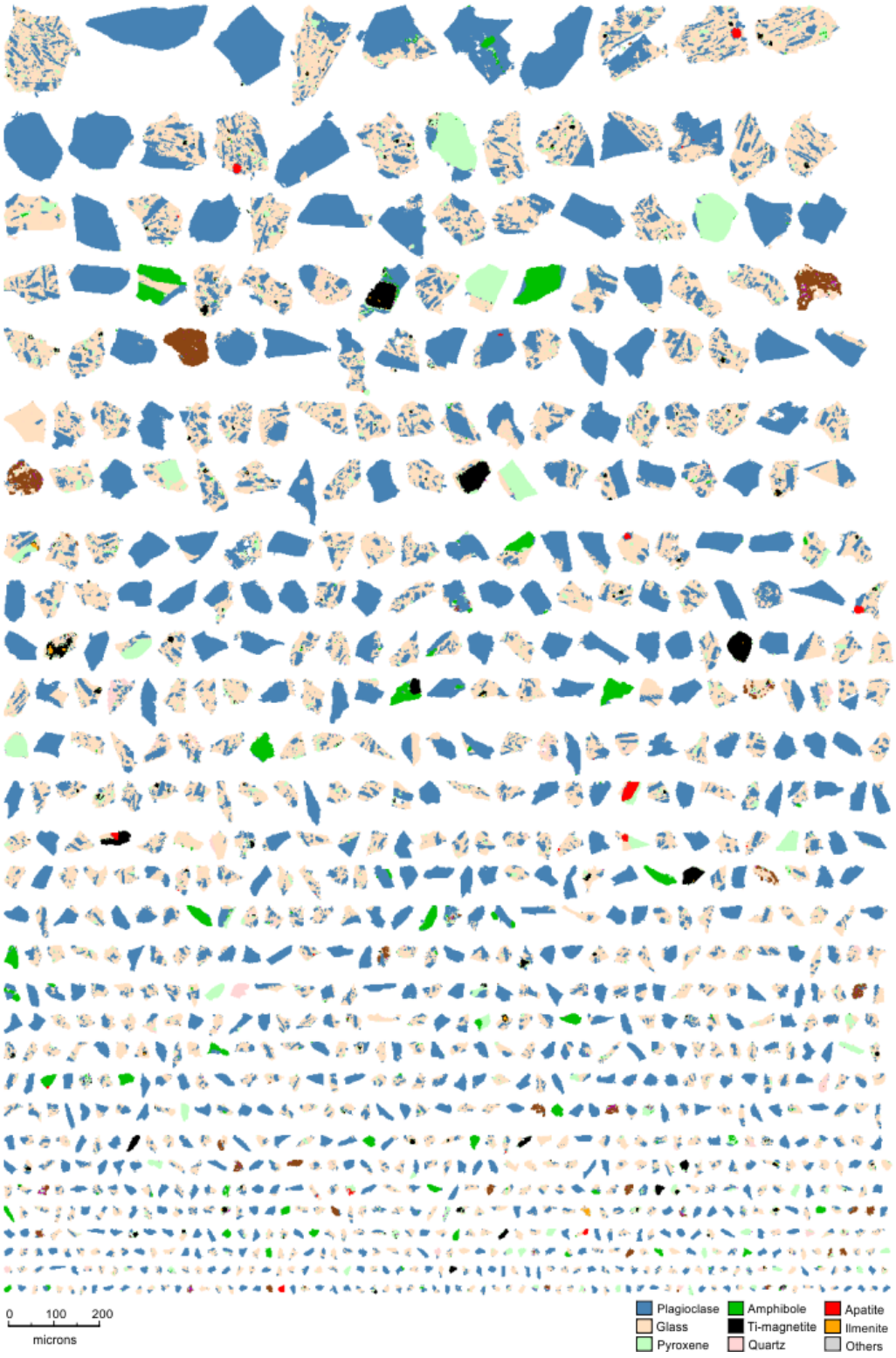

Figure 5.11. *QEMSCAN® PMA image output for sample DC (polished section) at 2 µm resolution (1 pixel = 4 µm^2). Any colors not included in the key represent minor phases (altogether comprising <2% total phase area) and are included in 'Others' in all analyses.*

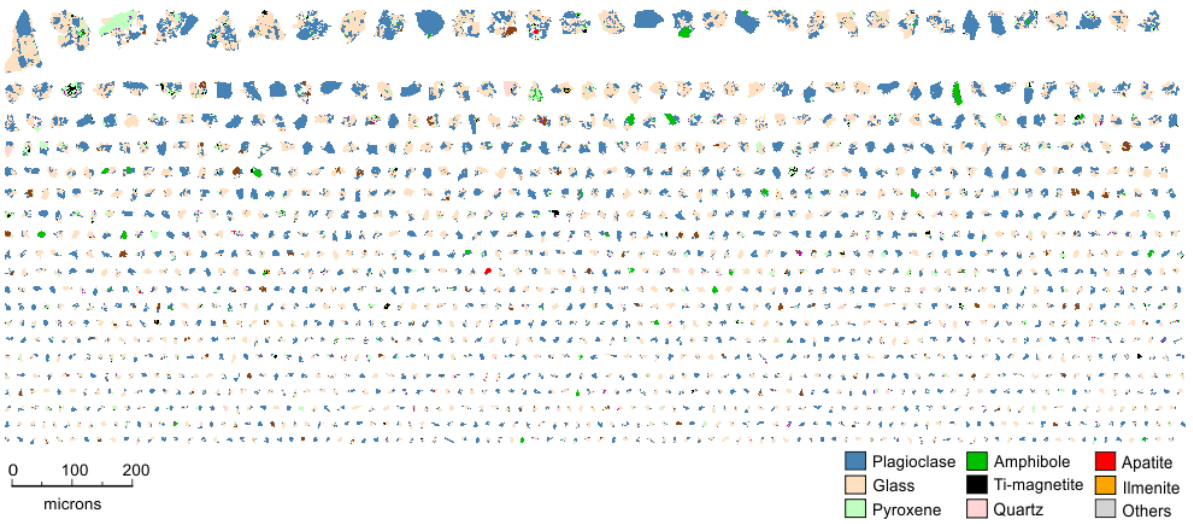

Figure 5.12. *QEMSCAN® PMA image output for sample DC (unpolished stub) at 2 µm resolution (1 pixel = 4 µm^2). Any colors not included in the key represent minor phases (altogether comprising <2% total phase area) and are included in 'Others' in all analyses.*

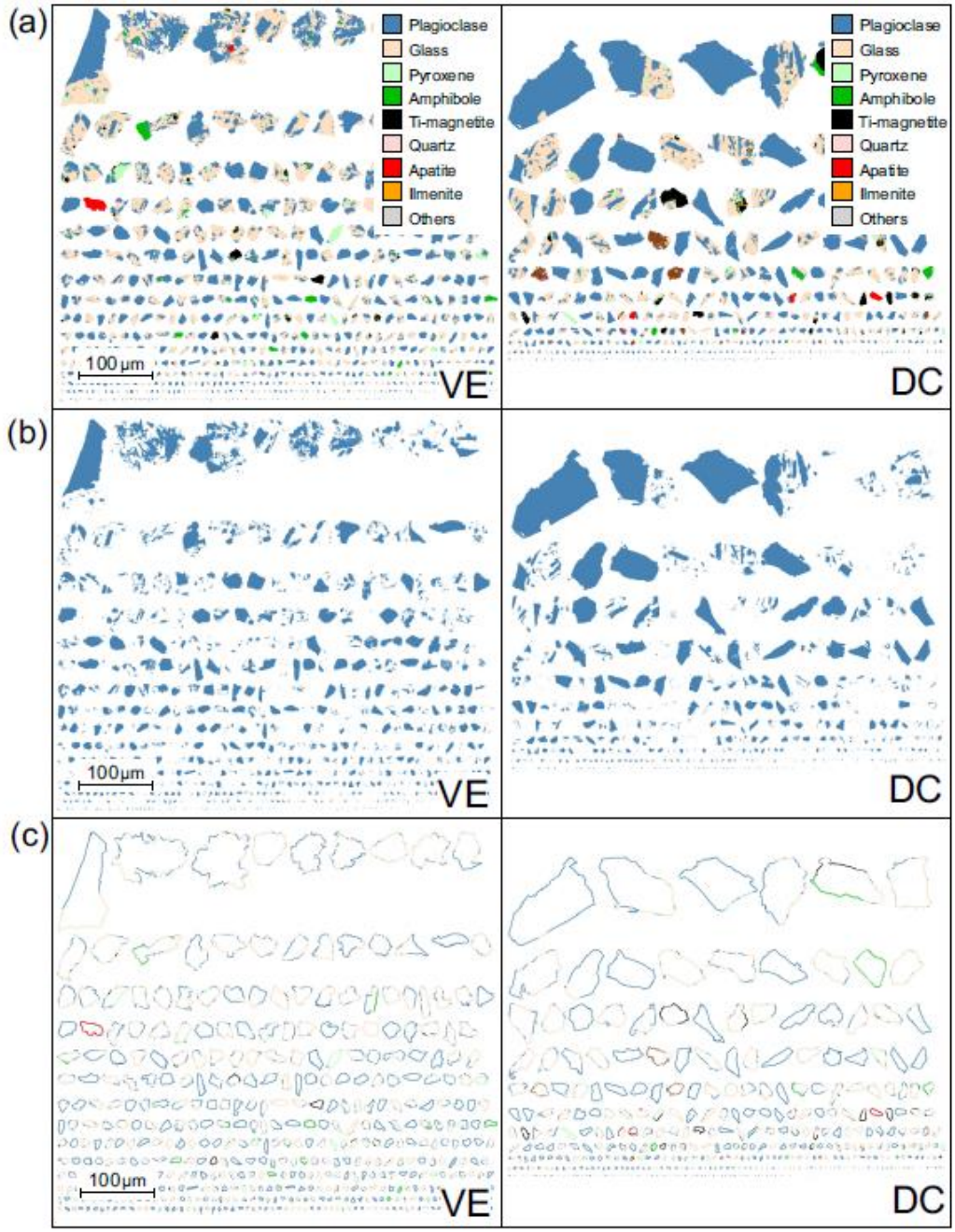

Figure 5.13: *QEMSCAN particle mineralogical analysis (PMA) images used in image analysis for sample VE (left column) and DC (right column); (a) Unaltered QEMSCAN® PMA images showing phase distribution within ash particles at 1 µm resolution; Particles are sorted by size. The key shows the mineral or phase species identified during QEMSCAN® analysis, details shown in Table 1; (b) Single-phase images (see methods) isolating plagioclase feldspar within the particle population in each image. (c) Ash particle boundaries, with 2-pixel thickness, skeletonised using ImageJ. All phase colors in panels (b) and (c) are the same as shown in the key in part (a).*

Phase	VE Area (%)	VE Boundary (%)	DC Area (%)	DC Boundary (%)
Plagioclase	51.23	50.63	52.84	47.67
Glass	38.55	38.06	34.73	39.31
Pyroxene	5.44	6.15	4.67	5.64
Amphibole	2.07	2.08	2.35	2.01
Ti-magnetite	1.07	1.00	2.36	1.34
Quartz	0.97	1.28	1.19	1.74
Apatite	0.27	0.20	0.23	0.22
Ilmenite	0.06	0.05	0.08	0.06
Others	0.33	0.56	1.56	2.02

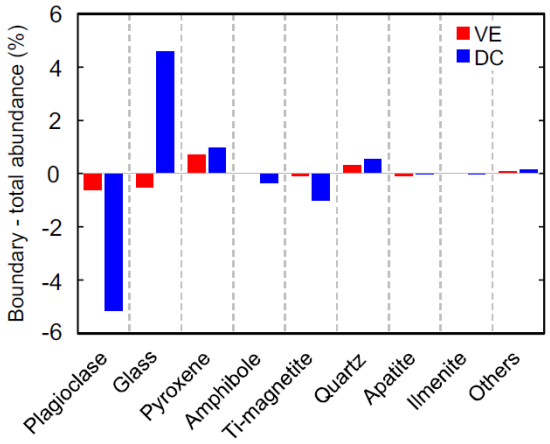

Figure 5.14: *The table shows phase area as a percentage of the total area of particles, and the particle boundary phase fraction (%) for all particles in ash samples VE and DC.The percentage total change in phase abundance at the cross-sectional particle boundaries to the bulk sample for the five most abundant phases is shown in a bar chart for sample VE (red bars) and sample DC (blue bars). Sample DC shows a depletion of plagioclase and enrichment of glass at the particle boundaries compared to sample VE.*

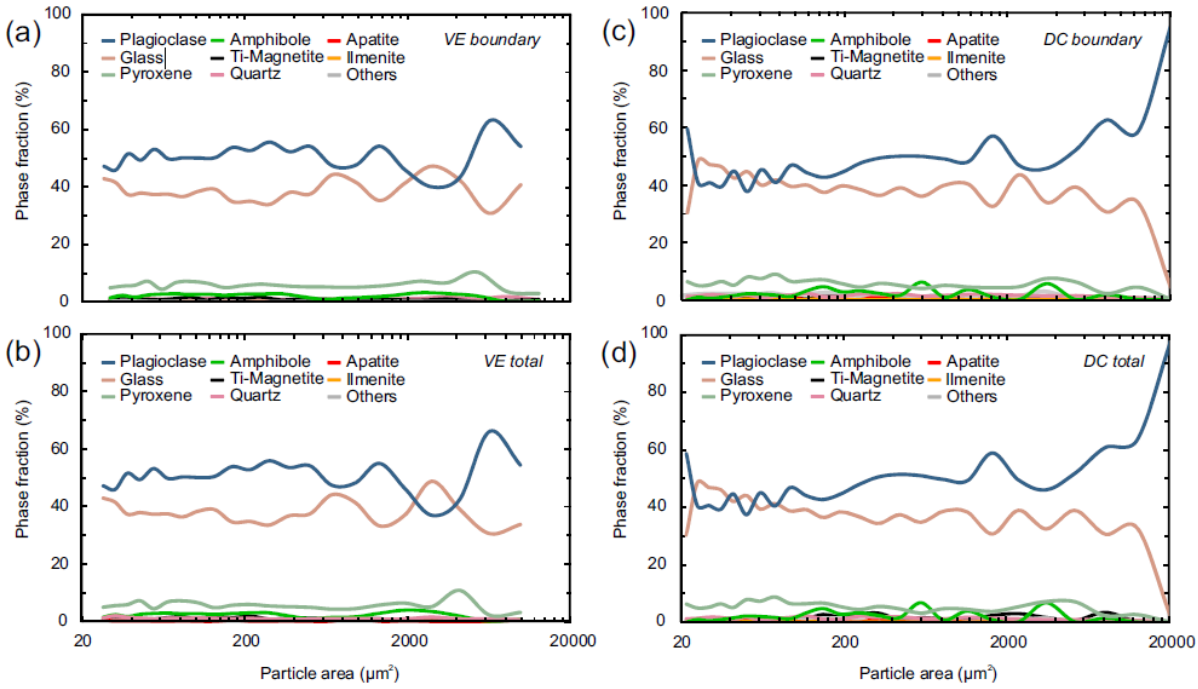

Figure 5.15. *(a) Solid colored lines show the percentage abundance of phases at particle boundaries (labelled boundary) for all particles within discreet grain size bins from 25-20000 μm² for sample VE (a); The phase abundance within whole particles (labelled total) within the same grain size bins is shown for sample VE (B); The same data is shown for sample DC in parts (c) and (d) for boundary and total phase abundance,*

respectively. The trends in abundance with varying grain size are very similar between whole particles and particle boundaries (e.g. between a vs b and c vs d).

We observed marked differences in the distribution of plagioclase and glass phases; glass is preferentially distributed (at the expense of plagioclase) along the boundary within the primary grain sizes between 200 and 4000 μm^2. The QEMSCAN® analysis presented here helps provide an unprecedented quantification of eruptive products, potentially shedding light on the dominant pre-, syn- and post-eruptive processes.

5.4. Interpretation

5.4.1. Fragmentation processes

The piston-like dynamics of the dome at Santiaguito, together with continuous extrusion, suggest that magmatic fragmentation as well as faulting and cataclasis (abrasion along faults) contribute to the generation of volcanic ash at Santiaguito. The products of the Vulcanian

explosion (VE) shows a complex GSD suggesting that recycling of previously fragmented and cataclastic ash occurred during the main magmatic fragmentation event. However the ash sample analyzed was not dominated by cataclasis, as concluded for the 2004-2008 eruption of Mount St. Helens (Rowe et al. 2008), because cataclasis in fault gouge would likely show higher values of rounding than those measured. The combined contribution of magmatic fragmentation and cataclasis is in agreement with the recent suggestion that sacrificial fragmentation, due to thermal vesiculation along active shallow faults, controls the localised development of gas-and-ash explosions, which stabilises the longevity of the dome structure (Lavallée et al., 2015). The products of the dome collapse event (DC) exhibit greater sorting and narrowness of a mostly unimodal GSD (Figure 6d), representing a simple fragmentation and transport history, in

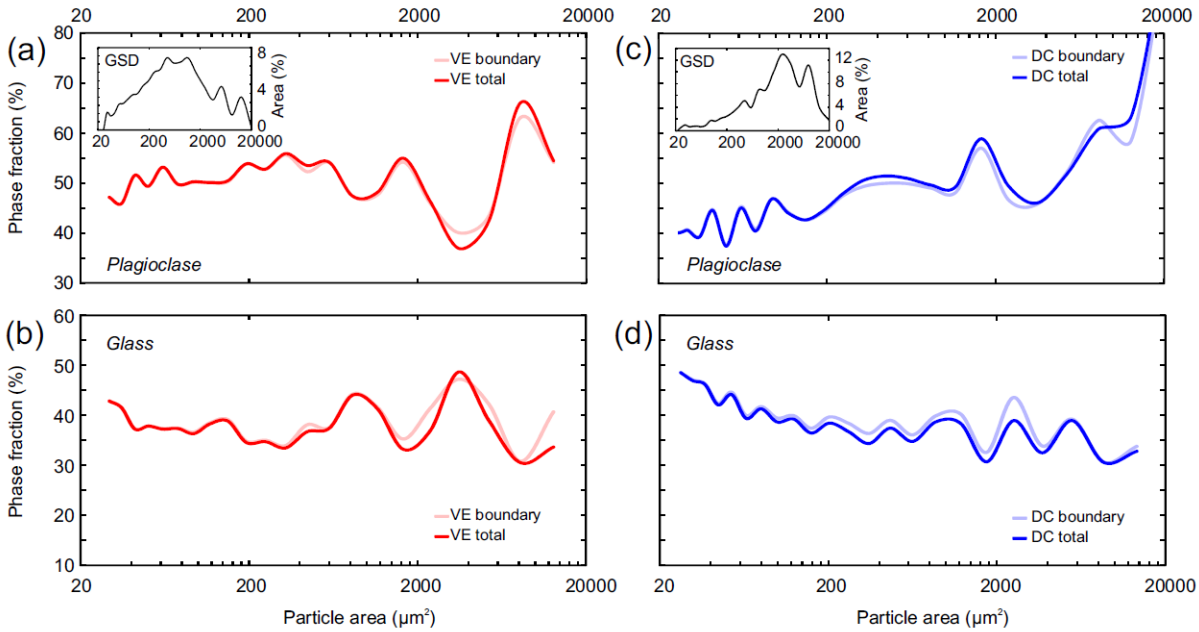

Figure 5.16*. The change in total and boundary abundance of plagioclase feldspar (**A** and **C**) and glass (right-hand panels **B** and **D**) are shown with increasing particle area. The total phase abundance, as a percentage for each particle is shown as a dark solid line, while the boundary fraction for each phase is shown as a lighter line, for sample VE (red colours and DC (blue colours). The grain size distribution of the particle used in this analysis are shown as insets in panel **A** and **C** for sample VE and DC respectively.*

agreement with formation and modification by a limited set of processes. Particle shapes shows smaller increases in ΔA and ΔP with coarsening particle size for sample DC, indicating greater rounding, characteristic of particle interactions [e.g. *Dufek et al.*, 2012] and milling [e.g. *Campbell et al.*, 2013] during transport, whether in pyroclastic flows [e.g. *Caballero et al.*, 2012] or through factures. Deconvolution of the GSD curves produce a significant subpopulation with mode ~2 μm diameter particles in sample DC, which again, is consistent with milling and abrasion during transport (Wohletz et al. 1989; Dufek and Manga 2008; Evans et al. 2009). This process has been well documented for large ignimbrite-forming events (Walker 1972; Sigurdsson and Carey 1989; Scarpati et al. 2014) however, in dome-collapse events a study of ash during the 1991 Mt. Unzen eruption has shown that low-volume PDCs undergo less segregation of fines into ash plumes (Watanabe et al. 1999); instead they used the importance of conchoidal fractures in poorly vesicular fragments to invoke a thermal stressing origin. Altogether the volcanic ash of the dome-collapse event appears to result from a smaller set of fragmentation mechanisms than

those of the Vulcanian event. We must therefore seek other characteristics to pursue the investigation of fragmentation processes at Santiaguito.

5.4.2. Mineralogical controls on volcanic ash fragmentation

Imaging of the mineralogy distribution within the volcanic ash particles developed during each eruption style provides one of the most striking constraints on the fragmentation processes. Plagioclase feldspar and glass are the most abundant phases (Figure 5.8) and their abundances are generally inversely proportional to each other (Figure 5.8), revealing an invaluable proxy for the relative time of residency at high temperature to allow crystallization of the interstitial melt (Cashman and Blundy 2000). The GSD and mineralogy support observations (in **Section 5.2.2**) that the Vulcanian event originated from the conduit, whilst the dome collapse triggered fragmentation of surficial material. The ash produced by the Vulcanian eruption contains more glass and no preferential phase distribution along the boundary, irrespective of grain size (Figure 5.9), suggesting that the fragmentation processes at work do not generate any differentiation. In contrast, the ash released by the dome collapse is more crystalline (Figure 8), indicative of long residency at high temperature during magma ascent, eruption and flow down the flanks of Caliente. Quantitative observations that the fines are more glass rich and that plagioclase is preferentially abundant in the coarse particles suggest that fragmentation mechanisms and/or transport induced a certain degree of material differentiation. This hypothesis is supported by the comparison between the distribution of glass and plagioclase in the ash and at the particle boundary (Figure 5.9). For the dominant grain sizes (200-3000 μm^2) present in the dome-related ash sample, we find a slight enrichment in the abundance of glass at the particle boundary. It has been previously noted that the fine fraction of co-ignimbrite ash may be enriched in glass due to milling, abrasion and segregation (Sparks and Walker 1977; Baxter et al. 1999; Bonadonna et al. 2002). Indeed, Freundt and Schmincke (1992) proposed that surficial fractures during milling preferentially abrade glass around crystals, leaving a glassy margin.

The influence of mineralogical assemblage on fragmentation processes eludes us; yet, it has long been known that minerals have different strength and hardness (Smith et al. 2009; Spray 2010). Liquids and glasses are generally stronger than individual crystals or crystalline materials (c.f. Heap et al. 2014a; Vasseur et al. 2015) and fragmentation generally produces complex conchoidal fracture sets (Wiederhorn 1974; Dürig and Zimanowski 2012), whereas often crystals break preferentially along crystallographic planes (e.g. Prior et al. 2009). Fracture development

in crystal-bearing magmas is generally controlled by the distribution of phenocrysts as they accumulate stress (Deubelbeiss and Connolly 2011) and break before the interstitial melt (Lavallée et al. 2007; Cordonnier et al. 2009). Here, the observations that Vulcanian explosions of ash (more enriched in interstitial glass than the ash from dome collapse) have less glass and more crystalline phases at particle margins suggest that magmatic fragmentation exploit the crystallographic weakness planes of the mineralogical assemblage, whereas milling, collision and abrasion in pyroclastic density currents preferentially fashions the glass phase (Horwell et al. 2001). Yet, it remains that the dome-collapse event lasted for nearly 6hrs, instead of the short-lived (~30 s) Vulcanian explosions, which may affect the final distribution of mineral phases in the erupted ash products.

5.4.3. Eruptive processes at Santiaguito

Santiaguito volcano is considered to be an open system volcano (Rose et al. 2013) and magma at shallow depth may efficiently outgas and densify via surface tension (Kennedy et al. 2016) or compaction (e.g. Ashwell et al. 2015). Cyclic inflation/deflation over 26±5 minutes indicates a repetitive pressurizing source of similar magnitude (Johnson et al. 2014). The fragmentation depth and mechanism during the Vulcanian explosions at Santiaguito appear to be stable during recent eruptive history .Separate gas- and ash-rich plumes are often observed, where a low volume gas-rich plume appears first and later followed by the ash-rich eruption (note the greater gas-rich plume height in Figure 1a-b). Inasmuch as the explosion are regular and similar in character, the volcanic ash produced suggests that particles previously fragmented by faulting and cataclasis get entrained during the magmatic fragmentation events responsible for the main portion of ash forming the eruptive products. The clearing of fragmental material in fractures present in a dome may be an important process at lava domes. At Santiaguito, it has been argued that the main fragmentation events takes place along active faults, which induce local temperature increase that triggers melting, vesiculation and fragmentation; this sacrificial fragmentation may create space to enhance the dome stability by facilitating further fault motion to accommodate the recurring inflation/deflation cycles (Lavallée et al. 2015a). This may explain the overall dense nature of the volcanic ash collected. As for the dome-collapse event, the GSD suggest a mostly unimodal grain size distribution and as such, we advance that one fragmentation mechanism dominates ash production, with a mild overprint of abrasion during transport.

The results of this study point to overlaps in fragmentation mechanisms between the two samples, possibly due to similarities in ash production processes in relatively dense crystal-rich lavas. Although further work is required to fully interpret our observations, such changes in the componentry at the particle boundaries in sample DC suggest mechanism-based controls on ash-forming fracture locations, which in turn influences the surface mineralogy and chemistry of the resulting ash population. The surface phases and composition of ash grains are of great importance in assessing environmental and respiratory health hazards (Horwell and Baxter 2006), aviation hazards (Song et al. 2016) aerosol scavenging within ash plumes (Ayris et al. 2014) and further investigation into the role of varying fragmentation modes and conditions on ash particle surfaces is strongly encouraged using the analytical method presented here.

5. Conclusions

Volcanic ash produced during a Vulcanian explosion and a dome-collapse event is analyzed using SEM and QEMSCAN® to provide a morphological and mineralogical quantification of the variables controlling fragmentation mechanisms..

The volcanic ash produced during Vulcanian eruptions is blocky and poorly vesicular, and the edges are generally smooth and simple. Deconvolution of grain size distributions and particle shape analysis show that the ash associated with Vulcanian explosive activity (without PDCs) are different in size and shape to those associated with partial dome collapse (with PDCs). The ash produced in the Vulcanian event has a complex grain size distribution that results from magmatic fragmentation along with the entrainment of ash (of different grain sizes) produced by rupture and cataclasis in the upper conduit magma. QEMSCAN® analysis shows that the ash exhibit no preferential distribution of mineral phases or glass inside or along the margins of the particles; yet, the ash is more glass-rich than that formed during dome collapse, perhaps as it originates from within the upper conduit (in contrast to the ash formed from the surficial lava during dome collapse). The ash produced during the dome collapse event shows a higher glass abundance along the particle margin, despite its higher crystallinity (than the ash from Vulcanian activity) suggesting the importance of abrasion during transport, whether through fracture in the lava carapace or in the PDC.

We distinguish the ash produced by a typical gas-and-ash explosion to ash produced by dome collapse through the following properties: 1) A relative depletion in very fine ash (<10 μm diameter), 2) greater increases in defect area (ΔA) and excess perimeter (ΔP) with increasing grain size, 3) A more complex GSD, comprising several important subpopulations and 4) a relative depletion of interstitial glass at particle boundaries for particles <3000 μm^2. We conclude that integrated analysis of ash morphology and mineralogy using QEMSCAN® imaging provides a powerful quantitative tool to describe particle properties, and more work is required in order to match particle characteristics, such as phase distribution, to fragmentation mechanisms, in order to understand and predict the particle characteristics of ash produce during volcanic eruptions.

Chapter Six

Summary and Outlook

6.1. Summary

In this doctoral project, the investigations of three problems, using multidisciplinary methods, have helped to constrain brittle processes at active lava domes. Each investigation has focused on a different brittle process; in **Chapter 3**, incremental and seismogenic faulting of highly viscous magma at Mt Unzen was investigated to constrain the viability of frictional melting as a regulator to fault-bound, spine extrusion dynamics. Seismic analysis of spine extrusion suggests that the extrusion of the spine occurred through numerous slip events, averaging 9 cm displacement at an average rate of 0.75 $m.s^{-1}$; Under such conditions, the experimental investigation has shown that rapid heat input from fault friction can readily produce frictional melt (pseudotachylyte) along the fault zone. Rheological modelling of the pseudotachylyte produced in this manner shows that it would act as a viscous brake on slip, and thus magma ascent, at shallow depths, resulting in pulsatory ascent dynamics. The propensity for dome magmas to produce pseudotachylyte during faulting requires greater appreciation of the implications for fault mechanics and thermomechanical processes within the shallow conduit of silicic volcanoes.

The onset of fault slip may be triggered or preceded by the failure of magma and dome material during gas pressurisation or strain localisation near conduit boundaries. During magma ascent, dome lavas may readily produce tensile or shear fractures, controlling phases of explosive eruption or passive degassing. The timescales of deformation are crucial in determining the deformation mode of silicic magmas, and small fluctuations in deformation rate may initiate rapid changes in eruptive activity. As such a study of the tensile strength of dome magmas (**Chapter 4**) under volcanic temperatures and timescales of (monitored) deformation at Santiaguito was carried out. The findings demonstrate the importance of temperature and strain rate in controlling the proportion of viscous and brittle deformation leading to failure. The lava becomes increasingly brittle with an increase in strain rate, with a decrease in temperature and with a decrease in interstitial melt fraction. At higher temperatures, increased strain rates are required to generate fractures within the same timescale. The findings suggest that tensile fractures may readily form in shallow volcanic conduits and argue that fractures likely propagate upward from a pressurisation source to the dome surface.

Faulting events at Santiaguito may also accompany explosive eruptions. The link between volcanic faulting and explosive activity has been advocated using a combination of textural evidence, experiments and a geophysical monitoring dataset, demonstrating that intense heat

input along conduit fault zones may lead to thermally-induced melting and vesiculation, triggering fragmentation and explosive Vulcanian eruptions (Lavallée et al. 2015b; see **Appendix B**). The ash particles produced by such Vulcanian explosions at Santiaguito have been characterised and compared against the ash produced by partial dome collapse (**Chapter 5**). Grain size analysis and QEMSCAN® imaging has been used to describe the physical and mineralogical properties of the ash, showing that ash particles produced during Vulcanian eruption are dense and display a complex grain size distribution revealing the contribution of multiple fragmentation events; the ash further exhibits an affinity for the presence of plagioclase crystals along the ash boundary, pointing toward the importance of this phase on magmatic fragmentation. In contrast, the ash from dome collapse displays a simple grain size distribution resulting from a single dominant brittle process; the presence of a glass-enriched rind around the ash suggests that modification of ash during transport in pyroclastic density currents (such milling or abrasion) may favour fracture through glass during fragmentation. The study demonstrates the power of QEMSCAN® imaging as a tool to characterise volcanic ash with an unprecedented level of detail, providing a means to constrain mineralogical controls on fragmentation processes.

The prevalence for brittle processes at lava dome volcanoes is expressed by the abundant seismicity produced during unrest as well as by examination of eruptive products (both in the form of ash and in exposed dome structures). Alone, the analysis of geophysical signals has provided invaluable insight into the rates, patterns and nature of brittle processes, but it is through the integration of geophysical monitoring data to experimental simulations as well as petrological, mineralogical, textural, and rheological analyses that the present investigations has significantly contributed to our description of brittle processes at lava domes. I strongly recommend the integration of multidisciplinary methodologies in the study of eruptive processes – this approach has informed my understanding of lava dome eruptions and I hope to continue in this vein during postdoctoral research.

6.2. Outlook

The research conducted in this PhD has opened up several avenues for further investigation. Collaboration with Amy Collinson, numerical modeller at the University of Leeds, will add further constraints to the study of magma fracture in tension with regard to lava dome eruption

dynamics. This study will be submitted for publication once the modelling is complete and integrated with the experimental work. Interdisciplinary research between numerical modelling and experimental rock mechanics allows mutually beneficial constraints on the robustness and application of the research results. I hope to conduct further experimental collaboration with numerical modelling efforts to constrain and shed light on eruptive processes at shallow depth, and further constrain the mechanisms behind transitions between effusive and explosive activity at dome volcanoes.

The investigation into phase distributions within ash particles has provoked further multidisciplinary efforts, and I hope to employ image analysis techniques within my future research efforts. An essential step towards the robust interpretation textural and physical properties of volcanic ash is a calibration with particles produced from differing fragmentation processes under controlled experimental conditions. Ongoing research is taking place at LMU Munich, and current collaboration will help to define the surface characteristics of ash produced under controlled conditions; this work will help to interpret natural ash samples, and assess hazards to the environment, aviation and health due to ash produced during lava dome eruptions. The application of image analysis techniques has proved a powerful and efficient means to characterise complex ash samples.

Recent volcanic ash samples collected from Santiaguito volcano during Workshops on Volcanoes in January 2016 represent a timely research opportunity to interpret a transition in explosive behaviour. Since December 2015 Santiaguito has generated intermittent powerful explosions producing pyroclastic flows and ejecting bombs several kms from the Caliente vent. These explosions have continued into February 2016 and present a dramatically greater hazard in the vicinity of the dome complex. Superficially, four recent ash samples appear significantly coarser and enriched in lithic fragments, possibly providing evidence for conduit-excavating explosions at Santiaguito. Further study of these samples using QEMSCAN®, Coulter particle size measurements and image analysis will help to define changes in conduit processes and eruptive behaviour during this transition. Multidisciplinary monitoring efforts during Workshops on Volcanoes will produce by far the most detailed geophysical characterisation of eruptive activity at Santiaguito; and to my knowledge, of activity any volcano in Central and South America. Continued collaboration with principal scientists from the workshop is likely to produce unparalleled insights into eruptive processes at Santiaguito in the near future.

The recent study on thermal vesiculation of magma at Santiaguito has important implications for eruptive behaviour at dome volcanoes, and may be widely applicable. Further investigation is necessary quantify the magnitude and timescales of magmatic processes following rapid heat generation and faulting. Changes in the mechanical strength of foaming magmas are of vital importance, as well as constraints on thermal diffusivity and conductivity of conduit magma. Analytical and experimental studies, supported by geophysical and textural evidence, are required to describe the effects of thermal vesiculation at dome volcanoes. I hope to engage in further efforts to unravel this important new process, and present forthcoming research into eruptive activity at Santiaguito in the near future.

For the next academic position, I aim to continue engaging in multidisciplinary research, in particular the integration of geophysical datasets with laboratory, experimental and modelling efforts. I am currently preparing an application for a Marie Curie Research Fellowship in order to fund my career development at the LMU Munich. In this regard, the experimental facilities and broad academic network at LMU Munich would be an ideal base for further research and collaboration in the EU and worldwide.

References

Alatorre-Ibargüengoitia MA, Scheu B, Dingwell DB, et al (2010) Energy consumption by magmatic fragmentation and pyroclast ejection during Vulcanian eruptions. Earth Planet Sci Lett 291:60–69. doi: 10.1016/j.epsl.2009.12.051

Albino F, Pinel V, Massol H, Collombet M (2011) Conditions for detection of ground deformation induced by conduit flow and evolution. J Geophys Res Solid Earth 116:1–18. doi: 10.1029/2010JB007871

Alidibirov M, Dingwell DB (2000) Three fragmentation mechanisms for highly viscous magma under rapid decompression. J Volcanol Geotherm Res 100:413–421. doi: 10.1016/S0377-0273(00)00149-9

Alidibirov M, Dingwell DB (1996) Magma fragmentation by rapid decompression. Nature 380:146–148. doi: 10.1038/380146a0

Alidibirov M, Dingwell DB, Stevenson RJ, et al (1997) Physical properties of the 1980 Mount St. Helens cryptodome magma. Bull Volcanol 59:103–111. doi: 10.1007/s004450050178

Almberg LDD, Larsen JFF, Eichelberger JCC, et al (2008) Comparison of eruptive and intrusive samples from Unzen Volcano, Japan: Effects of contrasting pressure–temperature–time paths. J Volcanol Geotherm Res 175:60–70. doi: 10.1016/j.jvolgeores.2008.03.020

Anderson K, Lisowski M, Segall P (2010) Cyclic ground tilt associated with the 2004–2008 eruption of Mount St. Helens. J Geophys Res 115:B11201. doi: 10.1029/2009JB007102

Anderson SW, Fink JH, Rose WI (1995) Mount St. Helens and Santiaguito lava domes: The effect of short-term eruption rate on surface texture and degassing processes. J Volcanol Geotherm Res 69:105–116. doi: 10.1016/0377-0273(95)00022-4

Andrews BJ (2014) Magmatic storage conditions, decompression rate, and incipient caldera collapse of the 1902 eruption of Santa Maria Volcano, Guatemala. J Volcanol Geotherm Res 282:103–114. doi: 10.1016/j.jvolgeores.2014.06.009

Aoyama H, Oshima H (2008) Tilt change recorded by broadband seismometer prior to small phreatic explosion of Meakan-dake volcano, Hokkaido, Japan. Geophys Res Lett 35:1–7. doi: 10.1029/2007GL032988

Arámbula-Mendoza R, Lesage P, Valdés-González C, et al (2011) Seismic activity that accompanied the effusive and explosive eruptions during the 2004–2005 period at Volcán de Colima, Mexico. J Volcanol Geotherm Res 205:30–46. doi: 10.1016/j.jvolgeores.2011.02.009

Arciniega-Ceballos A, Alatorre-Ibargüengoitia M, Scheu B, et al (2014) Seismological analysis of conduit dynamics in fragmentation experiments. J Geophys Res Solid Earth 119:2215–2229. doi: 10.1002/2013JB010646

Ashby MF, Sammis CG (1990) The damage mechanics of brittle solids in compression. Pure Appl Geophys PAGEOPH 133:489–521. doi: 10.1007/BF00878002

Ashwell PA, Kendrick JE, Lavallée Y, et al (2015) Permeability of compacting porous lavas. J

Geophys Res B Solid Earth 120:1605–1622. doi: 10.1002/2014JB011519

Atkinson BK, Meredith PG (1987) The theory of subcritical crack growth with applications to minerals and rocks. In: Fracture mechanics of rock. pp 66–111

Auker MR, Sparks RSJ, Siebert L, et al (2013) A statistical analysis of the global historical volcanic fatalities record. J Appl Volcanol 2:2. doi: 10.1186/2191-5040-2-2

Autin-Erickson A, Büttner R, Dellino P, et al (2008) Phreatomagmatic explosions of rhyolitic magma: Experimental and field evidence. J Geophys Res Solid Earth 113:1–12. doi: 10.1029/2008JB005731

Ayris PM, Delmelle P, Cimarelli C, et al (2014) HCl uptake by volcanic ash in the high temperature eruption plume: Mechanistic insights. Geochim Cosmochim Acta 144:188–201. doi: 10.1016/j.gca.2014.08.028

Balme MR, Rocchi V, Jones C, et al (2004) Fracture toughness measurements on igneous rocks using a high-pressure, high-temperature rock fracture mechanics cell. J Volcanol Geotherm Res 132:159–172. doi: 10.1016/S0377-0273(03)00343-3

Barberi F, Cioni R, Rosi M, et al (1989) Magmatic and phreatomagmatic phases in explosive eruptions of Vesuvius as deduced by grain-size and component analysis of the pyroclastic deposits. J Volcanol Geotherm Res 38:287–307. doi: 10.1016/0377-0273(89)90044-9

Baxter PJ, Bonadonna C, Dupree R, et al (1999) Cristobalite in Volcanic Ash of the Soufrière Hills Volcano, Montserrat, British West Indies. Science (80-) 283:1142–1145. doi: 10.1126/science.283.5405.1142

Bayhurst GK, Wohletz KH, Mason AS (1994) A Method for characterizing Volcanic Ash from the December 15, 1989, Eruption of Redoubt Volcano, Alaska. Volcan Ash Aviat Saf US Geol Surv Bull 2047:13–18.

Bean C, Lokmer I, O'Brien G (2008) Influence of near-surface volcanic structure on long-period seismic signals and on moment tensor inversions: Simulated examples from Mount Etna. J Geophys Res Solid Earth. doi: 10.1029/2007JB005468

Bean CJ, De Barros L, Lokmer I, et al (2013) Long-period seismicity in the shallow volcanic edifice formed from slow-rupture earthquakes. Nat Geosci 7:71–75. doi: 10.1038/ngeo2027

Beeler NM, Tullis TE, Goldsby DL (2008) Constitutive relationships and physical basis of fault strength due to flash heating. J Geophys Res 113:B01401. doi: 10.1029/2007JB004988

Bell AF, Naylor M, Heap MJ, Main IG (2011) Forecasting volcanic eruptions and other material failure phenomena: An evaluation of the failure forecast method. Geophys Res Lett 38:1–5. doi: 10.1029/2011GL048155

Benson PM, Heap MJ, Lavallée Y, et al (2012) Laboratory simulations of tensile fracture development in a volcanic conduit via cyclic magma pressurisation. Earth Planet Sci Lett 349–350:231–239. doi: 10.1016/j.epsl.2012.07.003

Benson PM, Vinciguerra S, Meredith PG, Young RP (2008) Laboratory simulation of volcano seismicity. Science 322:249–252. doi: 10.1126/science.1161927

Bizzarri A (2014) The Destiny of a Clast within a Molten Pseudotachylyte Vein. Bull Seismol

Soc Am 104:2399–2411. doi: 10.1785/0120140084

Blott SJ, Croft DJ, Pye K, et al (2004) Particle size analysis by laser diffraction. Geol Soc London, Spec Publ 232:63–73. doi: 10.1144/GSL.SP.2004.232.01.08

Blower J (2001) Factors controlling permeability-porosity relationships in magma. Bull Volcanol 63:497–504. doi: 10.1007/s004450100172

Bluth GJS, Rose WI (2004) Observations of eruptive activity at Santiaguito volcano, Guatemala. J Volcanol Geotherm Res 136:297–302. doi: 10.1016/j.jvolgeores.2004.06.001

Bluth GJS, Rose WI (2002) Collaborative studies target volcanic hazards in Central America. Eos, Trans Am Geophys Union 83:429. doi: 10.1029/2002EO000309

Bonadonna C, Houghton BF (2005) Total grain-size distribution and volume of tephra-fall deposits. Bull Volcanol 67:441–456. doi: 10.1007/s00445-004-0386-2

Bonadonna C, Mayberry GC, Calder ES, et al (2002) Tephra fallout in the eruption of Soufrière Hills Volcano, Montserrat. Geol Soc London, Mem 21:483–516. doi: 10.1144/GSL.MEM.2002.021.01.22

Borselli L, Sarocchi D (2015) DECOLOG - Deconvolution of mixture's components inside particle size distributions. CONACYT Proy Cienc Basica CB-2012/18:www.decolog.org.

Bowden FP, Persson PA (1961) Deformation, Heating and Melting of Solids in High-Speed Friction. Proc R Soc London A Math Phys Eng Sci 260:433–458. doi: 10.1098/rspa.1961.0044

Brantut N, Heap MJ, Baud P, Meredith PG (2014) Rate- and strain-dependent brittle deformation of rocks. J Geophys Res Solid Earth 119:1818–1836. doi: 10.1002/2013JB010448

Brown KM, Fialko Y (2012) "Melt welt" mechanism of extreme weakening of gabbro at seismic slip rates. Nature 488:638–41. doi: 10.1038/nature11370

Bruno MS, Nakagawa FMM (1991) Pore pressure influence on tensile fracture propagation in sedimentary rock. Int. J. Rock Mech. Min. Sci. & Geomech. Abstr. 28:261–273.

Burgisser A, Degruyter W (2015) Magma Ascent and Degassing at Shallow Levels. In: Encyclopedia of Volcanoes, Second Edition. pp 225–236

Burlini L, Vinciguerra S, Di Toro G, et al (2007) Seismicity preceding volcanic eruptions: New experimental insights. Geology 35:183–186. doi: 10.1130/G23195A.1

Büttner R, Dellino P, Raue H, et al (2006) Stress-induced brittle fragmentation of magmatic melts: Theory and experiments. J Geophys Res 111:B08204. doi: 10.1029/2005JB003958

Buurman H, West ME (2010) Seismic precursors to volcanic explosions during the 2006 eruption of Augustine Volcano. US Geol Surv Prof Pap 1769:41–57.

Byerlee J (1978) Friction of rocks. Pure Appl Geophys 116:615–626.

Caballero L, Sarocchi D, Borselli L, Cárdenas AI (2012) Particle interaction inside debris flows: Evidence through experimental data and quantitative clast shape analysis. J Volcanol

Geotherm Res 231–232:12–23. doi: 10.1016/j.jvolgeores.2012.04.007

Cabrera A, Weinberg RF, Wright HMN (2015) Magma Fracturing and Degassing Associated with Obsidian Formation: The Explosive-Effusive Transition. J Volcanol Geotherm Res 298:71–84. doi: http://dx.doi.org/10.1016/j.jvolgeores.2014.07.004

Calder ES, Lavallée Y, Kendrick JE, Bernstein M (2015) Lava Dome Eruptions. In: Encyclopedia of Volcanoes, Second Edition. pp 343–362

Campbell ME, Russell JK, Porritt LA (2013) Thermomechanical milling of accessory lithics in volcanic conduits. Earth Planet Sci Lett 377–378:276–286. doi: 10.1016/j.epsl.2013.07.008

Caricchi L, Burlini L, Ulmer P, et al (2007) Non-Newtonian rheology of crystal-bearing magmas and implications for magma ascent dynamics. Earth Planet Sci Lett 264:402–419. doi: 10.1016/j.epsl.2007.09.032

Caricchi L, Pommier A, Pistone M, et al (2011) Strain-induced magma degassing: insights from simple-shear experiments on bubble bearing melts. Bull Volcanol 73:1245–1257. doi: 10.1007/s00445-011-0471-2

Carlslaw HS, Jaeger JC (1959) Conduction of Heat in Solids,.

Carn SA, Pallister JS, Lara L, et al (2009) The Unexpected Awakening of Chaitén Volcano, Chile. Eos, Trans Am Geophys Union 90:205–206. doi: 10.1029/2009EO240001

Carn SA, Watts RB, Thompson G, Norton GE (2004) Anatomy of a lava dome collapse. J Volcanol Geotherm Res 131:241–264. doi: 10.1029/2002GL014863

Carr BB, Clarke AB, Vanderkluysen L (2016) The 2006 lava dome eruption of Merapi Volcano (Indonesia): Detailed analysis using MODIS TIR. J Volcanol Geotherm Res 311:60–71. doi: 10.1016/j.jvolgeores.2015.12.004

Carr MJ, Feigenson MD, Patino LC, Walker JA (2003) Volcanism and Geochemistry in Central America: Progress and Problems. In: Eiler J, Abers G (eds) Inside the Subduction Factory. AGU Geophysical Monograph Series, pp 153–179

Cas RAF, Wright J V. (1987) Volcanic Successions Modern and Ancient. Springer Netherlands, Dordrecht

Cashman K, Biggs J (2014) Common processes at unique volcanoesâ€"a volcanological conundrum. Front Earth Sci 2:1–4. doi: 10.3389/feart.2014.00028

Cashman K, Blundy J (2000) Degassing and crystallization of ascending andesite and dacite. Philos Trans R Soc A Math Phys Eng Sci 358:1487–1513. doi: 10.1098/rsta.2000.0600

Cashman K V, Thornber C, Pallister JS (2008) From Dome to Dust : Shallow Crystallization and Fragmentation of Conduit Magma During the 2004 – 2006 Dome Extrusion of Mount St . Helens , Washington. In: Sherrod D, Scott WE, Stauffer PH (eds) A Volcano Rekindled: The Renewed Eruption of Mount St. Helens, 2004–2006 Edited by David R. Sherrod, William E. Scott, and Peter H. Stauffer U.S. Geological Survey Professional Paper 1750, 2008. pp 387–413

Cassidy M, Cole PD, Hicks KE, et al (2015) Rapid and slow: Varying magma ascent rates as a mechanism for Vulcanian explosions. Earth Planet Sci Lett 420:73–84. doi:

10.1016/j.epsl.2015.03.025

Castro JM, Bindeman IN, Tuffen H, Ian Schipper C (2014) Explosive origin of silicic lava: Textural and deltaD–H2O evidence for pyroclastic degassing during rhyolite effusion. Earth Planet Sci Lett 405:52–61. doi: 10.1016/j.epsl.2014.08.012

Castro JM, Burgisser A, Schipper CI, Mancini S (2012a) Mechanisms of bubble coalescence in silicic magmas. Bull Volcanol 74:2339–2352. doi: 10.1007/s00445-012-0666-1

Castro JM, Cordonnier B, Tuffen H, et al (2012b) The role of melt-fracture degassing in defusing explosive rhyolite eruptions at volcán Chaitén. Earth Planet Sci Lett 333–334:63–69. doi: 10.1016/j.epsl.2012.04.024

Castro JM, Dingwell DB (2009) Rapid ascent of rhyolitic magma at Chaitén volcano, Chile. Nature 461:780–3. doi: 10.1038/nature08458

Chang JC, Lockner D a., Reches Z (2012) Rapid acceleration leads to rapid weakening in earthquake-like laboratory experiments. Science 338:101–5. doi: 10.1126/science.1221195

Chevrel MO, Cimarelli C, DeBiasi L, et al (2015) Viscosity measurements of crystallizing andesite from Tungurahua volcano (Ecuador). Geochemistry, Geophys Geosystems 16:870–889. doi: 10.1002/2014GC005661

Chigna G, Cornejo J, Rojas Á (2012) Boletin vulcanologico diario 28 de noviembre de 2012.

Chouet B (1988) Resonance of a fluid-driven crack: Radiation properties and implications for the source of long-period events and harmonic tremor. J Geophys Res 93:4375. doi: 10.1029/JB093iB05p04375

Chouet BA, Matoza RS (2013) A multi-decadal view of seismic methods for detecting precursors of magma movement and eruption. J Volcanol Geotherm Res 252:108–175. doi: 10.1016/j.jvolgeores.2012.11.013

Chouet B, Dawson PB, Arciniega-Ceballos A (2005) Source mechanism of Vulcanian degassing at Popocatépetl Volcano, Mexico, determined from waveform inversions of very long period signals. J Geophys Res 110:B07301. doi: 10.1029/2004JB003524

Christopher T, Edmonds M, Taisne B, et al (2014) Periodic sulphur dioxide degassing from the Soufriere Hills Volcano related to deep magma supply. Geol Soc London, Spec Publ 410:123–141. doi: 10.1144/SP410.11

Ciccotti M (2009) Stress-corrosion mechanisms in silicate glasses. J Phys D Appl Phys 42:1–18. doi: 10.1088/0022-3727/42/21/214006

Cichy SB, Botcharnikov RE, Holtz F, Behrens H (2010) Vesiculation and Microlite Crystallization Induced by Decompression: a Case Study of the 1991-1995 Mt Unzen Eruption (Japan). J Petrol 52:1469–1492. doi: 10.1093/petrology/egq072

Cimarelli C, Alatorre-Ibarguengoitia MA, Kueppers U, et al (2013) Experimental generation of volcanic lightning. Geology 42:79–82. doi: 10.1130/G34802.1

Cimarelli C, Costa A, Mueller S, Mader HM (2011) Rheology of magmas with bimodal crystal size and shape distributions: Insights from analog experiments. Geochemistry, Geophys Geosystems 12:Q07024. doi: 10.1029/2011GC003606

Cioni R, D'Oriano C, Bertagnini A (2008) Fingerprinting ash deposits of small scale eruptions by their physical and textural features. J Volcanol Geotherm Res 177:277–287.

Clayton JD (2009) Deformation, fracture, and fragmentation in brittle geologic solids. Int J Fract 163:151–172. doi: 10.1007/s10704-009-9409-5

Cole PD, Smith PJ, Stinton AJ, et al (2014) Vulcanian explosions at Soufrière Hills Volcano, Montserrat between 2008 and 2010. Geol Soc London, Mem 39:93–111. doi: 10.1144/M39.5

Collinson ASD, Neuberg JW (2012) Gas storage, transport and pressure changes in an evolving permeable volcanic edifice. J Volcanol Geotherm Res 243–244:1–13. doi: 10.1016/j.jvolgeores.2012.06.027

Collombet M (2009) Two-dimensional gas loss for silicic magma flows: Toward more realistic numerical models. Geophys J Int 177:309–318. doi: 10.1111/j.1365-246X.2008.04086.x

Cordonnier B, Caricchi L, Pistone M, et al (2012a) The viscous-brittle transition of crystal-bearing silicic melt: Direct observation of magma rupture and healing. Geology 40:611–614. doi: 10.1130/G3914.1

Cordonnier B, Hess K-U, Lavallée Y, Dingwell DB (2009) Rheological properties of dome lavas: Case study of Unzen volcano. Earth Planet Sci Lett 279:263–272. doi: 10.1016/j.epsl.2009.01.014

Cordonnier B, Schmalholz SM, Hess K-U, Dingwell DB (2012b) Viscous heating in silicate melts: An experimental and numerical comparison. J Geophys Res 117:B02203. doi: 10.1029/2010JB007982

Costa A, Caricchi L, Bagdassarov N (2009) A model for the rheology of particle-bearing suspensions and partially molten rocks. Geochemistry, Geophys Geosystems 10:Q03010. doi: 10.1029/2008GC002138

Costa A, Melnik O, Sparks RSJ (2007) Controls of conduit geometry and wallrock elasticity on lava dome eruptions. Earth Planet Sci Lett 260:137–151. doi: 10.1016/j.epsl.2007.05.024

Costa A, Wadge G, Melnik O (2012) Cyclic extrusion of a lava dome based on a stick-slip mechanism. Earth Planet Sci Lett 337–338:39–46. doi: 10.1016/j.epsl.2012.05.011

Costa A, Wadge G, Stewart R, Odbert H (2013) Coupled subdaily and multiweek cycles during the lava dome eruption of Soufrière Hills Volcano, Montserrat. J Geophys Res Solid Earth 118:1895–1903. doi: 10.1002/jgrb.50095

David C, Wong TF, Zhu W, Zhang J (1994) Laboratory measurement of compaction-induced permeability change in porous rocks: Implications for the generation and maintenance of pore pressure excess in the crust.

De Angelis S (2009) Seismic source displacement by coda wave interferometry at Soufrière Hills Volcano, Montserrat, WI. Nat Hazards Earth Syst Sci 9:1341–1347. doi: 10.5194/nhess-9-1341-2009

De Angelis S, Henton SM (2011) On the feasibility of magma fracture within volcanic conduits: Constraints from earthquake data and empirical modelling of magma viscosity. Geophys Res Lett 38:L19310. doi: 10.1029/2011GL049297

De Angelis S, Lamb OD, Lamur A, et al (2016) Characterization of moderate ash-and-gas explosions at Santiaguito volcano, Guatemala, from infrasound waveform inversion and thermal infrared measurements. Geophys Res Lett 43:6220–6227. doi: 10.1002/2016GL069098

De Angelis SHH, Larsen J, Coombs M, et al (2015) Amphibole reaction rims as a record of pre-eruptive magmatic heating: An experimental approach. Earth Planet Sci Lett 426:235–245. doi: 10.1016/j.epsl.2015.06.051

Degruyter W, Bachmann O, Burgisser A, Manga M (2012) The effects of outgassing on the transition between effusive and explosive silicic eruptions. Earth Planet Sci Lett 349–350:161–170. doi: 10.1016/j.epsl.2012.06.056

Delle Donne D, Ripepe M, De Angelis S, et al (2014) Thermal, acoustic and seismic signals from pyroclastic density currents and Vulcanian explosions at Soufriere Hills Volcano, Montserrat. Geol Soc London, Mem 39:169–178. doi: 10.1144/M39.9

Denlinger RP (1990) A Model for Dome Eruptions at Mount St. Helens, Washington Based on Subcritical Crack Growth. In: Fink J (ed) Lava Flows and Domes. Springer Berlin Heidelberg, pp 70–87

Deubelbeiss Y, Connolly JAD (2011) Potential causes for the non- Newtonian rheology of crystal-bearing magmas. Geochemistry, Geophys Geosystems 12:1–22. doi: 10.1029/2010GC003485

Di Genova D, Morgavi D, Hess K-U, et al (2015) Approximate chemical analysis of volcanic glasses using Raman spectroscopy. J Raman Spectrosc 46:1235–1244. doi: 10.1002/jrs.4751

Di Genova D, Romano C, Giordano D, Alletti M (2014) Heat capacity, configurational heat capacity and fragility of hydrous magmas. Geochim Cosmochim Acta 142:314–333. doi: 10.1016/j.gca.2014.07.012

Di Toro G (2006) Natural and Experimental Evidence of Melt Lubrication of Faults During Earthquakes. Science (80-) 311:647–649. doi: 10.1126/science.1121012

Di Toro G, Han R, Hirose T, et al (2011) Fault lubrication during earthquakes. Nature 471:494–8. doi: 10.1038/nature09838

Dieterich JH (1979) Modeling of rock friction: 1. Experimental results and constituve equations. J Geophys Res 84:2161–2168. doi: 10.1007/BF00876539

Dieterich JH (1978) Time-dependent friction and the mechanics of stick-slip. Pure Appl Geophys 116:790–806. doi: 10.1007/BF00876539

Dieterich JH, Kilgore BD (1994) Direct observation of frictional contacts: New insights for state-dependent properties. Pure Appl Geophys 143:283–302. doi: 10.1007/BF00874332

Dingwell D, Webb S (1989) Structural relaxation in silicate melts and non-Newtonian melt rheology in geologic processes. Phys Chem Miner 16:508–516. doi: 10.1007/BF00197020

Dingwell DB (1991) Redox viscometry of some Fe-bearing silicate melts. Am Mineral 76:1560–1562.

Dingwell DB (1996) Volcanic Dilemma--Flow or Blow? Science (80-.). 273:1054–1055.

Dingwell DB (2006) Transport Properties of Magmas: Diffusion and Rheology. Elements 2:281–286. doi: 10.2113/gselements.2.5.281

Dingwell DB, Hess K-U, Romano C (2000) Viscosities of granitic (sensu lato) melts : Influence of the anorthite component. Am Mineral 85:1342–1348.

Dingwell DB, Lavallée Y, Kueppers U (2012) Volcanic ash: A primary agent in the Earth system. Phys Chem Earth, Parts A/B/C 45–46:2–4. doi: 10.1016/j.pce.2011.07.007

Dingwell DB, Romano C, Hess K-U (1996) The effect of water on the viscosity of a haplogranitic melt under P-T-X conditions relevant to silicic volcanism. Contrib to Mineral Petrol 124:19–28. doi: 10.1007/s004100050170

Dmitrieva K, Hotovec-Ellis AJ, Prejean S, Dunham EM (2013) Frictional-faulting model for harmonic tremor before Redoubt Volcano eruptions. Nat Geosci 6:652–656. doi: 10.1038/ngeo1879

Duclosi R, Paquet J (1991) High-temperature Behaviour of Basalts Role of Temperature and Strain Rate on Compressive Strength and Kit Toughness of Partially Glassy Basalts at Atmospheric Pressure. Int J Rock Mech Min Sci Geomech 28:71–76. doi: 10.1016/0148-9062(91)93234-W

Dufek J, Manga M (2008) In situ production of ash in pyroclastic flows. J Geophys Res 113:B09207. doi: 10.1029/2007JB005555

Dufek J, Manga M, Patel A (2012) Granular disruption during explosive volcanic eruptions. Nat Geosci 5:561–564. doi: 10.1038/ngeo1524

Dürig T, Zimanowski B (2012) "Breaking news" on the formation of volcanic ash: Fracture dynamics in silicate glass. Earth Planet Sci Lett 335–336:1–8. doi: 10.1016/j.epsl.2012.05.001

Dvorak JJ, Dzurisin D (1997) Volcano geodesy: The search for magma reservoirs and the formation of eruptive vents. Rev Geophys 35:343–384. doi: 10.1029/97RG00070

Ebmeier SK, Biggs J, Mather TA, et al (2012) Measuring large topographic change with InSAR: Lava thicknesses, extrusion rate and subsidence rate at Santiaguito volcano, Guatemala. Earth Planet Sci Lett 335–336:216–225. doi: 10.1016/j.epsl.2012.04.027

Edmonds M, Herd RA (2007) A volcanic degassing event at the explosive-effusive transition. Geophys Res Lett 34:1–6. doi: 10.1029/2007GL031379

Eichelberger JC (1995) Silicic Volcanism: Ascent of Viscous Magmas from Crustal Reservoirs. Annu Rev Earth Planet Sci 23:41–63. doi: 10.1146/annurev.ea.23.050195.000353

Einstein A (1911) Berichtigung zu meiner Arbeit: "Eine neue Bestimmung der Molekuldimensionen." Ann. Phys. 591–592.

Einstein A (1906) A new determination of molecular dimensions. Ann Phys 4:289–306.

Escobar-Wolf R, Gomez OM, Rose WI (2010) Santiaguito Dome Geologic Map 2006 Domes and lava flows. Geol Soc Am Digit Map Chart Ser. doi: 10.1130/2010.DMCH008.

Evans B, Fredrich JT, Wong T-F (2013) The Brittle-Ductile Transition in Rocks: Recent Experimental and Theoretical Progress. Geophys Monogr Ser 56:1–20. doi: 10.1029/GM056p0001

Evans JR, Huntoon JE, Rose WI, et al (2009) Particle sizes of andesitic ash fallout from vertical eruptions and co-pyroclastic flow clouds, Volcán de Colima, Mexico. Geology 37:935–938. doi: 10.1130/G30208A.1

Eyre TS, Bean CJ, De Barros L, et al (2015) A brittle failure model for long-period seismic events recorded at Turrialba Volcano, Costa Rica. J Geophys Res Solid Earth 120:1452–1472. doi: 10.1002/2014JB011108

Farquharson J, Heap MJ, Baud P, et al (2016a) Pore pressure embrittlement in a volcanic edifice. Bull Volcanol 78:6. doi: 10.1007/s00445-015-0997-9

Farquharson J, Heap MJ, Varley NR, Baud P (2015a) Permeability and porosity relationships of edifice-forming andesites: A combined field and laboratory study. J Volcanol Geotherm Res 297:52–68. doi: 10.1016/j.jvolgeores.2015.03.016

Farquharson JI, Heap MJ, Lavallée Y, et al (2016b) Evidence for the development of permeability anisotropy in lava domes and volcanic conduits. J Volcanol Geotherm Res 323:163–185. doi: 10.1016/j.jvolgeores.2016.05.007

Farquharson JI, James MR, Tuffen H (2015b) Examining rhyolite lava flow dynamics through photo-based 3D reconstructions of the 2011–2012 lava flowfield at Cordón-Caulle, Chile. J Volcanol Geotherm Res 304:336–348. doi: 10.1016/j.jvolgeores.2015.09.004

Faulkner DR, Lewis AC, Rutter EH (2003) On the internal structure and mechanics of large strike-slip fault zones: Field observations of the Carboneras fault in southeastern Spain. Tectonophysics 367:235–251. doi: 10.1016/S0040-1951(03)00134-3

Faulkner DR, Mitchell TM, Behnsen J, et al (2011) Stuck in the mud? Earthquake nucleation and propagation through accretionary forearcs. Geophys Res Lett 38:1–5. doi: 10.1029/2011GL048552

Ferrazzini V, Aki K (1987) Slow waves trapped in a fluid-filled infinite crack: Implication for volcanic tremor. J Geophys Res 92:9215. doi: 10.1029/JB092iB09p09215

Fialko Y (2004) Temperature fields generated by the elastodynamic propagation of shear cracks in the Earth. J Geophys Res 109:B01303. doi: 10.1029/2003JB002497

Fialko Y, Khazan Y (2005) Fusion by earthquake fault friction: Stick or slip? J Geophys Res 110:B12407. doi: 10.1029/2005JB003869

Fink JH, Griffiths RW (1998) Morphology, eruption rates, and rheology of lava domes: Insights from laboratory models. J Geophys Res 103:527. doi: 10.1029/97JB02838

Flower VJB, Carn SA (2015) Characterising volcanic cycles at Soufrière Hills Volcano, Montserrat: Time series analysis of multi-parameter satellite data. J Volcanol Geotherm Res 304:82–93. doi: 10.1016/j.jvolgeores.2015.07.035

Freundt A, Schmincke HU (1992) Abrasion in pyroclastic flows. Geol Rundschau 81:383–389. doi: 10.1007/BF01828605

Fulcher GS (1925) ANALYSIS OF RECENT MEASUREMENTS OF THE VISCOSITY OF GLASSES. J Am Ceram Soc 8:339–355. doi: 10.1111/j.1151-2916.1925.tb16731.x

Gaunt HE, Sammonds PR, Meredith PG, et al (2014) Pathways for degassing during the lava dome eruption of Mount St. Helens 2004-2008. Geology 42:947–950. doi: 10.1130/G35940.1

Genareau K, Clarke AB, Hervig RL (2009) New insight into explosive volcanic eruptions: Connecting crystal-scale chemical changes with conduit-scale dynamics. Geology 37:367–370. doi: 10.1130/G25561A.1

Gent AN (1960) Theory of the parallel plate viscometer. Br J Appl Phys 11:85–87. doi: 10.1088/0508-3443/11/2/310

Giordano D, Nichols ARL, Dingwell DB (2005) Glass transition temperatures of natural hydrous melts: A relationship with shear viscosity and implications for the welding process. J Volcanol Geotherm Res 142:105–118. doi: 10.1016/j.jvolgeores.2004.10.015

Giordano D, Russell JK, Dingwell DB (2008) Viscosity of magmatic liquids: A model. Earth Planet Sci Lett 271:123–134. doi: 10.1016/j.epsl.2008.03.038

Goldsby DL, Tullis TE (2011) Flash Heating Leads to Low Frictional Strength of Crustal Rocks at Earthquake Slip Rates. Science (80-) 334:216–218. doi: 10.1126/science.1207902

Gonnermann H, Manga M (2003) Explosive volcanism may not be an inevitable consequence of magma fragmentation. Nature 426:8–11. doi: 10.1038/nature02159.1.

Goto A (1999) A new model for volcanic earthquake at Unzen Volcano: Melt Rupture Model. Geophys Res Lett 26:2541–2544. doi: 10.1029/1999GL900569

Goto Y, Nakada S, Kurokawa M, et al (2008) Character and origin of lithofacies in the conduit of Unzen volcano, Japan. J Volcanol Geotherm Res 175:45–59. doi: 10.1016/j.jvolgeores.2008.03.041

Gottlieb P, Wilkie G, Sutherland D, et al (2000) Using quantitative electron microscopy for process mineralogy applications. Jom 52:24–25. doi: 10.1007/s11837-000-0126-9

Gottsmann J, Dingwell DB (2001) Cooling dynamics of spatter-fed phonolite obsidian flows on Tenerife, Canary Islands. J Volcanol Geotherm Res 105:323–342. doi: 10.1016/S0377-0273(00)00262-6

Green DN, Neuberg J, Cayol V (2006) Shear stress along the conduit wall as a plausible source of tilt at Soufri??re Hills volcano, Montserrat. Geophys Res Lett 33:2–6. doi: 10.1029/2006GL025890

Griffith WA, Di Toro G, Pennacchioni G, Pollard DD (2008) Thin pseudotachylytes in faults of the Mt. Abbot quadrangle, Sierra Nevada: Physical constraints for small seismic slip events. J Struct Geol 30:1086–1094. doi: 10.1016/j.jsg.2008.05.003

Grunewald U, Sparks RSJ, Kearns S, Komorowski JC (2000) Friction marks on blocks from pyroclastic flows at the Soufriere Hills volcano, Montserrat: Implications for flow mechanisms. Geology 28:827. doi: 10.1130/0091-7613(2000)28<827:FMOBFP>2.0.CO;2

Haberlah D, Strong C, Pirrie D, et al (2011) Automated petrography applications in Quaternary

Science. Quat Australas 28:3–12.

Hale AJ, Wadge G (2008) The transition from endogenous to exogenous growth of lava domes with the development of shear bands. J Volcanol Geotherm Res 171:237–257. doi: 10.1016/j.jvolgeores.2007.12.016

Hall ML, Steele AL, Bernard B, et al (2015) Sequential Plug Formation, Desintegration By Vulcanian Explosions, And The Generation Of Granular Pyroclastic Density Currents At Tungurahua Volcano (2013-2014), Ecuador. J Volcanol Geotherm Res. doi: 10.1016/j.jvolgeores.2015.09.009

Handin J (1969) On the Coulomb-Mohr Failure Criterion. J Geophys Res 74:5343–5348.

Haney MM, Chouet BA, Dawson PB, Power JA (2013) Source characterization for an explosion during the 2009 eruption of Redoubt Volcano from very-long-period seismic waves. J Volcanol Geotherm Res 259:77–88. doi: 10.1016/j.jvolgeores.2012.04.018

Harrington RM, Brodsky EE (2007) Volcanic hybrid earthquakes that are brittle-failure events. Geophys Res Lett 34:L06308. doi: 10.1029/2006GL028714

Harris A, Rose W, Flynn L (2003) Temporal trends in lava dome extrusion at Santiaguito 1922–2000. Bull Volcanol 1973:77–89. doi: 10.1007/s00445-002-0243-0

Heap MJ, Farquharson JI, Wadsworth FB, et al (2015a) Timescales for permeability reduction and strength recovery in densifying magma. Earth Planet Sci Lett 1:1–11. doi: 10.1016/j.epsl.2015.07.053

Heap MJ, Faulkner DR, Meredith PG, Vinciguerra S (2010) Elastic moduli evolution and accompanying stress changes with increasing crack damage: Implications for stress changes around fault zones and volcanoes during deformation. Geophys J Int 183:225–236. doi: 10.1111/j.1365-246X.2010.04726.x

Heap MJ, Lavallée Y, Petrakova L, et al (2014a) Microstructural controls on the physical and mechanical properties of edifice-forming andesites at Volcán de Colima, Mexico. J Geophys Res Solid Earth 119:2925–2963. doi: 10.1002/2013JB010521

Heap MJ, Xu T, Chen C feng (2014b) The influence of porosity and vesicle size on the brittle strength of volcanic rocks and magma. Bull Volcanol 76:856. doi: 10.1007/s00445-014-0856-0

Heap MJ, Xu T, Kushnir ARL, et al (2015b) Fracture of magma containing overpressurised pores. J Volcanol Geotherm Res 301:180–190. doi: 10.1016/j.jvolgeores.2015.05.016

Heiken G, Wohletz K (1987) Tephra deposits associated with silicic domes and lava flows. Geol Soc Am Spec Pap 212:55–76. doi: 10.1130/SPE212-p55

Heilbronner R, Barrett S (2014) Image Analysis in Earth Sciences. 389–409. doi: 10.1007/978-3-642-10343-8

Hendrasto M, Eto T, Kimata F, et al (1997) Magma transport at Mt. Unzen associated with the 1990-1995 activity inferred from levelling data.

Hess KU, Cordonnier B, Lavallée Y, Dingwell DB (2007) High-load, high-temperature deformation apparatus for synthetic and natural silicate melts. Rev Sci Instrum 78:1–5. doi:

10.1063/1.2751398

Hess K-U, Dingwell DB (1996) Viscosities of hydrous leucogranitic melts: A non-Arrhenian model. Am Mineral 81:1297–1300.

Hess KU, Dingwell DB, Webb SL (1996a) The influence of alkaline-earth oxides (BeO, MgO, CaO, SrO, BaO) on the viscosity of a haplogranitic melt: Systematics of non-Arrhenian behaviour. Eur J Mineral 8:371–381.

Hess K-UU, Dingwell DB, Rössler E, Rossler E (1996b) Parametrization of viscosity-temperature relations of aluminosilicate melts. Chem Geol 128:155–163. doi: 10.1016/0009-2541(95)00170-0

Hirose T, Mizoguchi K, Shimamoto T (2012) Wear processes in rocks at slow to high slip rates. J Struct Geol 38:102–116. doi: 10.1016/j.jsg.2011.12.007

Hirose T, Shimamoto T (2005) Growth of molten zone as a mechanism of slip weakening of simulated faults in gabbro during frictional melting. J Geophys Res 110:B05202. doi: 10.1029/2004JB003207

Hirose T, Shimamoto T (2003) Fractal dimension of molten surfaces as a possible parameter to infer the slip-weakening distance of faults from natural pseudotachylytes. J Struct Geol 25:1569–1574. doi: 10.1016/S0191-8141(03)00009-9

Holland ASP, Watson IM, Phillips JC, et al (2011) Degassing processes during lava dome growth: Insights from Santiaguito lava dome, Guatemala. J Volcanol Geotherm Res 202:153–166. doi: 10.1016/j.jvolgeores.2011.02.004

Hornby AJ, Kendrick JE, Lamb OD, et al (2015a) Spine growth and seismogenic faulting at Mt. Unzen, Japan. J Geophys Res B Solid Earth 120:1–21. doi: 10.1002/2014JB011660.Received

Hornby AJ, Kendrick JE, Lamb OD, et al (2015b) Spine growth and seismogenic faulting at Mt. Unzen, Japan. J Geophys Res Solid Earth 120:4034–4054. doi: 10.1002/2014JB011660

Horwell CJ, Baxter PJ (2006) The respiratory health hazards of volcanic ash: A review for volcanic risk mitigation. Bull Volcanol 69:1–24. doi: 10.1007/s00445-006-0052-y

Horwell CJ, Braña LP, Sparks RSJ, et al (2001) A geochemical investigation of fragmentation and physical fractionation in pyroclastic flows from the Soufrière Hills volcano, Montserrat. J Volcanol Geotherm Res 109:247–262. doi: 10.1016/S0377-0273(00)00319-X

Hotta K, Iguchi M, Ohkura T, Yamamoto K (2016) Multiple-pressure-source model for ground inflation during the period of high explosivity at Sakurajima volcano, Japan - Combination analysis of continuous GNSS, tilt and strain data -. J Volcanol Geotherm Res 310:12–25. doi: 10.1016/j.jvolgeores.2015.11.017

Husain T, Elsworth D, Voight B, et al (2014) Influence of extrusion rate and magma rheology on the growth of lava domes: Insights from particle-dynamics modeling. J Volcanol Geotherm Res 285:100–117. doi: 10.1016/j.jvolgeores.2014.08.013

ISRM (1978) Suggested Methods For Determining Tensile Strength of Rock Materials. Int Soc Rock Mech Comm Stand Lab F Tests 15:99–103. doi: 10.1016/0148-9062(78)90003-7

Iverson R (2008) Dynamics of Seismogenic Volcanic Extrusion Resisted by a Solid Surface Plug, Mount St. Helens, 2004-2005. US Geol Surv Prof Pap 1750:2004–2006.

Iverson RM, Dzurisin D, Gardner C a, et al (2006) Dynamics of seismogenic volcanic extrusion at Mount St Helens in 2004-05. Nature 444:439–43. doi: 10.1038/nature05322

James MR, Varley N (2012) Identification of structural controls in an active lava dome with high resolution DEMs: Volcn de Colima, Mexico. Geophys Res Lett 39:1–5. doi: 10.1029/2012GL054245

Japanese Meteorological Association (1995) Geological report of eruption at Unzen during a period from November 1994 to February 1995. Tech Rep Japan Meteorol Agency 61:69–77.

Japanese Meteorological Association (1994) Volcanic Activity of Mt. Unzen Volcano (June-October 1994). Tech Rep Japan Meteorol Agency 60:69–84.

Jellinek a M, Bercovici D (2011) Seismic tremors and magma wagging during explosive volcanism. Nature 470:522–525. doi: 10.1038/nature09828

Johnson JB, Lees JM (2010) Sound produced by the rapidly inflating Santiaguito lava dome, Guatemala. Geophys Res Lett 37:n/a-n/a. doi: 10.1029/2010GL045217

Johnson JB, Lees JM, Gerst A, et al (2008) Long-period earthquakes and co-eruptive dome inflation seen with particle image velocimetry. Nature 456:377–81. doi: 10.1038/nature07429

Johnson JB, Lyons JJ, Andrews BJ, Lees JM (2014) Explosive dome eruptions modulated by periodic gas-driven inflation. Geophys Res Lett 41:6689–6697. doi: 10.1002/2014GL061310

Johnson JB, Palma JL (2015) Lahar infrasound associated with Volcán Villarrica's 3 March 2015 eruption. Geophys Res Lett 42:6324–6331. doi: 10.1002/2015GL065024

Johnson JB, Ripepe M (2011) Volcano infrasound: A review. J Volcanol Geotherm Res 206:61–69. doi: 10.1016/j.jvolgeores.2011.06.006

Johnson JB, Ronan TJ (2015) Infrasound from volcanic rockfalls. J Geophys Res Solid Earth 120:8223–8239. doi: 10.1002/2015JB012436

Johnson JB, Sanderson R, Lyons J, et al (2009) Dissection of a composite volcanic earthquake at Santiaguito, Guatemala. Geophys Res Lett. doi: 10.1029/2009GL039370

Jones TJ, McNamara K, Eychenne J, et al (2016) Primary and secondary fragmentation of crystal bearing intermediate magma. J Volcanol Geotherm Res. doi: 10.1016/j.jvolgeores.2016.06.022

Jordan SC, Dürig T, Cas RAF, Zimanowski B (2014) Processes controlling the shape of ash particles: Results of statistical IPA. J Volcanol Geotherm Res 288:19–27. doi: 10.1016/j.jvolgeores.2014.09.012

Kendrick JE, Lavallée Y, Ferk A, et al (2012) Extreme frictional processes in the volcanic conduit of Mount St. Helens (USA) during the 2004–2008 eruption. J Struct Geol 38:61–76. doi: 10.1016/j.jsg.2011.10.003

Kendrick JE, Lavallée Y, Hess K, et al (2013a) Tracking the permeable porous network during strain-dependent magmatic flow. J Volcanol Geotherm Res 260:117–126. doi: 10.1016/j.jvolgeores.2013.05.012

Kendrick JE, Lavallée Y, Hess K-U, et al (2014a) Seismogenic frictional melting in the magmatic column. Solid Earth 5:199–208. doi: 10.5194/se-5-199-2014

Kendrick JE, Lavallée Y, Hirose T, et al (2014b) Volcanic drumbeat seismicity caused by stick-slip motion and magmatic frictional melting. Nat Geosci 7:438–442. doi: 10.1038/ngeo2146

Kendrick JE, Lavallée Y, Varley N, et al (2016) Blowing off steam: Tuffisite formation as a regulator for lava dome eruptions. Front Earth Sci. doi: 10.3389/feart.2016.00041

Kendrick JE, Smith R, Sammonds P, et al (2013b) The influence of thermal and cyclic stressing on the strength of rocks from Mount St. Helens, Washington. Bull Volcanol 75:728. doi: 10.1007/s00445-013-0728-z

Kennedy BM, Wadsworth FB, Vasseur J, et al (2016) Surface tension driven processes densify and retain permeability in magma and lava. Earth Planet Sci Lett 433:116–124. doi: 10.1016/j.epsl.2015.10.031

Kennedy LA, Russell JK (2012) Cataclastic production of volcanic ash at Mount Saint Helens. Phys Chem Earth, Parts A/B/C 45–46:40–49. doi: 10.1016/j.pce.2011.07.052

Kennedy LA, Russell JK, Nelles E (2009) Origins of Mount St. Helens cataclasites: Experimental insights. Am Mineral 94:995–1004. doi: 10.2138/am.2009.3129

Ketner D, Power J (2013) Characterization of seismic events during the 2009 eruption of Redoubt Volcano, Alaska. J Volcanol Geotherm Res 259:45–62. doi: 10.1016/j.jvolgeores.2012.10.007

Kilburn CRJ, Voight B (1998) Slow rock fracture as eruption precursor at Soufriere Hills Volcano, Montserrat. Geophys Res Lett 25:3665. doi: 10.1029/98GL01609

Kim J-W, Ree J-H, Han R, Shimamoto T (2010) Experimental evidence for the simultaneous formation of pseudotachylyte and mylonite in the brittle regime. Geology 38:1143–1146. doi: 10.1130/G31593.1

Kim K, Fee D, Yokoo A, Lees JM (2015) Acoustic source inversion to estimate volume flux from volcanic explosions. Geophys Res Lett 42:5243–5249. doi: 10.1002/2015GL064466

Kim K, Lees JM, Ruiz MC (2014) Source mechanism of Vulcanian eruption at Tungurahua Volcano, Ecuador, derived fromseismic moment tensor inversions. J Geophys Res Solid Earth 119:1145–1164. doi: 10.1002/2013JB010590

Kirkpatrick JD, Rowe CD (2013) Disappearing ink: How pseudotachylytes are lost from the rock record. J Struct Geol 52:183–198. doi: 10.1016/j.jsg.2013.03.003

Kohno Y, Matsushima T, Shimizu H (2008) Pressure sources beneath Unzen Volcano inferred from leveling and GPS data. J Volcanol Geotherm Res 175:100–109. doi: 10.1016/j.jvolgeores.2008.03.022

Koizumi Y, Otsuki K, Takeuchi A, Nagahama H (2004) Frictional melting can terminate

seismic slips: Experimental results of stick-slips. Geophys Res Lett 31:L21605. doi: 10.1029/2004GL020642

Kokelaar P (2007) Friction melting, catastrophic dilation and breccia formation along caldera superfaults. J Geol Soc London 164:751–754. doi: 10.1144/0016-76492006-059

Kolzenburg S, Heap MJ, Lavallée Y, et al (2012) Strength and permeability recovery of tuffisite-bearing andesite. Solid Earth 3:191–198. doi: 10.5194/se-3-191-2012

Kolzenburg S, Russell JK (2014) Welding of pyroclastic conduit infill: A mechanism for cyclical explosive eruptions. J Geophys Res Solid Earth 119:5305–5323. doi: 10.1002/2013JB010931

Koyaguchi T, Mitani NK (2005) A theoretical model for fragmentation of viscous bubbly magmas in shock tubes. J Geophys Res Solid Earth 110:1–21. doi: 10.1029/2004JB003513

Krieger IM, Dougherty TJ (1959) A Mechanism for Non-Newtonian Flow in Suspensions of Rigid Spheres.

Kueppers U, Perugini D, Dingwell D (2006) "Explosive energy" during volcanic eruptions from fractal analysis of pyroclasts. Earth Planet Sci Lett 248:800–807. doi: 10.1016/j.epsl.2006.06.033

Kueppers U, Putz C, Spieler O, Dingwell DB (2012) Abrasion in pyroclastic density currents: Insights from tumbling experiments. Phys Chem Earth 45–46:33–39. doi: 10.1016/j.pce.2011.09.002

Kusakabe M, Sato H, Nakada S, Kitamura T (1999) Water contents and hydrogen isotopic ratios of rocks and minerals from the 1991 eruption of Unzen volcano, Japan. J Volcanol Geotherm Res 89:231–242.

Lamb OD, De Angelis S, Lavallée Y (2015a) Using infrasound to constrain ash plume rise. J Appl Volcanol 4:20. doi: 10.1186/s13617-015-0038-6

Lamb OD, De Angelis S, Umakoshi K, et al (2015b) Cyclic fracturing during spine extrusion at Unzen volcano, Japan. Solid Earth Discuss 7:2109–2149. doi: 10.5194/sed-7-2109-2015

Lamb OD, De Angelis S, Umakoshi K, et al (2015c) Repetitive fracturing during spine extrusion at Unzen volcano, Japan. Solid Earth 6:1277–1293. doi: 10.5194/se-6-1277-2015

Lamb OD, Varley NR, Mather TA, et al (2014) Similar cyclic behaviour observed at two lava domes, Volcán de Colima (Mexico) and Soufrière Hills volcano (Montserrat), with implications for monitoring. J Volcanol Geotherm Res 284:106–121. doi: 10.1016/j.jvolgeores.2014.07.013

Landi P, Rosi M, Polacci M, et al (2004) Role of conduit shear on ascent of the crystal-rich magma feeding the 800-year-b.p. Plinian eruption of Quilotoa Volcano (Ecuador). Bull Volcanol 66:307–321. doi: 10.1007/s00445-003-0312-z

Lautze NC, Houghton BF (2007) Linking variable explosion style and magma textures during 2002 at Stromboli volcano , Italy. Bull Volcanol 69:445–460. doi: 10.1007/s00445-006-0086-1

Lavallée Y, Benson PM, Heap MJ, et al (2012a) Volcanic conduit failure as a trigger to magma

fragmentation. Bull Volcanol 74:11–13. doi: 10.1007/s00445-011-0544-2

Lavallée Y, Benson PM, Heap MJ, et al (2013) Reconstructing magma failure and the degassing network of dome-building eruptions. Geology 41:515–518. doi: 10.1130/G33948.1

Lavallée Y, Dingwell DB, Johnson JB, et al (2015a) Thermal vesiculation during volcanic eruptions. Nature In Press:1–5. doi: 10.1038/nature16153

Lavallée Y, Heap MJ, Kueppers U, et al (2016) The fragility of Volcán de Colima – a material constraint. In: Varley NR, Komorowski J-C (eds) Volcán de Colima – Managing the Threat. Springer-Verlag, Berlin Heidelberg,

Lavallée Y, Hess K-U, Cordonnier B, Bruce Dingwell D (2007) Non-Newtonian rheological law for highly crystalline dome lavas. Geology 35:843. doi: 10.1130/G23594A.1

Lavallée Y, Hirose T, Kendrick JE, et al (2014) A frictional law for volcanic ash gouge. Earth Planet Sci Lett 400:177–183. doi: 10.1016/j.epsl.2014.05.023

Lavallée Y, Hirose T, Kendrick JE, et al (2015b) Fault rheology beyond frictional melting. Proc Natl Acad Sci 201413608. doi: 10.1073/pnas.1413608112

Lavallée Y, Meredith PG, Dingwell DB, et al (2008) Seismogenic lavas and explosive eruption forecasting. Nature 453:507–10. doi: 10.1038/nature06980

Lavallée Y, Mitchell TM, Heap MJ, et al (2012b) Experimental generation of volcanic pseudotachylytes: Constraining rheology. J Struct Geol 38:222–233. doi: 10.1016/j.jsg.2012.02.001

Lavallée Y, Varley NR, Alatorre-Ibargüengoitia MA, et al (2011) Magmatic architecture of dome-building eruptions at Volcán de Colima, Mexico. Bull Volcanol 74:249–260. doi: 10.1007/s00445-011-0518-4

Legros F, Cantagrel J, Devouard B (2000) Pseudotachylyte (Frictionite) at the Base of the Arequipa Volcanic Landslide Deposit (Peru): Implications for Emplacement Mechanisms. J Geol 108:601–611. doi: 10.1086/314421

Lejeune A-M, Richet P (1995) Rheology of crystal-bearing silicate melts: An experimental study at high viscosities. J Geophys Res 100:4215. doi: 10.1029/94JB02985

Lejeune AMM, Bottinga Y, Trull TWW, Richet P (1999) Rheology of bubble-bearing magmas. Earth Planet Sci Lett 166:71–84. doi: 10.1016/S0012-821X(98)00278-7

Lensky NG, Sparks RSJ, Navon O, Lyakhovsky V (2008) Cyclic activity at Soufrière Hills Volcano, Montserrat: degassing-induced pressurization and stick-slip extrusion. Geol Soc London, Spec Publ 307:169–188. doi: 10.1144/SP307.10

Lesher CE, Spera FJ (2015) Thermodynamic and Transport Properties of Silicate Melts and Magma. In: The Encyclopedia of Volcanoes. Elsevier, pp 113–141

Li D, Li CC, Li X (2011) Influence of sample height-to-width ratios on failure mode for rectangular prism samples of hard rock loaded in uniaxial compression. Rock Mech Rock Eng 44:253–267. doi: 10.1007/s00603-010-0127-0

Li D, Wong LNY (2013) The brazilian disc test for rock mechanics applications: Review and

new insights. Rock Mech Rock Eng 46:269–287. doi: 10.1007/s00603-012-0257-7

Lin H, Xiong W, Yan Q (2016) Three-Dimensional Effect of Tensile Strength in the Standard Brazilian Test Considering Contact Length. Geotech Test J 39:20140268. doi: 10.1520/GTJ20140268

Liu EJ, Cashman KV, Rust AC (2015) Optimising shape analysis to quantify volcanic ash morphology. GeoResJ 8:14–30. doi: 10.1016/j.grj.2015.09.001

Liu S, Xu J (2015) An experimental study on the physico-mechanical properties of two post-high-temperature rocks. Eng Geol 185:63–70. doi: 10.1016/j.enggeo.2014.11.013

Lockner D (1993) The role of acoustic emission in the study of rock fracture. Int J Rock Mech Min Sci Geochem Abstr 30:883–899.

Loughlin SC, Luckett R, Ryan G, et al (2010) An overview of lava dome evolution, dome collapse and cyclicity at Soufrière Hills Volcano, Montserrat, 2005-2007. Geophys Res Lett 37:n/a-n/a. doi: 10.1029/2010GL042547

Lyons JJ, Haney MM, Werner C, et al (2016) Long period seismicity and very long period infrasound driven by shallow magmatic degassing at Mount Pagan, Mariana Islands. J Geophys Res Solid Earth 121:188–209. doi: 10.1002/2015JB012490

Lyons JJ, Waite GP, Ichihara M, Lees JM (2012) Tilt prior to explosions and the effect of topography on ultra-long-period seismic records at Fuego volcano, Guatemala. Geophys Res Lett 39:L08305. doi: 10.1029/2012GL051184

Maddock RH (1992) Effects of lithology, cataclasis and melting on the composition of fault-generated pseudotachylytes in Lewisian gneiss, Scotland. Tectonophysics 204:261–278. doi: 10.1016/0040-1951(92)90311-S

Mader HM, Zhang Y, Phillips JC, et al (1994) Experimental simulations of explosive degassing of magma. Nature 372:85–88. doi: 10.1038/372085a0

Mader HMM, Llewellin EWW, Mueller SPP (2013) The rheology of two-phase magmas: A review and analysis. J Volcanol Geotherm Res 257:135–158. doi: 10.1016/j.jvolgeores.2013.02.014

Magloughlin JF, Spray JG (1992) Frictional melting processes and products in geological materials: introduction and discussion. Tectonophysics 204:197–204. doi: 10.1016/0040-1951(92)90307-R

Mahabadi OK, Cottrell BE, Grasselli G (2010) An example of realistic modelling of rock dynamics problems: FEM/DEM simulation of dynamic brazilian test on Barre Granite. Rock Mech Rock Eng 43:707–716. doi: 10.1007/s00603-010-0092-7

Mahabadi OK, Tatone BS a, Grasselli G (2014) Influence of microscale heterogeneity and microstructure on the tensile behavior of crystalline rocks. J Geophys Res Solid Earth 119:5324–5341. doi: 10.1002/2014JB011064

Mair K, Main I, Elphick S (2000) Sequential growth of deformation bands in the laboratory. J Struct Geol 22:25–42. doi: 10.1016/S0191-8141(99)00124-8

Maire E, Le Bourlot C, Adrien J, et al (2016) 20 Hz X-ray tomography during an in situ tensile

test. Int J Fract. doi: 10.1007/s10704-016-0077-y

Major JJ, Lara LE (2013) Overview of Chaitén Volcano, Chile, and its 2008-2009 eruption. Andean Geol. doi: 10.5027/andgeoV40n2-a01

Manga M, Castro J, Cashman K V., Loewenberg M (1998) Rheology of bubble-bearing magmas. J Volcanol Geotherm Res 87:15–28. doi: 10.1016/S0377-0273(98)00091-2

Maria A, Carey S (2007) Quantitative discrimination of magma fragmentation and pyroclastic transport processes using the fractal spectrum technique. J Volcanol Geotherm Res 161:234–246. doi: 10.1016/j.jvolgeores.2006.12.006

Marone C (1998a) Laboratory-Derived Friction Laws and Their Application To Seismic Faulting. Annu Rev Earth Planet Sci 26:643–696. doi: 10.1146/annurev.earth.26.1.643

Marone C (1998b) The effect of loading rate on static friction and the rate of fault healing during the earthquake cycle. Nature 391:69–72.

Marone C, Scholz CH (1989) Particle-size distribution and microstructures within simulated fault gouge. J Struct Geol 11:799–814. doi: 10.1016/0191-8141(89)90099-0

Martel C, Schmidt BC (2003) Decompression experiments as an insight into ascent rates of silicic magmas. Contrib to Mineral Petrol 144:397–415. doi: 10.1007/s00410-002-0404-3

Marti J, Soriano C, Dingwell DB (1999) Tube pumices as strain markers of the ductile ± brittle transition during magma fragmentation.

Martin RS, Mather TA, Pyle DM, et al (2009) Size distributions of fine silicate and other particles in masaya's volcanic plume. J Geophys Res Atmos 114:1–13. doi: 10.1029/2008JD011211

Maryanto S, Iguchi M, Tameguri T (2008) Constraints on the source mechanism of harmonic tremors based on seismological, ground deformation, and visual observations at Sakurajima volcano, Japan. J Volcanol Geotherm Res 170:198–217. doi: 10.1016/j.jvolgeores.2007.10.004

Masotta M, Ni H, Keppler H (2014) In situ observations of bubble growth in basaltic, andesitic and rhyodacitic melts. Contrib to Mineral Petrol 167:976. doi: 10.1007/s00410-014-0976-8

Massol H, Jaupart C (2009) Dynamics of magma flow near the vent: Implications for dome eruptions. Earth Planet Sci Lett 279:185–196. doi: 10.1016/j.epsl.2008.12.041

Matoza RS, Chouet BA, Dawson PB, et al (2015) Source mechanism of small long-period events at Mount St. Helens in July 2005 using template matching, phase-weighted stacking, and full-waveform inversion. J Geophys Res B Solid Earth 120:6351–6364. doi: 10.1002/2015JB012279

Maxwell JC (1867) On the Dynamical Theory of Gases. Philos Trans R Soc London 157:49–88. doi: 10.1098/rstl.1867.0004

McGuinness MJ, Scheu B, Fowler AC (2012) Explosive fragmentation criteria and velocities for vesicular magma. J Volcanol Geotherm Res 237–238:81–96. doi: 10.1016/j.jvolgeores.2012.05.019

McLeod CL, Brandon AD, Fernandes VA, et al (2016) Constraints on formation and evolution of the lunar crust from feldspathic granulitic breccias NWA 3163 and 4881. Geochim Cosmochim Acta 187:350–374. doi: 10.1016/j.gca.2016.04.032

Melnik O, Barmin AA, Sparks RSJ (2005) Dynamics of magma flow inside volcanic conduits with bubble overpressure buildup and gas loss through permeable magma. J Volcanol Geotherm Res 143:53–68. doi: 10.1016/j.jvolgeores.2004.09.010

Meredith PG, Atkinson BK (1985) Fracture toughness and subcritical crack growth during high-temperature tensile deformation of Westerly granite and Black gabbro. Phys Earth Planet Inter 39:33–51. doi: 10.1016/0031-9201(85)90113-X

Meredith PG, Atkinson BK (1983) Stress corrosion and acoustic emission during tensile crack propagation in Whh Sill dolerite and other basic rocks. Geophys J R astr Soc 75:1–21. doi: 10.1111/j.1365-246X.1983.tb01911.x

Meredith PG, Main IG, Jones C (1990) Temporal variations in seismicity during quasi-static and dynamic rock failure. Tectonophysics 175:249–268. doi: 10.1016/0040-1951(90)90141-T

Michaut C, Bercovici D, Sparks RSJ (2009) Ascent and compaction of gas rich magma and the effects of hysteretic permeability. Earth Planet Sci Lett 282:258–267. doi: 10.1016/j.epsl.2009.03.026

Michaut C, Ricard Y, Bercovici D, Sparks RSJSJ (2013) Eruption cyclicity at silicic volcanoes potentially caused by magmatic gas waves. Nat Geosci 6:856–860. doi: 10.1038/ngeo1928

Miwa T, Geshi N, Shinohara H (2013) Temporal variation in volcanic ash texture during a vulcanian eruption at the Sakurajima volcano, Japan. J Volcanol Geotherm Res 260:80–89. doi: 10.1016/j.jvolgeores.2013.05.010

Mizoguchi K, Hirose T, Shimamoto T, Fukuyama E (2007) Reconstruction of seismic faulting by high-velocity friction experiments: An example of the 1995 Kobe earthquake. Geophys Res Lett 34:L01308. doi: 10.1029/2006GL027931

Mizoguchi K, Hirose T, Shimamoto T, Fukuyama E (2008) Internal structure and permeability of the Nojima fault, southwest Japan. J Struct Geol 30:513–524. doi: 10.1016/j.jsg.2007.12.002

Mizoguchi K, Hirose T, Shimamoto T, Fukuyama E (2009) High-velocity frictional behavior and microstructure evolution of fault gouge obtained from Nojima fault, southwest Japan. Tectonophysics 471:285–296. doi: 10.1016/j.tecto.2009.02.033

Mogi K (1958) Relations between the eruptions of various volcanoes and the deformations of the ground surfaces around them. Bull. Earthq. Res. Inst. 36:99–134.

Mogi K (1971) Fracture and flow of rocks. Tectonophysics 13:541–568.

Moore BPL, Iverson NR, Iverson RM (2008) Frictional Properties of the Mount St . Helens Gouge. In: A Volcano Rekindled: The Renewed Eruption of Mount St. Helens, 2004–2006 Edited by David R. Sherrod, William E. Scott, and Peter H. Stauffer U.S. Geological Survey Professional Paper 1750, 2008. pp 2004–2006

Mueller S, Llewellin EW, Mader HM (2010) The rheology of suspensions of solid particles. Proc R Soc A Math Phys Eng Sci 466:1201–1228. doi: 10.1098/rspa.2009.0445

Mueller S, Llewellin EW, Mader HM (2011) The effect of particle shape on suspension viscosity and implications for magmatic flows. Geophys Res Lett 38:L13316. doi: 10.1029/2011GL047167

Mueller S, Melnik O, Spieler O, et al (2004) Permeability and degassing of dome lavas undergoing rapid decompression: An experimental determination. Bull Volcanol 67:526–538. doi: 10.1007/s00445-004-0392-4

Mueller S, Scheu B, Spieler O, Dingwell DB (2008) Permeability control on magma fragmentation. Geology 36:399–402. doi: 10.1130/G24605A.1

Mueller SB, Kueppers U, Ayris PM, et al (2016) Experimental volcanic ash aggregation : Internal structuring of accretionary lapilli and the role of liquid bonding. Earth Planet Sci Lett 433:232–240. doi: 10.1016/j.epsl.2015.11.007

Mueller SB, Lane SJ, Kueppers U (2014) Lab-scale ash production by abrasion and collision experiments of porous volcanic samples. J Volcanol Geotherm Res 16:2661. doi: 10.1016/j.jvolgeores.2015.07.013

Nakada S, Miyake Y, Sato H, et al (1995) Endogenous growth of dacite dome at Unzen volcano (Japan), 1993–1994. Geology 23:157. doi: 10.1130/0091-7613(1995)023<0157:EGODDA>2.3.CO;2

Nakada S, Motomura Y (1999) Petrology of the 1991–1995 eruption at Unzen: effusion pulsation and groundmass crystallization. J Volcanol Geotherm Res 89:173–196. doi: 10.1016/S0377-0273(98)00131-0

Nakada S, Shimizu H, Ohta K (1999) Overview of the 1990–1995 eruption at Unzen Volcano. J Volcanol Geotherm Res 89:1–22. doi: 10.1016/S0377-0273(98)00118-8

Nakada S, Uto K, Sakuma S, et al (2005) Scientific Results of Conduit Drilling in the Unzen Scientific Drilling Project (USDP). Sci Drill 18–22. doi: 10.2204/iodp.sd.1.03.2005

Nakamura M, Otaki K, Takeuchi S (2008) Permeability and pore-connectivity variation of pumices from a single pyroclastic flow eruption: Implications for partial fragmentation. J Volcanol Geotherm Res 176:302–314. doi: 10.1016/j.jvolgeores.2008.04.011

Namiki A, Manga M (2008) Transition between fragmentation and permeable outgassing of low viscosity magmas. J Volcanol Geotherm Res 169:48–60. doi: 10.1016/j.jvolgeores.2007.07.020

Namkung H, Xu L-H, Kim CH, et al (2016) Effect of mineral components on sintering of ash particles at low temperature fouling conditions. Fuel Process Technol 141:82–92. doi: 10.1016/j.fuproc.2015.06.004

Nara Y, Kaneko K (2005) Study of subcritical crack growth in andesite using the Double Torsion test. Int J Rock Mech Min Sci 42:521–530. doi: 10.1016/j.ijrmms.2005.02.001

Neuberg JW, Tuffen H, Collier L, et al (2006) The trigger mechanism of low-frequency earthquakes on Montserrat. J Volcanol Geotherm Res 153:37–50. doi: 10.1016/j.jvolgeores.2005.08.008

Nielsen S, Di Toro G, Hirose T, Shimamoto T (2008) Frictional melt and seismic slip. J Geophys Res 113:B01308. doi: 10.1029/2007JB005122

Nishi K, Ono H, Mori H (1999) Global positioning system measurements of ground deformation caused by magma intrusion and lava discharge: the 1990–1995 eruption at Unzendake volcano, Kyushu, Japan. J Volcanol Geotherm Res 89:23–34. doi: 10.1016/S0377-0273(98)00119-X

Nishimura K, Kawamoto T, Kobayashi T, et al (2005) Melt inclusion analysis of the Unzen 1991–1995 dacite: implications for crystallization processes of dacite magma. Bull Volcanol 67:648–662. doi: 10.1007/s00445-004-0400-8

Nishimura T, Iguchi M, Kawaguchi R, et al (2012) Inflations prior to Vulcanian eruptions and gas bursts detected by tilt observations at Semeru Volcano, Indonesia. Bull Volcanol 74:903–911. doi: 10.1007/s00445-012-0579-z

Noguchi S, Toramaru A, Nakada S (2008) Relation between microlite textures and discharge rate during the 1991–1995 eruptions at Unzen, Japan. J Volcanol Geotherm Res 175:141–155. doi: 10.1016/j.jvolgeores.2008.03.025

Odbert HM, Ryan GA, Mattioli GS, et al (2014) Chapter 11 Volcano geodesy at the Soufriere Hills Volcano, Montserrat: a review. Geol Soc London, Mem 39:195–217. doi: 10.1144/M39.11

Ohminato T (2006) Characteristics and source modeling of broadband seismic signals associated with the hydrothermal system at Satsuma-Iwojima volcano, Japan. J Volcanol Geotherm Res 158:467–490. doi: 10.1016/j.jvolgeores.2006.08.004

Ohminato T, Takeo M, Kumagai H, et al (2006) Vulcanian eruptions with dominant single force components observed during the Asama 2004 volcanic activity in Japan. Earth, Planets Sp 58:583–593.

Ohtomo Y, Shimamoto T (1994) Significance of thermal fracturing in the generation of fault gouge during rapid fault motion: An experimental verification. J Tecton Res Group, Japan 39:135–144.

Okumura S, Nakamura M, Nakano T, et al (2010) Shear deformation experiments on vesicular rhyolite: Implications for brittle fracturing, degassing, and compaction of magmas in volcanic conduits. J Geophys Res 115:B06201. doi: 10.1029/2009JB006904

Okumura S, Nakamura M, Takeuchi S, et al (2009) Magma deformation may induce non-explosive volcanism via degassing through bubble networks. Earth Planet Sci Lett 281:267–274. doi: 10.1016/j.epsl.2009.02.036

Okumura S, Nakamura M, Uesugi K, et al (2013) Coupled effect of magma degassing and rheology on silicic volcanism. Earth Planet Sci Lett 362:163–170. doi: 10.1016/j.epsl.2012.11.056

Okumura S, Sasaki O (2014) Permeability reduction of fractured rhyolite in volcanic conduits and its control on eruption cyclicity. Geology 1–4. doi: 10.1130/G35855.1

Okumura S, Uesugi K, Nakamura M, Sasaki O (2015) Rheological transitions in high-temperature volcanic fault zones. J Geophys Res Solid Earth 120:2974–2987. doi: 10.1002/2014JB011532

Pallister JS, Cashman K V., Hagstrum JT, et al (2013) Faulting within the Mount St. Helens

conduit and implications for volcanic earthquakes. Geol Soc Am Bull 125:359–376. doi: 10.1130/B30716.1

Papale P (1999) Strain-induced magma fragmentation in explosive eruptions. Nature 397:425–428.

Paterson MS (1958) EXPERIMENTAL DEFORMATION AND FAULTING IN WOMBEYAN MARBLE. Geol Soc Am Bull 69:465–476. doi: 10.1130/0016-7606(1958)69[465:EDAFIW]2.0.CO;2

Paterson MS (2001) A granular flow theory for the deformation of partially molten rock. Tectonophysics 335:51–61. doi: 10.1016/S0040-1951(01)00045-2

Paterson MS, Wong T-FF (2005) Experimental Rock Deformation - The Brittle Field, 2nd Editio. Springer Berlin Heidelberg, New York

Perras MA, Diederichs MS (2014) A Review of the Tensile Strength of Rock: Concepts and Testing. Geotech Geol Eng 32:525–546. doi: 10.1007/s10706-014-9732-0

Perugini D, Kueppers U (2012) Fractal analysis of experimentally generated pyroclasts: A tool for volcanic hazard assessment. Acta Geophys 60:682–698. doi: 10.2478/s11600-012-0019-7

Pirrie D, Butcher AR, Power MR, et al (2004) Rapid quantitative mineral and phase analysis using automated scanning electron microscopy (QemSCAN); potential applications in forensic geoscience. Geol Soc London, Spec Publ 232:123–136. doi: 10.1144/GSL.SP.2004.232.01.12

Pittarello L, Di Toro G, Bizzarri A, et al (2008) Energy partitioning during seismic slip in pseudotachylyte-bearing faults (Gole Larghe Fault, Adamello, Italy). Earth Planet Sci Lett 269:131–139. doi: 10.1016/j.epsl.2008.01.052

Plail M, Edmonds M, Humphreys MCS, et al (2014) Geochemical evidence for relict degassing pathways preserved in andesite. Earth Planet Sci Lett 386:21–33. doi: 10.1016/j.epsl.2013.10.044

Prior DJ, Mariani E, Wheeler J (2009) EBSD in the Earth Sciences: Applications, Common Practice, and Challenges. In: Schwartz AJ (ed) Electron Backscatter Diffraction in Materials Science. Springer Berlin Heidelberg, pp 345–360

Ray SK (1999) Transformation of cataclastically deformed rocks to pseudotachylyte by pervasion of frictional melt: inferences from clast-size analysis. Tectonophysics 301:283–304. doi: 10.1016/S0040-1951(98)00229-7

Reyes CG, West ME (2011) The Waveform Suite: A Robust Platform for Manipulating Waveforms in MATLAB. Seismol Res Lett 82:104–110. doi: 10.1785/gssrl.82.1.104

Riley CM, Rose WI, Bluth GJS (2003) Quantitative shape measurements of distal volcanic ash. J Geophys Res. doi: 10.1029/2001JB000818

Robert G, Russell JK, Giordano D, Romano C (2008) High-temperature deformation of volcanic materials in the presence of water. Am Mineral 93:74–80. doi: 10.2138/am.2008.2665

Rocchi V, Sammonds PR, Kilburn CRJ (2003) Flow and fracture maps for basaltic rock deformation at high temperatures. J Volcanol Geotherm Res 120:25–42. doi: 10.1016/S0377-0273(02)00343-8

Rodríguez LA, Watson IM, Rose WI, et al (2004) SO2 emissions to the atmosphere from active volcanoes in Guatemala and El Salvador, 1999-2002. J Volcanol Geotherm Res 138:325–344. doi: 10.1016/j.jvolgeores.2004.07.008

Rollinson GK, Andersen JCØO, Stickland RJ, et al (2011) Characterisation of non-sulphide zinc deposits using QEMSCAN®. Miner Eng 24:778–787. doi: 10.1016/j.mineng.2011.02.004

Romano C, Mungall JE, Sharp T, Dingwell DB (1996) Tensile strengths of hydrous vesicular glasses: An experimental study. Am Mineral 81:1148–1154.

Roscoe R (1952) The viscosity of suspensions of rigid spheres. Br J Appl Phys 3:267.

Rose W (1972) Santiaguito volcanic dome, Guatemala. Geol Soc Am Bull. doi: 10.1130/0016-7606(1972)83

Rose WI, Palma JL, Delgado Granados H, Varley N (2013) Open-vent volcanism and related hazards: Overview. In: Understanding Open-vent Volcanism and Related Hazards. Geological Society of America Special Publications, pp vii–xiii

Rose WI, Self S, Murrow PJ, et al (2008) Nature and significance of small volume fall deposits at composite volcanoes: Insights from the October 14, 1974 Fuego eruption, Guatemala. Bull Volcanol 70:1043–1067. doi: 10.1007/s00445-007-0187-5

Rowe MC, Thornber CR, Kent AJR (2008) Identification and Evolution of the Juvenile Component in. A Volcano Rekindled Renewed Erupt Mt St Helens, 2004–2006 2004–2006.

Rudnicki JW, Rice JR (1975) Conditions for the localization of deformation in pressure-sensitive dilatant materials. J Mech Phys Solids 23:371–394. doi: 10.1016/0022-5096(75)90001-0

Ruina A (1983) Slip instability and state variable friction laws. J Geophys Res Solid Earth 88:10359–10370. doi: 10.1029/JB088iB12p10359

Rust AC, Cashman K V., Wallace PJ (2004) Magma degassing buffered by vapor flow through brecciated conduit margins. Geology 32:349–352. doi: 10.1130/G20388.2

Rust AC, Manga M, Cashman K V (2003) Determining flow type, shear rate and shear stress in magmas from bubble shapes and orientations. J Volcanol Geotherm Res 122:111–132. doi: 10.1016/S0377-0273(02)00487-0

Sahetapy-Engel ST, Harris AJL, Marchetti E (2008) Thermal, seismic and infrasound observations of persistent explosive activity and conduit dynamics at Santiaguito lava dome, Guatemala. J Volcanol Geotherm Res 173:1–14. doi: 10.1016/j.jvolgeores.2007.11.026

Saito T, Ishikawa N (2012) Pre- and syn-eruptive conditions inferred from the magnetic petrology of Fe–Ti oxides from three historical eruptions of Unzen Volcano, Japan. J Volcanol Geotherm Res 247–248:49–61. doi: 10.1016/j.jvolgeores.2012.07.013

Salzer JT, Nikkhoo M, Walter TR, et al (2014) Satellite radar data reveal short-term pre-explosive displacements and a complex conduit system at VolcÃ¡n de Colima, Mexico.

Front Earth Sci 2:1–11. doi: 10.3389/feart.2014.00012

Sammis CG, Ashby MF (1986) The failure of brittle porous solids under compressive stress states. Acta Metall 34:511–526. doi: 10.1016/0001-6160(86)90087-8

Sanderson RWW, Johnson JBB, Lees JMM (2010) Ultra-long period seismic signals and cyclic deflation coincident with eruptions at Santiaguito volcano, Guatemala. J Volcanol Geotherm Res 198:35–44. doi: 10.1016/j.jvolgeores.2010.08.007

Sato H, Fujii T, Nakada S (1992) Crumbling of dacite dome lava and generation of pyroclastic flows at Unzen volcano. Nature 360:664–666. doi: 10.1038/360664a0

Scarpati C, Sparice D, Perrotta A (2014) A crystal concentration method for calculating ignimbrite volume from distal ash-fall deposits and a reappraisal of the magnitude of the Campanian Ignimbrite. J Volcanol Geotherm Res 280:67–75. doi: 10.1016/j.jvolgeores.2014.05.009

Scharff L, Hort M, Gerst A (2014) The dynamics of the dome at Santiaguito volcano, Guatemala. Geophys J Int. doi: 10.1093/gji/ggu069

Scharff L, Hort M, Varley NR (2015) Multiple-pulsed Vulcanian explosions: A characterization of eruption dynamics using Doppler radar. Geology 43:995–998. doi: 10.1130/G36705.1

Scholz CH (1998) Earthquakes and friction laws. Nature 391:37–42. doi: 10.1038/34097

Schwarzkopf L, Schmincke H-U, Troll V. (2001) Pseudotachylite on impact marks of block surfaces in block-and-ash flows at Merapi volcano, Central Java, Indonesia. Int J Earth Sci 90:769–775. doi: 10.1007/s005310000171

Scott JAJ, Mather TA, Pyle DM, et al (2012) The magmatic plumbing system beneath Santiaguito Volcano, Guatemala. J Volcanol Geotherm Res 237–238:54–68. doi: 10.1016/j.jvolgeores.2012.05.014

Scott JAJ, Pyle DM, Mather TA, Rose WI (2013) Geochemistry and evolution of the Santiaguito volcanic dome complex, Guatemala. J Volcanol Geotherm Res 252:92–107. doi: 10.1016/j.jvolgeores.2012.11.011

Self S, Wilson L, Nairn IA (1979) Vulcanian eruption mechanisms. Nature 277:440–443. doi: 10.1038/277440a0

Shand J, Shand SJ (1916) The pseudotachylyte of Parijs (Orange Free State) and its Relation to "Trap-Shotten Gneiss" and "Flinty Crush-Rock." J Geol Soc London 72:198–217. doi: 10.1144/GSL.JGS.1916.072.01-04.12

Sheorey PR (1994) A Theory for In Situ Stresses in Isotropic and Transversely Isotropic Rock. Int J Rock Mech Min Sci Geomech Abstr 31:23–34. doi: 10.1016/0148-9062(94)91070-7

Shimamoto T, Lin A (1994) Is frictional melting equilibrium melting, or non-equilibrium melting.

Shimamoto T, Nagahama H (1992) An argument against the crush origin of pseudotachylytes based on the analysis of clast-size distribution. J Struct Geol 14:999–1006. doi: 10.1016/0191-8141(92)90031-Q

Shimamoto T, Tsutsumi A (1994) A new rotary-shear high-speed frictional testing machine: its basic design and scope of research. J Tecton Res Group, Japan 39:65–78.

Sibson R (1975) Generation of pseudotachylyte by ancient seismic faulting. Geophys J Int 43:775–794. doi: 10.1111/j.1365-246X.1975.tb06195.x

Sigurdsson H, Carey S (1989) Plinian and co-ignimbrite tephra fall from the. Bull Volcanol 51:243–270. doi: 10.1007/BF01073515

Smellie JL, Millar IL, Rex DC, Butterworth PJ (1998) Subaqueous, basaltic lava dome and carapace breccia on King George Island, South Shetland Islands, Antarctica. Bull Volcanol 59:245–261. doi: 10.1007/s004450050189

Smith JV, Miyake Y, Oikawa T (2001) Interpretation of porosity in dacite lava domes as ductile–brittle failure textures. J Volcanol Geotherm Res 112:25–35. doi: 10.1016/S0377-0273(01)00232-3

Smith R, Kilburn C, Sammonds P (2007) Rock fracture as a precursor to lava dome eruptions at Mount St Helens from June 1980 to October 1986. Bull Volcanol 69:681–693. doi: 10.1007/s00445-006-0102-5

Smith R, Sammonds PR, Kilburn CRJ (2009) Fracturing of volcanic systems: Experimental insights into pre-eruptive conditions. Earth Planet Sci Lett 280:211–219. doi: 10.1016/j.epsl.2009.01.032

Smith R, Sammonds PR, Tuffen H, Meredith PG (2011) Evolution of the mechanics of the 2004–2008 Mt. St. Helens lava dome with time and temperature. Earth Planet Sci Lett 307:191–200. doi: 10.1016/j.epsl.2011.04.044

Sone H, Shimamoto T (2009) Frictional resistance of faults during accelerating and decelerating earthquake slip. Nat Geosci 2:705–708. doi: 10.1038/ngeo637

Song W, Hess KU, Damby DE, et al (2014) Fusion characteristics of volcanic ash relevant to aviation hazards. Geophys Res Lett 41:2326–2333. doi: 10.1002/2013GL059182

Song W, Lavallée Y, Hess K-U, et al (2016) Volcanic ash melting under conditions relevant to ash turbine interactions. Nat Commun 7:10795. doi: 10.1038/ncomms10795

Sparks RSJ (2000) The causes and consequences of eruptions of andesite volcanoes: opening remarks. Philos Trans R Soc A Math Phys Eng Sci 358:1435–1440. doi: 10.1098/rsta.2000.0596

Sparks RSJ (1997) Causes and consequences of pressurisation in lava dome eruptions. Earth Planet Sci Lett 150:177–189. doi: 10.1016/S0012-821X(97)00109-X

Sparks RSJSJ, Walker GP. PL (1977) Significance of vitric-enriched air-fall ashes associated with crystal-enriched ignimbrites. J Volcanol Geotherm Res 2:329–341. doi: 10.1016/0377-0273(77)90019-1

Sparks, Murphy, Lejeune, et al (2000) Control on the emplacement of the andesite lava dome of the Soufriere Hills volcano, Montserrat by degassing-induced crystallization. Terra Nov 12:14–20. doi: 10.1046/j.1365-3121.2000.00267.x

Spieler O, Kennedy B, Kueppers U, et al (2004) The fragmentation threshold of pyroclastic

rocks. Earth Planet Sci Lett 226:139–148. doi: 10.1016/j.epsl.2004.07.016

Spina L, Cimarelli C, Scheu B, et al (2016) On the slow decompressive response of volatile- and crystal-bearing magmas: An analogue experimental investigation. Earth Planet Sci Lett 433:44–53. doi: 10.1016/j.epsl.2015.10.029

Spray J (1995) Pseudotachylyte controversy: Fact or friction? Geology 23:1119. doi: 10.1130/0091-7613(1995)023<1119:PCFOF>2.3.CO;2

Spray JG (2010) Frictional Melting Processes in Planetary Materials: From Hypervelocity Impact to Earthquakes. Annu Rev Earth Planet Sci 38:221–254. doi: 10.1146/annurev.earth.031208.100045

Spray JG (2005) Evidence for melt lubrication during large earthquakes. Geophys Res Lett 32:L07301. doi: 10.1029/2004GL022293

Spray JG (1992) A physical basis for the frictional melting of some rock-forming minerals. Tectonophysics 204:205–221. doi: 10.1016/0040-1951(92)90308-S

Spray JG (1993) Viscosity determinations of some frictionally generated silicate melts: Implications for fault zone rheology at high strain rates. J Geophys Res 98:8053. doi: 10.1029/93JB00020

Spray JG (1997) Superfaults. Geology 25:579–582. doi: 10.1130/0091-7613(1997)025<0579:S>2.3.CO;2

Stix J, Torres RC, Narváez M L, et al (1997) A model of vulcanian eruptions at Galeras volcano, Colombia. J. Volcanol. Geotherm. Res. 77:285–303.

Suzuki-Kamata K, Kusano T, Yamasaki K (2009) Fractal analysis of the fracture strength of lava dome material based on the grain size distribution of block-and-ash flow deposits at Unzen Volcano, Japan. Sediment Geol 220:162–168. doi: 10.1016/j.sedgeo.2009.04.026

Takeuchi S, Tomiya A, Shinohara H (2009) Degassing conditions for permeable silicic magmas: Implications from decompression experiments with constant rates. Earth Planet Sci Lett 283:101–110. doi: 10.1016/j.epsl.2009.04.001

Thelen W, Malone S, West M (2011) Multiplets: Their behavior and utility at dacitic and andesitic volcanic centers. J Geophys Res Solid Earth 116:1–16. doi: 10.1029/2010JB007924

Thomas ME, Neuberg J (2012) What makes a volcano tick--A first explanation of deep multiple seismic sources in ascending magma. Geology 40:351–354. doi: 10.1130/G32868.1

Thomas ME, Neuberg JW (2014) Understanding which parameters control shallow ascent of silicic effusive magma. Geochemistry, Geophys Geosystems 15:4481–4506. doi: 10.1002/2014GC005529

Truby JM, Mueller SP, Llewellin EW, Mader HM (2015) The rheology of three-phase suspensions at low bubble capillary number. Proc Math Phys Eng Sci 471:20140557. doi: 10.1098/rspa.2014.0557

Tsutsumi A, Shimamoto T (1997a) High-velocity frictional properties of gabbro. Geophys Res Lett 24:699–702. doi: 10.1029/97GL00503

Tsutsumi A, Shimamoto T (1997b) Temperature measurements along simulated faults during seismic fault motion. Proc 30th Int Geol Congr 5:223–232.

Tuffen H, Dingwell D (2004) Fault textures in volcanic conduits: evidence for seismic trigger mechanisms during silicic eruptions. Bull Volcanol 67:370–387. doi: 10.1007/s00445-004-0383-5

Tuffen H, Dingwell DB, Pinkerton H (2003) Repeated fracture and healing of silicic magma generate flow banding and earthquakes? Geology 31:1089. doi: 10.1130/G19777.1

Tuffen H, Smith R, Sammonds PR (2008) Evidence for seismogenic fracture of silicic magma. Nature 453:511–4. doi: 10.1038/nature06989

Ulusay R (2015) The ISRM Suggested Methods for Rock Characterization, Testing and Monitoring: 2007-2014. Springer International Publishing, Cham

Umakoshi K, Itasaka N, Shimizu H (2011) High-frequency earthquake swarm associated with the May 1991 dome extrusion at Unzen Volcano, Japan. J Volcanol Geotherm Res 206:70–79. doi: 10.1016/j.jvolgeores.2011.07.004

Umakoshi K, Takamura N, Shinzato N, et al (2008) Seismicity associated with the 1991–1995 dome growth at Unzen Volcano, Japan. J Volcanol Geotherm Res 175:91–99. doi: 10.1016/j.jvolgeores.2008.03.030

Vallance JW, Schneider DJ, Schilling SP (2008) Growth of the 2004-2006 Lava-Dome Complex at Mount St. Helens, Washington. US Geol Surv Prof Pap 1750:169–208.

Varley N, Arámbula-Mendoza R, Reyes-Dávila G, et al (2010) Generation of Vulcanian activity and long-period seismicity at Volcán de Colima, Mexico. J Volcanol Geotherm Res 198:45–56. doi: 10.1016/j.jvolgeores.2010.08.009

Vasseur J, Wadsworth FB, Lavallée Y, et al (2013) Volcanic sintering: Timescales of viscous densification and strength recovery. Geophys Res Lett 40:5658–5664. doi: 10.1002/2013GL058105

Vasseur J, Wadsworth FB, Lavallée Y, et al (2015) Heterogeneity : The key to failure forecasting. Sci Rep. doi: 10.1038/srep13259

Venezky DY, Rutherford MJ (1999) Petrology and Fe–Ti oxide reequilibration of the 1991 Mount Unzen mixed magma. J Volcanol Geotherm Res 89:213–230. doi: 10.1016/S0377-0273(98)00133-4

Vetere FP (2006) Viscous flow of magmas from Unzen volcano , Japan – implication for magma mixing and ascent. Hannover

Violay M, Di Toro G, Gibert B, et al (2014) Effect of glass on the frictional behavior of basalts at seismic slip rates. Geophys Res Lett 41:348–355. doi: 10.1002/2013GL058601

Voight B (1999) Magma Flow Instability and Cyclic Activity at Soufriere Hills Volcano, Montserrat, British West Indies. Science (80-) 283:1138–1142. doi: 10.1126/science.283.5405.1138

von Aulock FW, Kennedy BM, Schipper CI, et al (2014) Advances in Fourier transform infrared spectroscopy of natural glasses: From sample preparation to data analysis. Lithos 206–

207:52–64. doi: 10.1016/j.lithos.2014.07.017

von Aulock FW, Nichols ARL, Kennedy BM, Oze C (2013) Timescales of texture development in a cooling lava dome. Geochim Cosmochim Acta 114:72–80. doi: 10.1016/j.gca.2013.03.012

Wadge G, Ryan G, Calder ES (2009) Clastic and core lava components of a silicic lava dome. Geology 37:551–554. doi: 10.1130/G25747A.1

Wadge G, Voight B, Sparks RSJ, et al (2014) An overview of the eruption of Soufriere Hills Volcano, Montserrat from 2000 to 2010. Geol Soc London, Mem 39:1–40. doi: 10.1144/M39.1

Wadsworth FB, Vasseur J, Scheu B, et al (2016) Universal scaling of fluid permeability during volcanic welding and sediment diagenesis. Geology 44:219–222. doi: 10.1130/G37559.1

Wadsworth FB, Vasseur J, von Aulock FW, et al (2014) Non-isothermal viscous sintering of volcanic ash. J Geophys Res Solid Earth n/a-n/a. doi: 10.1002/2014JB011453

Waite GP, Chouet BA, Dawson PB (2008) Eruption dynamics at Mount St. Helens imaged from broadband seismic waveforms: Interaction of the shallow magmatic and hydrothermal systems. J Geophys Res Solid Earth 113:B02305. doi: 10.1029/2007JB005259

Walker GPL (1971) Grain-size Characteristics of Pyroclastic Deposits. J Geol 79:696–714.

Walker GPL (1972) Crystal concentration in ignimbrites. Contrib to Mineral Petrol 36:135–146. doi: 10.1007/BF00371184

Walker JA, Singer B, Cameron BI, Carr MJ (2011) Monogenetic , behind-the-front volcanism in southeastern Guatemala and western El Salvador: 40Ar/39Ar ages and tectonic implications. Lithos 123:243–253. doi: 10.1016/j.lithos.2010.09.016

Wang W, Scholz CH (1994) Micromechanics of the velocity and normal stress dependence of rock friction. Pure Appl Geophys PAGEOPH 143:303–315. doi: 10.1007/BF00874333

Warr LN, van der Pluijm BA (2005) Crystal fractionation in the friction melts of seismic faults (Alpine Fault, New Zealand). Tectonophysics 402:111–124. doi: 10.1016/j.tecto.2004.12.034

Watanabe K, Ono K, Sakaguchi K, et al (1999) Co-ignimbrite ash-fall deposits of the 1991 eruptions of Fugen-dake, Unzen Volcano, Japan. J Volcanol Geotherm Res 89:95–112. doi: 10.1016/S0377-0273(98)00126-7

Watts RB, Herd R a., Sparks RSJ, Young SR (2002) Growth patterns and emplacement of the andesitic lava dome at Soufriere Hills Volcano, Montserrat. Geol Soc London, Mem 21:115–152. doi: 10.1144/GSL.MEM.2002.021.01.06

Wauthier C, Cayol V, Kervyn F, D'Oreye N (2012) Magma sources involved in the 2002 Nyiragongo eruption, as inferred from an InSAR analysis. J Geophys Res Solid Earth 117:1–20. doi: 10.1029/2011JB008257

Wawersik WR, Fairhurst C (1970) A study of brittle rock fracture in laboratory compression experiments. Int J Rock Mech Min Sci Geomech Abstr 7:561–575. doi: 10.1016/0148-

9062(70)90007-0

Webb S, Dingwell D (1990a) The onset of non-Newtonian rheology of silicate melts. Phys Chem Miner 125–132.

Webb SL, Dingwell DB (1990b) Non-Newtonian rheology of igneous melts at high stresses and strain rates: Experimental results for rhyolite, andesite, basalt, and nephelinite. J Geophys Res 95:15695. doi: 10.1029/JB095iB10p15695

Weinberg RF, Regenauer-Lieb K (2010) Ductile fractures and magma migration from source. Geology 38:363–366. doi: 10.1130/G30482.1

Whittington AG, Hellwig BM, Behrens H, et al (2009) The viscosity of hydrous dacitic liquids: implications for the rheology of evolving silicic magmas. Bull Volcanol 71:185–199. doi: 10.1007/s00445-008-0217-y

Wibberley CAJ, Yielding G, Di Toro G, et al (2008) Recent advances in the understanding of fault zone internal structure: a review. Geol Soc London, Spec Publ 299:5–33. doi: 10.1144/SP299.2

Wiederhorn SM (1974) Strength of glass--a fracture mechanics approach. Natl Tech Inf Serv 485:1–15.

Williams SCP (2013) Studying volcanic eruptions with aerial drones. Proc Natl Acad Sci U S A 110:10881. doi: 10.1073/pnas.1309922110

Williams SN, Self S (1983) The October 1902 plinian eruption of Santa Maria volcano, Guatemala. J Volcanol Geotherm Res 16:33–56. doi: 10.1016/0377-0273(83)90083-5

Wilson TM, Jenkins SF, Stewart C (2015) Volcanic ash fall impacts. In: Loughlin SC, Sparks S, Brown SK, et al. (eds) Global Volcanic Hazards and Risk. Cambridge University Press, Cambridge, pp 281–288

Wohletz KH (1983) Mechanisms of hydrovolcanic pyroclast formation: Grain-size, scanning electron microscopy, and experimental studies. J Volcanol Geotherm Res 17:31–63. doi: 10.1016/0377-0273(83)90061-6

Wohletz KH, Sheridan MF, Brown WK (1989) Particle Size Distributions and the Sequential Fragmentation / Transport Theory Applied to Volcanic Ash. J Geophys Res 94:15703–15721.

Wong T, Baud P, Klein E (2001) Localized failure modes in a compactant porous rock. Geophys Res Lett 28:2521–2524. doi: 10.1029/2001GL012960

Wong TF, Baud P (2012) The brittle-ductile transition in porous rock: A review. J Struct Geol 44:25–53. doi: 10.1016/j.jsg.2012.07.010

Wong T-F, David C, Zhu W (1997) The transition from brittle faulting to cataclasic flow in porous sandstones:Mechanical deformation. J Geophys Res 102:3009–3025. doi: 10.1029/96JB03282

Woods AW (1995) A model of vulcanian explosions. Nucl Eng Des 155:345–357. doi: 10.1016/0029-5493(94)00881-x

Wright HMN, Cashman K V., Rosi M, Cioni R (2007) Breadcrust bombs as indicators of Vulcanian eruption dynamics at Guagua Pichincha volcano, Ecuador. Bull Volcanol 69:281–300. doi: 10.1007/s00445-006-0073-6

Yamasato H (1998) Nature of Infrasonic Pulse Accompanying Low Frequency Earthquake at Unzen Volcano, Japan. Bull Volcanol Soc Japan 43:1–13.

Yamashina K, Matsushima T, Ohmi S (1999) Volcanic deformation at Unzen, Japan, visualized by a time-differential stereoscopy. J Volcanol Geotherm Res 89:73–80. doi: 10.1016/S0377-0273(98)00124-3

Zoback M Lou, Geist E, Pallister J, et al (2013) Advances in natural hazard science and assessment, 1963–2013. Geol Soc Am Spec Pap 501:81–154. doi: 10.1130/2013.2501(05)

Appendices

Appendix A

Thermal vesiculation during volcanic eruptions

I am including this multidisciplinary paper, in which I am a co-author, within the appendices because it has a direct relevance to the work presented in **Chapters 3 and 5,** and because I made significant contributions to the final manuscript as well as the fieldwork, conceptualisation, discussion, and editing processes. The essential idea (and subsequent work) developed within the experimental volcanology group in Liverpool through a comparison between textures found in natural ash and experimental HVR friction samples.

Candidate contribution:

Specific contributions to the paper are as follows:

I conducted the HVR friction experiment in Kochi, Japan, analysed the results and found evidence (using SEM) for bubbles in the melt phase adjacent to the experimental frictional melt zone, as reported in Figure 2 d-e. I found further evidence for heterogeneous melt filaments, reported in Extended data figure 3, and conducted SEM-EDS mapping on heterogeneous melt filaments (Extended data figure 4). I constructed the vesicularity gradient map shown in Extended data figure 7 and helped to conduct the tube furnace experiments and took the resulting SEM images shown in Extended data figure 8. I also made the Coulter grain size distribution measurements and plotted the results (Extended data figure 1)